

TECHNISCHE UNIVERSITÄT MÜNCHEN
Fakultät für Chemie
Lehrstuhl I für Technische Chemie

Shape Matters - Experimental and Numerical Study on the Catalyst Carrier's Geometry and the Utilization of 3d Printing herefor

Jennie Freifrau von Seckendorff-Gutend

Vollständiger Abdruck der von der Fakultät für Chemie der Technischen Universität München zur
Erlangung des akademischen Grades eines

Doktor-Ingenieurs (Dr.-Ing.)

genehmigten Dissertation.

Vorsitzender: Prof. Dr. Klaus Köhler

Prüfer der Dissertation: 1. Prof. Dr.-Ing. Kai-Olaf Martin Hinrichsen
2. Prof. Dr.-Ing. Dirk Weuster-Botz
3. Prof. Dr.-Ing. Gregor D. Wehinger

Die Dissertation wurde am 28.05.2020 bei der Technischen Universität München eingereicht
und durch die Fakultät für Chemie am 16.02.2021 angenommen.

Acknowledgements

The accomplishment of this Dissertation would not have been possible without the support and guidance of some very special people. I herewith would like to show my deepest gratitude to the following:

Prof. Dr.-Ing. Kai-Olaf Hinrichsen for the supervision and guidance through studies and the dissertation project. Without his persistent help, the goal of this project would not have been realized.

My colleagues for many technical discussions and guidance and for the great time spent together. I especially would like to thank Theresa Ludwig being my project partner and having a great and funny time exploring the capabilities of 3d printing, Thomas Burger for his inspiringly helpful attitude and Heidi Holweck for her selfless help whenever needed.

The project partners from Clariant, especially Dr. Normen Szesni for initiating the thesis topic and Dr. Markus Tonigold for the project lead. Moreover, I would like to thank Dr. Sebastian Werner who always was a little ahead of my thoughts and ideas. I would further like to thank the academic partners, especially Dr. Carsten Troll and Prof. Dr. Bernhard Rieger for being a prolific team. And finally, the MuniCat alliance between Technical University of Munich and Clariant, and its Coordinator Prof. Dr. Richard Fischer for generous substantial and financial support.

I would like to recognize the invaluable assistance by external partners, especially Tobias Abstreiter for designing and constructing my 3D Printer and Dr. Klaus Achterhold for running x-ray CT scans.

I wish to express my deepest gratitude to the students running most of the experiments as part of laboratory internships or their Bachelor's or Master's Theses: Joel Bachmann, Maike Beckenkamp, Teng Daquan, Christian Maier, Benedict Schäfer, Raphael Scherbauer, Julian Thomas and Markus Wolff - as well as our guests from TUM Asia Singapur: Adeline, Alex, Angie, Gen, Lim, Mark, Nadia, Pei Ling, Stanley, Yonqing and Yong Ren.

Nobody has been more important to me in the pursuit of this project than the members of my family. Many Thanks to all of you!

Zusammenfassung

In Anbetracht der bemerkenswerten Möglichkeiten hinsichtlich der Produktion komplexer Formen ist die Einbindung von additiver Fertigung (3D-Druck) in den Herstellungsprozess von Industriegütern und Prototypen von zunehmender Bedeutung. In der chemischen Industrie werden für den Einsatz in Festbettreaktoren katalytisch aktive Formkörper traditionell durch Extrusion, Tablettenpressen oder Granulation erzeugt, die jedoch nur geringe Spielräume der Formvariation zulassen. Für den Einsatz in Festbettreaktoren sind die Durchströmungseigenschaften, der Wärme- und der Stofftransport von entscheidender Bedeutung, die jedoch massgeblich von den eingesetzten Formkörpergeometrien abhängig sind.

Im Rahmen des vorliegenden Dissertationsprojektes wurde ein 3D-Drucker nach dem Pulver-Binder-Prinzip für labormaßstäbliches Materialscreening konzipiert, konstruiert und in Betrieb genommen. Die für additive Fertigung problematische Herstellung von mesoporösen Katalysatorträgern aus Keramik bei gleichzeitiger Gewährleistung ausreichender Festigkeit wurde erforscht und entsprechende Formkörper wurden produziert.

Zum Vermessen des Druckverlusts bei Durchströmung von zufälligen Füllkörperschüttungen wurde ein Teststand konzipiert und konstruiert. Mithilfe von 3D-gedruckten Modell-Formkörpern wurden die bekannten Korrelationen überprüft und erweitert.

Für ein abschließendes Formkörpergeometrie-Screening wurde ein numerisches Prozedere entwickelt, bestehend aus dem Design völlig neuartiger und komplexer Formkörper (Autodesk[®] Inventor[®]), dem Erstellen von zufälligen Füllkörperschüttungen mittels *Diskreter Element Methode* (DigiDEM[™], Blender[™]), der Strömungssimulation in OpenFOAM[®] und der Datenanalyse in Python[™]. Die Validierung erfolgte anhand von realen, an zuvor genanntem Teststand experimentell charakterisierten Kugelschüttungen, die mittels Computertomography in ein virtuelles 3D-Modell überführt werden konnten. Untersucht wurden Formkörpergeometrien basierend auf einer kugeligen Grundform kombiniert mit verschiedenen Teil-Geometrien wie Löcher, umlaufende Kanäle, Vertiefungen, Reifen und Buckel. Grundsätzlich muss zwischen einem bevorzugten Strömungsfeld und einem vorteilhaften Druckverlust entschieden werden, da diese gegenläufig von Geometrieänderungen beeinflusst werden. Als Entscheidungshilfe wurde eine dimensionslose Kennzahl entwickelt, die die relevanten Parameter Druckverlust, geometrische Oberfläche, Streuung des Geschwindigkeitsfeldes - stellvertretend für die Verweilzeitverteilung -, und die Strömung in radialer Richtung - stellvertretend für die radiale Dispersion - in ein Verhältnis setzt. Je nach anwendungsspezifischer Gewichtung dieses Parameters sind unterschiedliche Formkörpergeometrien von Vorteil.

Abstract

Considering the remarkable possibilities of producing complex shapes, the incorporation of additive manufacturing (3D printing) into the manufacturing process of industrial goods and prototypes is becoming increasingly important. In the chemical industry, catalytically active moldings are traditionally produced by extrusion, tablet presses or granulation for use in fixed-bed reactors, which, however, allow only slight freedom of form variation. Within these catalyst packings, the flow characteristics, the heat and the mass transfer are of crucial importance, but these are significantly dependent on the shaped body's geometries used.

As part of the dissertation project, a 3D printer based on the powder-binder principle for laboratory-scale material screening was designed, constructed and put into operation. The production of mesoporous catalyst carriers of ceramic, which is problematic for additive manufacturing while at the same time ensuring sufficient strength, has been investigated and corresponding moldings have been produced.

A testing set-up was designed and constructed to measure the pressure loss during flow through random packing. 3D-printed model moldings were used to verify and extend the known correlations.

For a final mold geometry screening, a numerical procedure was developed consisting of the design of completely new and complex moldings (Autodesk[®] Inventor[®]), the creation of random packed beds using the Discrete Element Method (DigiDEM[™], Blender[™]), the flow simulation in OpenFOAM[®] and the data analysis in Python[™] and Matlab[®]. The validation was carried out on the basis of sphere packings which were experimentally characterized at the previously mentioned testing set-up and which could be transferred into a virtual 3D model using also the experimental results of x-ray computer tomography. Shapes based on a sphere combined with different features such as holes, circumferential ducts, cavities, bellies, and drops were investigated. In general, a decision between preferred flow field characteristics and beneficial pressure drop values is required, as these are affected opposingly by geometry variations. As a decision-making tool, a dimensionless number was developed, proportioning the relevant parameters pressure drop, geometric surface area, flow field distribution - representing the width of residence time distribution -, and the flow in radial direction - representing radial dispersion. Depending on an application specific weighting of this parameter, different shapes become beneficial.

Contents

Abstract	v
Introduction	1
I Additive Manufacturing of Catalyst Support Structures	5
1 Review on Customization of Binder Jetting (3D Printing) for the Manufacturing of Alumina Catalyst Carriers	7
1.1 Introduction	9
1.1.1 Printing of (supported) Catalysts	9
1.1.2 Printing of Alumina Ceramics	10
1.2 Development of Custom Material Combinations	13
1.2.1 Printer Setup	13
1.2.2 Powder Feedstock	14
1.2.3 Formulation of Liquid Binder	17
1.2.4 Powder-Binder Interplay	20
1.2.5 Post-Processing	21
1.2.6 Concluding Remarks	23
1.3 Experimental	23
1.3.1 Printer Setup	23
1.3.2 Powder Characterization	24
1.3.3 Printer Validation	24
1.3.4 Binder Preparation	24
1.3.5 Post-Treatment and Characterization	25
1.4 Results and Discussion	25
1.4.1 Powder Characterization	25
1.4.2 Printer Setup Validation	30
1.4.3 Binder Formulation and Powder-Binder Interplay	31
1.4.4 Post-Processing and Analysis of Final Parts	31
1.5 Summary and Optimization Outlook	32
Nomenclature	35
Appendix	39
References	43

II	The Structure of Randomness - Experimental Investigation of Random Packed Beds	51
2	Review on the Structure of Random Packed Beds	53
2.1	Introduction	55
2.2	Experimental investigation of packed-bed structures	56
2.2.1	Regular arrangements of spatially extended mono-sized ideal spheres	56
2.2.2	Random packings of smooth mono-sized ideal spheres in cylindrical confining walls	56
2.2.3	Influence of particle shape	74
2.2.4	Influence of particle material	82
2.2.5	Influence of tube shape and material	83
2.3	Numerically packed-beds	83
2.3.1	Influence of material and packing procedure	84
2.3.2	Influence of the shape	84
2.3.3	Further notable results	87
2.4	Conclusion	88
	Nomenclature	90
	References	92
3	Experimental Study on the Influence of Filling Method and Particle Material on the Packed-Bed Porosity	107
3.1	Introduction	109
3.1.1	Wall Effect	109
3.1.2	Packing Mode	110
3.1.3	Particle Material	110
3.2	Experimental	110
3.3	Results and Discussion	111
3.3.1	Diameter Ratio λ and Filling Method	112
3.3.2	Filling Method and Material	113
3.3.3	Material and Diameter Ratio λ	113
3.4	Conclusion	115
	Nomenklatur	116
	References	117
4	Experimental Characterization of Random Packed Spheres, Cylinders and Rings, and their Influence on Pressure Drop	119
4.1	Introduction	121
4.1.1	Bulk packing characteristics	121
4.1.2	Confined packed-beds	123
4.1.3	Pressure drop	124
4.1.4	Objectives	125
4.2	Experimental setup	125
4.2.1	Experimental packing generation	125
4.2.2	Experimental determination of pressure drop	127

4.3	Results and discussion	128
4.3.1	Mean bed porosity and filling method	128
4.3.2	Influence of tube shape	134
4.3.3	Pressure drop of cylinder packings	138
4.4	Conclusion	141
	Nomenclature	144
	References	146
5	Experimental and Numerical Analysis of Void Structure in Random Packed Beds of Spheres	151
5.1	Introduction	153
5.2	State of the art	153
5.2.1	Axially- and azimuthally-averaged radial porosity profiles	153
5.2.2	Mean bed porosities	155
5.2.3	Numerical packed bed generation	157
5.3	Experimental and numerical setup	157
5.3.1	Analysis of local packing structure using X-ray CT	157
5.3.2	Image analysis	158
5.3.3	Calculation of axial and radial porosity profiles	158
5.3.4	Numerical packing generation with DigiDEM TM	159
5.4	Results an discussion	161
5.4.1	Experimental results of X-ray study	161
5.4.2	Validation of numerical packing generation	168
5.4.3	Extrapolation of results	169
5.5	Conclusion	177
	Nomenclature	179
	References	181
III	Shape Matters - Numerical Study on Shape Optimization	187
6	Numerical Shape Development Study in View of Random Packed Beds. Part I: The Yo-Yo Shape	189
6.1	Introduction	191
6.2	Theory	192
6.2.1	Packing structure	192
6.2.2	Fluid dynamics	193
6.3	Methods	194
6.3.1	Shape design	194
6.3.2	Numerical packing generation	196
6.3.3	Mesh creation and mesh study	196
6.3.4	Steady-state and dynamic flow simulation	197
6.3.5	Post-processing	198

6.4	Results and discussion	199
6.4.1	Geometrical considerations	199
6.4.2	Flow field features	203
6.4.3	Pressure drop characteristics	207
6.4.4	Residence time properties	209
6.5	Conclusion	210
	Nomenclature	212
	Appendix	214
	References	219
7	Numerical Shape Development Study in View of Random Packed Beds. Part II: The Design of Experiment	223
7.1	Introduction	225
7.1.1	Target Parameter	225
7.2	Numerical Setup	226
7.2.1	Shape Design and Design of Experiment	227
7.2.2	Numerical Packing Generation	227
7.2.3	Computational Fluid Dynamics	229
7.3	Results	229
7.3.1	Packing Structure	229
7.3.2	Design of Experiment	231
7.3.3	Extrapolation of Results	231
7.3.4	Packing Structure and Resulting Pressure Drop	232
7.4	Conclusion	233
	Nomenclature	234
	References	235
8	Numerical Shape Development Study in View of Random Packed Beds. Part III: Sphere Feature Evaluation	237
8.1	Introduction	239
8.1.1	Packing Structure	239
8.1.2	Fluid Dynamics	240
8.2	Simulation Procedure	241
8.2.1	Shape Design	241
8.2.2	Numerical Packing Generation	243
8.2.3	Numerical Fluid Dynamics	243
8.3	Results and Discussion	243
8.3.1	Geometrical Considerations	243
8.3.2	Flow Field Analysis	246
8.3.3	Packing Friction	248
8.3.4	Effective Porosity	250
8.3.5	Upgraded Bed Effectivity Parameter	251
8.4	Conclusion	253
	Nomenclature	255

Appendix	257
References	262
Abbildungsverzeichnis	267
Tabellenverzeichnis	273

Introduction

In chemical engineering, one of the major workhorses in heterogeneous catalysis is the packed bed reactor. The solid catalyst material is packed into the reactor tubes and flown through by the reaction substrates and products, in either single- or multiphase. While heterogeneously catalyzed single phase reactions are somewhat easy to describe, multi-phase reactions, especially those with gas-liquid phase transitions during the reaction, as for instance the Liquid Organic Hydrogen Carrier System, are significantly more demanding. Energy consumption, hot spot formation, catalyst deactivation, selectivity, and yield are only some parameters characterizing the efficiency of a reactor. These strongly depend on the selected operating point and the incorporated catalyst features. More precisely, fluid dynamics, heat and mass transfer conditions need to be optimized which for instance can be achieved by varying the incorporated catalyst packing type and shape.

Packing Types

Utilized packing types comprise random bulks of powders or small shaped packing elements, structured monoliths, unstructured foams, and structured cellular arrays. These packing types vary in their wall contact, pressure drop, radial dispersion, heat transfer, mass transfer, residence time distribution, occurrence of dead zones and channeling, required amount of active material, need for subsequent coating procedures, ease of handling and replacement, mechanical stability, reliability and consistency, production costs and lifetime. While random packed shaped elements come with a significantly larger pressure drop, novel cellular structures offer pronounced handling and replacement issues at a much higher production price. Thus, the selection of the appropriate packing type is very case sensitive and needs to be geared to the particular reaction system.

Despite some novel developments regarding structured packings, the random shaped element packing remains the industrial standard for packed-bed reactor fillings. The incorporated shaped catalysts can be produced easily, cheaply and with high rates by tablet pressing and extrusion processes. The catalysts are either produced directly or shaped carrier particles are subsequently coated, infiltrated, vapor deposited or impregnated with the respective active material. Almost any material can be processed with these tools. The drawbacks include a limited shape selection as typically only the geometry of the cross-section can be adjusted, inhomogeneities of the shapes due to the production technique (especially extrusion, where all particles come with different lengths and may be bent to certain degrees), a reduced mechanical strength leading to breakage issues, and the significantly larger pressure drop due to the higher solid content in the reactor. This pressure drop, however, may be reduced drastically by packing particles of

more complex shapes, for instance having holes in different directions. In order to produce these complex shapes, novel manufacturing techniques need to be implemented, especially additive manufacturing techniques, also known as 3d printing, have recently gained much attention and caused certain ambitions in the community.

Novel Issues

With the evaluation of 3d printing as a potential novel manufacturing technique for catalytic shapes questions arise including the material compatibility and which shapes to actually produce. Early optimism was overrun by reality, that not any stock material powder can be used in 3d printing right away. Only powders with certain properties were able to be processed at all. Researchers and industry realized that the introduction of additive manufacturing tools into the catalyst production scheme would require decent material optimization and variation.

Moreover, as with the classic manufacturing techniques, only a small shape selection is at all possible, the research regarding packed beds is limited to these easy shapes. So even, if 3d printing would be available as manufacturing technique right away, hardly any knowledge is on hand regarding the shapes to print.

Objectives of this thesis

The objectives of this thesis can thus be summarized by evaluating the potentials and limitations to print inert alumina catalyst carriers having a high BET surface area and sufficient mechanical strength using a powder-binder 3d printer, also known as binder jetting technique; and to simultaneously develop an optimized shape for random packing elements that can be produced with the very same printing technique.

In terms of the first objective, the actual printing of catalyst carriers, the major issue to be solved was the unavailability of an affordable laboratory scale printer, that is customizable in regard to the used powders and binder liquids. Most commercially available 3d printing systems are *closed systems*, not allowing material variation, except for the officially vendored products. Consequently, a major time fraction was spent on designing and constructing an own laboratory-scale multi-purpose and multi-material printer. The remaining time was used to perform proof-of-concept studies whose results are discussed in part I of this thesis (see Chapter 1). In this context, previous results of pre-material studies were published with shared authorship but are herein not further included:

T. Ludwig, J. von Seckendorff, C. Troll, R. Fischer, M. Tonigold, B. Rieger, O. Hinrichsen, Additive Manufacturing of Al₂O₃-based carriers for heterogeneous catalysis, *Chemie Ingenieur Technik*, **2018**, *90*, 703-707.

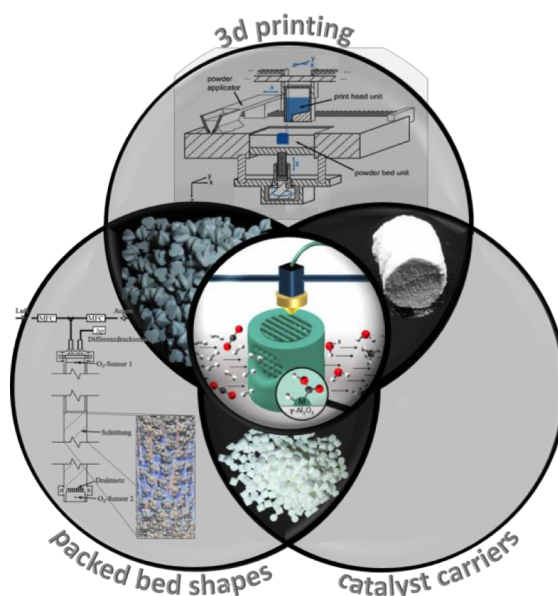


Figure: Schematic overview of objectives addressed in this thesis.

In terms of the second objective, the shape optimization, a holistic multi-step approach was implemented, comprising the two major subtasks of understanding packed beds of simple shapes and validate numerical tools based on these, and the actual shape optimization. These subtopics are addressed in *Part II: The Structure of Randomness - Experimental Investigation of Random Packed Beds* and *Part III: Shape Matters - Numerical Study on Shape Optimization* of this thesis, respectively. Herein, in part II, a literature review is conducted in regard to structural parameters of packed beds (see Chapter 2), followed by an experimental study comprising average packing conditions for a packed bed of spheres (see Chapter 3), an experimental study regarding the influence of simple shapes including cylinders and hollow cylinders (see Chapter 4), and an experimental study investigating local packing properties in packed beds of spheres using x-ray tomography including the numerical packing generation validation using this data (see Chapter 5). In this context, a paper was published with shared authorship comparing different numerical packing generation tools, but is not further included in this thesis:

J. Fernengel, J. von Seckendorff, O. Hinrichsen, Influence of cylinder-to-particle diameter ratio and filling speed on bed porosity of random packed beds of spheres, *Proceedings of the 28th European Symposium on Computer Aided Process Engineering*, **2018**, 97-102.

Part III of this thesis comprises a literature review of patented catalyst shapes combined with a systematical shape study incorporating the novel Yo-Yo shape (see Chapter 6), a Design of Experiment study regarding the very same Yo-Yo shape (see Chapter 7), and the final much broader shape study comprising all kinds of sphere-based shape variations (see Chapter 8). With this last chapter summarizing and concluding the knowledge gained throughout the thesis and arising future research questions it shall be seen as the outlook of this dissertation.

It is to be pointed out, that the knowledge gained in terms of random packed beds could be related back to the first major topic of this thesis, the 3d printing, as the most important part of a powder-binder printer is a powder-bed where the same rules apply to, except in a smaller size scale. Or easier put, besides catalytic packed bed reactors, powder-beds used in various additive manufacturing techniques constitute another perfect application example of random packings.

Part I

Additive Manufacturing of Catalyst Support Structures

1 Review on Customization of Binder Jetting (3D Printing) for the Manufacturing of Alumina Catalyst Carriers

Abstract

The integration of 3d printing into the actual manufacturing process of catalyst shaped bodies is of increasing concern, due to its conspicuous capability regarding to geometric freedom and flexibility. *Binder Jetting* was selected as 3d printing technique primarily due to easy scale-up options. A comprehensive literature review on the customization of binder jetting 3d printers has been performed. Based on this, a lab-scale printer was constructed in which powder and binder formulations were tested on a proof-of-principle basis. As example, spray dried γ -alumina powder having a high sphericity and a broad size distribution combined with a boehmite-sol as binding agent utilized in a pre-printing setup lead to cylindrical parts having specific surface areas (BET) of up to $190 \text{ m}^2 \text{ g}^{-1}$ while withstanding side crush loads of 19 N.

1.1 Introduction

The impressive opportunities 3d printing technologies seem to provide attract the attention throughout the whole palette of industrial sectors. Originally been used as mere prototyping tool, the integration of 3d printing into the actual manufacturing process is of increasing interest [1]. The production of heterogeneous catalysts among the chemical industry is only one example where the promising attempt is risked to evaluate the potentialities and limitations for the extension or replacement of existing production processes by Additive Manufacturing (AM) [2–4].

Within the manufacturing process, catalytic materials are shaped to structured or random packing elements that allow the reaction gases to pass low-drag through the reaction vessel while the reaction takes place at the catalyst's surface. Fluid dynamics, heat and mass transfer strongly depend on the shaped catalyst's geometry [4]. However, traditional shaping technologies, most predominantly tablet pressing and extrusion, are very limited regarding their contrivable geometric flexibility. Compared to this, additive manufacturing is theoretically capable to produce almost all imaginable, highly complex structures, giving rise to the question, if and to what extent catalyst material of comparable quality can be manufactured by 3d printing.

1.1.1 Printing of (supported) Catalysts

For a small selection of reactions, catalyst systems have been investigated concerning their printability. Among additive manufacturing of (micro) reactors and mixers [3, 5], these comprise catalysts for electrochemical reactions [6, 7], biological activity [8], organic synthesis [9–11], inorganic reactions [12–20], and adsorption processes [21].

Concerning chemical reactions, besides shape and size of the manufactured body, few reactions are fairly unpretentious regarding their catalyst requirements, however, most demand high specific surface areas, finely tuned pore systems (size, volume, distribution) and a tailored selection of involved chemical species (active catalyst, promoters, support) [22]. Frequently, supported catalysts are used, where small amounts of commonly valuable active components are affixed on primarily ceramic, for example alumina, silica and zirconia, or charcoaled carrier powders or shapes [23]. Preparation methods comprising precipitation, deposition and impregnation techniques (see [22–24] for more) add the catalyst species either before or after the shaping process, leading to active components evenly distributed throughout the whole shape, in confined layers or merely on the outer surface.

In general, the additive manufacturing of (supported) catalysts can be categorized into the following scenarios:

- Printing of a negative template (mold) followed by filling it with catalytic and/or support material (casting) and subsequent template removal;

- Printing of a solid core structure of any material with subsequent separate application of support and/or catalyst species by known methods such as coating;
- Printing of catalyst support with subsequent separate application of catalyst species by known methods such as impregnation;
- Direct printing of the (supported) catalyst.

For the first two scenarios, commercial printers and materials can be used right away. However, the casting approach, as described by Michorczyk et al. [25] and Hammel et al. [26] is laborious while wasting significant amounts of template materials and is thus of minor interest. On contrary, it was repeatedly shown, that the coating approach is feasible on a lab scale basis [13–15, 18–20, 27, 28]. Hereby, the challenge lies rather in the wash-coat application process and the adhesion between core structure and coating, then in the actual printing procedure.

The other two scenarios require extensive research concerning the material and printer interplay. Among the typically used additive manufacturing techniques, *Direct Ink Writing* (DIW), also called *Robocasting* or *3d Fiber Deposition*, is the most obvious approach as it resembles a small scale paste extrusion process, similar to the traditional catalyst shaping techniques. Furthermore, it is easy to handle, cheap to acquire and allows an incredible material variety with comparably low material requirements. Thus, some pioneering work concerning catalyst and/or carrier printing was already performed and presented [9–12, 16, 20, 29]. On the downside, surface accuracy, geometric level of detail and scaling up options constitute ambitious challenges yet not solved.

Other theoretically feasible 3d printing techniques for the manufacturing of catalysts and supports comprise *Direct Ink-Jet Printing* (DIP), *Fused Deposition Modelling* (FDM), *Fused Deposition of Ceramics* (FDC), *Stereolithography* (SLA), powder-binder-based systems and powder-laser-based techniques. An overview of the respective operating principles can be found elsewhere [2–4]. However, due to complex technical and material requirements, only occasional attempts regarding catalyst and/or support printing were described yet [29–33]. Recently, Ludwig et al. [29] compared DIW, SLA, FDC and powder-based *Binder Jetting* (BJ) technique, also referred to as *Powder-Binder 3d Printing*, regarding their suitability of printing alumina catalyst support structures with increased surface area, whereby only DIW gave results with good prospects.

1.1.2 Printing of Alumina Ceramics

The printing of alumina, as schematically depicted in Fig. 1.1, while targeting dense parts is widely described in literature. Techniques such as SLA [34–37], DIW [9, 11, 20, 38–40], FDC [41], powder-laser-based techniques [42], slurry-binder-based techniques [43], DIP [44–46] and Binder Jetting [33, 47–52] were successfully utilised. Hereby, densification is achieved due to sintering, either directly within the printing process or by subsequent post-processing of the green body. Green body strength is generally

obtained by commercial solvent-based and/or thermosetting binding agents that undergo gasification within the subsequent thermal treatment (debinding). However, the green part ceramic content is often not more than 60 vol-% - either due to low powder bed densities or due to high amounts of organics [42, 53, 54]. Thus, fully dense parts are hardly achieved and a significant amount of residual macroporosity is often found in literature [34, 52, 55].

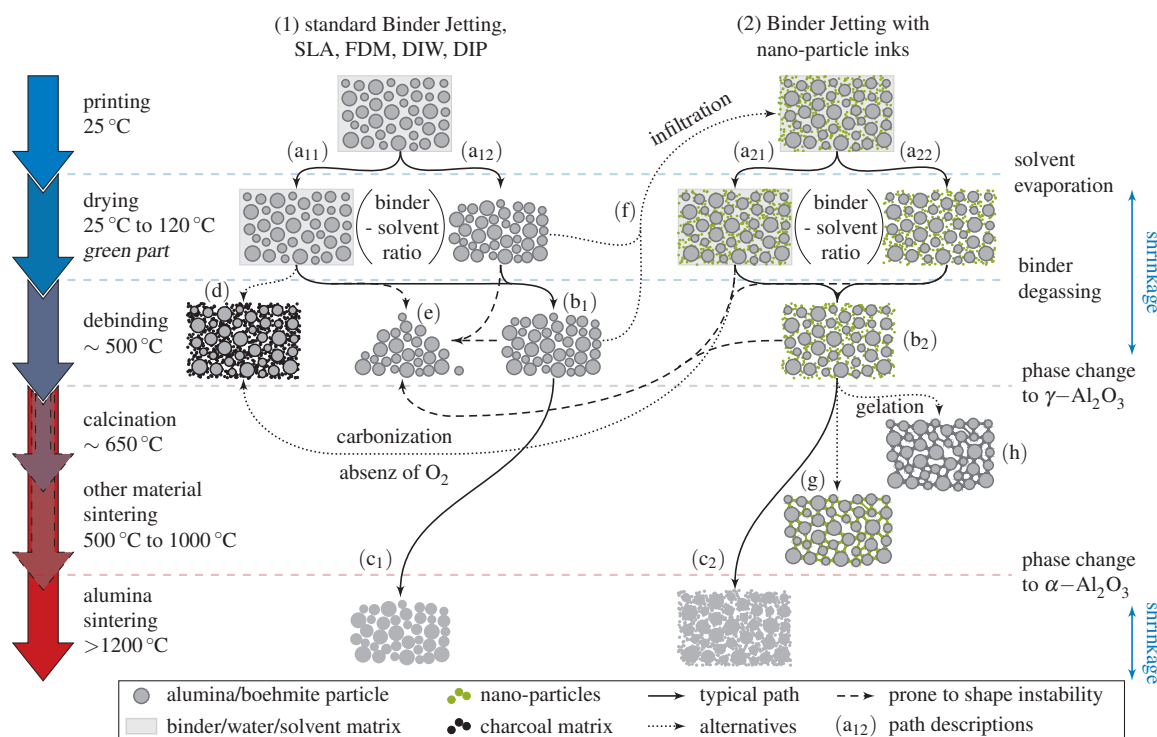


Figure 1.1: Schematic drawing of the standard alumina printing procedure (1) applying solvent and/or polymeric binders comprising the steps of solvent evaporation (a₁₂) (if present, else (a₁₁)), binder degassing (b₁) and subsequent sintering (c₁), most predominantly subjected to significant shrinkage and retaining residual macroporosity. Binder Jetting, incorporating alumina nano-particles directly (2) or by infiltrating green parts (f), the general path is scarcely varied (a₂) – (b₂) – (c₂) but resulting in higher final part densities, reduced shrinkage and increased mechanical stability. Alternative routes comprise debinding in inert atmosphere leading to carbonization of the organic binders (d), nano-particle inks with non-alumina species sintering at lower temperatures (g) and printing with alumina sols gelating upon solvent removal (h). Green and debinded parts are prone to mechanical instability due to the absence of particle cohesion leading to disintegration of the printed shape (e).

Compared to additive manufacturing, traditional catalyst shaping techniques result in only small amounts of macroporosity due to pressure application [29]. Unfortunately, the targeted mesoporosity (2 nm to 50 nm pore size) [56] which is typically present in the alumina precursor powders and which is responsible for the desired high specific surface areas of the final parts, is several magnitudes smaller than the pore size naturally obtained by 3d printing and known to degrade during sintering. As this is typically required to allow mechanical stability the following alternative approaches to combine both, mesoporosity and stability are conceivable:

- the pore structure is created during or after sintering/thermal treatment;

- the sintering species is different from the porous alumina species having a lower sintering temperature (multi-component systems);
- the green body made of porous alumina species is not sintered, thus strength must be gained by binder solely.

The first approach, has not been addressed yet, but if possible may allow gradual microporosity within parts, having a dense core and a porous outer interface, allowing both, high specific surface areas and sufficient strength. A starting point may be the reaction-bonded aluminum oxidation [57, 58], where pure aluminum is printed and in a subsequent step oxidised. According to Yao et al. [58] this leads to porous alumina parts with high strength, although being vague what kind of porosity is meant (micro, meso or macro). In general, engineering of pore structures in alumina parts is addressed by Hammel et al. [26], however implementing pore design into the printing process appears to be still a long way off.

Concerning the second approach some noteworthy works have been presented [59, 60], though not for ceramic materials nor targeting mesoporosity. They incorporate nano-particle inks or infiltration techniques pursuing higher final part densities (cf. Fig. 1.1(g)). However, single material systems are preferably sought as the introduction of other chemical species may interfere with any a posteriori added catalytic activity, which shelves this approach for the moment.

Last but not least, the third approach is the most promising and thus selected in this work. Concerning the additive manufacturing of porous structures having high specific surface areas, Couck et al. [21] presented a *Direct Ink Writing* formulation for zeolites including a silica sol binder (cf. Fig. 1.1(h)). Without sintering, stable parts allowing BET surface areas of about $300 \text{ m}^2 \text{ g}^{-1}$ after calcination at $550 \text{ }^\circ\text{C}$ could be obtained. BET surface areas of about $600 \text{ m}^2 \text{ g}^{-1}$ were obtained by Konarova et al. [16] after pyrolysis of printed starch (DIW) in oxygen-free conditions (cf. Fig. 1.1(d)) and subsequent KOH etching. Incorporating Ni and Mo into the starch formulation, resulting parts can be used as catalysts for the reaction of syngas to higher alcohols. Moreover, Fan et al. [41] describes a FDM formulation comprising θ -alumina having a BET surface area of $10 \text{ m}^2 \text{ g}^{-1}$ after sintering. Finally, Ludwig et al. [29] presented DIW alumina parts with BET surface areas of about $100 \text{ m}^2 \text{ g}^{-1}$ and noteworthy side crush strengths.

In the following, *Binder Jetting* is chosen as easy scale-up options, a comparably high surface accuracy and impressive geometric flexibility make this technique manufacturer's choice [3, 31–33, 53, 54]. *Binder Jetting* comprises the steps of spreading out a powder layer of desired layer thickness, the subsequent local application of binder liquid, and the alternating repetition until completion of the printed part.

For a proof-of-principle, it shall be investigated, if and to what extent *Binder Jetting* is capable to manufacture micro- or mesoporous alumina parts having both, high specific surface areas and sufficient mechanical strength for the use as catalyst carriers in heterogeneous catalysis. Findings concerning characteristics of the powder feedstock, binder formulations and printer setup are presented.

1.2 Development of Custom Material Combinations

Referring to Utela et al. [61, 62], the procedure for the development of new material combinations in Binder Jetting comprises the steps of:

- 1.) specification of printer setup parameters;
- 2.) formulation of the powder feedstock;
- 3.) formulation of liquid binder;
- 4.) testing of powder-binder interaction;
- 5.) specification of post-processing procedures.

Although, powder and binder properties need to be studied to ensure reliability and reproducibility, all parameters strongly depend not only on the process parameters and measurement techniques used but also on the printing machine itself [63]. Thus, powder and binder materials are frequently tailored to one specific printer. The transferability to other printing machines is not guaranteed. Nevertheless, some general trends and basic requirements are repeatedly found.

1.2.1 Printer Setup

Most frequently, the material development is tailored to a commercial printer not vice versa. Thereby, the printer may be selected due to availability, prize, speed, printer resolution or material flexibility. In contrary, custom printer setups are significantly more flexible, although it may take years of optimization until reaching the accuracy, reliability and stability commercial printers nowadays have. Customizing a printer setup for Binder Jetting, there are some options regarding powder application techniques, powder bed characteristics and binder ejection methods to choose from that will affect the final product's properties. However, the decision has frequently to be made weighing effort and benefit.

Concerning the powder application, possible selections include blades [64], coaters [65], rollers of various specifications including forward-rotating [64], backward-rotating [64], traverse-counter-rotating [66] or press rolling [67], besides rotating sieve drums [68], spray deposition [69] and some others [70]. Moreover, the applicator unit may be vibrated in order to enhance the powder flow [71, 72]. Whatever technique is chosen, a homogeneously powder spread allowing high bed densities is sought for. Numerical studies have been performed to investigate the powder application process by using the *Discrete Element Method* (DEM) [73–76]. Most pertinent, Haeri et al. [77] compared the two most frequently used powder spreading techniques: blade and roller. It was found that in general in terms of bed density a roller is preferred, however, for highly spherical particles, the difference in both methods is marginal. Concerning bed homogeneity and its dependence on bed location known results are opposing (cf. [75, 78] and [79]).

The powder bed may be created using dry or wet powder feedstocks. Slurries or wet powders may be advantageous as they allow smaller powder particles to be printed and thus yielding higher bed densities and surface finishes [50, 53, 61, 80]. However, dry powders are much easier to be processed. Moreover, for a further increase in the bed density, means of bed compaction can be utilized [68, 81, 82].

Various print head techniques exist, most predominantly classified into *Drop-on-Demand* (DOD) and *Continuous-Jet Printing*, depending whether single droplets of ink are formed or not. Most frequently DOD is used [64], whereby they may be further classified having either piezo-electric or thermal actuators. Exact working principles, advantages and limitations of each technique can be found elsewhere [43, 46, 51, 61, 83–85]. Besides, print heads delivering adjustable droplet sizes can be utilized, allowing scalable binder saturation values [64]. Typically (piezo-electric) print head orifices have a diameter of 20 μm to 75 μm [85, 86], most predominantly around 60 μm [45].

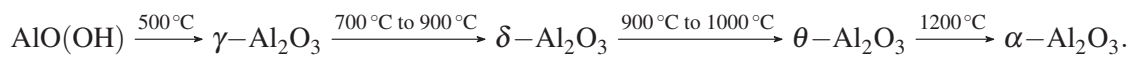
The regulation of the interplay of powder applicator, powder bed and print head in custom printers requires extensive coding. Frequently G-codes are used [87], a coding language developed for CNC milling machines.

1.2.2 Powder Feedstock

Important feedstock factors influencing the print process are the powder chemistry, morphology and microstructure [63].

Chemistry

The chemistry of incorporated powders strongly depends on the targeted purpose. Focussing on alumina catalyst supports, boehmite (aluminum oxide hydroxide, $\text{AlO}(\text{OH})$) is a frequently used precursor or binding agent [88–91]. During heating boehmite dehydrates and dehydroxylates before undergoing various transitional phase changes until reaching the thermodynamically stable α -phase by following the generally accepted route [90, 92, 93]:



The identification and characterization of these phases are reasonably well understood [90, 92]. As catalyst support, $\gamma\text{-Al}_2\text{O}_3$ is predominantly used when high specific surface areas are requested, whereas $\alpha\text{-Al}_2\text{O}_3$ is chosen especially for high-temperature applications as the specific surface area decreases to insignificant values due to sintering effects [90, 92]. The structure, acid-base properties and other aspects giving rise to $\gamma\text{-Al}_2\text{O}_3$ particular suitability as catalyst support are well known [93, 94]. The consecutive catalyst application by impregnation, coating or other methods [22] is state of the art and not further addressed here.

Morphology

The powder morphology, in particular particle size, particle size distribution (PSD), shape, and surface roughness strongly influence the packing efficiency of the powder bed. The quality is characterised by a high relative bed density ω_{bed} resulting in a high green part density and strength, and the uniformity of powder layers facilitating homogeneous final parts.

The ideal particle size is often discussed and frequently ranges from 15 μm [63] or 20 μm [53, 61, 95] to 90 μm [96], 100 μm [53] or 150 μm [63]. More precisely, Spierings and Levy [97] defined an ideal particle size range with the 10th percentile (D_{10}) of the PSD being above 5 μm and the powder layer thickness n should be 50 % higher than the 90th percentile (D_{10}) as an upper limit. The lower limit of particle size is substantiated with powder agglomeration as Van-der-Waals forces become dominant to gravitational forces at particle sizes around 1 μm to 5 μm [61, 98] leading to a decrease of powder flowability and bed density [53, 61, 96]. In Binder Jetting, the applied particle sizes determine the final parts surface roughness, so that particles in the small micron range or even sub-micron particles may be preferred [53]. This however, requires an artificial increase of particle size by spray or freeze drying [48, 52, 54], or a decrease of Van-der-Waals forces by using a plasma treatment [95].

Typical bed densities ω_{bed} , defined as the ratio of total solid volume V_{solid} per bed volume V_{bed} of somewhat spherical powder particles with monomodal size distributions are repeatedly reported to be about 60 % [65, 78, 99–101].

$$\omega_{\text{bed}} = \frac{V_{\text{solid}}}{V_{\text{bed}}} \quad (1.1)$$

The influence of powder shape is described by German [102] finding bed densities of 64 % for powder beds of monomodal spheres down to 40 % for particles having coarse shapes. The minimal bed density is at 25 % [53]. Moreover, DEM simulations were performed to study powder beds comprising various shaped particles [74, 77]. In summary, particles having a high sphericity are preferred, as they possess lower inter-particle friction leading to better powder flowabilities and thus higher bed densities [61, 103].

Concerning the influence of the particle size distribution it is generally accepted, that a wide or bimodal particle size distributions can increase the bed density as the smaller particles can fill the gaps in-between bigger particles [61, 78, 96, 99–101, 104]. Liu et al. [99] could increase the overall bed density from 63 % to 68 % by simply using a wider size distribution. Karapatis et al. [101] predict an increase of powder bed density of up to 15 %, when using multimodal powders with more than 30 wt-% of fines compared to powders similar in size. Zhu et al. [105] describe an increase in density to up to 77 %. According to McGearry [106] powder bed densities of 84 % can be reached under optimal conditions, meaning spherical particles with multimodal size distributions when a significant part is of fines. These trends have been confirmed by numerical results [76, 107, 108]. The size ratio D_{90}/D_{10} of a PSD can be used as a measure of PSD width. Hereby, Spierings and Levy [97] specify a desired value of at least 5, whereas Jacob et al. [79] present results with a ratio of 2 and 3. Lee et al. [76] investigate the influence of D_{90}/D_{10} ratio on packing density comparing experimental and numerical (DEM) results where both eventuate in a density increase

when using higher ratios. Additionally, a segregation of particles along the bed length can occur, with small particles being preferably deposited at the front end and larger particles at the rear end [79].

Researchers opinions differ concerning the influence of PSD on powder flowability, as a wider distribution may decrease [104] or increase [109] the powder flowability. Moreover, a difference in flowability does not necessarily result in an appropriate variation of bed density [110]. Thereby, the powder flowability can be characterised in three manners: a) the Hausner ratio is defined as the ratio of tapped bed density and apparent bed density (obtained by simple pouring) measured by weight according to ASTM [111] in a Hall funnel meter [78, 95, 96, 110], whereby values of 1.13 to 1.4 are used [95, 110]; b) the angle of repose α can be measured in a rotating cylinder, an angle around 25° indicates a good powder flowability [62, 112]; and c) the drag shear test resulting in a direct flowability measure ff_c , ideally in the range of 5 to 7 [95]. Whereas most researches prefer high flowabilities, Butscher et al. [95] spotlight a possible decrease in bed stability in case of too high flowabilities.

The influence of surface roughness of the powder particles is rather obvious with rough particles increasing inter-particle friction and thus decreasing both, bed density and layer homogeneity. Additionally, some researches indicate improvements in layer homogeneity when the ratio of mean particle size to layer thickness is in an appropriate range in order to reduce so called wall effect problems [78, 79, 101]. The wall effect of layers of spherical particles describes a bed density reduction due to void space formation at the layer borders and is more pronounced when the particle size to layer thickness ratio is small. This phenomenon was intensely described for spherical packings in cylindrical confining walls and depends on many parameters including particle size (distribution), material, packing method and shape [113]. For 3d powder bed printers this effect was investigated by Karapatis et al. [101], revealing a bed density reduction of up to 20% for layer thicknesses below $200\ \mu\text{m}$. For a better understanding of the wall effect, Fig. 1.2 describes three possible layer scenarios in powder based 3d printing: the application of a new powder layer onto (a) a solidified previous layer having a smooth solid surface as may be obtained by particle melting; (b) a previous not-solidified powder layer; and (c) a solidified previous layer having a coarse surface as may be obtained in Binder Jetting. To our opinion only the first scenario not applying to Binder

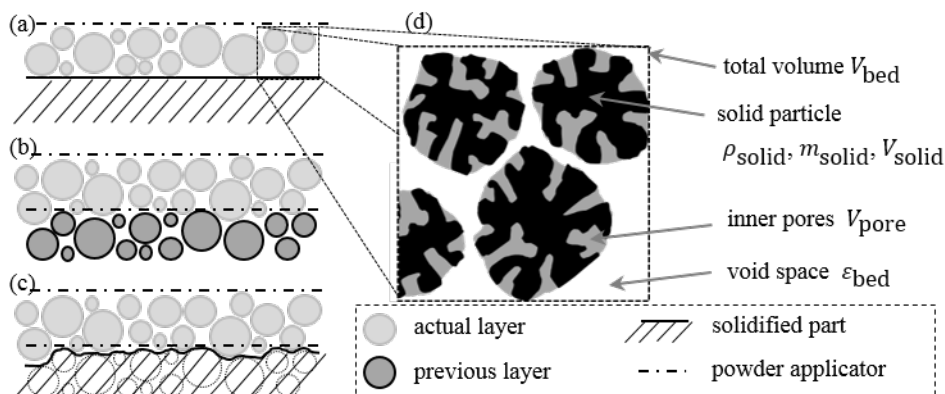


Figure 1.2: Wall effect considerations concerning the application of a new powder layer onto (a) a smooth surface, (b) the non-solidified powder, and (c) a coarse surface. The inset (d) represents the microstructure of the porous particles.

Jetting may be subjected to significant void formation as in the other two cases the powder particles can

embed nicely into the coarse surrounding. Thus, considerations concerning wall effect and reduced layer density will not be addressed here any further.

Microstructure

Porosity in parts intendedly or unintendedly resulting from low green part densities or intendedly generated as part of the printed geometry is often addressed and quantified. However, only very little research was performed concerning porosity that arises from pores within powder particles [63]. These intra-particulate pores are several magnitudes of order smaller than the often-addressed inter-particulate pores, generally in the small nano-meter range. In order to calculate the relative bed density excluding any inner pores, the general equation (1.1) [107] has to be extended to equation (1.2) based on Fig. 1.2(d):

$$\omega_{\text{bed}} = \frac{(V_{\text{solid}} + V_{\text{pore}})}{V_{\text{bed}}} = \frac{m_{\text{bed}}}{V_{\text{bed}}} \cdot \left(\frac{1}{\rho_{\text{solid}}} + v_{\text{pore}} \right). \quad (1.2)$$

Herein, V_{solid} and ρ_{solid} refer to the true volume and the true density of the solids, V_{bed} and m_{bed} refer to the overall bed volume and mass, V_{pore} and v_{pore} refer to the true and specific pore volume respectively. Pore size, volume and resulting surface area according to Brunauer, Emmett and Teller (BET) can be determined by means of gas adsorption. The determination of pore shape, size distribution and further microstructural characteristics in general [114] and for catalysts in particular [115] are well established.

1.2.3 Formulation of Liquid Binder

The liquid added during Binder Jetting may either be the binder itself or a solvent capable to solvate a solidified binder being present as distinct particles or enclosing the actual powder particles as an surrounding outer layer in the powder bed. These so called in-bed binders [61] are for example applied by Stumpf et al. [52] or Polzin et al. [49]. Independently, developing a binder system for Binder Jetting additive manufacturing is often described as the key element [51, 83] and comprises two major tasks: the selection of binding method and the facilitation of reliable binder deposition by the selected print head (ejectability).

Binding Method

Binding of powders to green bodies can occur by organic liquids such as thermosetting and/or crosslinking polymers, hydration processes, acid-base systems, inorganic binders, metal salts, solvents or phase changing systems [33, 51, 61, 62]. The binding can be provoked by heat or light exposure, solvent evaporation or by undergoing chemical reactions.

Although being frequently used, organic binders are not favoured for the present sinter-free application, as for catalyst supports a calcination step at temperatures around 600 °C is required that simultaneously

forces the degassing (debinding) of any present organic phase eliminating the particle-particle cohesion and significantly decreasing the green parts strength [29].

Little research was done concerning Binder Jetting with inorganic binders. This predominantly is the case in bone tissue engineering [83, 96]. More precisely, nano-suspension binders may be applied in order to improve the green part density and/or strength or to reduce shape distortion and/or shrinkage of sintered parts [60, 116–119]. Most frequently, nano-suspensions act as a permanent binder utilizing a size-dependant melting behaviour with nano-particles sintering at smaller temperatures than the micro-sized particles of the powder bed due to a comparatively high surface-to-volume ratio [59, 120]. Moreover, nano-particles concentrate at high curvature areas such as the powder particles contact points as the solvent dries last from these areas [121–123]. During heating, nano-particle sintering increases the neck size and thus reduces the particle bond stress. Thereby, the nano-particles may be added to the existing commercial binder systems, functioning as sintering aid [87, 116–118, 123], or the solvent-based nano-particle suspension acts as the binder itself facilitating green part strength alone [122, 123]. Targeting a single-material system of pure alumina, it was shown that significant pore sintering occurs before reaching the actual sintering temperature, indicated by a significant drop in specific surface area without any increase in parts strength [29, 92]. It is thus assumed that nano-pore and nano-particle sintering occur at about the same temperature and the above described size-dependent sintering behaviour can not be used as binding functionality in the present application. In contrary, Sachs et al. [51] described the usage of a 30 wt-% sol-gel binding systems based on silica colloids sacrificing any post-sintering.

Similarly, an inorganic binding system is selected, being composed of a boehmite-based sol. Herein, boehmite powders are secondary micro-sized particles consisting of numerous agglomerated nano-sized primary particles [124]. Disaggregation and dispersion of secondary particles may occur to a certain degree by mechanical attack but is highly favoured when adding aqueous acids forming a stable sol [124]. The mechanism of this peptization process was intensely studied and the interstitial formation of basic aluminum aquoxide salts is generally accepted [88, 91, 125, 126]. The reversible gelation of the sol, describing the coagulation of colloidal particles forming a 3d network occurs when the acid content is increased above a specific level [126]. The decomposition of the basic alumina salts and the evaporation of water leading to gelation upon calcination and phase change to γ -alumina form the new, if weak binder phase utilized in this work. Hereby, nitric acid is frequently used as peptization agent due to its residual free degassing at calcination temperature [92, 126], however, other acids are similarly studied [88]. The peptization process, especially the resulting size of colloidal particles affecting parameters such as fluidity depend on a variety of investigated parameters [89, 126] and shall not be addressed here any further.

Print Head Ejectability

Common to all print head specifications is the overall goal to ensure a reliable and consistent drop formation [46, 61]. More precisely, this comprises the ejection of droplets having the same size, speed and composition such as homogeneous particle loadings when using nano-suspensions. Thus, preferred binder liquids should be appropriate regarding rheology, stability and print head interaction.

Viscosity and surface tension are the most important rheological factors in regard to ejectability. Moreover, binder liquids should possess shear thinning behaviour [45, 46]. Thereby, the viscosity is preferably in the range of 5 mPas to 20 mPas [46, 83], but may be as high as 100 mPas [127]. Using nano-particle suspensions as binders, the viscosity is strongly dependent on the particle loading of the fluid and increases rapidly when increasing the solid content. An empirical relation between viscosity and particle loading is given by the modified Krieger-Dougherty equation [46, 128, 129]:

$$\eta = \eta_0 \cdot \left(1 - \frac{\phi}{\phi_{\max}}\right)^{-n}, \quad (1.3)$$

where η and η_0 are the viscosity of the suspensions and the particle-free base liquid respectively, ϕ and ϕ_{\max} represent the actual and maximal volume fraction of solids, and n is an empirical constant, such as 2 [130]. Employing sol-gel binders, the viscosity of the nano-suspension can be fine-tuned by changing the pH value [126] or in general by adding dispersants. Concerning surface tension, values higher than 35 mJN⁻¹ [127] or in the range of 35 mJN⁻¹ to 40 mJN⁻¹ [83] are preferred and may be altered by adding surfactants such as alcohols [61]. For an optimal interplay of viscosity and surface tension γ the dimensionless inverse of the Ohnesorge number Oh:

$$\text{Oh}^{-1} = \frac{\text{Re}}{\sqrt{\text{We}}} = \frac{\sqrt{\gamma \cdot \rho \cdot d}}{\eta} \quad (1.4)$$

should be between 1 and 10 [46, 83], with density ρ and the characteristic dimension d (taken as the print head orifice radius [46] or droplet radius [83]).

The change of fluid parameters (viscosity, surface tension, pH-value) over time characterizes the binder liquids stability [131]. Using nano-suspensions, the stability of the dispersion is of further interest. In general, Brownian forces F_B characterize the dispersion behaviour being dependent on electrostatic particle conditions, the zeta potential ζ . These conditions for Brownian motion can be varied for example by altering the pH value [132]. Unfavourable conditions, however, may lead to nano-particle agglomeration characterized by the occurrence of particle sedimentation as Gravitational forces F_G become dominant when nano-particle size d_{np} is increased [132]:

$$\frac{F_G}{F_B} = \frac{d_{\text{np}}^4 \cdot \Delta\rho \cdot g}{k_B \cdot T}, \quad (1.5)$$

where $\Delta\rho$ represents the density difference between particles and fluid, T is the temperature, g the acceleration due to gravity and k_B the Boltzmann constant. By way of example, assuming a density difference of about 3 g cm⁻³, the critical particle size for sedimentation is 0.6 μm .

The binder-print head interaction involves the functional characteristics of the print head such as orifice diameter and ejection frequency defining droplet volume and speed [85]. Thereby, optimal conditions for each binder liquid have to be found as for example bigger droplets may decrease accuracy but small droplets may be more sensitive for disturbances [133]. A high printing speed is generally favoured, but may affect the binder spreading and droplet trajectory. Incorporating nano-suspensions, a minimal ratio of orifice to particle diameter of 20 [46] or even 100 [87] should be guaranteed in order to reduce clogging problems. In general, clogging of print head orifices is an often-encountered problem [64], which

is technically solved by using binder liquids capable to self-rehydrate solidified clogs [61]. Moreover, the print head may be subjected to chemical attack when using oxidizing compounds such as acids or residual carbon when organic binders are heated above pyrolysis temperature in thermal ink-jet print heads. Additionally, the drop formation process of ink-jet print heads was thoroughly investigated in simulation studies [45, 134].

Regarding dispersion concentration, some noteworthy examples can be given. Hereby, very low concentrated nano-suspensions of about 0.5 % as used for example by Elliott et al. [117] are readily applicable but will have only minor effects on final parts characteristics. Therefore, Crane et al. [121] suggest the repetition of binder application of at least three times in order to increase the nano-particle content. Bai and Williams [122, 123] was able to print a nano-particle suspension with 20 wt-% solid content but observed significant clogging of the print head at concentrations beyond this limit. Finally, investigations with Direct Ink-Jet Printing (DIP) were performed concerning the ejectability of 5 % [45] to up to 40 wt-% [44, 46, 85] ceramic nano-suspensions.

1.2.4 Powder-Binder Interplay

The interaction of powder and binder is evaluated by the binding capability itself correlating with the permeability of binder through the powder bed (wettability) and the amount of binder added (binder saturation). For preliminary studies, pre-testing means such as post-infiltration of printed parts with a new binder [117, 121], filling of molds with powder-binder mixtures [62, 118] or adding of single droplets to a powder surface [61] can be used before transferring the optimized powder-binder combination to the actual 3d printer. Here, printing of primitives obtained by printing a single drop onto the powder bed and line printing, obtained by overlapping primitives can be a good starting [43, 61, 62], before heading on towards more complex (test) geometries.

Binder Saturation

The binder saturation S is defined as the volume of binder V_b added per available void space V_ε [135]:

$$S = \frac{V_b}{V_\varepsilon}. \quad (1.6)$$

Others use the so-called binder dose D , defined as the volume of binder per printed line length l° [43]:

$$D = \frac{V_b}{l^\circ}. \quad (1.7)$$

Using print heads capable to print various volumes, the binder saturation is easily adjustable, if not, overlaying droplets or print repetitions have to be performed to modify saturation levels [64]. Concerning binder saturation, higher values are generally favoured however at the price of possible loss of accuracy [133].

Wetting Behaviour

The binder permeability through the powder bed, the so-called wetting, is driven by capillary forces and depends on surface tension and viscosity of the liquid, the surface energy of the droplet's impact and the surface roughness and void size of the powder particles [43, 64]. Generally, the wettability is measured as the contact angle θ of the binder liquid on the powder surface [64, 114, 136, 137]. A low wettability/high contact angle will inhibit the binder drops to sufficiently permeate into the powder bed and thus may be moved away by the application of the next powder layer, leaving grooves within the bed surface or leading to an unsatisfactory layer connection. Using binders having a too high wettability/low contact angle might permeate further into the bed or spreading wider than desired, leading to inaccurate geometries [96]. However, it is well known, that the determination of the contact angle between liquids and powder beds is rather difficult [137]. While Galet et al. [136] recommend the *Washburn Capillary Rise* method, Nowak et al. [137] compare this method with the *Thin Layer Wicking* method and the *Sessile Drop* method and recommend the latter. Moreover, Moon et al. [43] investigated binder infiltration kinetics by determination of infiltration time t^* based on the Carman-Kozeny equation:

$$t^* = \frac{15 \cdot (h^\circ)^2}{\gamma \cdot \cos \theta} \cdot \frac{(1 - \varepsilon)}{\varepsilon^3} \cdot \frac{\eta}{\rho^2 \cdot d_p}, \quad (1.8)$$

where ε represents the bed porosity, γ is the liquid/vapour interfacial energy, herein used as surface tension and h° is the height of liquid column, herein used as printed line width assuming a circular cap-shaped line. The printed line width l^* can be calculated as a function of contact angle [43]:

$$l^* = 2 \cdot \sqrt{\frac{D \cdot (\sin \theta)^2}{\theta - \sin(\theta \cdot \cos \theta)}}. \quad (1.9)$$

Obviously, permeation depth h^* determined by evaluating primitives should not be smaller than the adjusted layer thickness to avoid layer disconnection effects.

1.2.5 Post-Processing

Binder Jetting requires at least one post-processing step [53, 54, 61], in order to increase parts strength and/or surface finish [61, 83]. Most commonly a precisely adjusted heat treatment comprising a debinding and a subsequent sintering step is implemented [53, 83]. Additionally or instead of, hot or cold isostatic pressing [42, 67, 138], as well as pressure, vacuum or each and any other infiltration technique [42, 48, 52, 139] may be utilized. Besides, coatings comprising small particles may be applied in order to improve the surface finish [52, 61].

Targeting catalyst supports with high specific surface area, a calcination step at around 600 °C to 650 °C is required, ensuring the phase change to γ -alumina. Simultaneously, any present organic compounds will undergo debinding at these temperatures. However, this temperature is too low to evoke any sintering including pore sintering. The latter is believed to occur at temperatures around 1000 °C [29].

Finally, the quality of the final parts has to be investigated, comprising the evaluation of surface roughness, dimensional accuracy and shrinkage, reproducibility, density, abrasion characteristics and mechanical strength. In general, strength of parts is measured with specific test bars as compressive, tensile or flexural strength. For fully dense, non-printed alumina, typical flexural strengths reach values up to 500 MPa and compressive strength may be more than 4000 MPa [140]. Using Additive Manufacturing, parts having a flexural strength of 512 MPa could be produced by stereolithography [36]. Concerning Binder Jetting, flexural strength is per se significantly smaller [96], frequently around 5 MPa [48, 49]. Compared to that, noteworthy compressive strengths around 120 MPa to 130 MPa were reported [47, 52]. Using infiltration techniques additional to the standard sintering, compressive and flexural strength can be significantly increased by around 60 MPa [48, 52].

In particular, the strength σ of catalyst bodies is measured as single pallet crush strength (compressive) [141–143], single pallet bending strength (flexural) [143–145], bulk crush strength [146–148] or by the impulsive drop test [145, 149]. Performing the impulsive drop test, test particles were dumped down onto a solid surface; the difference in particle size is evaluated [149]. For the bulk crush strength, beds of test particles are created and an external pressure is applied. The development of fines (fragments) with increasing pressure is studied [147]. A three-point bending apparatus is applied for measuring bending strength. The most commonly used test is the side crush strength test, where ideal cylinders tend to break along the plane passing through the two contact lines of the pressure application [144]. However, for significant results, high shape accuracy is needed, thus for extruded particles bending strength or drop test are preferred [149]. The compressive strength of a cylindrical pellet with dimensions l and d , σ_{comp} can be calculated based on the side crush loading force F_{SC} [150]:

$$\sigma_{\text{comp}} = \frac{2 \cdot F_{\text{SC}}}{\pi \cdot l \cdot d}. \quad (1.10)$$

Thereby, Weibull statistics are utilized in order to describe the variation in fracture strength of brittle materials. The possibility of failure P at a specific level of stress σ can be calculated according to Weibull [144, 151, 152]:

$$P(\sigma, V) = 1 - \exp \left[-\frac{V}{V_0} \cdot \left(\frac{\sigma}{\sigma_0} \right)^m \right], \quad (1.11)$$

with volume of specimen V , reference volume V_0 , characteristic strength σ_0 and Weibull modulus m , the measure of scatter of the distribution. If all pellets used have the same dimensions, the above equation reduces to [148]:

$$P = 1 - \exp \left[-\left(\frac{F}{F_0} \right)^m \right], \quad (1.12)$$

where the unknown parameters m and reference loading F_0 can be determined by linear least-square regression analysis. Concerning the strength of typical extruded or tableted catalysts, Li et al. [143] reveals loadings of 27 N for extruded and around 130 N to 160 N for tableted catalysts of various dimensions. Moreover, Staub et al. [144] investigated the side crush and bending strength of γ -alumina extruded catalyst support with high BET surface areas having either a monomodal or bimodal pore structure.

Having only mesopores, the tensile strength was around 13 MPa being drastically reduced to 1.7 MPa by the introduction of additional macropores.

1.2.6 Concluding Remarks

The development of custom powder binder material combinations is a complex task and its optimization and fine-tuning may take several iterations. A summary of the decisive parameters, their recommended dimension if known and appropriate measurement techniques and methods are given in Tables 1.A1 to 1.A4 in the appendix. Due to its significant complexity, the following investigation on additive manufacturing of catalyst supports by Binder Jetting is introduced on a proof-of-concept level and may lack certain statistical accuracy and scientific profoundness.

1.3 Experimental

1.3.1 Printer Setup

A powder binder printer as depicted in Fig. 1.3 consists of a horizontally (x-axis) moveable powder application unit with powder storage, a vertically (z-axis) moveable powder bed base plate and a printer head that can be moved horizontally in x and y direction. Motion is evoked along toothed belts with

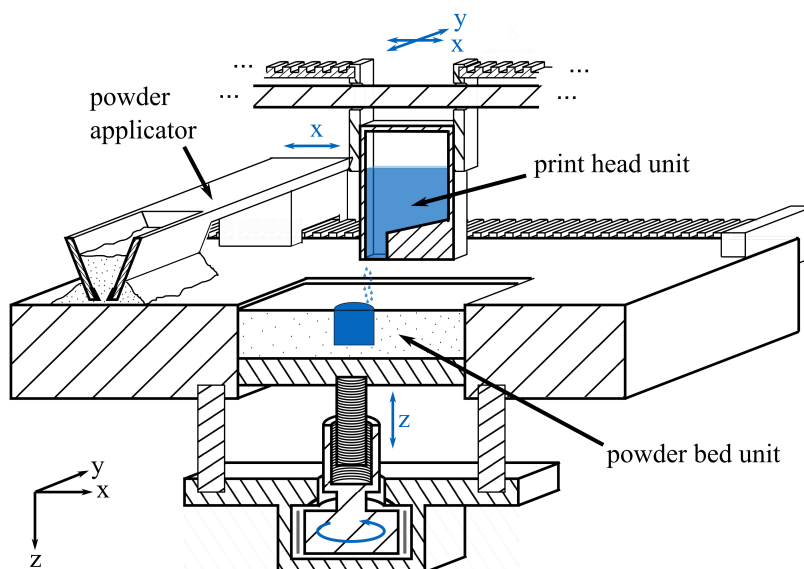


Figure 1.3: Schematics of the custom printer setup developed and used for Binder Jetting material development studies.

cogwheels or round threaded rods, driven by four stepper motors. The powder bed size ($l = b = 5.37$ cm) was selected to be very small in order to allow material studies with small amounts of material. The typically used layer thickness is 100 μ m or 200 μ m. An additional vibrator can be added to increase

flow ability and bed density. The print head is implemented with a commercial twelve-nozzle thermal ink-jet cartridge (*HP C6602A*). The printers control including the shape to be printed is implemented with *G-code*, a widely used numerical control programming language.

1.3.2 Powder Characterization

Four alumina powders, Disperal[®] 80, Pural[®] SB, Pural[®] SCC (all by *Sasol GmbH, Germany*) and spray dried DMS (by Saint Gobain NorPro) were selected and pre-tested as follows. The crystallite phase was determined by measuring the water content of the powders in a thermo-gravimetric apparatus (*Q5000, TA Instruments*, 10 K min⁻¹ to 600 °C in air). As a measure of fluidity, the angle of repose was determined according to Schulze [112] by the cylinder and the funnel method. The mean particle size and the particle size distribution was analysed in liquid dispersion and as the dry powder by laser diffraction analysis (*Universal Liquid Module and Tornado Dry Powder System, Laser Sizer 13320, Beckman Coulter*). Scanning electron microscopy (*TM-1000 Tabletop, Hitachi*) was used to investigate the particles' shape and texture. The BET surface area, pore size and pore volume were determined by N₂ physisorption measurements (*NOVAtouch LX-4, Quantachrome*). Therefore, samples of about 100 mg were weighted, degassed and dried for 3 h at 120 °C prior to analysis. The powder samples may be pre-treated in a muffle furnace at 650 °C, 800 °C, 1000 °C and 1400 °C with a heating rate of 1 K min⁻¹ and a holding time of 1 h to investigate pore sintering. The bulk density of the powder bed was determined by weighing a known powder bed volume.

1.3.3 Printer Validation

The printer setup and G-code programming were tested with organic binder liquids to print above listed alumina powders into cylindrical shapes. Hereby, a selection of organic binders were tested with polyethylene glycol (with molar mass 190 g mol⁻¹ to 210 g mol⁻¹, Merck KGaA) showing best results. The parts were debindered at 500 °C in air and subsequently sintered at 1150 °C. Additionally, carboxymethyl cellulose sodium salt (Sigma-Aldrich) alone and a 50 wt-% mixture with DMS alumina were used as powder feedstock with water added as binder liquid. Carbonization of the cylinders was studied in a thermo-gravimetric setup under absence of air with 4 K min⁻¹ heating rate to 650 °C, held for 1 h in argon.

1.3.4 Binder Preparation

Alumina sols were prepared by mixing boehmite powders called Disperal (*Sasol GmbH, Germany*) having various crystallite sizes (e.g. Disperal, Disperal 60, Disperal 80) with aqueous nitric acid. The mixtures were then stirred vigorously for at least 30 min until stable dispersions are obtained. Boehmite content and acid concentration are varied, a selection is displayed in Table 1.1, and primitives were obtained by adding droplets of binder onto the powder bed surface using a syringe with 0.33 mm needle

diameter. Additionally, layer connectivity is evaluated by adding two droplets at the same position, with the application of a fresh powder layer in between. In order to vary wettability, one part of ethylene glycol (EG) per four parts of sol composition may be added.

Table 1.1: Compositions of a selection of binder sols investigated.

no.	type	boehmite content [wt-%]	nitric acid concentration [%]
sol 1	Disperal	30	1
sol 2	Disperal 60	30	0.5
sol 3	Disperal 60	50	0.75
sol 4	Disperal 80	10	0.32

1.3.5 Post-Treatment and Characterization

Cylinders with $h = 6.5$ mm and $d = 5.5$ mm were fabricated using DMS powder and sol 1 mixed 4:1 with ethylene glycol as binder formulation. For proof-of-principle studies, the binder is applied using a syringe to the layerwise added powder. To allow shaping a mask is used. The produced parts were air-dried for 24 h and are subsequently calcined in a muffle furnace at 650 °C for 2 hour. The dimensions of the obtained cylinders and the lateral side crush strength were measured (*MultiTest 50*, SOTAX AG, Pharmatron). Means of at least four cylinders were calculated. With the fragments, N₂ physisorption measurements were performed after degassing for 3 h at 120 °C to determine the final BET surface area.

1.4 Results and Discussion

1.4.1 Powder Characterization

Four typically used catalyst support precursor powders were selected and investigated in view of their chemical, morphological and microstructural characteristics, regarding their applicability in powder bed generation.

Chemistry

Thermo-gravimetric analysis revealed a boehmite nature of Disperal 80, Pural SB and Pural SCC due to the presence of two weight loss steps, which can be allocated to the evaporation of moisture (≈ 1 % to 9 % weight loss) and the subsequent release of crystal water (≈ 14 % to 17 % weight loss). In contrary, DMS powder can be identified as γ -alumina.

Morphology

Mean particle size and size distribution are evaluated by light diffraction. In general, size measurements are performed with aqueous dispersions (-L) of the targeted powders, allowing higher accuracy than the investigation of the mere powder. But due to the agglomerate nature of many boehmites, reference measurements with the dry powders (-D) were conducted to exclude particle dissection during dispersion. Actually, a significant agglomerate dissection could be allocated to the Disperal 80 powder. Table 1.2

Table 1.2: Size distribution characteristics of investigated powders: Disperal 80, Pural SB, Pural SCC and DMS.

	Disperal-L	Disperal-D	Pural SB-L	Pural SCC-L	DMS-L
d_p [μm]	7.21	18.75	52.99	131.44	74.30
D_{10} [μm]	0.21	1.50	8.05	42.51	25.99
D_{50} [μm]	0.52	11.41	48.91	124.63	75.74
D_{90} [μm]	24.33	34.51	103.30	220.92	119.41
n [μm]	40	50	160	330	180
D_{90}/D_{10} [-]	115.9	23.0	12.8	5.2	4.6

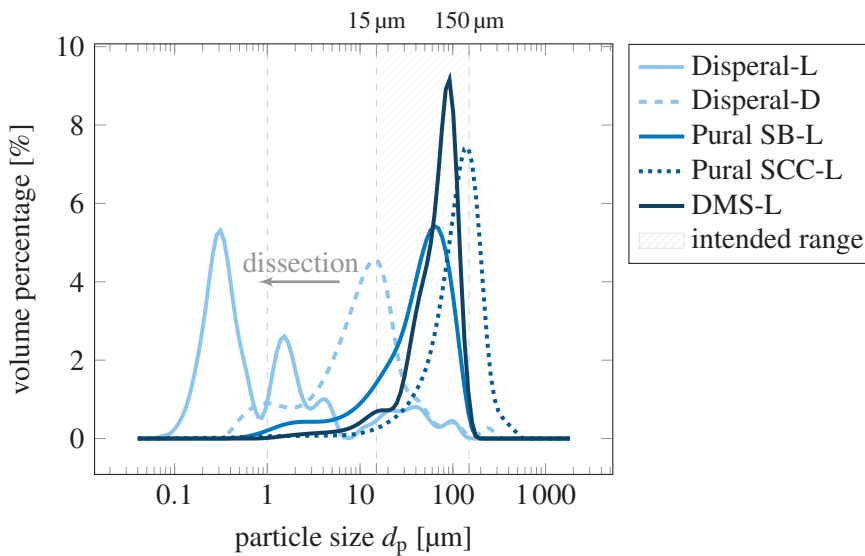


Figure 1.4: PSD of Disperal 80, Pural SB, Pural SCC and DMS powders as obtained by wet (-L) and dry (-D) laser diffraction; the shaded area marks the preferred size range as indicated by Sutton et al. [63].

and Fig. 1.4 outline typical size distribution characteristics of the investigated powders. While DMS corresponds best to the given standards of a 15 μm to 150 μm size range [63], Pural SCC comprises significant amounts of particles beyond the upper limit and Pural SB and Disperal 80 have fines below 15 μm . However, Pural SB's D_{10} is above 5 μm which is in accordance with Spierings et al.'s definition of lower PSD limit [97]. The minimal layer thickness n is calculated to be 50 % higher than D_{90} [97]. With an intended layer thickness between 100 μm to 200 μm , the Pural SCC powder clearly outranges this and is thus considered less suitable for the described application. The width of the distribution, characterised by the D_{90}/D_{10} ratio is in all cases close to or above 5 as desired [97], especially the Disperal 80 powder

features a significantly broad distribution over two to three orders of magnitude. Hence, it is unclear whether a too broad distribution has any negative effects on bed density or powder fluidity and should be matter of further research. The same holds true regarding the question if wide mono-modal or mixtures of distinct fractions forming bi-modal distributions should be preferred. In summary, all powders show a wide but mono-modal distribution, the particle size of the Pural SCC powder is possibly too large to be used in 3d printing and the Disperal 80 powder comprises significant amount of fines potentially leading to flowability issues.

The particle shape is investigated by scanning electron microscopy. Representative scans hereof are displayed in Fig. 1.5. More precisely, Fig. 1.5a depicts a rather un-spherical boehmite agglomerate consisting of various sized particles typical for Disperal 80. Pural SB's wide PSD can be clearly seen in Fig. 1.5b, however, agglomerate formation is not as pronounced as for Disperal indicated by higher sphericity, but is still visible. Higher sphericity paired with an observable particle surface roughness and no apparent agglomerate formation characterizes Pural SCC powder (Fig. 1.5c). An impressive sphericity and clearly recognisable smooth surface particles qualifies the DMS powder depicted in Fig. 1.5d. With favouring higher sphericities, especially those close to spherical shapes [61], the DMS powder appears to be the most appropriate in terms of shape.

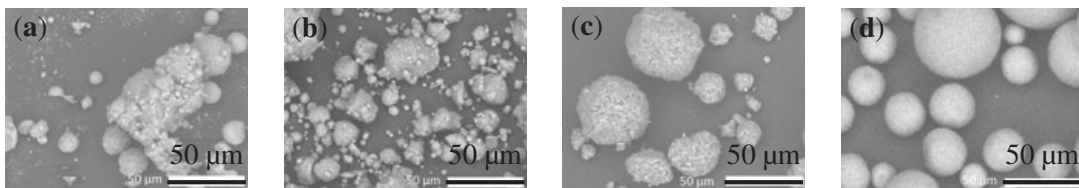


Figure 1.5: Representative scanning electron microscopy images of (a) Disperal 80, (b) Pural SB, (c) Pural SCC and (d) DMS powder; the scale bar represents 50 μm each.

The results for the angle of repose characterizing the fluidity of a powder are displayed in Table 1.3. Typically, an angle of about 25° qualifies a very good flowability [112]. Hence, the DMS powder is characterized having a good flowability, whereas Disperal 80 and Pural SB are rather poor. The Pural SCC powder, not displayed in Table 1.3, exhibits an angle of 30° and thus good flowing behaviour. Flowability is the manifestation of friction, which depends on particle shape, surface roughness, and the tendency for agglomerate formation occurring at small particle sizes. Unsurprisingly, Disperal 80 powder having significant amounts of fines and non-spherical particles exhibits the highest angle of repose, which is steadily improved by using particles with higher sphericity and decreasing amounts of fines.

Table 1.3: Powder characteristics concerning flowability, microstructure and bed density of Disperal 80, Pural SB and DMS powders.

	angle of repose α [°]	pore volume V_{pore} [cm ³ g ⁻¹]	surface area a_{BET} [m ² g ⁻¹]	bulk density $m_{\text{bed}}/V_{\text{bed}}$ [g cm ⁻³]	density ρ_{solid} [g cm ⁻³]	relative bed density ω_{bed} [-]
Disperal	43	0.149	83	0.42	3.02	0.2
Pural SB	37	0.244	183	0.70	3.02	0.4
DMS	28	0.746	223	0.71	3.95	0.7

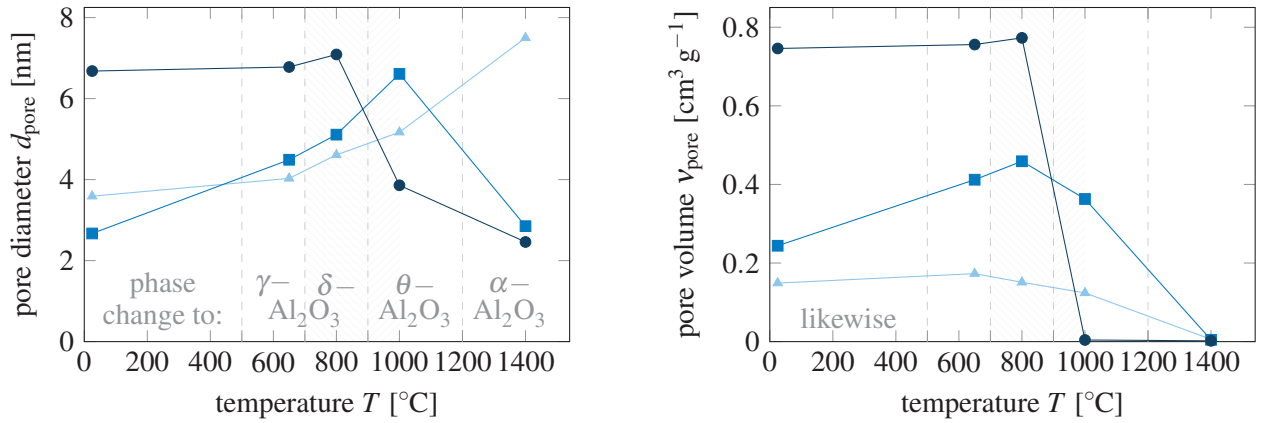
Primarily, powder flowability concerns the powder application process. Pre-tests with the final printing setup reveal the applicability of all powders, but powder beds made of Disperal 80 show obvious bed inhomogeneities. This could be drastically improved by using a vibrator connected to the applicator. While being obvious that powders with low flowability are not favoured for applications in which a constant and reliable powder flow must be guaranteed, it is questionable if a bottom limit exists under which the powder bed itself becomes instable due to the small amount of particle adhesion caused by the reduced presence of friction. Due to the lack of an profound powder characteristics study regarding powder bed printers (which include laser-based printing techniques), any generalization is delicate and controvertible. This is aggravated by the usage of different powder spreading techniques and a vast difference in utilized bed sizes.

Microstructure and Bed Density

The microstructure of the powders used in this study is evaluated by gas adsorption means. Herein, the Pural SCC powder is not considered any further, as the particle size is out of range. The results for BET surface area and pore volume of the mere powders are depicted in Table 1.3 and displayed in Fig. 1.6. Additionally, the mean pore size is at 3.7 nm, 2.8 nm and 6.8 nm for Disperal 80, Pural SB and DMS, respectively (also refer to Fig. 1.6a). Attention may be drawn to the significant difference in pore volume comparing Pural SB and DMS and the BET surface area considering Disperal 80 and DMS. Obviously, targeting final parts with high specific surface areas, the DMS powder should be favoured from a microstructural point of view.

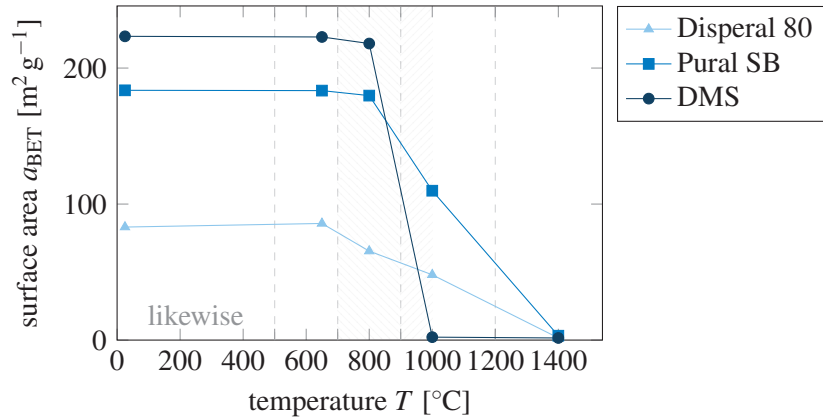
In order to later select an appropriate post-processing treatment, the temperature dependent change of microstructure was investigated with the results being displayed in Fig. 1.6. It is to be noted, that Disperal 80 and Pural SB powders are of boehmite nature, undergoing the phase change to γ - Al_2O_3 at about 500 °C, while DMS consists of γ - Al_2O_3 from the beginning. Furthermore, the indicated phase transformation temperatures are not to be understood as hard limits. They shall display typical starting points and the coexistence of more than one phase at certain temperatures is probable. The shaded area underlines the uncertainty regarding the δ - Al_2O_3 and θ - Al_2O_3 phase transformation limits.

Regarding pore diameter (Fig. 1.6a), the boehmite Disperal 80 and Pural SB powders have smaller values at the beginning but describing a pore size increase with increasing treatment temperature. This pore size increase is accompanied by an increase in pore volume (Fig. 1.6b) in case of Pural SB and constant values regarding Disperal 80 for temperatures up to 800 °C before declining to 0 transferring to the α -phase. In contrary, the DMS powder exhibits higher starting values regarding both, pore diameter and size, which are approximately constant for temperatures up to 800 °C before sharply decreasing upon reaching temperatures around 1000 °C, describing the θ -alumina phase transformation. As depicted in Fig. 1.6c, the BET surface area does not change significantly with heat treatment temperatures up to 800 °C for all three powders. Hereinafter, it decreases gradually (Disperal 80, Pural SB) or sharply (DMS) to insignificant values reaching temperatures at and above 1000 °C. This surface area reduction is caused by a phase change to θ -alumina at around 900 °C to 1000 °C and the final transition to the α -phase around 1200 °C inducing significant pore sintering. Consequently, a calcination treatment at 650 °C is thus assumed to



(a) Change of pore diameter with temperature.

(b) Change of pore volume with temperature.



(c) Change of BET surface area with temperature.

Figure 1.6: Change of microstructure of Disperal 80, Pural SB and DMS powder with treatment temperature; the respective phase changes from boehmite and γ - Al_2O_3 to α - Al_2O_3 is indicated in (a) but can be transformed likewise to subfigures (b) and (c).

not alter the microstructure of the parts critically. Moreover and as already assumed, final part sintering requiring temperatures of 1200 °C and above will dissect the desired microstructure.

For the final evaluation, the relative bed density is calculated according to equation (1.2) considering specific pore volume, bulk density and material density as displayed in Table 1.3. Considering Disperal, unfavourable powder shape and size lead to poor flowability and a very small relative bed density of 20 %, which is even slightly below the lower limit for powder bed densities as indicated by Zocca et al. [53]. The relative bed density of Pural SB, calculated to be around 40 %, is typical for a coarse particle bed according to German [102]. Compared to that, the preferred morphology characteristics of DMS lead to the highest flowability and an impressive relative bed density of 70 %.

1.4.2 Printer Setup Validation

The functionality of the printer setup was tested by printing cylinders of different dimensions horizontally

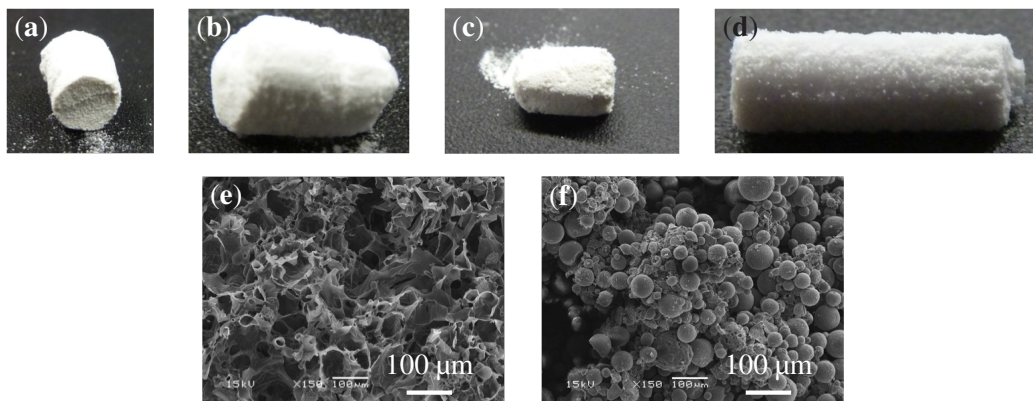


Figure 1.7: Binder Jetting with polyethylene glycol (a-d) and water (e,f) as binding agent; comprising powder species (a) Disperal 80, (b) Pural SB, (c) Pural SCC and (d) DMS, (e) carboxymethyl cellulose salt, and (f) a 50 % carboxymethyl cellulose salt - DMS blend.

and vertically into the powder bed. The standard pathway as described in Fig. 1.1(a₁) to (c₁) was performed, selecting polyethylene glycol as binding agent. Images of exemplary results for all four alumina powders are displayed in Figs. 1.7a to 1.7d. Although being sintered, final part's mechanical stability did not achieve the qualities reported in literature but successfully validated the printer setup. Moreover, alternative path (d) as described in Fig. 1.1 comprising the carbonization of organic binders in absence of air was performed and results are displayed in Figs. 1.7e and 1.7f. Herein, the actual binding agent, the carboxymethyl cellulose salt, was mixed with the alumina powder, jointly forming the powder bed. Furthermore, the water added through the print head acts as the solvent of the cellulose salt, forming the organic binder phase during bed permeation. SEM images taken from the charcoal matrix obtained by mere cellulose printing are displayed in Fig. 1.7e, the blending with alumina powders results in stable final parts with alumina particles embedded in the very same charcoal matrix as depicted in Fig. 1.7f. It is to be noted, that the thermo ink-jet cartridge utilized in this work had no problems printing water, but was struggling arbitrary clogging issues when using organic liquids. This was allocated to the formation of charcoal during the droplet ejection process.

1.4.3 Binder Formulation and Powder-Binder Interplay

Various Disperal sols were screened concerning the influence of Disperal type, acid and boehmite content on binding capability in a pre-printing test setup comprising manually addition of sol droplets on the powder bed surface. Moreover, ethylene glycol may be added to alter wettability as exemplarily depicted in Fig. 1.8. Herein, Fig. 1.8a and Fig. 1.8b show the result of a two-droplet test using sol 1, without and

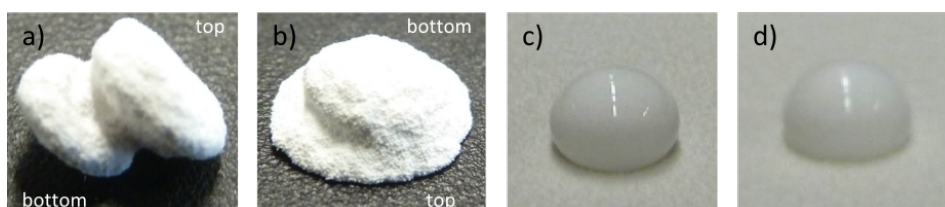


Figure 1.8: Droplet tests with 30 wt-% Disperal sol (a) without or (b) with ethylene glycol, and 30 wt-% Disperal 60 sol (c) without and (d) with ethylene glycol. Attention shall be drawn to the double-primitive in subfigure (b) which is photographed upside down.

with the addition of ethylene glycol, respectively. The pure sol results in two similar shaped primitives having a small contact area, whereas the addition of ethylene glycol increases this contact area to the dimensions of the first primitive. In contrary to that, sol 2 does not permeate into the powder bed while forming stable droplets on its surface as depicted in Fig. 1.8c. An addition of ethylene glycol does not alter this behaviour significantly, shown in Fig. 1.8d. A further increase of the solid content as in sol formulation 3 causes spontaneous gelation when stirring is stopped. In contrary, sol 4 can be applied well, however having obviously less binding strength than sol 1. Thus, the 30 wt-% Disperal sol (sol 1) with additional ethylene glycol was selected as binding agent for further investigations. The ejectability of all sols with the given thermo ink-jet print head was studied, however clogging occurred repeatedly. As of this, a syringe is used for binder addition in the following.

1.4.4 Post-Processing and Analysis of Final Parts

Cylindrical parts of 5.5 mm diameter and 6.5 mm in height were produced by layerwise application of DMS powder and dropwise addition of 30 wt-% Disperal binder under assistance of a mask to allow shaping. The powder bed may be compressed ("press.") after each layer addition and calcination ("calc.") at 650 °C may be performed as post-processing. Dimensional change, crush strength and specific surface area for each treatment pair (compressed-incompressed and calcined-noncalcined) are listed in Table 1.4. The crush strength is calculated according to equation (1.10) based on the mean measures of dimension and loading.

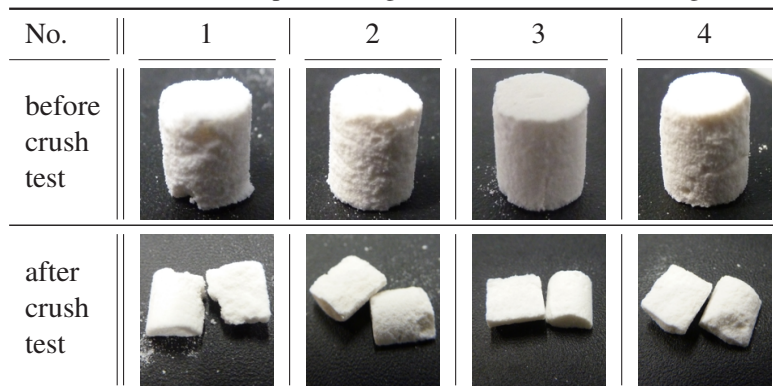
As displayed in Table 1.4, expectably no shrinkage occurs during post-processing. The crush strength increases after calcination and increases slightly with an increased powder bed density. The maximum crush loading obtained with a compressed bed and after calcination is at 18.2 N, which is only slightly below the lower limit of side crush strength for catalyst shaped bodies ($F_{\min} = 20$ N) as indicated in literature [29]. However, the overall crush strength is still below literature data (approx. 1 MPa to 2 MPa)

Table 1.4: Results of dimensional accuracy, crush strength and surface area for produced parts of DMS powder and 30 wt-% Disperal binder using compressed and uncompressed beds and calcination for post-processing.

No.	press.	calc.	diameter d [mm]	height h [mm]	side loading force F_{SC} [N]	crush force σ_{comp} [MPa]	crush strength σ_{comp} [MPa]	specific surface area a_{BET} [m ² g ⁻¹]
1	-	-	5.49 ± 0.08	6.27 ± 0.22	4.2 ± 1.2	0.078	0.078	224.8
2	-	✓	5.66 ± 0.11	6.47 ± 0.19	15.6 ± 2.6	0.27	0.27	199.1
3	✓	-	5.49 ± 0.23	6.34 ± 0.23	6.2 ± 1.2	0.11	0.11	220.7
4	✓	✓	5.52 ± 0.03	6.55 ± 0.13	18.2 ± 1.9	0.32	0.32	191.8

of comparable cylinders produced by traditional techniques [144]. The specific surface area decreases slightly during calcination and with increased compression. Nonetheless, the obtained specific surface area is significantly higher compared to literature data of catalyst carriers produced by additive manufacturing while withstanding similar crush loadings [29].

Furthermore, details of crushing behaviour are depicted in Table 1.5 showing an axial breakage of all produced cylinders which is a typical breakage pattern for traditionally shaped catalyst supports [144]. In contrary, additively manufactured parts tend to break along contact lines or areas of produced layers,

Table 1.5: Images taken from produced cylinders of green and calcined parts using compressed or uncompressed beds, and their respective fragments after side crush strength testing.

primitives or strands. Here, the expectably breakage in circumferential direction indicating an often observed insufficient cohesion of added layers is superimposed by a high binder saturation, where the high amounts of binder penetrate much further into the bed than necessary to bind one layer to another.

1.5 Summary and Optimization Outlook

Proof-of-principle studies were performed, in order to investigate if and to what extent Binder Jetting is capable to manufacture micro or mesoporous pure alumina parts having both, high specific surface areas and sufficient mechanical strength for the use as catalyst carriers in heterogeneous catalysis. With

the disclosed material combination of DMS powder and a 30 wt-% Disperal binder, parts having high BET surface areas around $190 \text{ m}^2 \text{ g}^{-1}$ and noteworthy mechanical strength could be produced. It is the first successful attempt to use the principles of Binder Jetting for the manufacturing of catalyst carriers and higher BET surface areas as disclosed for similar setups but different printing techniques could be obtained. However, in order to measure up to industrial standards, doubling or tripling of the disclosed strength values would be beneficial. In order to achieve this, powder bed and binder formulation need to be optimized.

Concerning the powder bed, this can be achieved predominantly by further increasing bed density. However, it is to be noted that only a limited selection of usable powders is available and that the herein disclosed DMS powder is already close to ideal characteristics. Another thinkable if not always available possibility is a change in printer setup, such as by using a more efficient powder application process including powder compaction of any means or by using powder slurries.

On the contrary, much more optimization effort can be done concerning the binder formulation. Here, numerous possibilities exist, that may change binding capability such as optimizing sol characteristics, evaluating additives and ejection behaviour. Concerning printer setup, the selection of print head itself and the adaption of the sol to the print head specifications should be considered.

However, as typically the characterization of powders and binders and its implications for the printing process are based on the specific printer setups used, generalizations may be treacherous. The lack of standardized powder bed creation and print head ejection methods make it difficult to put the obtained results into a scientific context. Consequently, powder and binder selection in common with printing preferences are frequently chosen by experience rather than profound statistics. A first attempt was done by the ASTM, trying to pool the existing empirical knowledge regarding laser-based powder bed fusion processes [79]. There is a certain need to enlarge upon this and spread to other additive manufacturing techniques to form a firm basis for future research.

Finally, post-processing techniques other than heat treatments should be investigated. Infiltration techniques may be a promising attempt that may lead to a further increase in final parts strength. In summary, it is assumed, that after serious optimization, printed parts may have comparable characteristics as parts obtained by traditional shaping techniques (e.g. having equal strength and specific surface area of a part of equal shape and dimensions). But, thinking of the great benefit of 3d printing – the manufacturing of hardly any imaginable shape - and especially in terms of catalysis, the production of filligrane structures with significantly improved fluid dynamic behaviour, higher strengths are needed to comply with industrial needs. Consequently, rather than imitating what industry is already capable of, the distant but overall target must be to facilitate the desired filligrane structures to have similar mechanical strengths compared to solid cylinders when traditionally shaped. Unfortunately, boehmite sols are considered to have weak binding strength that after all optimization may not be strong enough to allow this. Moreover, complex post-processing may outrun the benefits of 3d printing. It is thus questionable, if not a different but stronger binding species or method comprising other metals or metal oxides than alumina, as for instance silica sols, silicate based binders in common with silver or aluminum nano-particle inks sintering at

lower temperatures (cf. Fig. 1.1 path (g)) should be considered. However, this gives rise to compatibility questions with the targeted catalyst reactions.

Acknowledgements

The authors would like to thank Benedict Schäfer and Joel Bachmann for their contribution to the experiments.

Financial and substantial support of MuniCat, a strategic alliance between the Technical University of Munich (TUM) and Clariant AG is gratefully acknowledged. Jennie von Seckendorff would further like to thank the TUM Graduate School for generous support.

Nomenclature

Latin Symbols

A	surface area	m^2
a_{BET}	specific surface area according to BET	$\text{m}^2 \text{g}^{-1}$
b	width measure	m
d	characteristic diameter	m
D	binder dose	$\text{m}^3 \text{m}^{-1}$
D_{10}	diameter of 10 th percentile	μm
D_{90}	diameter of 90 th percentile	μm
F	(loading) force	N
F_{B}	Brownian force	N
F_{G}	Gravitational force	N
F_{SC}	side crush loading force	N
ff_c	flowability measure	-
g	constant of gravity	m s^{-2}
h	height measure	m
h^*	permeation depth	m
h°	height of liquid column	m
h_z	vertical distance between theoretical layer border and solid particle	m
k_{B}	Boltzmann constant	JK^{-1}
l	length measure	m
l^*	printed line width	m
l°	printed line length	m
m	mass	kg
m	Weibull modulus	-
n	empirical constant	-
n	layer thickness	μm
P	possibility of failure	-
S	binder saturation	-
T	temperature	K
t^*	infiltration time	s
V	volume	m^3
V_ε	void volume	m^3
V_b	volume of binder	m^3

Greek Symbols

α	angle of repose	$^\circ$
----------	-----------------	----------

γ	surface tension	N m^{-1}
ε	(bed) porosity	-
ε_z	surface roughness of particles	-
ζ	zeta potential	V
η	viscosity	Pa s
θ	contact angle	°
v	specific volume	$\text{m}^3 \text{kg}^{-1}$
ρ	density	kg m^{-3}
σ	strength	MPa
σ_{comp}	compressive strength	MPa
ϕ	volume fraction of solids	-
Ψ	sphericity	-
ω	relative density	-

Indices

0	reference or characteristic value
bed	powder bed content
max	maximal value
min	minimal value
np	nano particle
p	particle
pore	pore content
solid	solids content

Dimensionless Numbers

Oh	Ohnesorge number
Re	Reynolds number
We	Weber number

Abbreviations

ASTM	American Society for Testing and Materials
BET	Brunauer Emmett Teller
BJ	Binder Jetting
CNC	Computerized Numerical Control
DEM	Discrete Element Method
DIP	Direct Ink-jet Printing
DIW	Direct Ink Writing

DOD	Drop-on-Demand
EDS	energy-dispersive x-ray spectroscopy
EG	ethylene glycol
FDC	Fused Deposition of Ceramics
FDM	Fused Deposition Modeling
PSD	Particle Size Distribution
SLA	Stereolithography
TGA	thermogravimetric analysis
XPS	x-ray photoelectron spectroscopy
XRD	x-ray diffraction

Appendix

Table 1.A1: Overview of characterization techniques concerning powder and powder bed.

parameter	variable	recommended dimension	measurement technique
size	d_p	15 μm to 150 μm [63]	light diffraction
particle size distribution (PSD)	D_{90}/D_{10}	≥ 5 [97]	light diffraction
shape	sphericity $\Psi = \frac{\pi^{\frac{1}{3}} \cdot (6 \cdot V_p)^{\frac{2}{3}}}{A_p}$	≈ 1 [61]	microscopy & image analysis
particle surface roughness	-	-	microscopy
powder flowability	Hausner ratio	1.3 to 1.4 [95]	Hall funnel meter (ASTM D 7481)
	angle of repose α	$\leq 25^\circ$ [112]	e.g. rotating cylinder
	flowability ff_c	5 to 7 [95]	drag shear test
relative powder bed density	$\omega_{\text{bed}} = \frac{(V_{\text{solid}} + V_{\text{pore}})}{V_{\text{bed}}}$	$\geq 50\%$ to 60% [53, 101]	weighing or method by Jacob et al. [78]
powder layer homogeneity & roughness	surface roughness[77]: $\varepsilon_z = \frac{\sqrt{\langle (h_z - \langle h_z \rangle)^2 \rangle}}{d_p}$	-	microscopy, tomography
chemistry	-	-	x-ray diffraction (XRD), x-ray photoelectron spectroscopy (XPS), energy-dispersive x-ray spectroscopy (EDS), thermo-gravimetric analysis (TGA)
microstructure	e.g. a_{BET} , d_{pore} , V_{pore}	-	gas adsorption, microscopy

Table 1.A2: Overview of characterization techniques concerning binding agents.

parameter	variable	recommended dimension	measurement technique
chemistry of binder & binding method	-	-	e.g.: spectroscopy, thermo-gravimetric analysis (TGA)
rheology	viscosity [130]: $\eta = \eta_0 \cdot \left(1 - \frac{\phi}{\phi_{\max}}\right)^{-n}$	5 mPas to 20 mPas [46, 83], shear thinning	rheometer, for ϕ_{\max} method according to Liu et al. [153]
	surface tension γ	35 mN m ⁻¹ to 40 mN m ⁻¹	tensio meter
	ejectability $Oh^{-1} = \frac{Re}{\sqrt{We}} = \frac{\sqrt{\gamma \cdot \rho \cdot d}}{\eta}$	1 to 10 [46, 83]	-
dispersion characterization	(nano-particle) particle size d_{np}	$\frac{d_{\text{orifice}}}{d_{np}} = 20$ to 100 [46, 87]	light diffraction
	degree of sedimentation $\frac{F_G}{F_B} = \frac{d_{np}^4 \cdot \Delta\rho \cdot g}{k_B \cdot T}$	< 1 [132]	vertical light diffraction, turbidimeter, UV-VIS
	zeta potential ζ	-	zeta meter
	pH-value	-	pH meter
droplet formation (as a function of rheology and print head specification)	droplet shape, size d_d , speed u_d , trajectory		high speed video imaging [43, 45, 85], size: droplet counting & weighing
aging behaviour	change of rheology/dispersion over time	no aging	same as for rheology/dispersion characteristics

Table 1.A3: Characterization techniques regarding powder binder interplay.

parameter	variable	recommended dimension	measurement technique
binder saturation/-dose	$S = \frac{V_b}{V_\varepsilon}, D = \frac{V_b}{l^\circ}$	$S > 100\%$ [133]	-
binding capability	-	-	e .g. adding drops of binder to powder bed or mixing powder and binder and fill into molds [62], microscopy
permeability & wettability	contact angle θ	$\theta_{Al_2O_3} = 20^\circ$ to 40° [43]	Capillary Rise, Sessile Drop, Thin Layer Wicking [136, 137]
	primitive dimensions l^*, h^* [43] $l^* = 2 \cdot \sqrt{\frac{D \cdot (\sin \theta)^2}{\theta - \sin(\theta \cdot \cos \theta)}}$	-	adding single droplets by print head on powder bed, evaluation with microscope; repeat for gaining information on repeatability [43, 61, 62]
	infiltration kinetics [43]: $t^* = \frac{15 \cdot (h^\circ)^2}{\gamma \cdot \cos \theta} \cdot \frac{(1 - \varepsilon) \cdot \eta}{\varepsilon^3 \cdot \rho^2 \cdot d_p}$	fast infiltration	high speed video imaging [43]
printing of complex shapes	minimal feature size	-	printing of bridges and interstices with decreasing dimensions, evaluation of printing accuracy by microscopy

Table 1.A4: Overview of post-processing and final part analysis.

parameter	variable	recommended dimension	measurement technique
chemistry/physics of post-processing method	e.g. phase change, pyrolysis, residuals	-	e.g. spectroscopy, TGA, elementary analysis, microscopy
final parts accuracy	surface roughness	-	profilometer
	shrinkage/dimensional accuracy	-	microscopy
	final part density	-	pycnometer, weighing
final parts mechanical stability	abrasion	relative abrasion 0.1 to 0.7 according to Bonse et al.[154]	e.g. abrasion test [154]
	tensile strength, compressive strength [150]: $\sigma_{\text{comp}} = \frac{2 \cdot F_{\text{SC}}}{\pi \cdot l \cdot d}$, flexural strength, bulk strength	for technical ceramics: $\sigma_{\text{comp}} \geq 4000$ MPa [140]; binder jetted ceramics: $\sigma_{\text{comp}} \approx 180$ MPa [52]; catalyst carrier: $\sigma_{\text{comp}} \approx 1$ MPa to 2 MPa [144]	side crush test, 3-point bending test, impulsive drop test, bulk crush test
	Weibull characteristic [143]: $P = 1 - \exp \left[- \left(\frac{F}{F_0} \right)^m \right]$	-	linear least-square regression

References

- [1] I. Campbell, D. Bourell, I. Gibson, *Rapid Prototyping Journal* **2012**, *18*, 255–258.
- [2] C. Hurt, M. Brandt, S. S. Priya, T. Bhatelia, J. Patel, P. R. Selvakannan, S. Bhargava, *Catalysis Science and Technology* **2017**, *7*, 3421–3439.
- [3] C. Parra-Cabrera, C. Achille, S. Kuhn, R. Ameloot, *Chemical Society Reviews* **2018**, *47*, 209–230.
- [4] X. Zhou, C. Liu, *Advanced Functional Materials* **2017**, *27*, 1701134.
- [5] M. D. Symes, P. J. Kitson, J. Yan, C. J. Richmond, G. J. T. Cooper, R. W. Bowman, T. Vilbrandt, L. Cronin, *Nature Chemistry* **2012**, *4*, 349–354.
- [6] M. Woodhouse, B. A. Parkinson, *Chemistry of Materials* **2008**, *20*, 2495–2502.
- [7] J. M. Gregoire, C. Xiang, S. Mitrovic, X. Liu, M. Marcin, E. W. Cornell, J. Fan, J. Jin, *Journal of The Electrochemical Society* **2013**, *160*, F337–F342.
- [8] L. Goyos-Ball, E. García-Tunón, E. Fernández-García, R. Díaz, A. Fernández, C. Prado, E. Saiz, R. Torrecillas, *Journal of the European Ceramic Society* **2017**, *37*, 3151–3158.
- [9] J. Azauaje, C. R. Tubío, L. Escalante, M. Gómez, F. Guitián, A. Coelho, O. Caamano, A. Gil, E. Sotelo, *Applied Catalysis A: General* **2017**, *530*, 203–210.
- [10] A. Díaz-Marta, C. Tubío, C. Carbajales, C. Fernández, L. Escalante, E. Sotelo, F. Guitián, V. L. Barrio, A. Gil, A. Coelho, *ACS Catalysis* **2018**, *8*, 392–404.
- [11] C. R. Tubío, J. Azuaje, L. Escalante, A. Coelho, F. Guitián, E. Sotelo, A. Gil, *Journal of Catalysis* **2016**, *334*, 110–115.
- [12] K. Y. Chen, Y. Y. Chen, W. C. J. Wei, *Innovative Energy and Research* **2017**, *6*, 1000172.
- [13] S. Danaci, L. Protasova, J. Lefevre, L. Bedel, R. Guilet, P. Marty, *Catalysis Today* **2016**, *273*, 234–243.
- [14] S. Danaci, L. Protasova, F. Snijkers, W. Bouwen, A. Bengaouer, P. Marty, *Chemical Engineering and Processing – Process Intensification* **2018**, *127*, 168–177.
- [15] R. M. Ferrizz, J. N. Stuecker, J. Cesarano, J. E. Miller, *Industrial & Engineering Chemistry Research* **2005**, *44*, 302–308.
- [16] M. Konarova, W. Aslam, L. Ge, Q. Ma, F. Tang, V. Rudolph, J. N. Beltramini, *ChemCatChem* **2017**, *9*, 4132–4138.
- [17] M. Kramer, M. McKelvie, M. Watson, *Journal of Materials Engineering and Performance* **2018**, *27*, 21–32.
- [18] J. Lefevre, M. Gysen, S. Mullens, V. Meynen, J. van Noyen, *Catalysis Today* **2013**, *216*, 18–23.
- [19] J. van Noyen, A. de Wilde, M. Schroeven, S. Mullens, J. Luyten, *International Journal of Applied Ceramic Technology* **2012**, *9*, 902–910.
- [20] J. N. Stuecker, J. E. Miller, R. E. Ferrizz, J. E. Mudd, J. Cesarano, *Industrial & Engineering Chemistry Research* **2004**, *43*, 51–55.
- [21] S. Couck, J. Lefevre, S. Mullens, L. Protasova, V. Meynen, G. Desmet, G. V. Baron, J. F. M. Denayer, *Chemical Engineering Journal* **2017**, *308*, 719–726.

- [22] M. Campanati, G. Fornasari, A. Vaccari, *Catalysis Today* **2003**, *77*, 299–314.
- [23] P. Munnik, P. E. de Jongh, K. P. de Jong, *Chemical Reviews* **2015**, *115*, 6687–6718.
- [24] J. A. Schwarz, C. Contescu, A. Contescu, *Chemical Reviews* **1995**, *95*, 477–510.
- [25] P. Michorczyk, E. Hedrzak, A. Wegrzyniak, *Journal of Materials Chemistry A* **2016**, *4*, 18753–18756.
- [26] E. C. Hammel, O. L. Ighodaro, O. I. Okoli, *Ceramics International* **2014**, *40*, 15351–15370.
- [27] G. Do, T. Stiegler, M. Fiegl, L. Adler, C. Körner, A. Bösmann, H. Freund, W. Schwieger, P. Wasserscheid, *Industrial & Engineering Chemistry Research* **2017**, *56*, 13402–13410.
- [28] H. Freund, M. Lämmermann, C. Busse, W. Schwieger, *25th International Symposium on Chemical Reaction Engineering. Florence. Italy* **2018**.
- [29] T. Ludwig, J. von Seckendorff, C. Troll, R. Fischer, M. Tonigold, B. Rieger, O. Hinrichsen, *Chemie Ingenieur Technik* **2018**, *90*, 703–707.
- [30] M. R. Skorski, J. M. Esenther, Z. Ahmed, A. E. Miller, M. R. Hartings, *Science and Technology of Advanced Materials* **2016**, *17*, 89–97.
- [31] D. R. Coupland, *Patent Application*, US 2013/0230721, **2013**.
- [32] D. R. Coupland, *Patent Application*, EP 2752244, **2014**.
- [33] N. Kashani-Shirazi, V. Wloka, W. Gerlinger, A. Schmidt, K. Heinen, W. Kollenberg, *Patent Application*, US 2010/0222209, **2010**.
- [34] H. Wu, Y. Cheng, W. Liu, R. He, M. Zhou, S. Wu, X. Song, Y. Chen, *Ceramics International* **2016**, *42*, 17290–17294.
- [35] O. Santoliquido, G. Bianchi, P. D. Eggenschwiler, A. Ortona, *International Journal of Applied Ceramic Technology* **2017**, *14*, 1164–1173.
- [36] R. Felzmann, S. Gruber, G. Mitteramskogler, P. Tesavibul, A. R. Boccaccini, R. Liska, J. Stampfl, *Advanced Engineering Materials* **2012**, *14*, 1052–1058.
- [37] T. Chartier, C. Chaput, F. Doreau, M. Loiseau, *Journal of Materials Science* **2002**, *37*, 3141–3147.
- [38] E. Feilden, E. G. Blanca, F. Giuliani, E. Saiz, L. Vandeperre, *Journal of the European Ceramic Society* **2016**, *36*, 2525–2533.
- [39] J. Maurath, N. Willenbacher, *Journal of the European Ceramic Society* **2017**, *37*, 4833–4842.
- [40] T. Schlördt, S. Schwanke, F. Keppner, T. Fey, N. Travitzky, P. Greil, *Journal of the European Ceramic Society* **2013**, *33*, 3243–3248.
- [41] N. C. Fan, Y. Y. Chen, K. Y. Chen, W. C. J. Wei, B. H. Liu, A. B. Wang, R. C. Luo, *Journal of Ceramic Processing Research* **2017**, *18*, 676–682.
- [42] K. Shahzad, J. Deckers, J. Kruth, J. Vleugels, *Journal of Materials Processing Technology* **2013**, *213*, 1484–1494.
- [43] J. Moon, J. E. Grau, V. Knezevic, M. J. Cima, E. M. Sachs, *Journal of the American Ceramic Society* **2002**, *85*, 755–762.
- [44] K. A. M. Seerden, N. Reis, J. R. G. Evans, P. S. Grant, J. W. Halloran, B. Derby, *Journal of the American Ceramic Society* **2001**, *84*, 2514–2520.

- [45] N. Ramakrishnan, P. K. Rajesh, P. Ponnambalam, K. Prakasan, *Journal of Materials Processing Technology* **2005**, *169*, 372–381.
- [46] B. Derby, N. Reis, *MRS Bulletin* **2003**, *28*, 815–818.
- [47] J. A. Gonzalez, J. Mireles, Y. Lin, R. B. Wicker, *Ceramics International* **2016**, *42*, 10559–10564.
- [48] S. Maleksaeedi, H. Eng, F. E. Wiria, T. M. H. Ha, Z. He, *Journal of Materials Processing Technology* **2014**, *214*, 1301–1306.
- [49] C. Polzin, D. Günther, H. Seitz, *Journal of Ceramic Science and Technology* **2015**, *6*, 141–146.
- [50] E. Sachs, M. Cima, P. Williams, D. Brancazio, J. Cornie, *Journal of Engineering for Industry* **1992**, *114*, 481–488.
- [51] E. M. Sachs, J. S. Haggerty, M. J. Cima, P. A. Williams, *Patent*, US 5204055, **1993**.
- [52] M. Stumpf, N. Travitzky, P. Greil, T. Fey, *Journal of the European Ceramic Society* **2018**, *38*, 3603–3609.
- [53] A. Zocca, P. Colombo, C. M. Gomes, J. Günster, *Journal of the American Chemical Society* **2015**, *98*, 1983–2001.
- [54] N. Travitzky, A. Bonet, B. Dermeik, T. Fey, I. Filbert-Demut, L. Schlier, T. Schlordt, P. Greil, *Advanced Engineering Materials* **2014**, *16*, 729–754.
- [55] L. Yang, H. Miyajiri, *Proc. 28th Annual International Solid Freeform Fabrication Symposium – An Additive Manufacturing Conference. Austin. Texas* **2017**, 652–679.
- [56] J. Luyten, S. Mullens, I. Thijs, *KONA Powder and Particle Journal* **2010**, *28*, 131–142.
- [57] J.-S. Kim, K. Jiang, I. T. Chang, *Advanced Engineering Materials* **2009**, *11*, 106–110.
- [58] D. Yao, C. Wirth, Y. Zeng, D. Jiang, J. Günster, J. G. Heinrich, *Materials Letters* **2015**, *147*, 116–118.
- [59] J. G. Bai, K. D. Creehan, H. A. Kuhn, *Patent Application*, WO 2009/017648, **2009**.
- [60] N. B. Crane, J. Wilkes, E. Sachs, S. M. Allen, *Rapid Prototyping Journal* **2006**, *12*, 266–274.
- [61] B. Utela, D. Storti, R. Anderson, M. Ganter, *Journal of Manufacturing Processes* **2008**, *10*, 96–104.
- [62] B. R. Utela, D. Storti, R. L. Anderson, M. Ganter, *Journal of Manufacturing Science and Engineering* **2010**, *132*, 011008.
- [63] A. T. Sutton, C. S. Kriewall, M. C. Leu, J. W. Newkirk, *Proc. 27th Annual International Solid Freeform Fabrication Symposium – An Additive Manufacturing Conference. Austin. Texas* **2016**, 1004–1030.
- [64] H. Miyajiri, M. Orth, J. M. Akbar, L. Yang, *Frontiers of Mechanical Engineering* **2018**, *13*, 504–512.
- [65] Q. B. Nguyen, M. L. S. Nai, Z. Zhu, C. N. Sun, J. Wei, W. Zhou, *Engineering* **2017**, *3*, 695–700.
- [66] J. F. Brecht, T. Anderson, *Patent*, US 5902441, **1999**.
- [67] J. Yoo, M. J. Cima, S. Khanuja, E. M. Sachs, *Proc. 4th Annual International Solid Freeform Fabrication Symposium – An Additive Manufacturing Conference. Austin. Texas* **1993**, 40–50.

- [68] M. Cima, E. Sachs, T. Fan, J. F. Brecht, S. P. Michaels, S. Khanuja, A. Lauder, S.-J. J. Lee, D. Brancazio, A. Curodeau, D. Tuerck, *Patent*, US 5387380, **1995**.
- [69] Y. Wu, J. Du, K.-L. Choy, L. L. Hench, *Journal of the European Ceramic Society* **2007**, *27*, 4727–4735.
- [70] S. Yang, J. R. G. Evans, *Powder Technology* **2007**, *178*, 56–72.
- [71] C. M. Gaylo, I. J. Imiolek, *Patent*, US 5934343, **1999**.
- [72] S. Baskaran, G. L. Graff, *Patent*, US 5697043, **1997**.
- [73] J. Zielinski, S. Vervoort, H. Mindth, M. Megahed, *Berg- und Hüttenmännische Monatshefte* **2017**, *162*, 192–198.
- [74] E. J. R. Parteli, T. Pöschel, *Powder Technology* **2016**, *288*, 96–102.
- [75] U. Ali, Y. Mahmoodkhani, S. I. Shahabad, R. Esmaeilzadeh, F. Liravi, E. Sheydaeian, K. Y. Huang, E. Marzbanrad, M. Vlasea, E. Toyserkani, *Materials and Design* **2018**, *155*, 495–501.
- [76] Y. S. Lee, P. Nandwana, W. Zhang, *The International Journal of Advanced Manufacturing Technology* **2018**, *96*, 1507–1520.
- [77] S. Haeri, Y. Wang, O. Ghita, J. Sun, *Powder Technology* **2017**, *306*, 45–54.
- [78] G. Jacob, A. Donmez, J. Slotwinski, S. Moylan, *Measurement Science and Technology* **2016**, *27*, 115601.
- [79] G. Jacob, C. U. Brown, A. Donmez, *NIST Advanced Manufacturing Series 100-17* **2018**.
- [80] A. Butscher, M. Bohner, N. Doebelin, L. Galea, O. Loeffel, R. Müller, *Acta Biomaterialia* **2013**, *9*, 5369–5378.
- [81] E. M. Sachs, *Patent*, US 6036777, **2000**.
- [82] S. J. Gregorski, PhD thesis, Massachusetts Institute of Technology, **1996**.
- [83] S. F. S. Shirazi, S. Gharekhani, M. Mahrli, H. Yarmand, H. S. C. Metselaar, N. A. Kadri, N. A. A. Osman, *Science and Technology of Advanced Materials* **2015**, *16*, 033502.
- [84] A. Kamyshny, J. Steinke, S. Magdassi, *The Open Applied Physics Journal* **2011**, *4*, 19–36.
- [85] N. Reis, C. Ainsley, B. Derby, *Journal of the American Ceramic Society* **2005**, *88*, 802–808.
- [86] J. H. Song, M. J. Edirisinghe, J. R. G. Evans, *Journal of the American Ceramic Society* **1999**, *82*, 3374–3380.
- [87] D. Godlinski, S. Morvan, *Material Science Forum* **2005**, *492-293*, 679–684.
- [88] O. V. Levin, V. G. Sidel'kovskaya, R. R. Aliev, E. A. Leshcheva, *Chemistry and Technology of Fuels and Oils* **1997**, *33*, 97–100.
- [89] N. van Garderen, F. J. Clemens, C. G. Aneziris, T. Graule, *Ceramics International* **2012**, *38*, 5481–5492.
- [90] G. Paglia, C. E. Buckely, A. L. Rohl, R. D. Hart, K. Winter, A. J. Studer, B. A. Hunter, J. V. Hanna, *Chemistry of Materials* **2004**, *16*, 220–236.
- [91] D. Fauchadour, F. Kolenda, L. Rouleau, L. Barré, L. Normand, *Studies in Surface Science and Catalysis* **2000**, *143*, 453–461.

- [92] P. P. Nampi, S. Ghosh, K. G. Warriar, *Ceramics International* **2011**, *37*, 3329–3334.
- [93] M. Trueba, S. P. Trasatti, *European Journal of Inorganic Chemistry* **2005**, *17*, 3393–3403.
- [94] G. Paglia, C. E. Buckley, T. J. Udovic, A. L. Rohl, F. Jones, C. F. Maitland, J. Connolly, *Chemistry of Materials* **2004**, *16*, 1914–1923.
- [95] A. Butscher, M. Bohner, C. Roth, A. Ernstberger, R. Heuberger, N. Doebelin, P. von Rohr, R. Müller, *Acta Biomaterialia* **2012**, *8*, 373–385.
- [96] L. C. Hwa, S. Rajoo, A. M. Noor, N. Ahmad, M. B. Uday, *Current Opinion in Solid State and Materials Science* **2017**, *21*, 323–347.
- [97] A. B. Spierings, G. Levy, *Proc. 20th Annual International Solid Freeform Fabrication Symposium – An Additive Manufacturing Conference. Austin. Texas* **2009**, 342–353.
- [98] E. Vorndran, C. Moseke, U. Gbureck, *MRS Bulletin* **2015**, *40*, 127–136.
- [99] B. Liu, R. Wildman, C. Tuck, I. Ashcroft, R. J. M. Hague, *Proc. 22th Annual International Solid Freeform Fabrication Symposium – An Additive Manufacturing Conference. Austin. Texas* **2011**, 227–238.
- [100] A. M. Elliott, P. Nandwana, D. Siddel, B. G. Compton, *Proc. 27th Annual International Solid Freeform Fabrication Symposium – An Additive Manufacturing Conference. Austin. Texas* **2016**, 1031–1037.
- [101] N. P. Karapatis, G. Egger, P.-E. Gygax, R. Glardon, *Proc. 10th Annual International Solid Freeform Fabrication Symposium – An Additive Manufacturing Conference. Austin Texas* **1999**, 255–264.
- [102] R. M. German, *Powder Metallurgy Science, 1st edn.* Metal Powder Industries Federation, Princeton, N. J. USA, **1984**.
- [103] A. Strondl, O. Lyckfeldt, H. Brodin, U. Ackelid, *The Journal of The Minerals Metals & Materials Society* **2015**, *67*, 549–554.
- [104] A. Bodhmag, MA thesis, University of Saskatchewan, **2006**.
- [105] H. H. Zhu, J. Y. H. Fuh, L. Lu, *International Journal of Machine Tools and Manufacture* **2007**, *47*, 294–298.
- [106] R. K. McGeary, *Journal of the American Ceramic Society* **1961**, *44*, 513–522.
- [107] J. Zhou, Y. Zhang, J. K. Chen, *Journal of Manufacturing Science and Engineering* **2009**, *131*, 031004.
- [108] Z. Xiang, M. Yin, Z. Deng, X. Mei, G. Yin, *Journal of Manufacturing Science and Engineering* **2016**, *138*, 081002.
- [109] Y. Bai, G. Wagner, C. B. Williams, *Journal of Manufacturing Science and Engineering* **2017**, *139*, 081019.
- [110] J. Choi, G. Shin, H. Lee, D. Yang, S. Yang, C. Lee, M. Brochu, J. Yu, *Materials Transactions* **2017**, *58*, 294–297.
- [111] ASTM Standard D7481-18, Standard test methods for determining loose and tapped bulk densities of powders using a graduated cylinder, tech. rep., ASTM International, United States, **2018**.

- [112] D. Schulze, *Pulver und Schüttgüter*, Springer Vieweg Verlag Berlin Heidelberg, **2014**.
- [113] J. Pottbäcker, O. Hinrichsen, *Chemie Ingenieur Technik* **2017**, 89, 454–458.
- [114] L. M. Anovitz, D. R. Cole, *Reviews in Mineralogy and Geochemistry* **2015**, 80, 61–164.
- [115] G. Leofanti, M. Padovan, G. Tozzola, B. Venturelli, *Catalysis Today* **1998**, 41, 207–219.
- [116] J. G. Bai, K. D. Creehan, H. A. Kuhn, *Nanotechnology* **2007**, 18, 185701.
- [117] A. Elliott, A. AlSalihi, A. L. Marriman, M. M. Basti, *American Journal of Engineering and Applied Sciences* **2016**, 9, 128–133.
- [118] A. C. Bailey, A. Marriman, A. Elliott, M. M. Basti, *Proc. 27th Annual International Solid Freeform Fabrication Symposium – An Additive Manufacturing Conference. Austin. Texas* **2016**, 1069–1077.
- [119] H. Zhao, C. Ye, Z. Fan, Y. Shi, *Proc. 4th International Conference on Sensors Measurement and Intelligent Materials. Shenzhen. China* **2015**, 654–657.
- [120] N. Y. Sdobnyakov, V. M. Samsonov, A. N. Bazulev, D. A. Kul’pin, *Bulletin of the Russian Academy of Sciences: Physics* **2008**, 72, 1371–1373.
- [121] N. B. Crane, J. Wilkes, E. Sachs, S. M. Allen, *Proc. 16th Annual International Solid Freeform Fabrication Symposium – An Additive Manufacturing Conference. Austin. Texas* **2005**, 261–272.
- [122] Y. Bai, C. B. Williams, *Proc. 28th Annual International Solid Freeform Fabrication Symposium – An Additive Manufacturing Conference. Austin. Texas* **2017**, 249–260.
- [123] Y. Bai, C. B. Williams, *Nanotechnology* **2018**, 29, 395706.
- [124] Y. Zheng, J. Song, X. Xu, M. He, Q. Wang, L. Yan, *Industrial & Engineering Chemistry Research* **2014**, 53, 10029–10034.
- [125] E. Morgado, Y. L. Lam, S. M. C. Menezes, L. F. Nazar, *Journal of Colloid and Interface Science* **1995**, 176, 432–442.
- [126] J. Hille, U. Bollmann, W. Weinhold, H. Spindler, *Zeitschrift für anorganische und allgemeine Chemie* **1990**, 580, 188–198.
- [127] P. Greil, *Advanced Engineering Materials* **2000**, 2, 339–348.
- [128] I. M. Krieger, T. J. Dougherty, *Transactions of the Society of Rheology* **1959**, 3, 137–152.
- [129] L. Bergström, *Journal of the American Ceramic Society* **1996**, 79, 3033–3040.
- [130] D. M. Liu, W. J. Tseng, *Journal of Materials Science* **2000**, 35, 1009–1016.
- [131] J. F. Bredt, *Patent*, US 5660621, **1997**.
- [132] R. G. Larson, *The structure and rheology of complex fluids, 1st edn.* Oxford University Press, **1998**.
- [133] M. Vaezi, C. K. Chua, *International Journal of Advanced Manufacturing Technology* **2011**, 53, 275–284.
- [134] H.-C. Wu, H.-J. Lin, *Materials Transactions* **2010**, 51, 2269–2276.
- [135] P. Nandwana, A. M. Elliott, D. Siddel, A. Merriman, W. H. Peter, S. S. Babu, *Current Opinion in Solid State and Materials Science* **2017**, 21, 207–218.
- [136] L. Galet, S. Patry, J. Dodds, *Journal of Colloid and Interface Science* **2010**, 346, 470–475.

-
- [137] E. Nowak, G. Combes, E. H. Stitt, A. W. Pacey, *Powder Technology* **2013**, 233, 52–64.
- [138] W. Sun, D. J. Dcosta, F. Lin, T. El-Raghy, *Journal of Materials Processing Technology* **2002**, 127, 343–351.
- [139] I. Lee, *Journal of Materials Science Letters* **2001**, 20, 223–226.
- [140] P. Auerkari, *VTT Tiedotteita - Meddelanden - Research Notes 1792* **1996**.
- [141] ASTM Standard D4179-01, Standard test method for single pellet crush strength of formed catalyst shapes, tech. rep., ASTM International, United States, **2001**.
- [142] Y. Li, X. Li, L. Chang, D. Wu, Z. Fang, Y. Shi, *Catalysis Today* **1999**, 51, 73–84.
- [143] Y. Li, D. Wu, J. Zhang, L. Chang, D. Wu, Z. Fang, Y. Shi, *Powder Technology* **2000**, 113, 176–184.
- [144] D. Staub, S. Meille, V. L. Corre, J. Chevalier, L. Rouleau, *Oil & Gas Science and Technology* **2015**, 70, 475–486.
- [145] J. W. L. Beeckman, N. A. Fassbender, T. E. Datz, *AIChE Journal* **2016**, 62, 2658–2669.
- [146] ASTM Standard D7084-18, Standard test method for determination of bulk crush strength of catalysts and catalyst carriers, tech. rep., ASTM International, United States, **2018**.
- [147] J. W. L. Beeckman, M. Cunningham, N. A. Fassbender, T. E. Datz, *Chemical Engineering & Technology* **2017**, 40, 1844–1851.
- [148] D. Wu, J. Zhou, Y. Li, *AIChE Journal* **2007**, 53, 2618–2629.
- [149] J. W. L. Beeckman, N. A. Fassbender, T. E. Datz, *AIChE Journal* **2016**, 62, 639–647.
- [150] S. Timoshenko, J. N. Goodier, *Theory of elasticity, 3rd edn.* McGraw-Hill, New York, **1970**.
- [151] W. Weibull, *Journal of Applied Mechanics* **1951**, 18, 293–297.
- [152] C. Lu, R. Danzer, F. D. Fischer, *Journal of the European Ceramic Society* **2004**, 24, 3643–3651.
- [153] D. M. Liu, *Journal of the American Ceramic Society* **1999**, 82, 1162–1168.
- [154] D. Bonse, K.-H. Bretz, H. Derleth, M. Sell, M. Bischoff, *Patent Application*, WO 1993017790, **1993**.

Part II

The Structure of Randomness - Experimental Investigation of Random Packed Beds

2 Review on the Structure of Random Packed Beds

Abstract

Independent from their intended purpose, the understanding of structural characteristics of random packings of particles having defined shapes is important to understand and optimize fluid dynamic behaviour, heat, and mass transfer. The packing structure can be described by the coordination number, local porosity profiles, the average porosity, and pore characteristics, which are influenced by the wall and thickness effect; the material, shape, and size distribution of the packing particles; the packing and compaction mode; and the shape and material of the packing's containing walls. Therefore, existing knowledge on the structure of randomly packed mono-sized particles is reviewed to provide an updated selection of relevant parameters and their derived correlations obtained by experimental, numerical, and analytical means.

This article was published in:

The Canadian Journal of Chemical Engineering, J. von Seckendorff, O. Hinrichsen, Review on the structure of random packed beds, published online, Copyright Wiley (2020). DOI: 10.1002/cjce.23959.

Reprint Permission:

If you are the author of a published Wiley article, you have the right to reuse the full text of your published article as part of your thesis or dissertation. In this situation, you do not need to request permission from Wiley for this use.

2.1 Introduction

Random packings of particles having defined shapes are deployed in all kinds of industrial applications and come in all orders of magnitude. The most prominent examples comprise micro-sized particle beds as commonly used in chromatography packed columns [1–3], packed-bed reactors filled with catalytic shaped bodies having millimetre size [4, 5], packed columns used in separation processes such as distillation incorporating particles in the lower centimetre range [6, 7], and the pebble-bed reactor, which is a gas-cooled nuclear reactor, moderated by a packing of graphite spheres [8–10]. In addition to those, numerous less-known applications of packed-beds exist, ranging from powder-bed 3D printers [11], solar-energy storage systems [12], earth science [13], civil engineering [14, 15], and pharmaceutical processing [16], to the pyrolysis of pelletized wood fuels [17], to name but a few.

Irrespective of its intended purpose, the extent of a packed-bed is limited by a confining wall of commonly cylindrical shape, though flat plates and other container geometries are possible. Despite its generally random nature, close to this confinement the particles' placement is naturally forced to align with the wall's geometry. This imposed order reaches a couple of particle diameters into the packing and is usually named the wall effect. Its influence on the overall packed-bed characteristics decreases with increasing tube-to-particle diameter ratio $\lambda = D/d_p$. While most applications operate in an only sparsely affected λ -range, this effect becomes dominant, for instance, in catalytic multitubular reactors, typically performing at $\lambda = 4 - 7$ [18] or a single-pellet-string reactor with a $\lambda < 2$ [19]. Moreover, some packed-bed utilizations, especially chromatography columns, have very delicate requirements regarding bed homogeneity and its derived characteristics.

In general, random packed-beds are typically investigated in regard to the void distribution [20, 21], single- and multi-phase flow aspects [22], the extent of pressure loss along the bed height [23], axial and radial dispersion qualities [24] in common with inter- and intraparticle heat [25], and mass transfer properties. In this contribution, parameters that describe and influence the structural characteristics are reviewed, clustered, and compared. Parameters describing the packing structure comprise the coordination number \bar{N}_c , the radial porosity distribution $\varepsilon(r)$, the axial porosity distribution $\varepsilon(z)$, the average bed porosity $\bar{\varepsilon}$, and the pore size characteristics. These parameters are influenced by the wall effect, the thickness effect, the packing and compaction mode, the particle material, shape and size distribution, and the container's shape and material. Results can be obtained by partially elaborate experiments; however, the sheer number of recently published numerical approaches [26], including the generation of random packed-beds using, for instance, the *discrete element method* (DEM) with subsequent flow, heat and/or mass transfer simulation by known tools such as *COMSOL Multiphysics*[®], *Ansys*[®] *Fluent*, *STAR-CCM+*[®] or *OpenFOAM*[®], speaks for it. Although the developed numerical procedures require delicate validation, the gain in knowledge from employing the detailed resolution and visualization options is impressive.

The focus of this contribution is to review the different published methodologies and results to characterize the structure of random packed-beds using both experimental and numerical approaches.

2.2 Experimental investigation of packed-bed structures

Random packings of particles having a distinct shape are characterized by the size, distribution and the mean void fraction of the voids between the solids (porosity ε), the coordination number \bar{N}_c describing the average number of contact points between adjacent particles, and their average contact angle $\bar{\phi}_c$. Besides the tube-to-particle diameter ratio λ , these parameters may be influenced by the particle's material, shape and size distribution, the container's material and shape and the applied deposition and compaction methods [27, 28].

2.2.1 Regular arrangements of spatially extended mono-sized ideal spheres

Regular arrangements of spheres are characterized by a repeating pattern whose smallest repetition unit, the unit cell, represents the whole packing. It is the simplest case of a packed-bed and its structural characteristics can be derived by mathematical considerations [29, 30]. Table 2.1 summarizes typical

Table 2.1: Characteristics of regular sphere packings [14, 29–31]

Arrangement	Coordination number N_c [-]	Mean bed porosity $\bar{\varepsilon}$ [-]	Packing factor α_m [-]
Cubic	6	0.476	1
Orthorhombic	8	0.395	$\sqrt{3}/2$
Body-centered cubic	8	0.320	
Tetragonal-sphenoidal	10	0.302	0.75
Rhombohedral	12	0.260	$\sqrt{2}/2$

arrangements and their quantities. For more details, see some relevant reviews on this topic [13, 21, 31, 32]. Although these packed-beds are usually not utilized directly, they define the maximum porosity range a sphere packing can adapt to in the absence of a confining wall. Here, Taylor et al. [14] defined the packing factor α_m as the ratio between the volumes of the unit cells of the actual packing and the cubic packing of which the packing properties are compared. Moreover, regular arrangements can be used as a starting point to derive models for more realistic sphere packings [33], liquids [34], or other porous systems [14, 15].

2.2.2 Random packings of smooth mono-sized ideal spheres in cylindrical confining walls

Random packings of smooth, mono-sized, ideally spherical particles in cylindrical confining walls are frequently taken as the standard or reference packing arrangement. It is by far the most evaluated and researched packed-bed configuration, though in many cases not adequately representing the reality in industry.

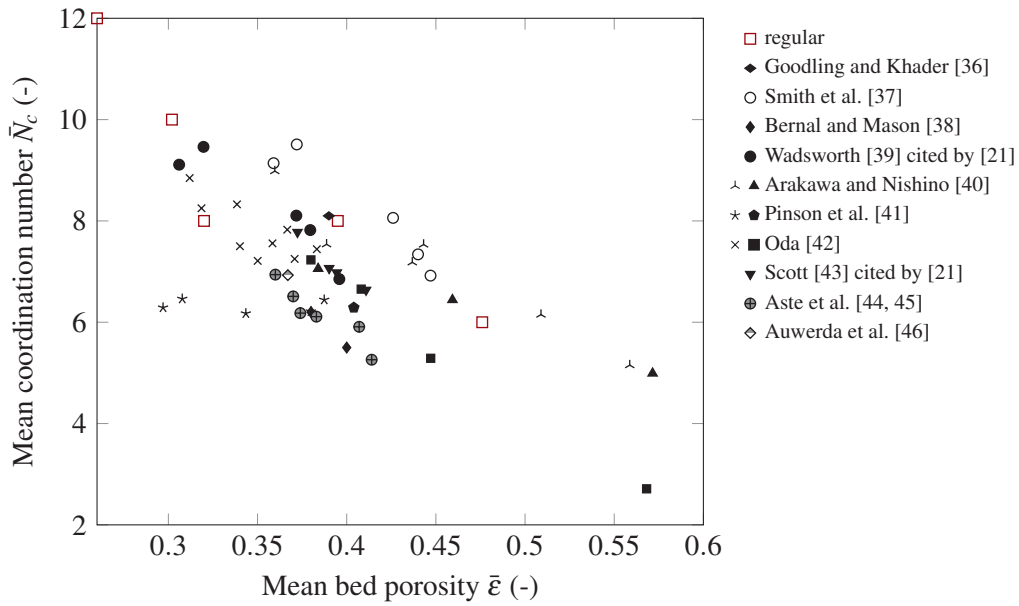


Figure 2.1: Experimental results obtained from the literature for the mean coordination number \bar{N}_c as a function of porosity $\bar{\epsilon}$. Full symbols represent data of homogeneous spheres, crosses those of size mixtures [21, 36–46]

2.2.2.1 Coordination number and angle

The number of contact points between one particle and its neighbours in combination with the angular distribution of these along the surface of the particles is of special interest for heat transfer investigations [35] and the general modelling of transport phenomena [36]. While regular packings have one distinct coordination number for each arrangement, varying from 6 - 12 (Table 2.1), random packings are characterized by having a distribution of coordination numbers.

Experimental

The traditional experimental evaluation of the coordination number is obtained by filling the voids within a packed-bed of spheres with a marker liquid. After drainage, the marker liquid will be retained at the true contact points by capillary forces [37]. Furthermore, near contact points are marked as well, as capillary forces allow bridging of narrow gaps [38]. True and near contact points can be distinguished, as a circle of marker substance with a non-marked centre indicates true contact points, whereas near contact points are marked by a filled circle [38]. The number and the distribution of true and near contacts can be obtained by counting the marker dots on each sphere. The mean coordination numbers and their cumulative frequency distribution as obtained by experiments are displayed in Figs. 2.1 and 2.2.

Some of the first researchers to address the experimental evaluation of the coordination number was Smith et al. [37]. They used a packing of lead shot and acetic acid, forming white lead acetate as marker liquid. However, it was noted that the data was erroneous [21] and it was eventually re-evaluated by Wadsworth [39].

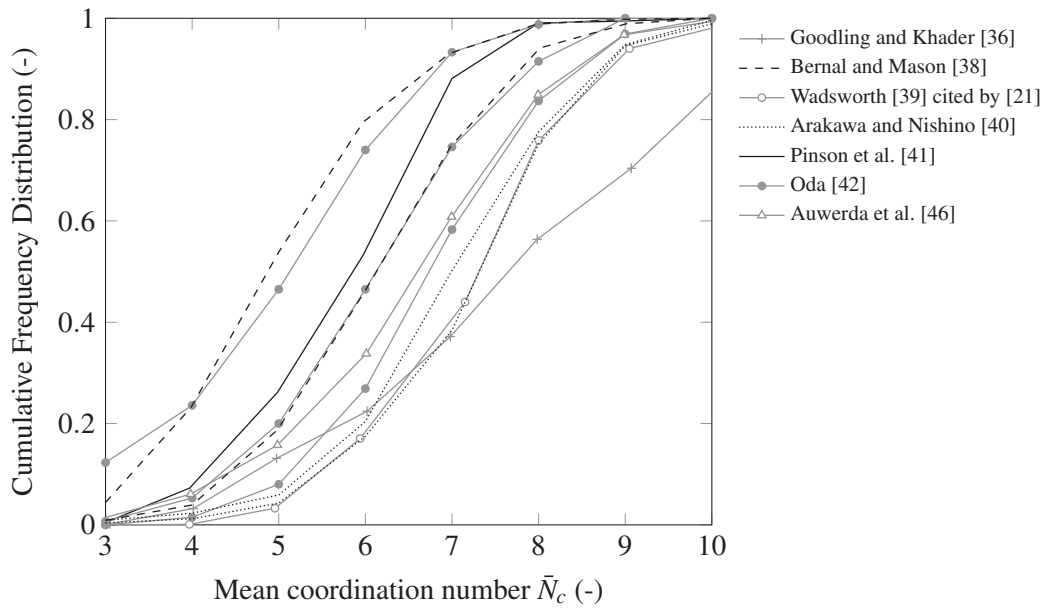


Figure 2.2: Experimental results obtained from the literature for the cumulative frequency distribution of the mean coordination number \bar{N}_c [21, 36, 38–42, 46]

A similar approach was selected by Bernal and Mason [38], except for the fact that they used ball bearings with black paint as a marker. They were the first to distinguish between true and near contacts and investigated two packed-bed densities. The same procedure was selected by Oda [42], investigating mono-sized sphere packings as well as binary and quaternary mixtures. While Arakawa and Nishino [40] used red ink to mark contact points between spheres, the utilization of shellac in methylated spirit was preferred by Pinson et al. [41] and Zou et al. [47].

A completely different approach was selected by Goodling and Khader [36]. Here, a packed-bed of spheres was solidified with epoxy resin, layers were cut, and photographs were taken. It was ensured that each sphere was cut at least twice so that the centre of each sphere could be determined. The contact points of each sphere were then obtained by mathematical considerations.

Modern imaging techniques allow the highly resolved determination of packed-bed structures. Aste et al. [44, 45] used X-ray computed tomography for the evaluation of the contacts between mono-sized spheres. Here too, uncertainty remained as to the distinction between true and near contacts due to voxel resolution. Similar studies were performed by Georgalli and Reuter [48], Reimann et al. [49–51], and Auwerda et al. [46].

The radial distribution function

For further investigations of the contact behaviour, Scott [52] determined the sphere centres in a packed-bed by filling the voids with molten wax, and after solidification removed each sphere separately from the matrix while noting each sphere's position. From this, he computed a radial density distribution using the distance normalized by the sphere diameter of the centres of the spheres from the wall of the random

packed-bed. This distribution was averaged for 25 randomly selected spheres. Mason and Clark [53, 54] added a direct sphere distance measuring technique in order to refine the near contacts portion [38]. The obtained plot is known as the *radial distribution function* and is used to model fluids (spheres represent atoms or molecules) or colloids (see Scott and Mader [55], Finney [56], Urquidi et al. [57], Dohn et al. [58], and Soper [59].) It is to be noted, that any investigation of radial distribution functions requires the absence of confinement influence.

Extrapolation and analytical considerations

When it comes to deriving mean contact number-porosity correlations it has to be considered that stable and realistic sphere packings only come in a small porosity range. It is generally accepted that the simple cubic arrangement constitutes the lower limit of a stable sphere packing. The range of realistic packings is even smaller. In order to overcome this barrier, Meissner et al. [60] tried to extrapolate available coordination number data by investigating sphere arrangements looser than the regular cubic packing. Similar approaches were performed by Melmore [61] and Heesch and Laves [62]. Further analytical investigations regarding extra loose sphere packings were performed in the context of sedimentation processes [63, 64]. Bennett [65] investigated packings artificially packed according to local and global criteria.

A completely different approach to overcome the problem that stable sphere packings only come in a very small porosity range is proposed by evaluating micro- and nanosized particles, as the porosity increases with decreasing particle size [66–69]. However, in this size range, the contact behaviour can only be determined numerically [66, 70].

In contrast to this, pure analytical approaches were described by Liu and Davies [71], who derived sphere contact information from the radial distribution function. Beck and Volpert [72] used the gapped gapless packing model [73–76] in combination with a fixed fraction annular and a self-same contact distribution to derive the contact behaviour of homogeneous spheres and binary mixtures. A similar approach was used by Richard et al. [77], incorporating radical and Voronoï tessellation as well as the navigation map. Other analytical-parametric models were developed by Yu and Standish [78] and Iwata and Homma [79].

Furthermore, investigations of the contact behaviour of numerically generated packed-beds were conducted [70, 80–90]. Among these, Clarke and Jónsson [86] could confirm the results of Bernal and Mason [38]. Most others focussed on multi-component packings. An et al. [90] tried to determine whether the packing of uniform spheres under gravity is quasi-universal. Therefore, extensive numerical screening was done, trying to extrapolate the known results by comparing micro- and normal-sized particles, vibrated and non-vibrated beds, filling beds in liquid, and air surroundings. Packing porosities between 0.8-0.26 are obtained, relating to a clear trend in regard to the coordination number.

Results collected from literature

A comprehensive selection of derived correlations obtained by the above-described experiments, analytical models, and extrapolation approaches is summarized in Fig. 2.3 and Table 2.2.

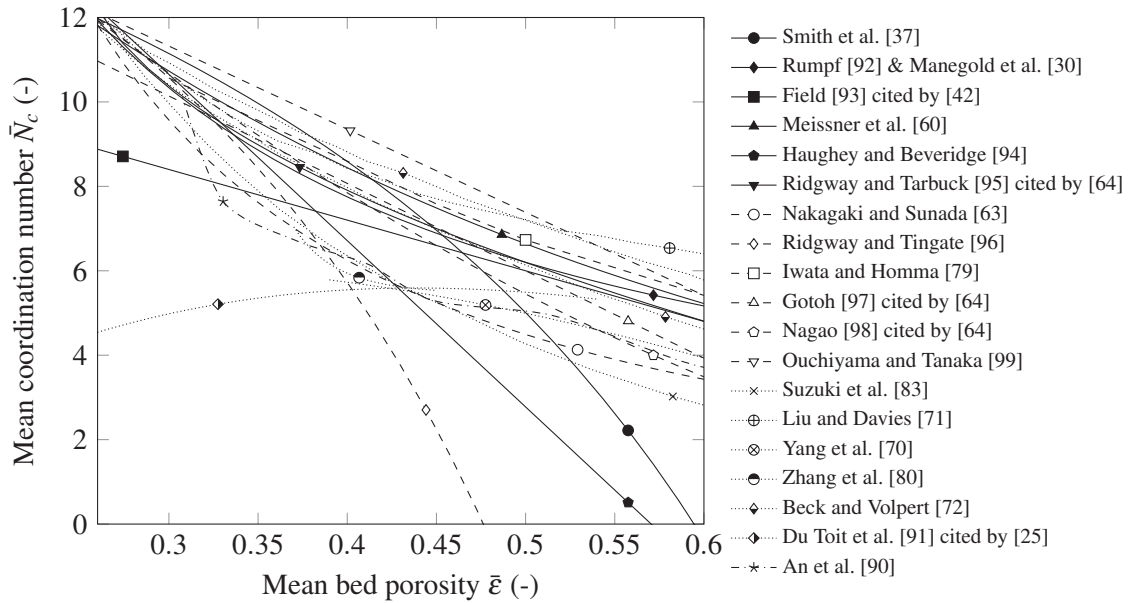


Figure 2.3: Comparison plot of known correlations regarding the relation of mean coordination number \bar{N}_c and mean packed-bed porosity \bar{e} for random packings and abstract arrangements of mono-sized spheres [25, 30, 37, 42, 60, 63, 64, 70–72, 79, 80, 83, 90–99]

The mean coordination number of sphere packings as obtained by experiments ranges from 6–8. From regular packings it is obvious that a packed-bed may have different coordination numbers for the very same porosity (refer to Table 2.1). Incorporating analytical and numerical data, a mean coordination number of around 6 is generally accepted for a typical packed-bed of mono-sized spheres [41, 44, 45, 47, 56, 70, 85, 87, 88, 101]. For a random close packing, a value of up to 7 is determined [44, 45, 49]. Deviations between experiments are often explained by the poor discrimination of true and near contacts.

While most researchers exclude the particles close to the confining walls, the wall effect on the mean coordination number was explicitly investigated by Pinson et al. [41], Goodling and Khader [36], Auwerda et al. [46], and Reimann et al. [49]. A decrease in the coordination number is observed only for the outermost and potentially the second ring of spheres adjacent to the wall, whereas Du Toit et al. [25, 91] observed a significant difference in mean coordination number between bulk and near-wall region. Furthermore, Reimann et al. [49] investigated the influence of the flat container bottom, finding a constant coordination number of 9 for the very bottom layer of spheres, while a coordination number of just below 12 could be obtained for the following three sphere layers in quasi-close packing conditions.

Table 2.2: Overview of known correlations relating the mean contact number \bar{N}_c to the packing porosity $\bar{\epsilon}$ of smooth mono-sized sphere packings

Source	Formula	Scope
Smith et al. [37]	$\bar{N}_c = \frac{15.75 - 26.49 \cdot \bar{\epsilon}}{1 - \bar{\epsilon}}$	$0.259 < \bar{\epsilon} \leq 0.476$
Rumpf [92] & Manegold et al. [30]	$\bar{N}_c = \frac{3.1}{\bar{\epsilon}}$	$0.259 < \bar{\epsilon} \leq 1$
Field [93] cited by Oda [42]	$\bar{N}_c = 12 \cdot (1 - \bar{\epsilon})$	n.a.
Meissner et al. [60]	$\bar{N}_c = 2 \cdot \exp(2.4 \cdot (1 - \bar{\epsilon}))$	$0.259 < \bar{\epsilon} \leq 1$
Haughey and Beveridge [94]	$\bar{N}_c = 22.47 - 39.39 \cdot \bar{\epsilon}$	$0.259 < \lambda \leq 0.5$
Ridgway and Tarbuck [95] cited by Suzuki and Oshima [64]	$\bar{N}_c = 13.84 - 116 \cdot (0.01724 \cdot \bar{\epsilon} - 0.00428)^{1/2}$	$0 < \bar{\epsilon} \leq 0.82$
Nakagaki and Sunada [63]	$\bar{N}_c = 1.61 \cdot \bar{\epsilon}^{-1.48}$	$0 < \bar{\epsilon} \leq 0.82$
Ridgway and Tingate [96]	$\bar{N}_c = 24 - \frac{2}{3} \cdot \left(\frac{\pi}{1 - \bar{\epsilon}} \right)^2$	$0.26 < \bar{\epsilon} \leq 0.47$
Gotoh [97] cited by Suzuki and Oshima [64]	$\bar{N}_c = 20.7 \cdot (1 - \bar{\epsilon}) - 4.35$	$0.3 < \bar{\epsilon} \leq 0.53$
	$\bar{N}_c = 36 \cdot \frac{1 - \bar{\epsilon}}{\pi}$	$\bar{\epsilon} > 0.53$
Nagao [98] cited by Suzuki and Oshima [64]	$\bar{N}_c = 21.80 \cdot (1 - \bar{\epsilon})^2$	n.a.
Ouchiyama and Tanaka [99]	$\bar{N}_c = \frac{32}{13} \cdot (7 - 8 \cdot \bar{\epsilon})$	n.a.
Suzuki et al. [83] cited by Suzuki and Oshima [64]	$\bar{N}_c = 2.812 \cdot \frac{(1 - \bar{\epsilon})^{-1/3}}{(b/d_p)^2 \cdot [1 + (b/d_p)^2]}$	$0.24 < \bar{\epsilon} \leq 54$
	with $(1 - \bar{\epsilon})^{-1/3} = \frac{1 + (b/d_p)^2}{1 + (b/d_p) \cdot \exp(d_p/b)^2 \cdot \text{Erfc}(d_p/b)}$	
Suzuki et al. [100] cited by Georgalli and Reuter [48]	with $\frac{b}{d_p} = 0.07318 + 2.193 \cdot \bar{\epsilon} - 3.357 \cdot \bar{\epsilon}^2 + 3.294 \cdot \bar{\epsilon}^3$	
Liu and Davies [71]	$\bar{N}_c = (1 - \bar{\epsilon}) \cdot \left(\frac{b}{r} \right)^3 - 1 +$ $+ \frac{24 \cdot (1 - \bar{\epsilon}) \cdot a \cdot (a^2 - c^2)}{r^3 \cdot (a^2 + c^2)^3} + \frac{6 \cdot (1 - \bar{\epsilon}) \cdot (3a^2 - c^2)}{r^2 \cdot (a^2 + c^2)^2} \cdot \frac{b}{r} + \frac{6 \cdot (1 - \bar{\epsilon}) \cdot a}{r \cdot (a^2 + c^2)} \cdot \left(\frac{b}{r} \right)^2$ with $b = 2 \cdot r + \frac{1}{c} \left(\frac{\pi}{2} + \arctan \frac{c}{a} \right)$, $a = \frac{2 \cdot \pi}{r} \left[4 \cdot \pi \cdot \left(\frac{\bar{\epsilon}}{1 - \bar{\epsilon}} \right)^2 \right]$ and $c = 2 \cdot \pi \cdot \frac{1 - \bar{\epsilon}}{r}$	$0.22 < \bar{\epsilon} \leq 0.66$
Yang et al. [70]	$\bar{N}_c = 2.02 \cdot \frac{1 + 87.38 \cdot (1 - \bar{\epsilon})^4}{1 + 25.81 \cdot (1 - \bar{\epsilon})^4}$	$0.39 < \bar{\epsilon} \leq 1$
Zhang et al. [80]	$\bar{N}_c = \frac{1}{0.183 - 659.248 \cdot (1 - \bar{\epsilon})^{20.961}}$	$0.37 < \bar{\epsilon} \leq 0.45$
Du Toit et al. [91] cited by Antwerpen et al.[25]	$\bar{N}_c = 25.952 \cdot \bar{\epsilon}^3 - 62.362 \cdot \bar{\epsilon}^2 + 39.724 \cdot \bar{\epsilon} - 2.02$	$0.24 < \bar{\epsilon} \leq 0.54$

Contact angle

The angular distribution was experimentally determined by Scott and Mader [55], finding certain angular structures at about 60° , 120° and 180° by using an averaged polar plot of the surface of the spheres. Reimann et al. [49, 50] divided the contact angle into the poloidal angle ϕ_c , describing orientation along the container axis and the azimuthal angle ψ , describing the orientation in the radial direction. In the bulk region, the angle distribution is quite homogeneous, but developing a certain structure at 30° and 150° in the poloidal orientation and 0° , 180° and 360° in the azimuthal orientation close to the confining sidewall and bottom. Du Toit et al. [25, 91] found a mean bulk contact angle in the poloidal direction of 31.97° which was detected to relate to the coordination number according to Eq. (2.1) [25].

$$\bar{\phi}_c = -6.1248 \cdot \bar{N}_c^2 + 73.419 \cdot \bar{N}_c - 186.68 \quad (2.1)$$

2.2.2.2 Radial porosity distribution

Regarding packings enclosed by a cylindrical wall, the structure of the random packings is typically characterized by plotting the circumferentially and axially averaged void space (porosity ε) against the radial position within the cylindrical tube starting at the tube wall and normalized to the particle diameter (d_p), $z_r = (R-r)/d_p$. The occurrence of local deviations from the theoretical bulk packing porosity in random packings is regarded as an indicator of the influence of the confining wall on the near-wall packing structure.

Experimental

Referring to Schneider and Rippin [102, 103], four kinds of general experimental procedures can be clustered to determine the local void fraction distribution within packed-beds:

1. The first is solidification and incremental removal. The experimental investigation of axially-averaged radial porosity profiles was historically conducted by filling the voids between the packing particles with molten wax or curable resins and the subsequent cutting or machining of the solidified matrix into thin radial or axial slices. Either the filler material is removed and the weight difference noted [104–108], or photographs of the slices can be subjected to image analysis resulting in the filled void content of each slice [103, 109–115]. Due to the small size of many packed-beds combined with the inaccuracy of cutting tools, these early investigations result in quite coarse and potentially erroneous curves. Moreover, loss of particles during the cutting procedure due to insufficient bonding strength between the particles and the filler material are commonly reported [104, 105, 109]. As an improvement, the resin can be mixed with metal powders [107] or hardening additives [103, 107].

2. Incremental filling is a completely different approach, comprising a centrifuged packed-bed to which small amounts of liquid, predominantly water, are added. The liquid forms an annular layer and the increment in layer thickness for a known amount of added water depends on the available void space, assuming a homogeneous void distribution for each radial section [116–120]. However, the precise determination of small variances in liquid level, especially considering the meniscus, makes this technique challenging. Lerou and Froment [119] improved this setup by accurately measuring the water level using a pressure transducer.
3. Individual particle measurement is the easiest way, if quite erroneous, involving the use a grid on a transparent container and counting the particles of which the centres are within a certain grid cell [121]. For more accurate results, the packed-beds can again be solidified with resin, and each and every sphere can be scratched out from the resin basis after noting its position [52–54]. Schuster and Vortmeyer [122] used a piston with sticky tape to remove the spheres of a packed-bed layer by layer, taking a photograph of each layer and subsequently allocating each sphere to a grid of position on the piston.
4. Projection of the bed is the last procedure. Initially, the solidified and cut packed-bed slices were scanned with an X-ray beam in order to improve data acquisition [109]. Later, X-ray tomography was used for non-destructive analysis of the whole packed-bed [10, 46, 49, 50, 123–128]. A stack of sliced packed-bed images is obtained where subsequent image analysis has to be performed. Most frequently, the computer-based image analysis includes the binarization of the obtained grayscale images in order to specify solid and void area. From these, the void ratio at a certain radial position can be estimated directly or the centre position of each sphere can be determined, requiring the subsequent mathematical calculation of radial profiles. The specification of the black-white threshold is frequently identified as the major source of error. Additionally, Buchlin et al. [129], whose work was later adopted by Schneider and Rippin [102], used the fluorescence of a slightly impure organic liquid having the same refractive index as transparent spheres to visualize the particle locations. Besides X-ray tomography, magnetic resonance imaging may be used as well to investigate local structures within packed-beds [130–134]. Again, a proper image analyzing procedure is required [131].

Results collected from literature

Regarding the obtained radial porosity data, some specific properties are generally accepted including [20]:

- The porosity directly at the tube wall has a value of 1.
- The curve resembles a damped oscillatory function with distinct extrema until reaching 4-5 particle diameters into the tube.
- The first minimum is at $z_r = d_p/2$ and the first maximum is at $z_r = d_p$.

Further properties of the radial porosity distribution under discussion comprise the initial shape of two consecutive parabolas transitioning to a sinusoidal variation when moving further away from the tube wall, the non-constant period of oscillation within a specific bed, and the amplitude, which varies when different experimental results and the derived correlations are compared [20].

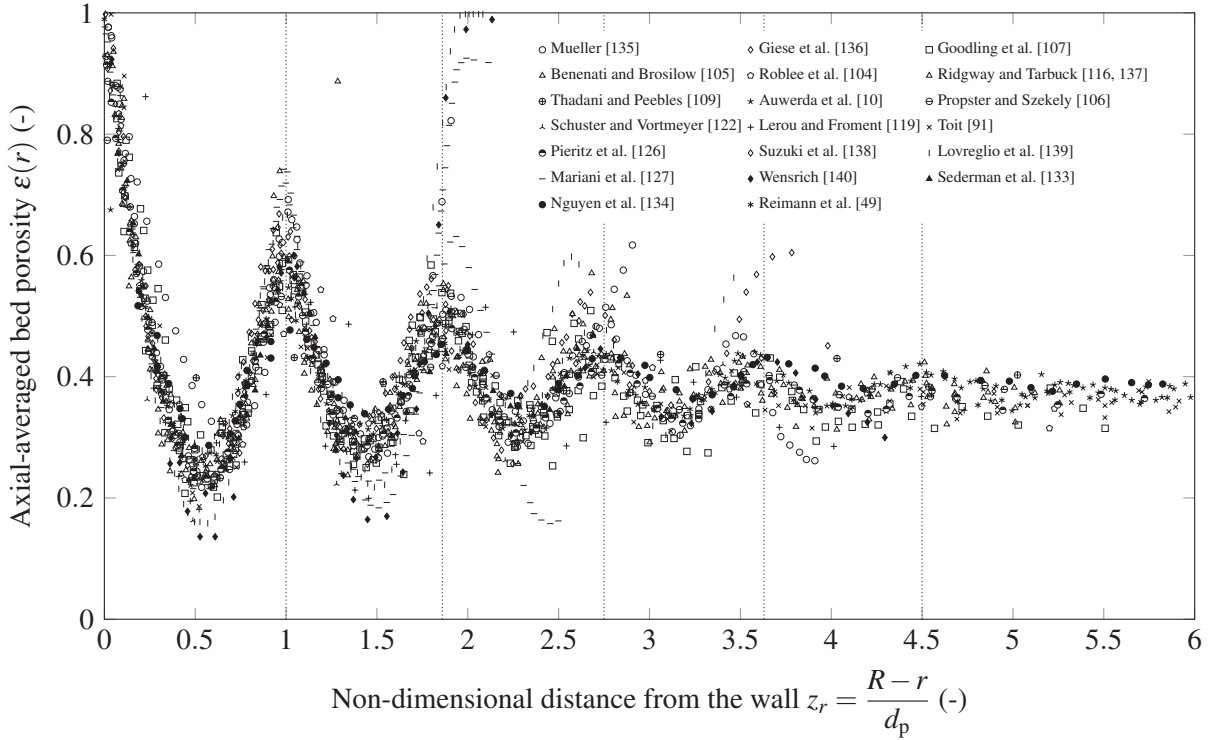


Figure 2.4: Gathered experimental literature data of radial porosity distributions $\varepsilon(r)$ obtained by using various experimental methods and packing procedures and containing spheres of different materials enclosed by a cylindrical confining wall [10, 49, 91, 104–107, 109, 116, 119, 122, 126, 127, 133–140]

Gathering the majority of experimental data ranging from $\lambda = 2$ to $\gg 10$ as presented in the literature into a single figure (Fig. 2.4), reveals a surprising consensus even without preference in regard to packing mode and material specifications. Significant differences can be seen for packed-beds of low tube-to-particle diameter ratios where the values in the tube centre are significantly larger at $z_r \approx 1$ (data of Benenati and Brosilow [105]), $z_r \approx 2$ (data of Lovreglio et al. [139], Mariani et al. [127], Mueller [135], Wensrich [140]), $z_r \approx 3$ (data of Mueller [135]) and $z_r \approx 4$ (data of Lovreglio et al. [139], and Giese et al. [136]).

In Fig. 2.4, the experimental studies of Schwartz and Smith [141] and Shaffer [117] are not considered as absurd bulk porosity values for sphere packings of as low as 0.32 and 0.28 were obtained, respectively. Furthermore, the study of Pillai [121] and Korolev et al. [123] could not be considered, as the data is incomplete. The study of Al-Falahi and Al-Dahhan [125] is not considered since obvious deviations from the generally accepted oscillatory behaviour is seen, as well as questionable porosity values close to the wall. The experimental study of Ismail et al. [112, 113] is not considered because the results for the radial porosity profile do not fit with all other results in the following points: the extrema positions are overall slightly shifted to higher numbers and the curve shape of especially the first maximum appears very smooth.

Schneider and Rippin [102] evaluated the radial locations of the minima and maxima of their own data and those from [105] and [107] depending on λ . It was found that the locations of the extrema are independent of λ in the tested range (2.5 – 15), so that the maxima occur at 1.00, 1.86, 2.75, 3.63 and 4.50 sphere diameters from the tube wall. Except for the very first maximum, the period of oscillation appears constant with 0.86 to 0.88 sphere diameters between consecutive minima and maxima. For validation, the detected maxima positions are marked as dotted lines in Fig. 2.4 showing a great consensus with the gathered experimental data.

Derived Correlations

The above-described experiments led to a selection of empirical correlations being derived to describe the tangentially and axially averaged radial porosity profile, complemented by some (semi-)analytical models. A comprehensive selection of correlations are shown in Table 2.3. These can generally be

Table 2.3: Selection of known wall effect correlations for the radial void distribution $\varepsilon(r)$ of spherical packed-beds in cylindrical confinements

Source	Formula	$\bar{\varepsilon}_{\text{inf}}$	Scope
De Klerk [20]	$\varepsilon(r) = 2.14 \cdot z_r^2 - 2.53 \cdot z_r + 1$ $\varepsilon(r) = \bar{\varepsilon}_{\text{inf}} + 0.29 \exp(-0.6 \cdot z_r) \cdot [\cos(2.3 \cdot \pi \cdot (z_r - 0.16))]$ $+ 0.15 \exp(-0.9 \cdot z_r)$	- n.a.	$z_r \leq 0.637$ $0.637 < z_r$
Johnson [142] cited by Roshani [103]	$\varepsilon(r) = \bar{\varepsilon}_{\text{inf}} + 0.62 \cdot \exp[-1.7 \cdot (z_r)^{0.434}] \cdot [\cos(6.67 \cdot (z_r)^{1.13})]$ $\varepsilon(r) = \bar{\varepsilon}_{\text{inf}}$	0.38 0.38	$z_r \leq 4$ $4 < z_r$
Moallemi [143] cited by Roshani [103]	$\varepsilon(r) = \bar{\varepsilon}_{\text{inf}} - 0.6 \cdot (1 - \exp[-1.7 \cdot (z_r)^{0.52}] \cdot [\cos(5.57 \cdot (z_r)^{1.25})])$	n.a.	n.a.
Chandrasekhara and Vortmeyer [144]	$\varepsilon(r) = \bar{\varepsilon}_{\text{inf}} \cdot (1 + b \cdot \exp(-c \cdot x))$ with $b = 1$ $c = 3$	n. a.	n. a.
Martin [145]	$\varepsilon(r) = \varepsilon_{\text{min}} + (1 - \varepsilon_{\text{min}}) \cdot (2 \cdot z_r - 1)^2$ $\varepsilon(r) = \bar{\varepsilon}_{\text{inf}} + (\varepsilon_{\text{min}} - \bar{\varepsilon}_{\text{inf}}) \cdot \exp[-0.25 \cdot (2 \cdot z_r - 1)] \cdot [\cos(\pi/a \cdot (2 \cdot z_r - 1))]$ for $\lambda = 20.3$: $\varepsilon_{\text{min}} = 0.23$ $a = 0.876$	- 0.39	$z_r \leq 0.5$ $0.5 < z_r$
Cohen and Metzner [146]	$\varepsilon(r) = 1 - (1 - \bar{\varepsilon}_{\text{inf}}) \cdot 4.5 \cdot (z_r - \frac{7}{9}) \cdot (z_r)^2$ $\varepsilon(r) = \bar{\varepsilon}_{\text{inf}} + (1 - \bar{\varepsilon}_{\text{inf}}) \cdot 0.3463 \cdot \exp(-0.4273 \cdot z_r) \cdot \cos((2.45 \cdot z_r - 2.2011) \cdot \pi)$ $\varepsilon(r) = \bar{\varepsilon}_{\text{inf}}$	n. a. n.a.	$z_r \leq 0.25$ $0.25 < z_r < 8$ $8 < z_r$
Mueller [135]	$\varepsilon(r) = \bar{\varepsilon}_{\text{inf}} + (1 - \bar{\varepsilon}_{\text{inf}}) \cdot J_0(a \cdot z_r) \cdot \exp(-b \cdot z_r)$ with $a = 7.45 - \frac{3.15}{\lambda}$ $b = 0.315 - \frac{0.725}{\lambda}$ or $a = 7.45 - \frac{11.25}{\lambda}$ $b = 0.315 - \frac{0.725}{\lambda}$	0.365 - -	$\lambda \geq 2.02$ $2.02 \leq \lambda \leq 13.0$ $\lambda \geq 13.0$
Bey and Eigenberger [147]	$\varepsilon(r) = \varepsilon_{\text{min}} + (1 - \varepsilon_{\text{min}}) \cdot (\frac{z_r}{z_{\text{min}}} - 1)^2$ $\varepsilon(r) = \bar{\varepsilon}_{\text{inf}} + (\varepsilon_{\text{min}} - \bar{\varepsilon}_{\text{inf}}) \cdot \exp[-0.1 \cdot (\frac{z_r}{z_{\text{min}}} - 1)] \cdot [\cos(\pi/0.876 \cdot (\frac{z_r}{z_{\text{min}}} - 1))]$ for $\varepsilon_{\text{min}} = 0.24$ $z_{\text{min}} = \frac{\lambda}{2} \cdot (1 - \sqrt{1 - \frac{2}{\lambda}})$	- 0.375	$\frac{z_r}{z_{\text{min}}} - 1 \leq 0$ $0 < \frac{z_r}{z_{\text{min}}} - 1$
Giese [148]	$\varepsilon(r) = \bar{\varepsilon}_{\text{inf}} \cdot (1 + 1.36 \cdot \exp(-5.0 \cdot z_r))$	-	-
Vortmeyer and Schuster [149]	$\varepsilon(r) = \bar{\varepsilon}_{\text{inf}} \cdot \left(1 + \frac{1 - \bar{\varepsilon}_{\text{inf}}}{\bar{\varepsilon}_{\text{inf}} \cdot \exp(1)} \cdot \exp(1 + z_r)\right)$	-	-
Suzuki et al. [138]	$\varepsilon(r) = \bar{\varepsilon}_{\text{inf}} + a \cdot \exp(-b \cdot z_r^c) \cdot \cos(2 \cdot \pi \cdot z_r^d)$ $a = 0.018 \cdot \ln(\lambda) + 0.483$; $b = 0.312 \cdot \ln(\lambda) + 0.58$; $c = 0.2061 \cdot \ln(\lambda) + 0.128$; $d = -0.033 \cdot \ln(\lambda) + 1.177$	n.a.	$\lambda \geq 4.5$

classified into the following categories: (a) exponential decay functions [144, 148–152], which completely

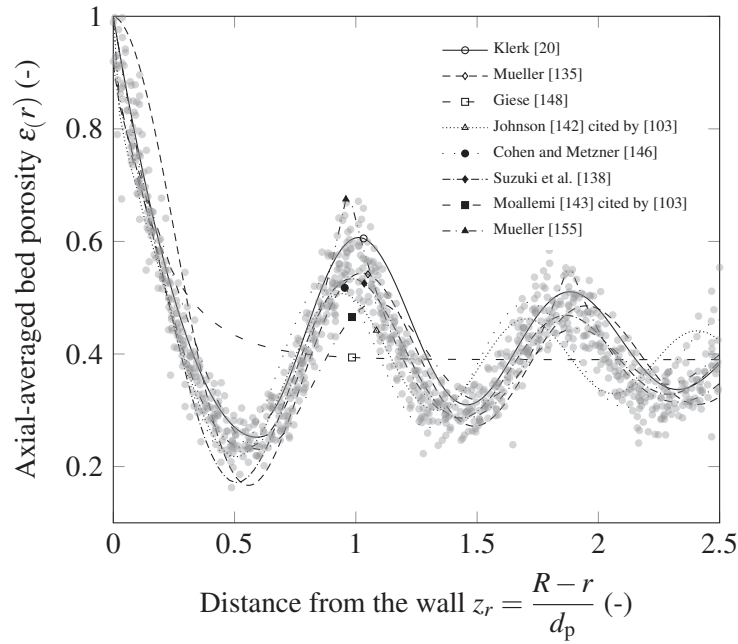


Figure 2.5: Comparison of anonymized experimental radial void distribution data $\varepsilon(r)$ obtained with $\lambda > 5.0$ and a selection of empirical and semi-analytical correlations as presented in the literature [20, 103, 135, 138, 142, 143, 146, 148, 155]

ignore the oscillation close to the wall; (b) damped oscillatory functions, combining a cosine oscillation with an exponential decay [20, 110, 145–147] or by using a Bessel function of zero order [135, 153, 154]; (c) scaleable approaches, that take λ -specific differences into account [135, 138, 155]; and (d) statistical sphere centre re-estimations based on experimental radial porosity profiles with subsequent re-calculation of the radial porosity distribution [33, 156–159]. This last approach was adopted for $\lambda < 2$ where the sphere locations can be expressed analytically assuming a regular packing arrangement based on λ -dependant unit cell considerations [160]. However, while actually not being a correlation but an inconvenient mathematical approach, it becomes obsolete when sphere centres are determined as experimental output.

Herein, Martin [145], Chandrasekhara and Vortmeyer [144], Vortmeyer and Schuster [149], and Johnson [142] used the data of Benenati and Brosilow [105] to derive their correlations. Cohen and Metzner [146] averaged the experimental data of Roblee et al. [104] and Ridgway and Tarbuck [137]. De Klerk [20] and Bey and Eigenberger [147] incorporated a larger selection of existing experimental data. However, the calculation of minima position z_{\min} as proposed by Bey and Eigenberger [147] is questionable: for a $\lambda < 2$ no results can be obtained and for $\lambda = 2$, the minima position is at one particle diameter from the wall. The position value decreases with increasing λ approaching 0.5 for infinite λ . Replacing z_{\min} with a constant 0.5 is more realistic and in accordance with other results. Doing so, this equation becomes similar to one by Martin [145].

For comparison, a selection of correlations are plotted for a specific tube-to-particle diameter ratio $\lambda = D/d_p = 5$ as displayed in Fig. 2.5 with the anonymized experimental data taken from Fig. 2.4. Here, only data for packed-beds with $\lambda > 5$ are considered, as packings with lower λ behave significantly different, and seem to be not representable by current correlations [161].

While a good consensus among experimental data exists in regard to amplitude and period of the radial void distribution, most empirical correlations struggle to project in particular the correct oscillation period which becomes evident at higher z_r . Only the semi-analytical correlation of [155] trying to describe the obtained radial void distribution behaviour with a string of parabolas rather than a damped cosine function can correctly reproduce the oscillation period and amplitude of the used data pool. This may be explained with the known inconsistent oscillation period, where the first period is 1.00 and the following periods are around 0.87 [102]. The slight overprediction at $z_r < 0.5$ of the Bessel function proposed by Mueller [135] and queried by Theuerkauf et al. [161] can be decreased using a recently published functional improvement [153].

Some experimental procedures result in the provision of sphere centre points rather than directly in the void size distribution. From the centre point coordinates and the sphere's dimensions, axial and radial porosity profiles can be calculated by cutting imaginary plane and cylindrical slices through the mathematically reconstructed spheres [155, 162–166]. These slices may have a designated thickness characterizing the volume-based method or not, resulting in the area-based method.

In summary, a wide selection of experimental methods are known for the determination of the tangentially and axially averaged radial porosity distribution, a key parameter for the evaluation of packing structure, though most come with unsatisfactory accuracy for a single measurement. However, when gathering all available literature data regarding packings of spheres into one plot, an impressive consensus can be seen. This consensus cannot be reproduced by most available correlations, especially regarding the oscillation period.

2.2.2.3 Pore size and shape

Characterizing the size and shape of the voids within a packed-bed is rather challenging, as pores are non-circular and irregularly converge, diverge, and intersect [21].

The void size and distribution characterization were first performed in a 2D analytical setup, packing mono-sized circles [167] later size-distributed circles [168]. The obtained models were then transformed into 3D packings of mono-sized spheres, typically investigated in sliced, solidified packings by image analysis showing circles of different sizes [114, 169]. However, several different definitions of pore size exist: Alonso et al. [167, 169] define the void size as the probability of finding a circle (2D) or sphere (3D) having a certain diameter completely fitting into a void (no particle intersection), whereas Gotoh et al. [170] search for spheres of certain diameter not overlapping with solid sphere centres allowing particle intersections. Moreover, the diameter of void spheres with centres equidistant from four particle centres may be searched [171, 172]. Besides spherical void representations, the void size may be calculated by arbitrarily setting a point into the void of a packed-bed and measuring the distance in the axis directions to the next solid boundary [173]. This allows a separate void characterization in the radial and axial directions.

Du et al. [114] investigated the pore size and pore size distribution. Although using non-uniform natural packings, the general trends are clear. The larger the particles, the larger the voids while the breadth of distribution is unaffected. The lower the porosity, the smaller the voids and the higher the sphericity of the particles, the broader the distribution.

Pore shapes within packed-beds of random spheres are considered to have distorted tetrahedral and octahedral shape commonly used to describe regular packing arrangements and crystal unit cells [171]. A detailed classification of pore shapes was for instance done by Frost [172]. The mean packing configuration and thus the void shape can be related to the radial distribution function. Configurational entropy can be derived to describe the structural randomness of packings.

In summary, pores have been evaluated rarely; however, no clarity exists in regard to the definition of the pore size measure and the actual necessity of evaluation.

2.2.2.4 The thickness effect (influence of the tube height-to-particle diameter ratio)

The influencing effect of the confining base (and top) plate analogous to the wall effect was first addressed by Wadsworth [39] (cited by Haughey and Beveridge [21]) noting that the coordination number decreased from the second to the eighth layer, expressed as the tube height-to-particle diameter ratio $\kappa = H/d_p$ of the packing, indicating a decreasing order. Furthermore, Haughey and Beveridge [21] mention that the first plane layer is found to be perfectly regular. With decreasing distance, however, the distinct layers disappear due to increasing sphere placement options causing an increased amount of randomness.

The thickness effect was further investigated by several research groups [28, 49, 103, 111, 113, 120, 126, 128, 174] resulting in various recommendations in regard to the minimal packing height that is required to neglect the thickness effect. It was repeatedly shown that at least the bottom plate has an effect similar to that of the surrounding confinement, reaching 4-5 particle diameters into the tube [120, 126].

The most comprehensive study so far regarding the influence of packing height was presented by Zou and Yu [175] investigating the mean porosity with systematically varying κ from 2.5 - 100. A sharp decrease in porosity is found increasing κ from 2.5 to around 15 ($\Delta\bar{\epsilon} = 0.06$). From there on, a slight linear decrease can be observed ($\Delta\bar{\epsilon} = 0.03$). The obtained results are displayed in Figs. 2.6 and 2.7. As a consequence, there are two options in order to study packings independently from the top and bottom effects: either a κ large enough to ensure that the effects of the top and bottom are negligible needs to be selected, which is according to their data $\kappa > 20$; or the top and bottom fraction need to be cut away completely.

The thickness effect can also be derived from the axial porosity profiles. Starting from the container's bottom, axial porosity profiles show a similar damped oscillating trend as the radial porosity profiles for the first 3-5 particle diameters. This is then reduced to a noisy constant bulk porosity value throughout the bulk of the packing, before porosity variations increase again when reaching the top of the packing. Only rarely do experimental studies discuss the axial porosity profiles, such as Reimann et al. [49] for packings

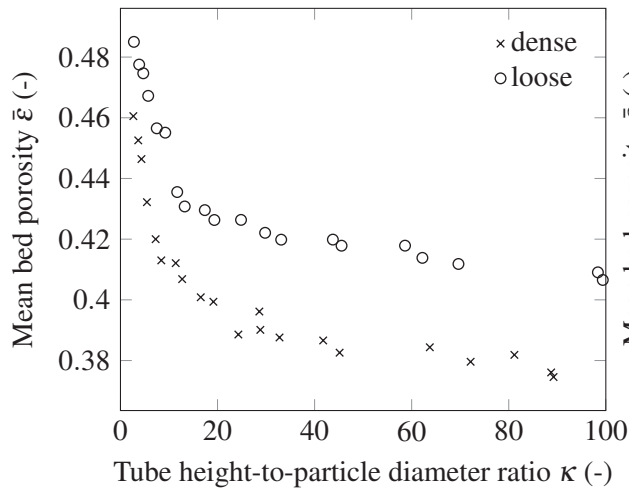


Figure 2.6: Influence of packing height-to-particle diameter ratio κ on the overall bed porosity $\bar{\epsilon}$ as of Zou and Yu [175] for a dense and a loose random packing arrangement

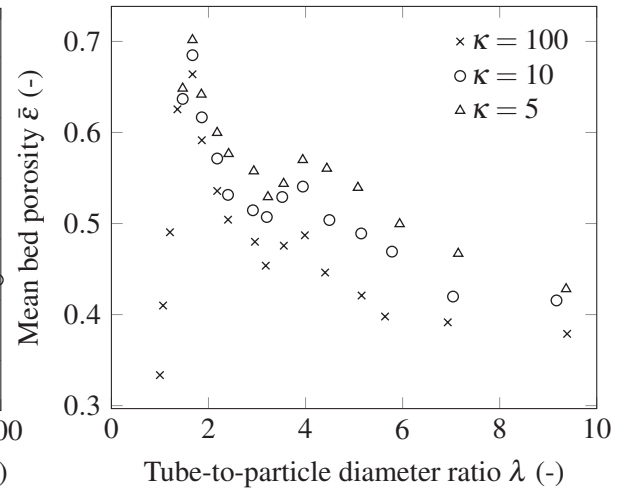


Figure 2.7: Influence of both λ and κ on the overall bed porosity $\bar{\epsilon}$ for a dense packing arrangement as of Zou and Yu [175]

with large λ and Du Toit [162] presenting the recalculated axial porosity profiles of Mueller's [135]. Only recently, Du Toit [176] presented profiles for packings of $\lambda < 2$ showing a very regular arrangement of particles in the axial direction. However, the axial porosity distribution is a measure of the consistency of the packed bed along the tube height and should therefore be at least included as an illustration in future research work.

2.2.2.5 Tube-to-particle diameter ratio

Despite the detailed information local porosity distributions may offer, in some applications and for a general overview it is frequently sufficient to only know the globally averaged bed porosity $\bar{\epsilon}$. The reduced information is remedied by significantly easier experimentation and thus availability of large data sets. Especially in applications of large λ and κ , where the influence of the confinement surfaces (eg, wall and bottom) is neglectable, the averaged bed porosity may be the primary structural parameter.

Experimental

The most commonly used methods to determine the mean bed porosity are the water displacement method [112, 174, 177–180], determining the volume of water needed to completely fill the voids of a packing, and the weighing method [181, 182], which simply weighs all packed-bed particles and determines the void volume via the particle density. The water displacement method is challenging in regard to the elimination of air pockets, the proper determination of the meniscus level, and the pre-soaking of the porous particles. It is of further importance which packing mode is selected; it is therefore thoroughly discussed in Section 2.2.2.6.

Results collected from literature

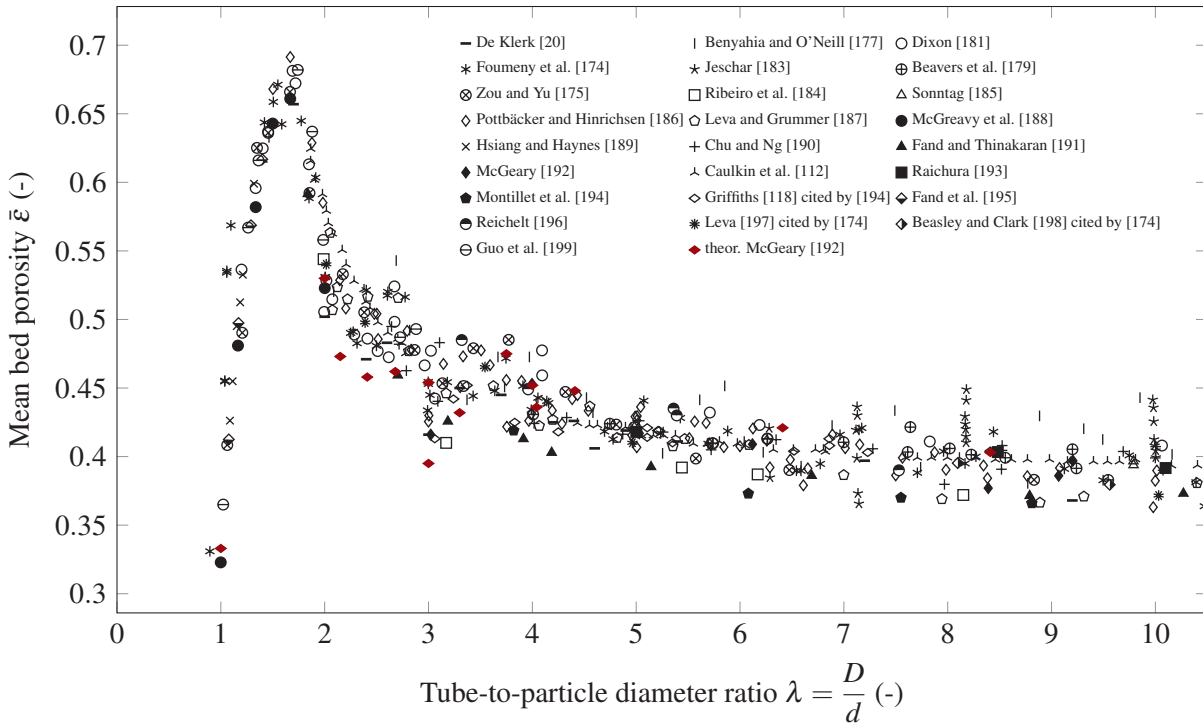


Figure 2.8: Summary of experimental literature results for the average bed porosity $\bar{\epsilon}$ when varying the tube-to-particle diameter ratio λ for smooth spheres [20, 112, 118, 174, 175, 177, 179, 181, 183–199]

The known experimental average bed porosity data depending on the tube-to-particle diameter ratio λ has been summarized in Fig. 2.8. A clear trend and a good consensus of data points can be seen. According to this, the mean packed-bed porosity increases sharply before reaching a global maximum around $\lambda \approx 1.7$, followed by a sharp decrease until reaching $\lambda \approx 2$, and hereinafter flattens out until $\lambda \approx 10$. Besides the clear global maximum, further extrema, especially a minimum at $\lambda = 3.0$ and two possible maxima around $\lambda = 2.7$ and $\lambda = 3.7$, are at least indicated by the given data. In this low- λ range, the possible packing arrangements of spheres in very thin containers significantly affect the porosity. While for $\lambda < 2$ no two spheres fit next to each other into the container, a very regular packing arrangement is obtained and may be described using unit cell considerations. The original results by Govindarao et al. [160] have recently been upgraded by Du Toit. [176] Additionally, Guo et al. [200] thoroughly investigated packings of $2 < \lambda < 3$ using an analytical approach and experiments. The optimal packing size for integral sphere layers at low λ was studied by McGeary [192]. These theoretically obtained results are added to Fig. 2.8 and the following structural characteristics were identified for the $\lambda = 2 - 5$ region. For a sphere number up to five per layer, only one ring can be formed inside the container. One inner sphere fits into a complete ring of 5-7 spheres (making 6-8 spheres in total), three inner spheres can be placed into an inner ring of 6-9 spheres (making 9-12 spheres in total). From there on, an orthorhombic arrangement is assumed where the innermost ring has four, the next one 10, and if needed the following 17, 24, 31, and so on. Based on these findings, a sharp porosity minimum at $\lambda = 3.0$ and a subsequent maximum at $\lambda = 3.75$ can be identified. A smaller minimum/maximum pair can be found at $\lambda = 2.41$ and $\lambda = 2.68$ and for $\lambda = 4.04$ and $\lambda = 4.41$. It must be noted that for $\lambda = 3.0$ two configurations exist comprising either 6 or 7 spheres.

While the seven-sphere arrangement causes the minimum, the six-sphere arrangement fits perfectly into the generally assumed decreasing function. Furthermore, de Klerk [20] mentions bed voidage values higher or lower than expected for tube-to-particle diameter ratios 2.4, 3.0, and 4.6. Moreover, for a diameter ratio of 3.0, two data points were recorded, deviating considerably from the average to higher values. This last finding is in agreement with the study of McGeary [192].

Derived correlations

Based on the obtained experimental data, a large number of correlations regarding the influence of tube-to-particle diameter ratio on the average packing porosity were derived. A comprehensive summary can be found in Table 2.4. For comparison, these correlations were plotted in Fig. 2.9 together with the

Table 2.4: Overview of known wall effect correlations

Source	Formula	$\bar{\epsilon}_{\text{inf}}$	Scope
Carman [201]	$\bar{\epsilon} = 1 - \frac{2}{3} \cdot \left(\frac{1}{\lambda}\right)^3 \cdot \frac{1}{\sqrt{\frac{2}{\lambda} - 1}}$	-	$1 < \lambda \leq 1.866$
Aerov [202]	$\bar{\epsilon} = \bar{\epsilon}_{\text{inf}} + \frac{0.07}{\lambda} + \frac{0.54}{\lambda^2}$	0.39	$\lambda \geq 2$
Sonntag [185]	$\bar{\epsilon} = \bar{\epsilon}_{\text{inf}} + (1 - \bar{\epsilon}_{\text{inf}}) \cdot \frac{0.526}{\lambda}$	0.359	$10 \leq \lambda \leq 30$
Jeschar [183]	$\bar{\epsilon} = \bar{\epsilon}_{\text{inf}} + \frac{0.34}{\lambda}$	0.375	$6.25 \leq \lambda \leq 100$
Ayer and Soppet [182]	$\bar{\epsilon} = \bar{\epsilon}_{\text{inf}} + 0.216 \cdot \exp(-0.313 \cdot \lambda)$	0.365	$3 \leq \lambda \leq 32$
Beavers et al. [179]	$\bar{\epsilon} = \bar{\epsilon}_{\text{inf}} \cdot \left[1 + \frac{2}{\lambda} \cdot \left(\frac{\bar{\epsilon}_w}{\bar{\epsilon}_{\text{inf}}} - 1\right)\right]$	0.368	$4 \leq \lambda < 45$ $\bar{\epsilon}_w = 0.476$
Froment and Bischoff [203]	$\bar{\epsilon} = \bar{\epsilon}_{\text{inf}} + 0.073 \cdot \left[1 - \frac{(\lambda - 2)^2}{\lambda^2}\right]$	0.38	n.a.
Griffiths [118] cited by Roshani [103]	$\bar{\epsilon} = \bar{\epsilon}_{\text{inf}} + \frac{0.035}{(\lambda - 3.5)^{0.27}}$	0.38	$\lambda > 3.5$
Dixon [181]	$\bar{\epsilon} = \bar{\epsilon}_{\text{inf}} + \frac{0.05}{\lambda} + \frac{0.412}{\lambda^2}$	0.40	$\lambda \geq 2$
Fand and Thinakaran [191]	$\bar{\epsilon} = \bar{\epsilon}_{\text{inf}} + \frac{0.151}{\lambda - 1}$	0.36	$2.033 \leq \lambda < 40$
Fand and Thinakaran [191]	$\bar{\epsilon} = 1.8578 - 0.6649 \cdot \lambda$	-	$1.866 \leq \lambda < 2.033$
Foumeny et al. [174]	$\bar{\epsilon} = \bar{\epsilon}_{\text{inf}} + 0.254 \cdot \frac{\lambda^{-0.923}}{\sqrt{0.723 \cdot \lambda - 1}}$	0.383	$1.866 \leq \lambda < 22$
Mueller [135]	$\bar{\epsilon} = \bar{\epsilon}_{\text{inf}} + \frac{0.220}{\lambda}$	0.365	$\lambda \geq 2.02$
Zou and Yu [175]	$\bar{\epsilon} = \bar{\epsilon}_{\text{inf}} + 0.002 \cdot \left[\exp\left(\frac{15.306}{\lambda}\right) - 1\right]$	0.372	$3.95 \leq \lambda < 35$
Zou and Yu [175]	$\bar{\epsilon} = 0.681 - \frac{1.363}{\lambda} + \frac{2.241}{\lambda^2}$	-	$1.866 \leq \lambda < 3.95$
De Klerk [20]	$\bar{\epsilon} = \bar{\epsilon}_{\text{inf}} + 0.35 \exp(-0.39 \cdot \lambda)$	n.a.	$2 \leq \lambda < 20$
Benyahia and O'Neill [177]	$\bar{\epsilon} = \bar{\epsilon}_{\text{inf}} + \frac{1.74}{(\lambda + 1.14)^2}$	0.39	$1.5 \leq \lambda < 50$
Puschnov [204]	$\bar{\epsilon} = 12.6 \cdot \lambda^{6.1} \cdot \exp(-3.6 \cdot \lambda)$	-	$1 \leq \lambda < 2.4$
Puschnov [205]	$\bar{\epsilon} = \bar{\epsilon}_{\text{inf}} + \frac{1}{\lambda^2}$	-	$2 \leq \lambda < 20$
Cheng [206]	$\bar{\epsilon} = \left[\frac{1}{(0.8 \cdot (\lambda - 1)^{0.27})^3} + \frac{1}{(\bar{\epsilon}_{\text{inf}} \cdot (1 + (\lambda - 1)^{-1.9}))^3}\right]^{-1/3}$	0.38	$1 \leq \lambda < 100$
Ribeiro et al. [184]	$\bar{\epsilon} = \bar{\epsilon}_{\text{inf}} + 0.917 \exp(-0.824 \cdot \lambda)$	0.373	$2 \leq \lambda < 19$

anonymized literature data as displayed in Fig. 2.8.

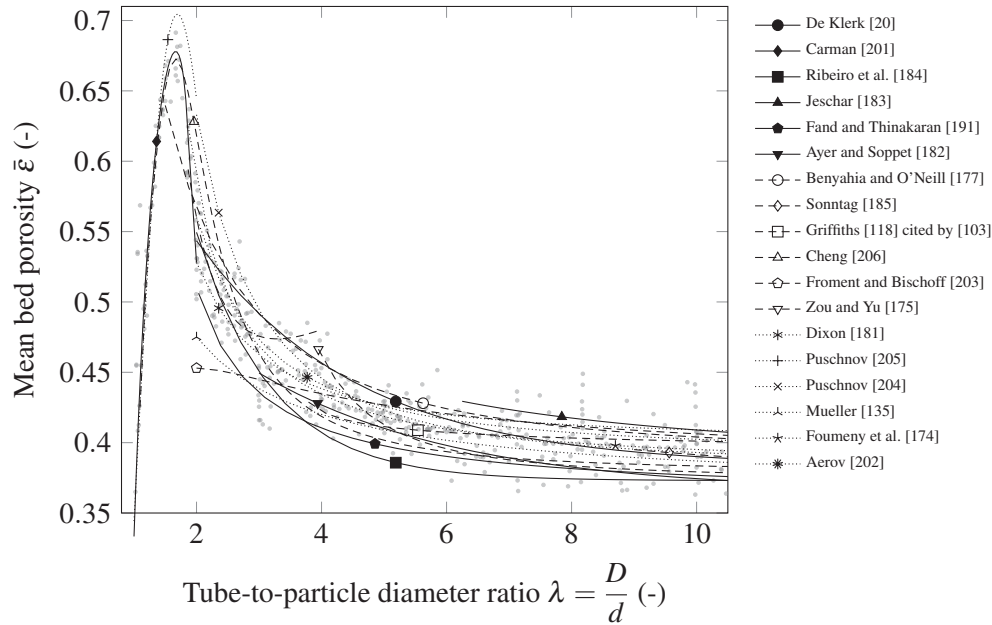


Figure 2.9: Anonymized experimental literature data as displayed in Fig. 2.8 and known correlations regarding the influence of tube-to-particle diameter ratio λ on the mean bed porosity $\bar{\epsilon}$ of smooth spheres [20, 103, 118, 135, 174, 175, 177, 181–185, 191, 201–206]

While the given correlations fit the overall scope of the experimental data well, they vary in regard to the infinite bed porosity obtained for $\lambda \rightarrow \infty$, which is strongly dependent on the packing method and material characteristics. From the considered correlations, the one presented by Foumeny et al. [174] represents the overall trend best. It must be noted that no further extrema than the obvious global peak are considered in the known correlations. Only Zou and Yu [175] included a detected maximum at around $\lambda = 4.0$ into their piecewise defined correlation.

In summary, a large data pool is available relating the average bed porosity to the tube-to-particle diameter ratio of a packing. These data can be well represented by a large selection of known correlations, except some details such as local extrema.

2.2.2.6 Influence of Packing Mode

Haughey and Beveridge [20, 21] determined four particular methods of bed formation. The associated porosity ranges are based on a range of literature data and are valid when wall effects are insignificant ($\lambda \rightarrow \infty$). The modes comprise:

1. Very loose random packing ($\bar{\epsilon} \approx 0.44$) obtained by settling a fluidized bed, by sedimentation, or by inversion of the bed container.
2. Loose random packing ($\bar{\epsilon} \approx 0.40 - 0.41$) obtained by letting the spheres roll individually into place, individual hand packing, or by dropping the spheres as complete loose mass.

3. Poured random packing ($\bar{\epsilon} \approx 0.375 - 0.391$), obtained by pouring particles into the container.
4. close random packing ($\bar{\epsilon} \approx 0.359 - 0.375$) obtained by vibrating, shaking, or tapping of the container.

Thus, compared to regular packings where the mean bed porosity varies between 0.26 and 0.48 depending on their arrangement (see Table 2.1), random packings may take on values between 0.36 (Random Close Packing (RCP)) and 0.44 (Random Loose Packing (RLP)) [21] when not confined. A comprehensive overview of experimental data sorted by packing mode based on the above classification was collected by Roshani [103]. Another packing state, the so-called maximally random jammed state (MRJ), evolved in physical contexts which are mathematically precise equivalents to the RCP state [207, 208].

The upper limit, so-called RLP, was for example studied by Onoda and Liniger [209] in settling experiments under zero gravitational force and in shear-cell experiments with glass spheres. A value of up to 0.445 ± 0.005 was obtained as an upper limit. in settling experiments under zero gravitational force and in shear-cell experiments with glass spheres. A value of up to 0.445 ± 0.005 was obtained as an upper limit. Furthermore, it was repeatedly shown that packed-beds generated without significant effort to form extra loose or dense beds show packing porosities around 0.38 - 0.39 [174, 186, 210]. Consequently, this small range is generally accepted as the standard packing porosity of a sphere packing.

Regarding the evaluation of the porosity of the densest possible sphere packing in the absence of global order, Susskind and Becker [211] removed the air from balloons filled with spherical particles. For a typical packing a value of $\bar{\epsilon}_{\text{inf}} = 0.362$ could be obtained. This value was lowered to $\bar{\epsilon}_{\text{inf}} = 0.348$ by rigorous vibration. However, Bernal and Finney [212] remarked that even when using a non-rigid balloon, confinement effects cannot be neglected and recalculated the data to a RCP porosity of around 0.36 [38, 43]. Nonetheless, using appropriate experimental conditions, vibrated packed-beds may adopt a global order, allowing porosities slightly below the RCP limit [49].

In-detail studies on packing densification were performed using vibration [174, 213–217] or tapping [218, 219]. Typically, packed-bed porosity decreases until the densification is saturated [213, 215, 217, 219]. Optimal vibration frequency and amplitude settings are required to gain the densest packings (cf. [213–215, 220]). Furthermore, interparticle diffusion during vibration was investigated [215]. Besides vibration, the achieved packing densification by tapping n taps and a certain relaxation time τ can be described as below [219, 221, 222].

Sequential addition compared to shaking was done by Baker and Kudrolli [220]. Another filling method called sock filling was performed by Bazmi et al. [223]. Afandizadeh and Foumeny [28] investigated three different packing methods: fast pouring, slow pouring, and the so-called snow storm filling [224], where the packing material is passed over wire meshes to interrupt its free fall inside the tube. The mean bed porosity decreased for longer filling times and a filling speed of 0.5-5 mm bed length per second is suggested to obtain more reproducible packings. Moreover, Macrae and Gray [225] investigated the influence of particle drop height, deposition intensity, and filling rate (particle number per filling time). It

was found that the packing porosity decreases with a higher drop height before reaching a final value, with a reduced particle filling rate and lower deposition intensity.

Besides the influence of densification on the average bed density, structural studies reveal that an increase in oscillation amplitude and a decrease in the oscillation period affect the radial porosity distribution [49, 226] along with the increased bed densification. The more ordered a packing gets, the more distinct the parabolic shape of the radial void distribution gets. Very ordered packings form tiny intermediate parabolas so that the radial porosity distribution resembles a chain of large and small parabolas [33, 49].

The influence of packing formation in fluids other than air was also studied. Stanek and Eckert [120] compared particle damping in air and ethanol during the packed-bed formation, finding a decreased mean porosity when damped in a liquid. Furthermore, Chu and Ng [190] packed the spheres in water. Feng and Yu [67] found an increasingly damped packing behaviour (resulting in higher porosities) using wetted particles with increasing liquid content. Regarding liquid characteristics, surface tension alters the packing structure but small variations in viscosity had no effect.

In summary, the packing mode is one of the most crucial parameters regarding the packing structure and average porosity. Some explicit packing modes have been identified and allocated to certain porosity ranges. Furthermore, packing densification was studied by several research groups leading to lower overall bed porosities and higher packing order.

2.2.3 Influence of particle shape

Industrially used shapes comprise cubes and hollow cubes, four-hole cylinders, hollow cylinders with a single bridge or cross web and grooved cylinders, and a selection of saddles and ring shapes [28, 177, 227–229]. In experiment, shapes comprising cylinders [114, 124, 230, 231], Pall rings [124], Raschig rings [232] and Hama beads [124], prisms [230, 231], ellipsoids [231–233], trilobes [218, 223], cubes [114, 231], polyhedrons [232, 234], and platonic shapes [220, 235] were investigated.

In order to compare shapes other than spheres, a characteristic diameter is used, typically the Sauter diameter $d_{p,s}$ or the diameter of a volume-equivalent sphere $d_{p,v}$:

$$d_{p,s} = 6 \cdot \frac{v_p}{a_p} \quad (2.2)$$

$$d_{p,v} = \left(\frac{6 \cdot v_p}{\pi} \right)^{1/3} \quad (2.3)$$

Further equivalent diameters (see [236] for a comprehensive list) based on physical properties are the equivalent sphere diameter having the same sedimentation velocity as the investigated particle $d_{p,w}$ and the equivalent sphere diameter having the same resistance to flow $d_{p,d}$.

The true sphericity Ψ_W as defined by Wadell [237] is a frequently used shape factor to describe shape variations in regard to spheres:

$$\Psi_W = \frac{\pi^{1/3} \cdot (6 \cdot v_p)^{2/3}}{a_p} \quad (2.4)$$

This parameter was occasionally used to correlate shape and packing porosity at infinite λ . Table 2.5 gives an overview of the obtained correlations and Fig. 2.10 shows a selection of experimental data points and plotted correlations. In general, there is for an infinite packed bed a tendency towards a larger packing

Table 2.5: Overview of shape-porosity correlations based on the sphericity

Source	Formula	Scope and parameters	Shapes	No. of data-points
Benyahia and O'Neill [177]	$\bar{\epsilon}_{\text{inf}} = 0.1504 + \frac{0.2024}{\Psi_W}$		Sphere, cylinder, hollow cylinder, 4-hole cylinder	9
Brown [227]	$\bar{\epsilon}_{\text{inf}} = \bar{\epsilon}_{\text{inf},s}^{1.785 \cdot \Psi_W^{1.585} - 0.785 \cdot \Psi_W^{4.897}}$	$\bar{\epsilon}_{\text{inf},s} = 0.47$ (loose), 0.36 (dense) or 0.42 (mean)	Spheres, hollow cylinders, saddles	29
Yu and Standish [228]	$\bar{\epsilon}_{\text{inf}} = \bar{\epsilon}_{\text{inf},s}^{15.521 \cdot \Psi_W^{3.853} - 14.521 \cdot \Psi_W^{4.342}}$	$\bar{\epsilon}_{\text{inf},s} = 0.40$ (loose), 0.36 (dense) or 0.38 (mean)	Spheres, hollow cylinders, saddles	Data of [238–240]
Zou and Yu [231, 241]	$\bar{\epsilon}_{\text{inf}} = \exp(\Psi_W^{5.58} \cdot \exp(5.89 \cdot (1 - \Psi_W)) \cdot \ln(0.40))$ $\bar{\epsilon}_{\text{inf}} = \exp(\Psi_W^{0.6} \cdot \exp(0.23 \cdot (1 - \Psi_W)^{0.45}) \cdot \ln(0.40))$	Dense packing: 6.74, 8.00, 0.36 Dense packing: 0.63, 0.64, 1.0, 0.36	cylinders, disks, balls, beads, beans, lentils, cubes, prisms	36
Warren et al. [242]	$\Psi_W = 0.079 + 0.831 \cdot (1 - \bar{\epsilon}_{\text{inf}}) + 1.53 \cdot (1 - \bar{\epsilon}_{\text{inf}})^3$			
Lanfrey et al. [229]	$\Psi_W = \sqrt{\frac{1.23}{T} \cdot \frac{(1 - \bar{\epsilon}_{\text{inf}})^{4/3}}{\bar{\epsilon}_{\text{inf}}}}$	Tortuosity $T = 2.12$ in mean, between 1 - 3 in general	Berl, Intalox and Torus saddles, Raschig, Pall and Ralu Rings, different material and size	> 100
Parkhouse and Kelly [243]	$\bar{\epsilon}_{\text{inf}} = 1 - 2 \cdot \ln(a_1)/a_1$ with $\Psi_W = 2.621 \frac{a_1^{2/3}}{1 + 2 \cdot a_1}$	$a_1 > 7$	Elongated cylinder	4
Blouwolf and Fraden [244]	$\bar{\epsilon}_{\text{inf}} = \frac{5.4}{a_1}$ with $\Psi_W = 2.621 \frac{a_1^{2/3}}{1 + 2 \cdot a_1}$		Elongated cylinder, different material	6
Rahli [245] cited by Novellani et al. [246]	$\bar{\epsilon}_{\text{inf}} = 1 - \frac{11}{\frac{\pi}{2 \cdot a_1} + 6 + 2 \cdot a_1}$ with $\Psi_W = 2.621 \frac{a_1^{2/3}}{1 + 2 \cdot a_1}$		Elongated cylinder	

porosity, but no clear trend nor a single all inclusive correlation can be deduced. However, it was not possible to diversify this plot for different packing modes or packing materials used by the researchers, which have a strong influence on the packing porosity obtained for infinite packed beds. According to Zou and Yu [231], three branches can be identified in the sphericity-porosity plot corresponding to elongated cylinders (upper branch), flat disks (lower branch), and all other shapes, especially hollow cylinders and saddles in between these two borders. Still, the sphericity alone is obviously not capable of describing or predicting the packing porosity of an arbitrarily shaped particle.

As a second shape parameter, Lanfrey et al. [229] utilized the tortuosity T together with the sphericity in order to estimate packed-bed porosities. The tortuosity is typically defined as the ratio of the actual fluid flow path and the packing height. It reaches values around 1.4 to 1.5 for spheres [251, 252] and

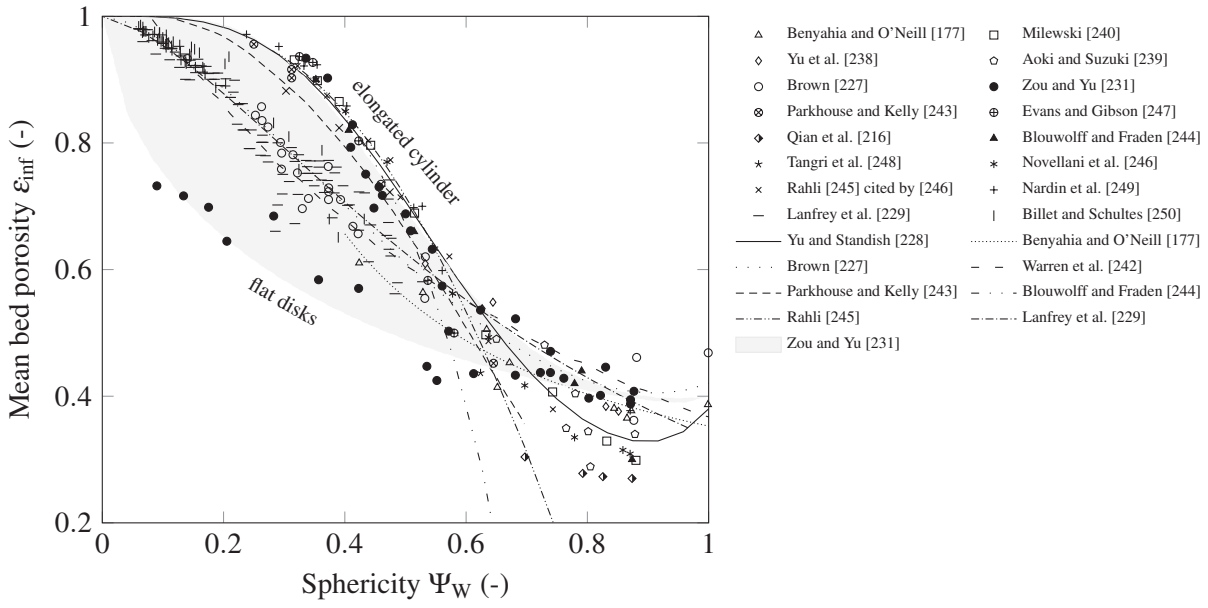


Figure 2.10: Experimental literature data regarding the sphericity Ψ_W dependent evaluation of packed-bed bulk porosity ε_{inf} [177, 216, 227–229, 231, 238–240, 242–250]

may be correlated to the packing porosity [253–257]. Unfortunately, a large number of data points of the elongated cylinders displayed in Fig. 2.10 would be allocated a tortuosity value below unity when applying Lanfrey et al.’s correlation [229] to Fig. 2.10.

Moreover, Yu and Standish [228] developed a characteristic packing diameter d_{pack} that can be used together with the sphericity to describe packings of arbitrary shapes or size variations. This packing diameter is defined as the diameter of a sphere that leads to a maximum packing porosity in a binary mixture with the investigated shape. This attempt is inconvenient as it requires a large number of experiments for the determination of a single characteristic diameter and was tested for a small selection of convex shapes only [228, 231]:

$$\frac{d_{p,v}}{d_{\text{pack}}} = \Psi_W^{2.785} \cdot \exp[2.946 \cdot (1 - \Psi_W)]. \quad (2.5)$$

Other shape factors are known in the context of characterizing undesignated granular material, as for instance the empirical Heywood factor [236, 258, 259]. Herein, flatness m and elongation n of a particle are defined and related to the shape’s sphericity [231]:

$$\Psi_W = \frac{2.418}{(m \cdot n^{-2})^{1/3} + (m^{-2} \cdot n)^{1/3} + (m \cdot n)^{1/3}}. \quad (2.6)$$

Moreover, a correlation of the sphericity and the Hausner ratio known from powder beds and describing the compressibility of a packing was found [241, 260, 261]. A tendency of a larger Hausner ratio and thus

packing compressibility was obtained with decreasing shape sphericity but with a large data scatter [231]:

$$H_r = 1.478 \cdot 10^{-0.136 \cdot \Psi_w}. \quad (2.7)$$

Despite a large number of available randomly packed shapes, only a small selection is studied in further detail. With higher complexity in particle shape, the predictability of the packing structure becomes increasingly elaborate. While a single sphere within a packing can basically be described by two parameters, the centre location and the (characteristic) diameter, a cylindrical shape needs to be further characterized by its orientation (eg, rotation matrix) and a shape factor called aspect ratio defining its height-to-diameter ratio a_1 . Further improvement of the simple cylindrical shape is done by cutting a straight axial hole and obtaining a hollow cylinder often called Raschig ring. The list of parameters required to entirely describe this shape is enlarged by a second aspect ratio giving the inner to outer ring diameter a_2 . Similarly, an ellipsoid can be described completely by two aspect ratios. Any more complex shape requires a whole set of aspect ratios while any variation in these parameters will presumably affect the packing characteristics (even when keeping other influences like material or packing mode constant). It is still possible to describe the packing of a specific complex shape by performing the relevant studies, but it is hard to predict the performance of an arbitrary shape or even geometrically similar shapes from the obtained results. Thus, experimental studies exist and will be described in the following regarding packing properties for cylinders and rings, although the database is much smaller compared to spheres. A comprehensive list of experimental studies involving shapes other than spheres is presented in Table 2.6.

The most notable results from this list are summarized in Fig. 2.11 regarding radial void distribution and average bed porosity for equilateral cylinders, non-equilateral cylinders, and hollow cylinders, respectively. It was not possible when comparing the data from the respective plots as was done for spheres, as the data showed significant differences when comparing the data from different research groups. Clustering was thus impossible. Consequently, the reproduced data are selected due to their extent, not their claim of correctness compared to other data sets. However, some general trends may be derived and are discussed in the following.

Equilateral cylinders

The equilateral cylinder is a cylinder with equal height and diameter. Regarding the available radial void distributions (cf. Fig. 2.11a) of cylinder packings at various tube-to-particle diameter ratios [103] in comparison to a packing of spheres (cf. Fig. 2.11a), similarities in the general oscillatory trend can be seen. However, the amplitude, period and bulk porosity take on slightly different values. Consequently, very similar correlations can be derived, namely Küfner and Hofmann [110], based on Vortmeyer and Schuster [149]:

$$\varepsilon(z_r) = \bar{\varepsilon}_{\text{inf}} \cdot \left(1 - \frac{1 - \bar{\varepsilon}_{\text{inf}}}{\bar{\varepsilon}_{\text{inf}} \cdot \exp(1)} \cdot \exp(1 + z_r) \cdot \cos(2 \cdot \pi \cdot z_r)\right), \quad (2.8)$$

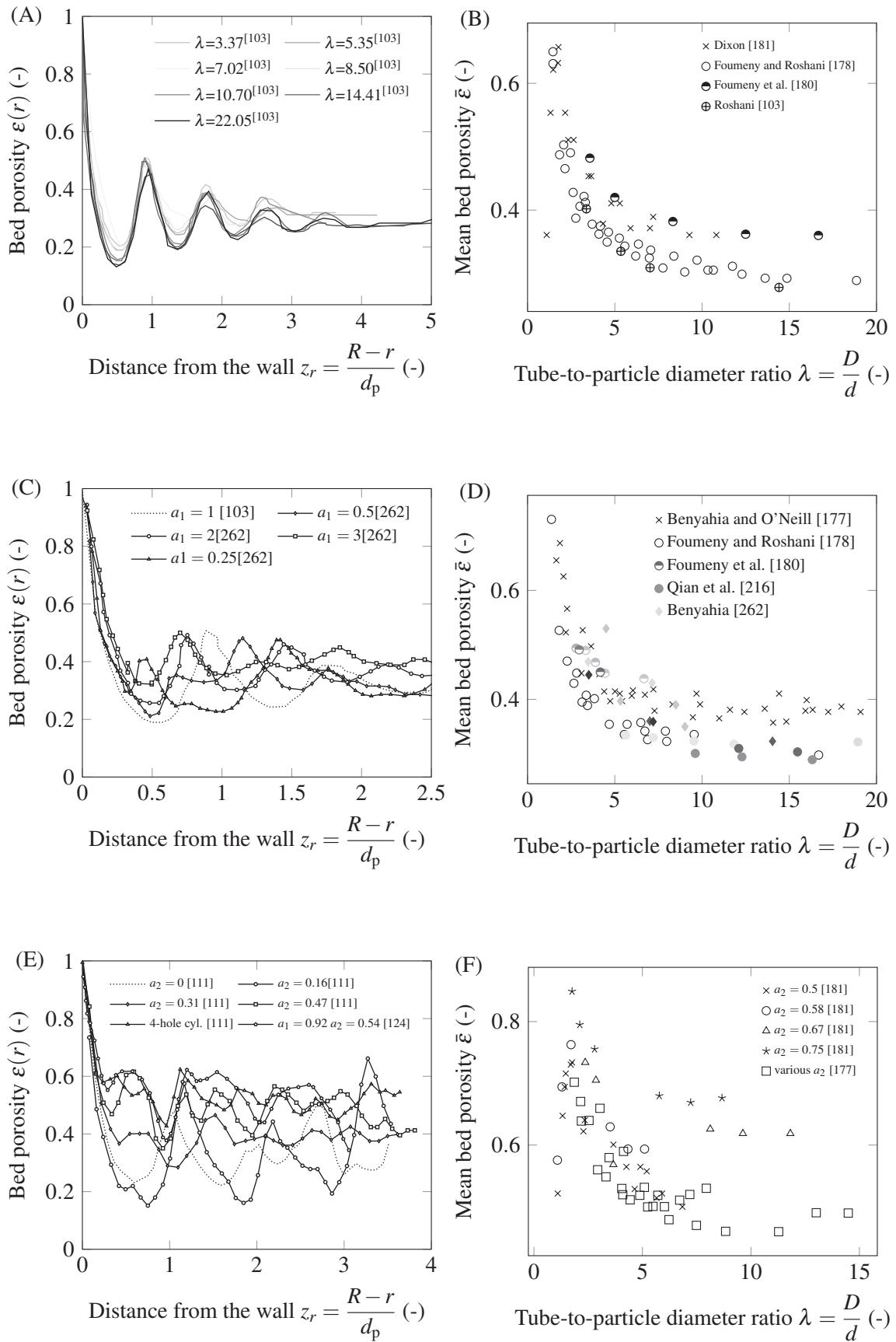


Figure 2.11: Radial porosity distribution $\varepsilon(r)$ for A, equilateral cylinders; C, non-equilateral cylinders; E, hollow cylinders, and average packing porosity $\bar{\varepsilon}$ for B, equilateral cylinders; D, non-equilateral cylinders; F, hollow cylinders [103, 111, 124, 177, 178, 180, 181, 216, 262]

Table 2.6: Overview of experimental studies relating to the structural analysis of packed-beds of non-spherical particles

Source	Shape	Aspect ratio $1/a_1$	Aspect ratio a_x	λ_v	$\bar{\varepsilon}(\lambda)$	$\varepsilon(r)$	$\varepsilon(z)$
Giese et al. [136]	Cylinder	1	-	9.15	1	1	-
	Hollow cylinder	1	0.75	9.15	1	1	-
	Deformed sphere	-	-	> 10	1	1	-
Benyahia [262]	Cylinder	0.25 to 3	-	3.51 - 14.04	10	10	10
Caulkin et al. [111]	Cylinder	1	-	7.1	1	1	1
	Hollow cylinder	1	0.16 - 0.47	7.2 - 7.7	3	3	3
	4-hole cylinder	1	-	7.4	1	1	1
Baker and Kudrolli [220]	Platonic	4 - 20 faces	-	5 - 7	6	-	-
Baker and Kudrolli [220]	Cylinder	1	-	4.44/9.33	1	1	-
Benyahia and O'Neill [177]	Cylinder	0.76 - 1.78	-	1.7 - 26.3	> 10	-	-
	Hollow cylinder	0.38 - 1.06	Not specified	1.9 - 14.5	> 10	-	-
	4-hole cylinder	1.14 - 1.26	Not specified	1.9 - 8.4	> 10	-	-
Roblee et al. [104]	Cylinder	1	-	11.75	-	1	-
	Hollow cylinder	1	0.72	11.75	-	1	-
	Berl saddle	Regular	> 10	-	-	1	-
Sonntag [185]	Cylinder	1	-	11 - 40	>10	(✓)	-
	Hollow cylinder	1	0.62 - 0.78	5.6 - 25	>10	(✓)	-
Lerou and Froment [119]	Cylinder	1	-	5.35	1	1	-
	Hollow cylinder	0.94	0.43	n.a.	1	1	-
Bey and Eigenberger [147]	Cylinder	0.833 - 3.333	-	5.35	4	-	-
	Hollow cylinder	1	0.44 - 0.63	3.33 - 10	4	-	-
Blouwolff and Fraden [244]	Cylinder	0.4 - 50	-	n.a.	6	-	-
Chikhi et al. [230]	Cylinder, prism	0.88 - 1.4	> 10	-	6	-	-
Comiti and Renaud [263]	Parallelepiped	0.102 - 0.44	> 10	-	5	-	-
Foumeny and Roshani [178]	Cylinder	0.5 - 2	-	2 - 32	> 10	-	-
Foumeny et al. [180]	Cylinder	0.5 - 2	-	2.76 - 16.67	> 10	-	-
Xie et al. [214]	Cube, cuboid	1 - 4	1 - 2	5.5 - 11.5	12	-	-
Xia et al. [264]	Ellipsoid	0.51	1	> 10	1	-	-
Wang et al. [265]	Ring	n. a.	n. a.	> 10	3	3	-
Zhang et al. [226]	Cylinder	1	-	> 10	1	1	-
Lumay and Vandewalle [219]	Cylinder	1.67 - 90	-	n.a.	> 10	-	-
Novellani et al. [246]	Cylinder	1.2 - 50.5	-	n.a.	10	-	-
Man et al. [266]	Ellipsoid	1.25:1:0.8	-	6.7 - 11	5	1	-
Jaoshvili et al. [267]	Tetrahedra	reg.	-	n.a.	7	-	-
Parkhouse and Kelly [243]	Cylinder	6.8 - 143	-	n.a.	-	-	-
Qian et al. [216]	Cylinder	0.5 - 5	-	>10	16	-	-
Zou and Yu [241]	Cylinder	1 - 100	-	4 - 40	> 10	-	-
Montillet and Coq [115]	Cylinder	5.3	-	16.3	1	1	-
	Parallelepiped	0.209	-	17.7	1	1	-
Nguyen et al. [134]	Cylinder	1.1	-	15	1	1	-
	Trilobe	n.a.	-	24	1	1	-
	Ring	1	0.1 - 0.2	> 10	2	2	-
Wehinger et al. [268]	Hexagons	1.1	-	6.3,4,6	2	2	-

Roshani [103]:

$$\varepsilon(z_r) = 1 - 0.695 \cdot (1 - \exp(-1.83 \cdot (z_r)^{0.34})) \cdot \cos(6.65 \cdot (z_r)^{1.08}), \quad (2.9)$$

and Bey and Eigenberger [147]:

$$\begin{aligned} \varepsilon(z_r) &= \varepsilon_{\min} + (1 - \varepsilon_{\min}) \cdot (z' - 1)^2 \quad \text{for } z' \leq 1 \\ \varepsilon(z_r) &= \bar{\varepsilon}_{\inf} + (\varepsilon_{\min} - \bar{\varepsilon}_{\inf}) \cdot \exp[-0.5 \cdot (z' - 1)] \cdot [\cos(\pi/0.876 \cdot (z' - 1))] \quad \text{for } 1 < z' \quad (2.10) \\ \text{with } \varepsilon_{\min} &= 0.275 \quad z' = \left(1.8 - \frac{2}{\lambda}\right) \cdot \left(\frac{R-r}{d}\right). \end{aligned}$$

Regarding the average bed porosity as a function of the tube-to-particle diameter ratio in Fig. 2.11b, a very similar behaviour compared to spheres can be seen: the sharp porosity increase at the beginning, the

global maximum, the sharp decrease, and the flattening out after reaching $\lambda = 10$. There is a difference in the significantly larger data scattering, especially at large λ and the overall smaller porosity. The densest cylindrical packing is found to be 0.27 [216]. Further dense packed packings have porosities around 0.3 [244] and between 0.28 - 0.31 [218]. Again, correlations were derived basically by adjusting the coefficients of the already known correlations for spheres, namely Dixon [181]:

$$\bar{\varepsilon} = \bar{\varepsilon}_{\text{inf}} + \frac{0.1}{\lambda_v} + \frac{0.7}{\lambda_v^2} \quad \text{with} \quad 1.67 \leq \lambda_v \leq 20 \quad \bar{\varepsilon}_{\text{inf}} = 0.36 \quad (2.11)$$

$$\bar{\varepsilon} = 1 - \frac{0.763}{\lambda_v^2} \quad \text{with} \quad \lambda_v \leq 1.24, \quad (2.12)$$

and Foumeny and Roshani [178]:

$$\bar{\varepsilon} = \bar{\varepsilon}_{\text{inf}} + 0.684 \cdot \lambda_v^{-0.85} \cdot \frac{1}{\sqrt{(1.837 \cdot \lambda_v - 1)}} \quad \text{with} \quad \lambda_v \leq 1.44 \quad \bar{\varepsilon}_{\text{inf}} = 0.293. \quad (2.13)$$

Additionally, particle orientation effects become relevant. The X-ray study of Caulkin et al. [124] reveals a particle axis orientation peak for angles of 50 - 60° to the tube axis, decreasing in both directions. Especially particles orientated at 0 - 30° are rarely found.

Non-equilateral cylinders

Regarding non-equilateral cylinders, the radial porosity distribution shows a completely different and quite irregular pattern. As displayed in Fig. 2.11c, the peak and minima occurrences do not appear to follow a specific rule, or at least this rule can not be identified with the small amount of available data. This accounts for flat disks as well as for elongated cylinders. However, the overall variance (or amplitude) seems to be smaller compared to equilateral cylinders. Thus, no appropriate correlation could be derived so far to describe the radial void distribution for non-equilateral cylinders.

The average bed porosity as a function of tube-to-particle diameter ratio for selected available data is displayed in Fig. 2.11d. Here, the data appears to follow a similar pattern as observed for spheres and equilateral cylinders. The influence of aspect ratio on the porosity of an infinite bed was already discussed above, where the densest packing was obtained with equilateral cylinders. Regarding confined packings at low tube-to-particle diameter ratios and low cylinder aspect ratio variation between 0.5 and 2, a difference in packing porosity was either too small to differentiate [178, 180, 241, 262] or results indicate a slight influence similar to the porosity of an infinite bed, where packing porosity increases as the aspect ratios move away from unity [216, 262]. In Fig. 2.11d, the aspect ratio is displayed as the gray scale of the markers, with a mean gray representing an aspect ratio of 1. However, the deviations between the data sets and the limited number of data per set do not allow a definite conclusion. Nonetheless, some correlations

were derived including or explicitly excluding the influence of the aspect ratio comprising Foumeny and Roshani [178, 269]:

$$\bar{\varepsilon} = \bar{\varepsilon}_{\text{inf}} \cdot \Psi_{\text{W}}^a + 0.254 \cdot \Psi_{\text{W}}^b \cdot (\lambda_{\text{v}})^{-0.293 \cdot \Psi_{\text{W}}^c} \cdot \frac{1}{(0.723 \cdot \Psi_{\text{W}}^d \cdot \lambda_{\text{v}} - 1)^{0.5}} \quad \text{with} \quad \bar{\varepsilon}_{\text{inf}} = 0.383, \quad (2.14)$$

and Benyahia and O'Neill [177]:

$$\bar{\varepsilon} = \bar{\varepsilon}_{\text{inf}} + \frac{1.703}{(\lambda + 0.611)^2} \quad \text{with} \quad \bar{\varepsilon}_{\text{inf}} = 0.373. \quad (2.15)$$

Hollow cylinders and rings

In order to describe hollow cylinders, a second aspect ratio a_2 of the inner and outer ring diameters is included. A selection of radial porosity profiles obtained from hollow cylinders [111, 124] with different aspect ratios a_2 are displayed in Fig. 2.11e. Accordingly, larger values of a_2 result in a significantly higher and smoother porosity distribution. The minima in particular are clearly smoothed compared to solid cylinders. On the contrary, new intermediate maxima of which the height increases as a_2 are developed. No correlations have been derived so far.

The sparsely available experimental data in the literature of average bed porosity values for different λ and aspect ratios a_2 are summarized in Fig. 2.11f. The general trend is in accordance with solid cylinders and spheres; however, the porosity of an infinite bed increases significantly with increasing a_2 . The most comprehensive study in this context was performed by Dixon [181] investigating equilateral hollow cylinders with $a_2 = 0.5, 0.58, 0.65$ and 0.75 . As correlation, the calculated solid cylinder base $\bar{\varepsilon}_{\text{sc}}$ Eq. (2.11), corrected with the inner void is used:

$$(1 - \bar{\varepsilon}_{\text{sc}}) = \frac{1 - \bar{\varepsilon}}{f * (1 - (a_2)^2)}. \quad (2.16)$$

Regarding interpenetration of hollow cylinders with large holes, a correction f of this correlation for $a_2 > 0.5$ is suggested:

$$f = 1 + 2 * (a_2 - 0.5)^2 * \left(1.145 - \frac{1}{\lambda_{\text{v}}} \right). \quad (2.17)$$

Similarly, Bey and Eigenberger [147] suggest the use of the correlation for solid cylinders with the inner void correction by Dixon [181], while Foumeny and Benyahia [269] defined the interpenetration factor f^* with $f^* = f \cdot (1/a_2^2 - 1)$. This factor may take values ranging from 0.95 - 1.0, especially 0.97, depending on the aspect ratio a_2 . In contrast, Benyahia and O'Neill [177] suggested a correlation suitable for all investigated aspect ratios:

$$\bar{\varepsilon} = \bar{\varepsilon}_{\text{inf}} + \frac{2.030}{(\lambda + 1.033)^2} \quad \text{with} \quad 1.9 \leq \lambda_{\text{v}} \leq 14.5 \quad \bar{\varepsilon}_{\text{inf}} = 0.465. \quad (2.18)$$

Finally, investigations of the orientation distribution reveal that the majority of rings have their opening not facing in the main flow direction [124].

In summary, a certain number of shapes, especially cylinders and hollow cylinders, have been investigated in the manner of packings of spheres. However, the existing data is not complete and differs significantly between the different sources consulted. While wall effect corrections have been derived for cylinders and hollow cylinders, the inclusion of the respective aspect ratios is inconsistent. Consequently, much more research is needed in order to understand the influence of simple shapes, such as cylinders and hollow cylinders alone, before thinking about more complex geometries.

2.2.4 Influence of particle material

Although most researchers do not take any material effects into consideration, Schuster and Vortmeyer [122] realized a significant difference in the radial porosity profiles comparing glass and steel spheres of the same size. Susskind and Becker [211] compared steel and glass packings in random close packing arrangements, where the steel packing has a slightly higher overall porosity.

Regarding material diversity, packed shapes made of almost any imaginable material have been utilized. This includes glass [20, 67, 119, 120, 122, 125, 129, 175, 179, 180, 190, 191, 193, 211, 270], ceramic [119, 124], steel [122, 186, 193, 211], stone [196, 217], metal [182, 192], lead [103, 105, 106, 108, 111–113, 217], wood [121, 231, 240, 241, 247], beans [114, 231], or other edibles [114, 232, 243], and plastic [107, 109, 116, 123, 180, 232] particles.

A small selection of studies evaluated packing material influences, but with contradictory results. While Crawford and Plumb [270] revealed a strong increase in packing porosity (from 0.356 to 0.442 and 0.467) with increasing surface roughness alias friction, while the in-depth material study performed by Macrae and Gray [225] resulted in only a minor influence of the coefficient of friction, if at all, but a significant impact of the coefficient of restitution where higher values decrease the packing porosity. Finally, Pottbäcker and Hinrichsen [186] observed both a decrease of porosity with lower friction and higher restitution values.

In summary, most researchers unjustifiably neglect the existing influence of material on the packing structure which may be problematic when comparing results with values taken from arbitrarily selected literature obtained under different conditions. However, the independent evaluation of the effect of material parameters remains impossible in experiments, as material parameters cannot be varied independently. Here, numerical tools are required to understand material-related features.

2.2.5 Influence of tube shape and material

While almost all investigations employ cylindrical confinements, in some studies tubes with square cross-sections are used [129, 179]. Comparing the average bed porosity data in a square duct [179] with those in a cylindrical duct [135], very similar values are obtained. A range of studies relate to annular ring packings where the packing is interrupted in the bulk part by one or more introduced tubes [102, 108, 111]. These annular packings are typically applied in nuclear engineering. Furthermore, non-rigid containers (eg, balloons) were investigated by Susskind and Becker [211]. Additionally, Man et al. [266] and Donev et al. [271] used spherical containers in their studies; however, the difference between the results and those obtained for cylindrical containers was not discussed.

Besides the shape of the tube's cross-section, tubes having a wall structure comprised of hemispheres were investigated [272–274]. It was found that this adjustment may significantly flatten the porosity profile in the packings of spheres, especially close to the wall. Similarly, Foumeny et al. [174, 178] tried to improve the wall-section of a packing by introducing smaller particles into the wall region, forming a so-called stratified bed. In summary, the tube's shape and material are only seldomly discussed and evaluated probably as if they have only a minor effect on the overall packing conditions.

2.3 Numerically packed-beds

Numerical packing generation can be performed by a large selection of commercial or free software packages or an even larger selection of in-house produced codes and algorithms presented in the literature (see Bennett [65], Clarke and Jónsson [86], Jodrey and Tory [88], Tory et al. [89], Visscher and Bolsterli [275], Nolan and Kavanagh [276], Yang et al. [277], and Zhong et al. [26] and Zhu et al. [278] for an overview). While the intention of this review is not to discuss advantages and disadvantages of each packing procedure, the DEM [279] is by now the most established tool for the numerical packing generation incorporating spheres with a physically accurate description of the particle packing process (see eg, [80] for details). Unfortunately, in order to pack particles other than spheres this method needs adaptation. For some distinct non-spherical shape classes, theoretical separate model developments exist (see Lu et al. [280] for a general review, for more details also Zhao et al. [281], Kodam et al. [282, 283], Guo et al. [284]). However, for the simulation of arbitrary shapes, it may be required to assemble the desired shape using a sufficiently large number of overlapping spheres [248, 283, 285–291]. Another attempt comprises the transfer of the DEM algorithm and the underlying physics to voxels (cubes) and the subsequent assembly of the desired shape by voxels [112, 292–295]. Or, ignoring certain physical conditions, shapes can be represented by a surface grid [296, 297]. A good comparison of some methods with regard to packing generation was presented by Fernengel et al. [298] for spheres, Caulkin et al. [291] for cylinders, and Flaischlen and Wehinger [299], who investigated packings of cylinders, hollow cylinders, and some more complex shapes.

These numerical packing algorithms are frequently used to generate packings for subsequent fluid dynamics [139, 287, 300–311], heat [288, 296, 312–320], or mass transfer simulations [321–331]. The numerical procedures are well capable of geometric packing analysis, allowing separate material property variation, packing procedure evaluation, and shape factor analysis on a large scale and in a fast and cost-efficient manner. In general, two settings have to be distinguished, one setting incorporating the confining wall (see Zhao et al. [281], and Mueller [332]) and one setting having periodic boundaries and thus neglecting of the influence of the confining wall (see Zhao et al. [285], and Delaney and Cleary [333]). When using confined packings, it is required to use the bulk part of the packing for porosity calculation to exclude top and bottom effects [232]. Unfortunately, validation is frequently a major problem, as typically not enough experimental data is available, and the available data frequently has a large error or is obtained under uncertain or vague packing and material conditions.

2.3.1 Influence of material and packing procedure

Zhang et al. [80] evaluated packing procedure properties and found a decrease in porosity when using higher particle drop heights and lower deposition intensities (number of particles filled per second). Additionally, material properties have been evaluated predicting a lower porosity when having a lower damping coefficient which directly correlates to the coefficient of restitution and a lower coefficient of friction [80]. Similar results were obtained by other scientists [248]. The decrease in porosity for a smaller coefficient of friction values was repeatedly obtained [140, 161, 290, 297, 334–337]. Furthermore, the porosity increases with increasing E-modulus [248, 334], a decrease in the coefficient of restitution [297, 335, 336], and an increase in surface energy [335]. The porosity is not dependent on the particle's stiffness [335]. The extent to which it is influenced by certain material parameters can be best evaluated using a sensitivity analysis [338]. However, the respective material parameters are often not known, they need to be guessed and adjusted by comparing experimental and numerical outputs [339].

Packing densification using vibration [213, 286, 340], tapping [341, 342], or air impact densification [343] was studied finding optimal densification parameters to gain the densest packings. Furthermore, a lower porosity can be obtained with fewer particles added at the same time [80, 298, 336]. Thus, numerical packing generation tools are very important for the evaluation of material or packing procedure parameters and thus understanding of these influences, because it is impossible to vary these independently in an experiment.

2.3.2 Influence of the shape

Numerical studies investigating shape effects on packing structure, most predominantly aspect ratio variations, are reviewed in Table 2.7 clustered according to the evaluated shapes and respective aspect ratio ranges, and the evaluated packing parameters including mean coordination number \bar{N}_C , bulk porosity ϵ_{inf} and $\bar{\epsilon}(\lambda)$, local porosity distributions $\epsilon(r)$, and the particle orientation angle θ . Additionally, the data obtained from the literature for the calculated average bed porosity as a function of the respective

Table 2.7: Literature review on numerical packing generation studies sorted by shape

Source	Shape	Aspect ratio $1/a_1$	Aspect ratio a_x	\bar{N}_c	ε_{inf}	$\bar{\varepsilon}(\lambda)$	$\varepsilon(r)$	θ
Wu et al. [286]	Cube	1	-	✓	✓	✓	✓	-
Zhao et al. [285]	Frustrums, cylinder, cone	0.5 - 1.5	0 - 1	-	✓	-	-	-
Xie et al. [344]	Cube	0.3 - 1.5	-	✓	✓	-	-	-
Zhao et al. [345]	Spherocylinder	1 - 11	-	✓	✓	-	-	✓
Wouterse et al. [346]	Spherocylinder	1 - 160	-	✓	✓	-	-	-
Wouterse et al. [347]	Spherocylinder	1 - 6	-	✓	✓	-	-	-
Wouterse et al. [347]	Ellipsoid	0.1 - 5	-	✓	✓	-	-	-
Donev et al. [271]	Ellipsoid	0.3 - 3.5	-	✓	✓	-	-	-
Donev et al. [271]	Aspherical ellipsoid	1 - 2	-	✓	✓	-	-	-
Williams and Philipse [348]	Spherocylinder	1 - 161	-	✓	✓	-	-	-
Sherwood [349]	Ellipsoids	0.07 - 15	-	-	✓	-	-	-
various [46, 90, 108, 112, 139, 161, 276, 297, 298, 300, 304, 309, 320, 332, 350–355]	Sphere	-	-	(✓)	(✓)	✓	(✓)	-
Qian et al. [356]	Cylinder	0.1 - 10	-	✓	✓	-	-	-
Zhou et al. [334]	Ellipsoid	0.1 - 7	-	✓	✓	✓	-	-
Zhao et al. [357]	Superellipsoid	0.3 - 2.5	0.5 - 1.4	✓	✓	-	-	✓
Zhao et al. [281]	Tetrahedra	0.4 - 3.0	-0.75 - 1.00	✓	✓	✓	-	✓
Zhao et al. [358]	Sphero-tetrahedra	0.12 - 1.84	-0.75 - 1.00 0.05 - 10	-	✓	✓	-	-
Lathan et al. [359]	Tetrahedra	1 - 1.8	-	-	✓	-	-	-
Li et al. [360]	Tetrahedra	0.5 - 1.5	-	-	✓	-	-	-
Niegodajew and Marek [361]	Hollow cylinder	0.33 - 3.0	const. 0.8	-	✓	✓	-	✓
Nan et al. [335]	Spherocylinder	5 - 20	-	✓	✓	-	-	-
Nan et al. [362]	Spherocylinder	5 - 50	-	✓	✓	-	-	✓
Meng et al. [207]	Spherocylinder	1 - 7	-	✓	✓	-	-	-
McGrother et al. [363]	Spherocylinder	4 - 6	-	-	(✓)	-	-	-
Liu et al. [364]	Cube	0.3 - 6.0	-	-	✓	-	-	-
Delaney and Cleary [333]	Superellipsoids	0.33 - 3.5	2 - 5	✓	✓	-	-	-
Li et al. [289]	Cone	0.5 - 1.5	-	-	✓	-	-	-
	Cylinder	0.5 - 1.5	-	-	✓	-	-	-
	Ellipsoid	0.5 - 1	1 - 2	-	✓	-	-	-
	Spherocylinder	0.5 - 1.5	-	-	✓	-	-	-
	Tetrahedron	0.5 - 1.5	-	-	✓	-	-	-
Kyrylyuk and Philipse [365]	Spherocylinders	1 - 11	-	-	✓	-	-	-
Jiao and Torquato [366]	Platonic shapes	Regular	-	-	✓	-	-	-
Jiao et al. [367]	Superballs	Regular	0 - ∞	✓	✓	-	-	-
Jia et al. [293]	Cylinder	0.1 - 30	-	-	✓	-	-	-
	Spherocylinder	1 - 4.5	-	-	✓	-	-	-
Gan et al. [368]	Ellipsoids	0.25 - 3.5	-	✓	✓	-	-	-
Evans and Ferrar [369]	Spherocylinder	1 - 25	-	-	✓	-	-	✓
Dong et al. [319, 370]	Cylinder	0.3 - 2.5	-	-	✓	-	-	-
	Ellipsoids	0.3 - 2.5	-	-	✓	✓	-	-
Desmond and Franklin [371]	Ellipse	5 - 50	-	-	✓	-	-	-
Das et al. [310]	Cube	0.33 - 1	-	-	✓	✓	✓	✓
Ferreiro-Córdova and Duijn- eveltdt [372]	Spherocylinder	1 - 11	-	-	✓	-	-	-
Coelho et al. [311]	Ellipsoid	0.1 - 10	-	-	✓	-	-	-
	Cylinder	0.1 - 10	-	-	✓	-	-	-
	Parallelepiped	0.1 - 10	-	-	✓	-	-	-
Chaikin et al. [373]	Ellipsoid	1 - 3	0 - 1	✓	✓	-	-	-
Bolhuis and Frenkel [374]	Spherocylinder	1 - 4	-	-	(✓)	-	-	-
Blaak et al. [375]	Cylinder	0.1 - 10	-	-	-	-	-	(✓)
Baule et al. [376]	Lens	0.45 - 1	-	✓	✓	-	-	-
	Dimer	1 - 2	-	✓	✓	-	-	-
	Spherocylinder	1 - 2	-	✓	✓	-	-	-
Bargiel [377]	Spherocylinder	1 - 80	-	-	✓	-	-	-
Kyrylyuk et al. [378]	Spherocylinder	1 - 4	-	-	✓	-	-	-
Abreu et al. [379]	Spherocylinder	1 - 4.5	-	-	✓	-	-	-
Freeman et al. [380]	Spherocylinder	5 - 35	-	-	✓	-	✓	-
Lumay and Vandewalle [219]	Cylinder	5 - 90	-	-	✓	-	-	-

aspect ratio are summarized in Fig. 2.12, especially regarding (a) ellipsoid shapes, (b) spherocylinders, (c) cylindrical shapes, and (d) platonic shapes. In some cases, correlations for calculating the porosity

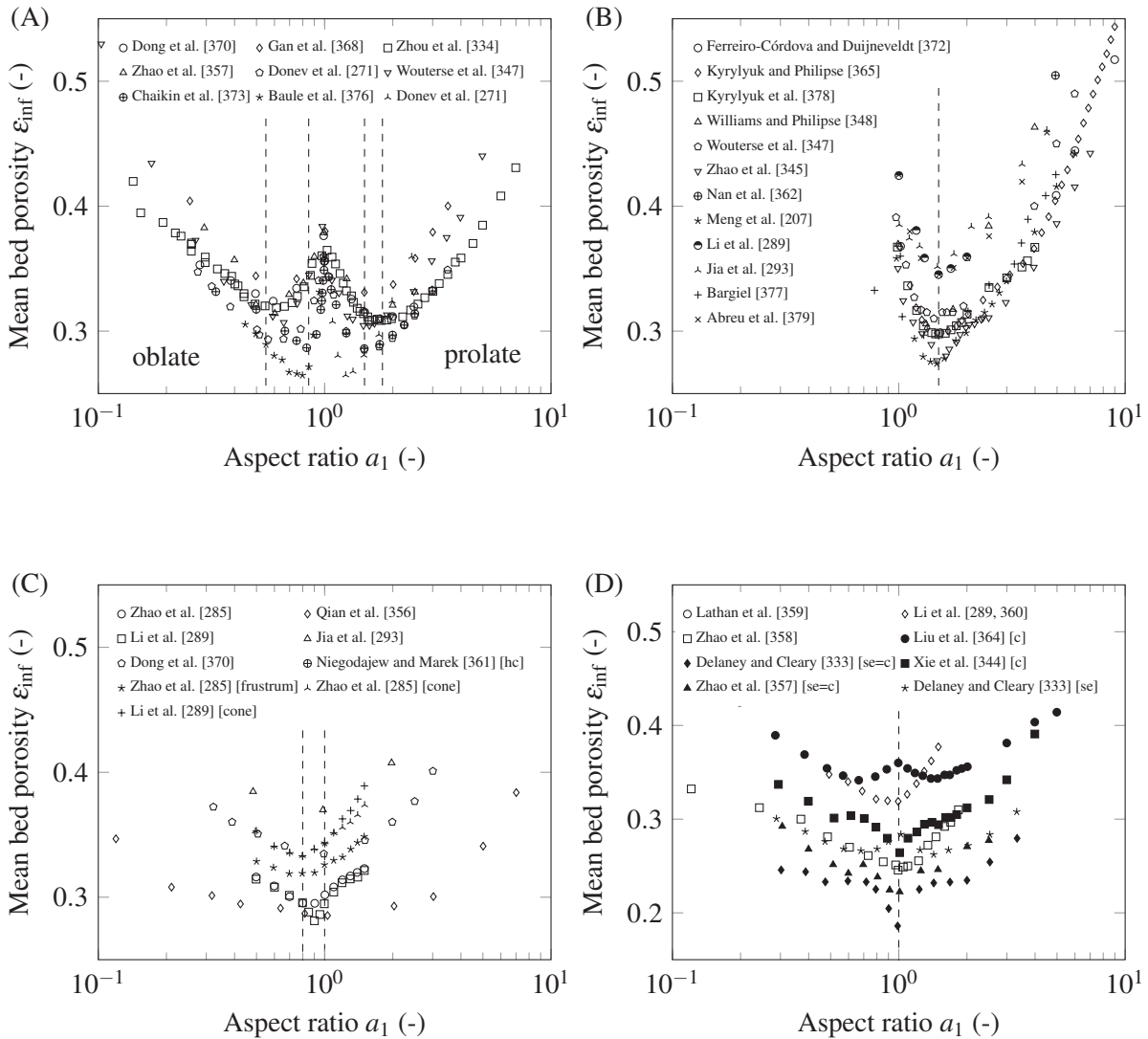


Figure 2.12: Mean bed porosity under the absence of confinement as a function of the aspect ratio of packings consisting of: A, ellipsoids, aspherical ellipses (Donev et al. [271]) and lenses (Baule et al. [376]); B, spherocylinders; C, cylinders (empty marks), hollow cylinders [hc], frustums and cones; and D, tetrahedra (empty marks), cubes (solid marks) and superellipsoids (star). The vertical line marks the range of minima occurrence [207, 271, 285, 289, 293, 333, 334, 344, 345, 347, 348, 356–362, 364, 365, 368, 370, 372, 373, 376–379]

based on the respective aspect ratios are suggested [285]. The influence of curl index when packing curved spherocylinders was studied [362], along with the influence of particle orientation [361, 362]. For instance, in a packing of hollow cylinders, the particle orientation is increasingly perpendicular to the container axis with increasing aspect ratio a_1 [361].

Comparing different geometries [289, 381], a shape packing density order was identified. Accordingly, the lowest porosity values were obtained with cubes followed by ellipsoids, cylinders and spherocylinders, tetrahedrons, cones, and finally spheres with the highest bulk porosity [289]. As shown in Fig. 2.12, the aspect ratios with the lowest packing porosity were identified to be around unity, except for the spherocylinders and ellipsoids, where the minima are around 1.35 and 0.7.

Despite the usage of rather mathematical shapes, Partopour and Dixon [296] compared packings of actual catalyst shapes such as hollow cylinders and multi-holed/fluted versions. Similarly, Moghaddam et al. [336] compared sphere, cylinder, and hollow cylinder packings in cylindrical confining walls, especially regarding the radial porosity distribution and λ -relation. Karthik and Buwa [328] compared single-pellet-string packings of six different pellet shapes used in catalysis, comprising multi-holed cylinders, cross-web cylinders, and polylobes, and Caulkin et al. [111, 124] investigated packings of cylinders with different hole geometries and reactor setups. Finally, trilobes were further studied by Boccardo et al. [297].

In summary, numerical packing generation tools have been frequently used to evaluate particle aspect ratio variations affecting the bulk porosity. However, as the range of imaginable shapes and their aspect ratio variations are infinite, we are far away from understanding a general shape influence on packed beds. Moreover, comparing the obtained results, large deviations can be seen relating to different material and packing mode conditions. Consequently, before being able to evaluate a universal shape dependence, the definition of standard packing conditions is required. Otherwise, results are impossible to compare.

2.3.3 Further notable results

Besides the often studied shape, material, and packing mode variations, some further notable studies were performed, for instance comprising confinement shape variations including cylindrical, half-cylindrical, square, and rectangular cross-sections [307, 319]. Moreover, studies were performed addressing the porosity increase and packing compression for packing particle sizes $< 1000 \mu\text{m}$ where interparticle forces become relevant [1, 368, 382, 383]. Further studies address the effect of particle size distribution or bi-, tri-, and multimodal particle mixtures of the same shape or of different shapes (see Caulkin et al. [112], Kyrylyuk et al. [378], and Dorai et al. [384]), but this is outside the scope of this review.

2.4 Conclusion

The knowledge of random packings of mono-sized particles gained over the last hundred years of research was reviewed and clustered. Available studies regarding the influence of shape, size, and material properties of the particles, the packing and densification mode characterizing the bed formation, and the influence of the confining tube including tube shape and material, were taken into consideration. Explicitly excluded is the influence of shape inhomogeneity and multi-modal or multi-shape particle mixtures. Furthermore, the reviewed data is restricted to a minimum particle size of 1 mm where gravity is the predominant force. The structural characteristics investigated comprise the mean coordination number, the radial and axial porosity distributions, and the average bed porosity. While a significant amount of complementary studies with regard to packed-beds of spheres are known to result in a good understanding of structural bed characteristics, there is still a significant lack of knowledge with regard to the influence of particle shape. While this cannot be attributed to a lack of data, as there are numerous studies addressing shape influences on all levels, the research field is simply too large for these studies to lead to a complete fundamental understanding. However, numerical tools capable of producing and evaluating huge data sets in short time frames open up the possibility to take the research on packing characteristics to another level, and the overall complexity will rise when transferring to the real applications of packed-beds. Structural impacts on fluid dynamics, heat, and mass transfer are far away from being comprehensively understood while trial and error remain the standard development method. Consequently, the development of packing shapes might be an interesting application example where machine learning tools might become relevant in the future.

Acknowledgements

Financial and substantial support of MuniCat, a strategic alliance between the Technical University of Munich (TUM) and Clariant AG is gratefully acknowledged. Jennie von Seckendorff would further like to thank the TUM Graduate School for generous support.

Conflict of interest

The authors declare no potential conflict of interests.

Author Contributions

The research "Review on the Structure of Random Packed-Beds" was initiated by Jennie von Seckendorff and supervised by Olaf Hinrichsen. The review was written by Jennie von Seckendorff and supported by Olaf Hinrichsen.

Nomenclature

Latin Symbols

a, b, c, d	pre-factor parameters	-
a_1	height to diameter aspect ratio	-
a_2	inner to outer diameter aspect ratio	-
a_3	upper to lower diameter aspect ratio	-
a_p	particle surface area	m^2
a_x	any other aspect ratio	-
$c_D(Re)$	drag coefficient	-
d	real particle diameter	m
d_i	inner particle diameter of hollow cylinder	m
d_p	particle diameter	m
$d_{ps}, d_{pv}, d_{pw},$ d_{pd}, d_{pack}	equivalent particle diameter	m
D	diameter of tube	m
f	hollow cylinder interpenetration correction	-
F_D	drag force	N
g	acceleration of gravity	$m s^{-2}$
h	real height of a particle	m
H	height of tube	m
H_r	Hausner ratio	-
m	flatness ratio	-
n	number of taps per second	s^{-1}
n	elongation ratio	-
\bar{N}_c	mean contact number	-
r	radial position	m
R	tube radius	m
u_0	superficial velocity	$m s^{-1}$
u_s	sedimentation velocity	$m s^{-1}$
T	tortuosity	-
v_p	particle volume	m^3
z	axial position	m
z_{min}	radial location of first porosity minimum	-
z_r	non-dimensional radial position	-
z_z	non-dimensional axial position	-

Greek Symbols

ε	porosity	-
---------------	----------	---

$\bar{\varepsilon}$	average bed porosity	-
ε_{inf}	average bed porosity with $\lambda \rightarrow \infty$	-
ε_{min}	local porosity at the first minimum close to the tube wall	-
$\bar{\varepsilon}_{\text{sc}}$	average reference porosity of a solid cylinder	-
$\varepsilon(r)$	radial porosity distribution	-
$\varepsilon(z)$	axial porosity distribution	-
$\bar{\varepsilon}(\lambda)$	average porosity as a function of λ	-
λ	tube to particle diameter ratio	-
λ_v	tube to particle diameter ratio based on volume equivalent particle diameter	-
$\bar{\rho}_\varepsilon$	packing density, $= 1 - \bar{\varepsilon}$	-
ρ_f	fluid density	kg m^{-3}
ρ_p	particle density	kg m^{-3}
τ	relaxation time	s^{-1}
κ	tube height-to-particle diameter ratio	-
Ψ_w	sphericity	-
ψ	azimuthal contact angle	$^\circ$
θ	particle orientation in packing	$^\circ$
$\bar{\phi}_c$	mean (poloidal) contact angle	$^\circ$

Abbreviations

DEM	Discrete Element Method
Erfc	Error function
J_0	Bessel function of first kind and zero order
MRJ	maximally random jammed
RCP	random close packing
RLP	random loose packing

References

- [1] M. Dorn, F. Eschbach, D. Hekmat, D. Weuster-Botz, *Journal of Chromatography A* **2017**, *1516*, 89–101.
- [2] K. K. Unger, R. Skudas, M. M. Schulte, *Journal of Chromatography A* **2008**, *1184*, 393–415.
- [3] G. Guiochon, T. Farkas, H. Guan-Sajonz, J.-H. Koh, M. Sarker, B. J. Stanley, T. Yun, *Journal of Chromatography A* **1997**, *762*, 83–88.
- [4] F. S. Mederos, J. Ancheyta, J. Chen, *Applied Catalysis A: General* **2009**, *355*, 1–19.
- [5] G. Eigenberger in *Handbook of Heterogeneous Catalysis*, 2nd ed. (Eds.: C. Ertl, H. Knözinger, F. Schüth, J. Weitkamp), Wiley-VCH, Weinheim, **2008**.
- [6] M. Baerns, A. Behr, A. Brehm, J. Gmehling, K.-O. Hinrichsen, H. Hofmann, U. Onken, R. Palkovits, A. Renken, *Technische Chemie*, 2nd ed., Wiley-VCH, Weinheim, **2014**.
- [7] A. Mersmann, M. Kind, J. Stichlmair, *Thermal Separation Technology: Principles, Methods, Process Design*, Springer-Verlag Berlin Heidelberg, **2011**.
- [8] A. Koster, H. D. Matzner, D. R. Nicholisi, *Nuclear Engineering and Design* **2003**, *222*, 231–245.
- [9] S. Thomas, *Energy Policy* **2011**, *39*, 2431–2440.
- [10] G. J. Auwerda, J. L. Kloosterman, A. J. M. Winkelman, J. Groen, V. van Dijk, *Advances in Reactor Physics to Power the Nuclear Renaissance Pittsburgh USA* **2010**.
- [11] G. Jacob, C. U. Brown, A. Donmez, *NIST Advanced Manufacturing Series 100-17* **2018**.
- [12] H. Singh, R. P. Saini, J. S. Saini, *Renewable and Sustainable Energy Reviews* **2010**, *14*, 1059–1069.
- [13] C. D. F. Rogers, T. A. Dijkstra, I. J. Smalley, *Earth-Science Reviews* **1994**, *36*, 59–82.
- [14] S. W. Taylor, P. C. D. Milly, P. R. Jaffré, *Water Resources Research* **1990**, *26*, 2161–2169.
- [15] A. J. Cooke, R. K. Rowe, *Journal of Environmental Engineering* **1999**, *125*, 126–136.
- [16] A. I. Rodarte-Morales, G. Feijoo, M. T. Moreira, J. M. Lema, *Biochemical Engineering Journal* **2012**, *66*, 38–45.
- [17] M. Horttanainen, J. Saastamoinen, P. Sarkomaa, *Energy & Fuels* **2002**, *16*, 676–686.
- [18] E. López, E. Heracleous, A. Lemonidou, D. Borio, *Chemical Engineering Journal* **2008**, *145*, 308–315.
- [19] A. Klyushina, K. Pacultová, L. Obalová, *Reaction Kinetics Mechanisms and Catalysis* **2015**, *115*, 651–662.
- [20] A. de Klerk, *AIChE Journal* **2003**, *49*, 2022–2029.
- [21] D. P. Haughey, G. S. G. Beveridge, *The Canadian Journal of Chemical Engineering* **1969**, *47*, 130–140.
- [22] B. Einfeld, K. Schnitzlein, *Chemical Engineering Science* **2005**, *60*, 4105–4117.
- [23] E. Erdim, Ö. Akgiray, I. Demir, *Powder Technology* **2015**, *283*, 488–504.
- [24] J. M. P. Q. Delgado, *Heat and Mass Transfer* **2006**, *42*, 279–310.

- [25] W. van Antwerpen, C. G. du Toit, P. G. Rousseau, *Nuclear Engineering and Design* **2010**, *240*, 1803–1818.
- [26] W. Zhong, A. Yu, X. Liu, Z. Tong, H. Zhang, *Powder Technology* **2016**, *302*, 108–152.
- [27] W.-C. Yang, *Handbook of Fluidization and Fluid-Particle Systems, 1st ed.* CRC Press, Boca Raton, FL, **2003**.
- [28] S. Afandizadeh, E. A. Foumeny, *Applied Thermal Engineering* **2001**, *21*, 669–682.
- [29] Y. Tsutsumi, *Powder Technology* **1973**, *7*, 181–188.
- [30] E. Manegold, R. Hofmann, K. Solf, *Kolloid-Zeitschrift* **1931**, *56*, 142–159.
- [31] L. C. Gratton, H. J. Fraser, *The Journal of Geology* **1935**, *43*, 785–909.
- [32] J. Hrubisek, *Kolloid-Beihefte* **1941**, *53*, 385–452.
- [33] J. Kubie, *Chemical Engineering Science* **1988**, *43*, 1403–1405.
- [34] J. D. Bernal, *Proceedings of the Royal Society A: Mathematical Physical and Engineering Sciences* **1964**, *280*, 299–322.
- [35] D. Kunii, J. M. Smith, *AIChE Journal* **1960**, *6*, 71–78.
- [36] J. S. Goodling, M. S. Khader, *Powder Technology* **1985**, *44*, 53–55.
- [37] W. O. Smith, P. D. Foote, P. F. Busang, *Physical Review* **1929**, *34*, 1271–1274.
- [38] J. D. Bernal, J. Mason, *Nature* **1960**, *188*, 910–911.
- [39] J. Wadsworth, Experimental examination of local processes in packed beds of homogeneous spheres, tech. rep., National Research Council of Canada, Mech. Eng. Report MT-41-Feb, NRC No. 5895, **1960**.
- [40] M. Arakawa, M. Nishino, *Journal of the Society of Materials Science Japan* **1973**, *22*, 658–662.
- [41] D. Pinson, R. P. Zou, A. B. Yu, P. Zulli, M. J. McCarthy, *Journal of Physics D: Applied Physics* **1998**, *31*, 457–462.
- [42] M. Oda, *Soils and Foundations* **1977**, *17*, 29–42.
- [43] G. D. Scott, *Nature* **1960**, *188*, 908–909.
- [44] T. Aste, M. Saadatfar, A. Sakellariou, T. J. Senden, *Physica A: Statistical Mechanics and Its Application* **2004**, *339*, 16–23.
- [45] T. Aste, M. Saadatfar, T. J. Senden, *Physical Review E* **2005**, *061302*, 71.
- [46] G. J. Auwerda, J.-L. Kloosterman, D. Lathouwers, T. H. J. J. van der Hagen, *Nuclear Technology* **2013**, *183*, 272–286.
- [47] R. P. Zou, X. Bian, D. Pinson, R. Y. Yang, A. B. Yu, P. Zulli, *Particle & Particle Systems Characterization* **2003**, *20*, 335–341.
- [48] G. A. Georgalli, M. A. Reuter, *Minerals Engineering* **2006**, *19*, 246–255.
- [49] J. Reimann, J. Vicente, E. Brun, C. Ferrero, Y. Gan, A. Rack, *Powder Technology* **2017**, *318*, 471–483.
- [50] J. Reimann, R. A. Pieritz, C. Ferrero, M. di Michiel, R. Rolli, *Fusion Engineering and Design* **2008**, *83*, 1326–1330.

- [51] J. Reimann, R. A. Pieritz, R. Rolli, *Fusion Engineering and Design* **2006**, *81*, 653–658.
- [52] G. D. Scott, *Nature* **1962**, *194*, 956–957.
- [53] G. Mason, W. Clark, *Nature* **1965**, *207*, 512.
- [54] G. Mason, W. Clark, *Nature* **1966**, *211*, 957.
- [55] G. D. Scott, D. L. Mader, *Nature* **1964**, *201*, 382–383.
- [56] J. L. Finney, *Proceedings of The Royal Society A* **1970**, *319*, 479–493.
- [57] J. Urquidi, S. Singh, C. H. Cho, G. W. Robinson, *Physical Review Letters* **1999**, *83*, 2348–2350.
- [58] A. O. Dohn, E. Biasin, K. Haldrup, M. M. Nielsen, N. E. Henriksen, K. B. Moller, *Journal of Physics B: Atomic Molecular and Optical Physics* **2015**, *48*, 244010.
- [59] A. K. Soper, *ISRN Physical Chemistry* **2013**, 279463.
- [60] H. P. Meissner, A. S. Michaels, R. Kaiser, *Industrial & Engineering Chemistry Process Design and Development* **1964**, *3*, 202–205.
- [61] S. Melmore, *Nature* **1942**, *149*, 412.
- [62] H. Heesch, F. Laves, *Zeitschrift für Kristallographie - Crystalline Materials* **1933**, *85*, 443–453.
- [63] M. Nakagaki, H. Sunada, *Yakugaku Zasshi* **1968**, *88*, 651–655.
- [64] M. Suzuki, T. Oshima, *KONA Powder and Particle Journal* **1989**, *7*, 22–28.
- [65] C. H. Bennett, *Journal of Applied Physics* **1972**, *43*, 2727–2734.
- [66] A. B. Yu, J. Bridgwater, A. Burbidge, *Powder Technology* **1997**, *92*, 185–194.
- [67] C. L. Feng, A. B. Yu, *Powder Technology* **1998**, *99*, 22–28.
- [68] J. V. Milewski, *Handbook of Fillers and Reinforcements for Plastics*, Van Nostrand Reinhold, New York, **1987**.
- [69] M. Suzuki, H. Sato, M. Hasegawa, M. Hirota, *Powder Technology* **2001**, *118*, 53–57.
- [70] R. Y. Yang, R. P. Zou, A. B. Yu, *Physical Review E* **2000**, *62*, 3900–3908.
- [71] J. X. Liu, T. J. Davies, *Powder Metallurgy* **1997**, *40*, 48–50.
- [72] J. M. Beck, V. A. Volpert, *Journal of Colloid and Interface Science* **2003**, *262*, 162–170.
- [73] M. E. Wise, *Philips Research Reports* **1952**, *7*, 321–343.
- [74] M. J. Hogendijk, *Philips Research Reports* **1963**, *18*, 109–126.
- [75] J. A. Dodds, *Journal of Colloid and Interface Science* **1980**, *77*, 317–327.
- [76] M. Leitzement, C. S. Lo, J. Dodds, *Powder Technology* **1985**, *41*, 159–164.
- [77] P. Richard, L. Oger, J. P. Troadec, A. Gervois, *The European Physical Journal E* **2001**, *6*, 295–303.
- [78] A. B. Yu, N. Standish, *Powder Technology* **1988**, *55*, 171–186.
- [79] H. Iwata, T. Homma, *Powder Technology* **1974**, *10*, 79–83.
- [80] Z. P. Zhang, L. F. Liu, Y. D. Yuan, A. B. Yu, *Powder Technology* **2001**, *116*, 23–32.
- [81] M. Suzuki, T. Oshima, *Powder Technology* **1985**, *44*, 213–218.
- [82] M. Suzuki, T. Oshima, *Powder Technology* **1983**, *35*, 159–166.

- [83] M. Suzuki, K. Makino, M. Yamada, K. Linoya, *Kagaku Kogaku Ronbunshu* **1980**, *6*, 59–64.
- [84] L. Oger, J. P. Troadec, D. Bideau, J. A. Dodds, M. J. Powell, *Powder Technology* **1986**, *46*, 121–131.
- [85] L. Y. Yi, K. J. Dong, R. P. Zou, A. B. Yu, *Industrial & Engineering Chemistry Research* **2011**, *2011*, 8773–8785.
- [86] A. S. Clarke, H. Jónsson, *Physical Review E* **1993**, *47*, 3975–3984.
- [87] L. Meng, P. Lu, S. Li, *Particuology* **2014**, *16*, 155–166.
- [88] W. S. Jodrey, E. M. Tory, *Physical Review A* **1985**, *32*, 2347–2351.
- [89] E. M. Tory, B. H. Church, M. K. T. A. M. Ratner, *The Canadian Journal of Chemical Engineering* **1973**, *51*, 484–493.
- [90] X. Z. An, K. J. Dong, R. Y. Yang, R. P. Zou, C. C. Wang, A. B. Yu, *Granular Matter* **2016**, *18*, 6.
- [91] C. G. du Toit, W. van Antwerpen, P. G. Rousseau, *ICAPP Conference 2009* **2009**, ID 9123.
- [92] H. Rumpf, *Chemie Ingenieur Technik* **1958**, *30*, 144–158.
- [93] W. G. Field, *Proceedings of the 4th Australian and New Zealand Conference on Soil Mechanics* **1963**, 143–148.
- [94] D. P. Haughey, G. S. G. Beveridge, *Chemical Engineering Science* **1966**, *21*, 905–915.
- [95] K. Ridgway, K. J. Tarbuck, *Britisch Chemical Engineering* **1967**, *12*, 384–388.
- [96] N. W. Ridgway, G. A. Tingate, *Australian Atomic Energy Commission* **1970**, *E202*, 16p.
- [97] K. Gotoh, *Journal of the Society of Powder Technology Japan* **1978**, *15*, 220–226.
- [98] T. Nagao, *Transactions of the Japan Society of Mechanical Engineers* **1978**, *44*, 1912–1922.
- [99] N. Ouchiyaama, T. Tanaka, *Industrial & Engineering Chemistry Fundamentals* **1980**, *19*, 338–340.
- [100] M. Suzuki, K. Makino, M. Yamada, K. Linoya, *International Chemical Engineering* **1981**, *21*, 482–488.
- [101] D. He, N. N. Ekere, L. Cai, *Physical Review E* **1999**, *60*, 7098–7104.
- [102] F. A. Schneider, D. W. T. Rippin, *Industrial & Engineering Chemistry Research* **1988**, *27*, 1936–1941.
- [103] S. Roshani, PhD thesis, University of Leeds, **1990**.
- [104] L. H. S. Roblee, R. M. Baird, J. W. Tierney, *AIChE Journal* **1958**, *4*, 460–464.
- [105] R. F. Benenati, C. B. Brosilow, *AIChE Journal* **1962**, *8*, 359–361.
- [106] M. Propster, J. Szekely, *Powder Technology* **1977**, *17*, 123–138.
- [107] J. S. Goodling, R. I. Vachon, W. S. Stelpflug, S. J. Ying, M. S. Khader, *Powder Technology* **1983**, *35*, 23–29.
- [108] C. G. du Toit, *Nuclear Engineering and Design* **2008**, *238*, 3073–3079.
- [109] M. C. Thadani, F. N. Peebles, *Industrial & Engineering Chemistry Process Design and Development* **1966**, *5*, 265–268.
- [110] R. Küfner, H. Hofmann, *Chemical Engineering Science* **1990**, *45*, 2141–2146.

- [111] R. Caulkin, A. Ahmad, M. Fairweather, X. Jia, R. A. Williams, *Computers and Chemical Engineering* **2009**, *33*, 10–21.
- [112] R. Caulkin, M. Fairweather, X. Jia, N. Gopinathan, R. A. Williams, *Computers and Chemical Engineering* **2006**, *30*, 1178–1188.
- [113] J. H. Ismail, M. Fairweather, K. H. Javed, *Chemical Engineering Research and Design* **2002**, *80*, 645–653.
- [114] W. Du, N. Quan, P. Lu, J. Xu, W. Wei, L. Zhang, *Chemical Engineering Research and Design* **2016**, *106*, 115–125.
- [115] A. Montillet, L. le Coq, *Powder Technology* **2001**, *121*, 138–148.
- [116] K. Ridgway, K. J. Tarbuck, *Journal of Pharmacy and Pharmacology* **1966**, *18*, 168S–175S.
- [117] M. R. Shaffer, MA thesis, Perdue University, Lafayette, **1953**.
- [118] N. B. Griffiths, PhD thesis, University of Cambridge, **1986**.
- [119] J. J. Lerou, G. F. Froment, *Chemical Reactor Design and Technology* **1986**, 729–736.
- [120] V. Stanek, V. Eckert, *Chemical Engineering Science* **1979**, *34*, 933–940.
- [121] K. K. Pillai, *Chemical Engineering Science* **1977**, *32*, 59–61.
- [122] J. Schuster, D. Vortmeyer, *Chemie Ingenieur Technik* **1980**, *52*, 848–849.
- [123] V. N. Korolev, N. I. Syromyatnikov, E. M. Tolmachev, *Journal of Engineering Physics* **1971**, *21*, 1475–1478.
- [124] R. Caulkin, X. Jia, C. Xu, M. Fairweather, R. A. Williams, H. Stitt, M. Nijemeisland, S. Aferka, M. Crine, A. Léonard, D. Toye, P. Marchot, *Industrial & Engineering Chemistry Research* **2009**, *48*, 202–213.
- [125] F. Al-Falahi, M. Al-Dahhan, *Nuclear Engineering and Design* **2016**, *310*, 231–246.
- [126] R. A. Pieritz, J. Reimann, C. Ferrero, *Advanced Engineering Materials* **2010**, *13*, 145–155.
- [127] N. J. Mariani, W. I. Salvat, M. A. Campesi, G. F. Barreto, O. M. Martinez, *International Journal of Chemical Reactor Engineering* **2009**, *7*, A82.
- [128] X. Gan, M. Kamlah, J. Reimann, *Fusion Engineering and Design* **2010**, *85*, 1782–1787.
- [129] J. M. Buchlin, M. Riethmuller, J. J. Ginoux, *Chemical Engineering Science* **1977**, *32*, 1116–1119.
- [130] R. Balzan, A. L. Sellerio, D. Mari, A. Comment, G. Gremaud, *Granular Matter* **2013**, *15*, 873–879.
- [131] R. Balzan, A. L. Sellerio, D. Mari, A. Comment, *Applied Magnetic Resonance* **2015**, *46*, 633–642.
- [132] R. Stannarius, *Review of Scientific Instruments* **2017**, *88*, 051806.
- [133] A. J. Sederman, P. Alexander, L. F. Gladden, *Powder Technology* **2001**, *117*, 255–269.
- [134] N. L. Nguyen, V. van Buren, R. Reimert, A. von Garnier, *Magnetic Resonance Imaging* **2005**, *23*, 395–396.
- [135] G. E. Mueller, *Powder Technology* **1992**, *72*, 269–275.
- [136] M. Giese, K. Rottschäfer, D. Vortmeyer, *AIChE Journal* **1998**, *44*, 484–490.
- [137] K. Ridgway, K. J. Tarbuck, *Chemical Engineering Science* **1968**, *23*, 1147–1155.

- [138] M. Suzuki, T. Shinmura, K. Iimura, M. Hirota, *Advanced Powder Technology* **2008**, *19*, 183–195.
- [139] P. Lovreglio, S. Das, K. A. Buist, E. A. J. F. Peters, L. Pel, J. A. M. Kuipers, *AIChE Journal* **2018**, *64*, 1896–1907.
- [140] C. M. Wensrich, *Powder Technology* **2012**, *219*, 118–127.
- [141] C. E. Schwartz, J. M. Smith, *Industrial & Engineering Chemistry* **1953**, *45*, 1209–1218.
- [142] G. Johnson, PhD thesis, University of Rochester, **1970**.
- [143] H. A. Moallemi, PhD thesis, University of Leeds, **1989**.
- [144] B. C. Chandrasekhara, D. Vortmeyer, *Wärme- und Stoffübertragung* **1979**, *12*, 105–111.
- [145] H. Martin, *Chemical Engineering Science* **1978**, *33*, 913–919.
- [146] Y. Cohen, A. B. Metzner, *AIChE Journal* **1981**, *27*, 705–715.
- [147] O. Bey, G. Eigenberger, *Chemical Engineering Science* **1997**, *52*, 1365–1376.
- [148] M. Giese, PhD thesis, Technische Universität München, **1998**.
- [149] D. Vortmeyer, J. Schuster, *Chemical Engineering Science* **1983**, *38*, 1691–1699.
- [150] P. Cheng, C. T. Hsu, *International Journal of Heat and Mass Transfer* **1986**, *29*, 1843–1853.
- [151] J. R. Sodré, J. A. R. Parise, *Experimental Thermal and Fluid Science* **1998**, *17*, 265–275.
- [152] M. L. Hunt, C. L. Tien, *Chemical Engineering Science* **1990**, *45*, 55–63.
- [153] G. E. Mueller, *Powder Technology* **2019**, *342*, 607–612.
- [154] G. E. Mueller, *Chemical Engineering Science* **1991**, *46*, 706–708.
- [155] G. E. Mueller, *Powder Technology* **2010**, *203*, 626–633.
- [156] V. M. H. Govindarao, G. F. Froment, *Chemical Engineering Science* **1986**, *41*, 533–539.
- [157] V. M. H. Govindarao, K. V. S. Ramrao, *Chemical Engineering Science* **1988**, *43*, 2544–2545.
- [158] V. M. H. Govindarao, M. Subbanna, A. V. S. Rao, K. V. S. Ramrao, *Chemical Engineering Science* **1990**, *45*, 362–364.
- [159] N. J. Mariani, W. I. Salvat, O. M. Martínez, G. F. Barreto, *The Canadian Journal of Chemical Engineering* **2002**, *80*, 186–193.
- [160] V. M. H. Govindarao, K. V. S. Ramrao, A. V. S. Rao, *Chemical Engineering Science* **1992**, *47*, 2105–2109.
- [161] J. Theuerkauf, P. Witt, D. Schwesig, *Powder Technology* **2006**, *165*, 92–99.
- [162] C. G. du Toit, *Powder Technology* **2019**, *342*, 475–485.
- [163] F. Lamarche, C. Leroy, *Computer Physics Communications* **1990**, *59*, 359–369.
- [164] N. J. Mariani, O. M. Martínez, G. F. Barreto, *Chemical Engineering Science* **2001**, *56*, 5693–5707.
- [165] G. E. Mueller, *Powder Technology* **2012**, *229*, 90–96.
- [166] N. J. Mariani, G. D. Mazza, O. M. Martinez, G. F. Barreto, *The Canadian Journal of Chemical Engineering* **2000**, *78*, 1133–1137.
- [167] M. Alonso, M. Satoh, K. Miyanami, *The Canadian Journal of Chemical Engineering* **1992**, *70*, 28–32.

- [168] K. Shinohara, T. Murai, *Journal of the Ceramic Society of Japan* **1993**, *101*, 1369–1373.
- [169] M. Alonso, E. Sainz, F. A. Lopez, K. Shinohara, *Chemical Engineering Science* **1995**, *50*, 1983–1988.
- [170] K. Gotoh, M. Nakagawa, M. Furuuchi, A. Yoshigi, *The Journal of Chemical Physics* **1986**, *85*, 3078–3080.
- [171] J. L. Finney, J. Wallace, *Journal of Non-Crystalline Solids* **1981**, *43*, 165–187.
- [172] H. J. Frost, *Acta Metallurgica* **1982**, *30*, 889–904.
- [173] S. Prager, *Chemical Engineering Science* **1963**, *18*, 227–231.
- [174] E. A. Foumeny, H. A. Moallemi, C. Mcgreavy, J. A. A. Castro, *The Canadian Journal of Chemical Engineering* **1991**, *69*, 1010–1015.
- [175] R. P. Zou, A. B. Yu, *Chemical Engineering Science* **1995**, *50*, 1504–1507.
- [176] C. G. du Toit, *Nuclear Engineering and Design* **2020**, *359*, 110451.
- [177] F. Benyahia, K. E. O'Neill, *Particulate Science and Technology* **2005**, *23*, 169–177.
- [178] E. A. Foumeny, S. Roshani, *Chemical Engineering Science* **1991**, *46*, 2363–2364.
- [179] G. S. Beavers, E. M. Sparrow, D. E. Rodenz, *Journal of Applied Mechanics* **1973**, *40*, 655–660.
- [180] E. A. Foumeny, A. Kulkarni, S. Roshani, A. Vatani, *Applied Thermal Engineering* **1996**, *16*, 195–202.
- [181] A. G. Dixon, *The Canadian Journal of Chemical Engineering* **1988**, *66*, 705–708.
- [182] J. E. Ayer, F. E. Soppet, *Journal of the American Ceramic Society* **1965**, *48*, 180–183.
- [183] R. Jeschar, *Archiv für das Eisenhüttenwesen* **1964**, *35*, 91–108.
- [184] A. M. Ribeiro, P. Neto, C. Pinho, *International Review of Chemical Engineering* **2010**, *2*, 40–46.
- [185] G. Sonntag, *Chemie Ingenieur Technik* **1960**, *32*, 317–329.
- [186] J. Pottbäcker, O. Hinrichsen, *Chemie Ingenieur Technik* **2017**, *89*, 454–458.
- [187] M. Leva, M. Grummer, *Chemical Engineering Progress* **1947**, *43*, 713–718.
- [188] C. McGreavy, E. A. Foumeny, K. H. Javed, *Chemical Engineering Science* **1986**, *41*, 787–797.
- [189] T. C. S. Hsiang, H. W. Haynes, *Chemical Engineering Science* **1977**, *32*, 678–681.
- [190] C. F. Chu, K. M. Ng, *AIChE Journal* **1989**, *35*, 148–158.
- [191] R. M. Fand, R. Thinakaran, *Journal of Fluids Engineering* **1990**, *112*, 84–88.
- [192] R. K. McGeary, *Journal of the American Ceramic Society* **1961**, *44*, 513–522.
- [193] R. C. Raichura, *Experimental Heat Transfer* **1999**, *12*, 309–327.
- [194] A. Montillet, E. Akkari, J. Comiti, *Chemical Engineering and Processing: Process Intensification* **2007**, *46*, 329–333.
- [195] R. M. Fand, M. Sundaram, M. Varahasamy, *Journal of Fluids Engineering* **1993**, *115*, 169–172.
- [196] W. Reichelt, *Chemie Ingenieur Technik* **1972**, *44*, 1068–1071.
- [197] M. Leva, *Chemical Engineering* **1949**, *55*, 115–117.

- [198] D. E. Beasley, J. A. Clark, *International Journal of Heat and Mass Transfer* **1984**, *27*, 1659–1669.
- [199] Z. Guo, Z. Sun, N. Zhang, M. Ding, J. Wen, *Chemical Engineering Science* **2017**, *173*, 578–587.
- [200] Z. Guo, Z. Sun, N. Zhang, X. Cao, M. Ding, *Powder Technology* **2019**, *354*, 842–853.
- [201] P. Carman, *Transactions of the Institution of Chemical Engineers* **1937**, *15*, 150–166.
- [202] M. E. Aerov, PhD thesis, Moscow, **1951**.
- [203] G. F. Froment, K. B. Bischoff, *Chemical Reactor Analysis and Design, 2nd ed. Vol. Wiley New York*, **1979**.
- [204] A. S. Puschnov, *Khim. Neft. Mashinostr.* **2005**, *6*, 10.
- [205] A. S. Puschnov, *Chemical and Petroleum Engineering* **2006**, *42*, 14–17.
- [206] N.-S. Cheng, *Powder Technology* **2011**, *210*, 261–266.
- [207] L. Meng, Y. Jiao, S. Li, *Powder Technology* **2016**, *292*, 176–185.
- [208] S. Torquato, T. M. Truskett, P. G. Debenedetti, *Physical Review Letters* **2000**, *84*, 2064–2067.
- [209] G. Y. Onoda, E. G. Liniger, *Physical Review Letters* **1990**, *64*, 2727–2730.
- [210] W. D. Treadwell, *Chemisches Zentralblatt* **1913**, *1*, 857.
- [211] H. Susskind, W. Becker, *Nature* **1966**, *212*, 1564–1565.
- [212] J. D. Bernal, J. L. Finney, *Nature* **1967**, *214*, 265–266.
- [213] H. Zhao, X. AN, Q. Qian, Y. Wu, L. Wang, W. Li, X. Yang, *Particulate Science and Technology* **2019**, *37*, 251–260.
- [214] Z. Xie, X. An, Y. Wu, L. Wang, Q. Qian, X. Yang, *Powder Technology* **2017**, *317*, 13–22.
- [215] C. X. Li, X. Z. An, R. Y. Yang, R. P. Zou, A. B. Yu, *Powder Technology* **2011**, *208*, 617–622.
- [216] Q. Qian, X. An, Y. Wang, Y. Wu, L. Wang, *Particuology* **2016**, *29*, 120–125.
- [217] S. Debbas, H. Rumpf, *Chemical Engineering Science* **1966**, *21*, 583–608.
- [218] S. Sharma, M. D. Mantle, L. F. Gladden, J. M. Winterbottom, *Chemical Engineering Science* **2001**, *56*, 587–595.
- [219] G. Lumay, N. Vandewalle, *Physical Review E* **2004**, *70*, 051314.
- [220] J. Baker, A. Kudrolli, *Physical Review E* **2010**, *82*, 061304.
- [221] E. Ben-Naim, J. B. Knight, E. R. Nowak, H. M. Jaeger, S. R. Nagel, *Physica D: Nonlinear Phenomena* **1998**, *123*, 380–385.
- [222] E. Caglioti, V. Loreto, H. J. Herrmann, M. Nicodemi, *Physical Review Letters* **1997**, *79*, 1575–1578.
- [223] M. Bazmi, S. H. Hashemabadi, M. Bayat, *Transport in Porous Media* **2013**, *97*, 119–132.
- [224] E. Harris, *Patent*, GB 606867, **1946**.
- [225] J. C. Macrae, W. A. Gray, *The British Journal of Applied Physics* **1961**, *12*, 164–172.
- [226] W. Zhang, K. E. Thompson, A. H. Reed, L. Beenken, *Chemical Engineering Science* **2006**, *61*, 8060–8074.

- [227] G. G. Brown, *Unit Operations*, Wiley, New York, **1950**.
- [228] A. B. Yu, N. Standish, *Powder Technology* **1993**, *74*, 205–213.
- [229] P.-Y. Lanfrey, Z. V. Kuzeljevic, M. P. Dudukovic, *Chemical Engineering Science* **2010**, *65*, 1891–1896.
- [230] N. Chikhi, R. Clavier, J.-P. Laurent, F. Fichot, M. Quintard, *Annals of Nuclear Energy* **2016**, *94*, 422–432.
- [231] R. P. Zou, A. B. Yu, *Powder Technology* **1996**, *88*, 71–79.
- [232] M. Gan, N. Gopinathan, X. Jia, R. A. Williams, *KONA* **2004**, *22*, 82–93.
- [233] F. M. Schaller, M. Neudecker, M. Saadatfar, G. Delaney, K. Mecke, G. E. Schröder-Turk, M. Schröter, *American Institute of Physics Conference Proceedings* **2013**, *1542*, 377–380.
- [234] T. Ikegami, *Journal of the American Ceramic Society* **1996**, *79*, 148–152.
- [235] A. G. Athanassiadis, M. Z. Miskin, P. Kaplan, N. Rodenberg, S. H. Lee, J. Merritt, E. Brown, J. Amend, H. Lipson, H. M. Jaeger, *Soft Matter* **2014**, *10*, 48–59.
- [236] T. Allen, *Particle Size Measurement*, Springer, Dordrecht, **1990**.
- [237] H. Wadell, *The Journal of Geology* **1935**, *43*, 250–280.
- [238] A. B. Yu, R. P. Zou, N. Standish, *Journal of the American Ceramic Society* **1992**, *75*, 2765–2772.
- [239] R. Aoki, M. Suzuki, *Powder Technology* **1971**, *4*, 102–104.
- [240] J. V. Milewski, PhD thesis, Rutgers University, **1973**.
- [241] R. P. Zou, A. B. Yu, *Chemical Engineering Science* **1996**, *51*, 1177–1180.
- [242] J. Warren, R. M. German, P. U. Gummerson, D. A. G. (eds.), *Modern Development in Powder Metallurgy, Vol. 18*, Metal Powder Industries Federation, Princeton, NJ., **1988**.
- [243] J. G. Parkhouse, A. Kelly, *Proceedings of the Royal Society A* **1995**, *451*, 737–746.
- [244] J. Blouwolff, S. Fraden, *Europhysics Letters* **2006**, *76*, 1095–1101.
- [245] O. Rahli, PhD thesis, University of Provence, **1997**.
- [246] M. Novellani, R. Santini, L. Tadrist, *The European Physical Journal B* **2000**, *13*, 571–578.
- [247] K. E. Evans, A. G. Gibson, *Composites Science and Technology* **1986**, *25*, 149–162.
- [248] H. Tangri, Y. Guo, J. S. Curtis, *Powder Technology* **2017**, *317*, 72–82.
- [249] M. Nardin, E. Papirer, J. Schultz, *Powder Technology* **1985**, *44*, 131–140.
- [250] R. Billet, M. Schultes, *Chemical Engineering Research and Design* **1999**, *77*, 498–504.
- [251] D. J. Gunn, *Chemical Engineering Science* **1987**, *42*, 363–373.
- [252] J. Bear, *Dynamic of Fluids in Porous Media*, Elsevier, New York, **1972**.
- [253] O. Umnova, K. Attenborough, K. M. Li, *The Journal of the Acoustical Society of America* **2000**, *107*, 3113–3119.
- [254] M. J. Yun, B. M. Yu, B. Zhang, M. T. Huang, *Chinese Physics Letters* **2005**, *22*, 1464–1467.
- [255] M. Matyka, A. Khalili, Z. Koza, *Physical Review E* **2008**, *78*, 026306.

- [256] W. Sobieski, S. Lipinski, *Technical Sciences* **2017**, *20*, 75–85.
- [257] M. Matyka, Z. Koza, *AIP Conference Proceedings* **2012**, *1453*, 17–22.
- [258] H. Heywood, *Symposium on Particle Size Analysis Institution of Chemical Engineers Supplement* **1947**, *25*, 14.
- [259] W. H. M. Robins, *British Journal of Applied Physics* **1954**, *5*, S82–S85.
- [260] J. K. Beddow, M. Kostelnik, H. H. H. (ed.), *Advances in Powder Metallurgy*, Vol. 4, Plenum Press, New York., **1971**.
- [261] C.-R. Chang, J. K. B. (ed.), M.-J. Yin, A. F. Vetter, G. Butters, D. L. O. Smith, *Particle Characterization in Technology*, Vol. 2, CRC Press, Boca Raton, Fl., **1984**.
- [262] F. Benyahia, *Particulate Science and Technology* **1996**, *14*, 221–237.
- [263] J. Comiti, M. Renaud, *Chemical Engineering Science* **1989**, *44*, 1539–1545.
- [264] C. Xia, K. Zhu, Y. Cao, H. Sun, B. Kou, Y. Wang, *Soft Matter* **2014**, *10*, 990–996.
- [265] Z. Wang, A. Afacan, K. Nandakumar, K. T. Chuang, *Chemical Engineering and Processing: Process Intensification* **2001**, *40*, 209–219.
- [266] W. Man, A. Donev, F. H. Stillinger, M. T. Sullivan, W. B. Russel, D. Heeger, S. Inati, S. Torquato, P. M. Chaikin, *Physical Review Letters* **2005**, *94*, 198001.
- [267] A. Jaoshvili, A. Esakia, M. Porrati, P. M. Chaikin, *Physical Review Letters* **2010**, *104*, 185501.
- [268] G. D. Wehinger, S. T. Kolaczowski, L. Schmalhorst, D. Beton, L. Torkuhl, *Chemical Engineering Journal* **2019**, *373*, 709–719.
- [269] E. A. Foumeny, F. Benyahia, *Heat Recovery Systems and CHP* **1991**, *11*, 127–130.
- [270] C. W. Crawford, O. A. Plumb, *Journal of Fluids Engineering* **1986**, *108*, 343–347.
- [271] A. Donev, I. Cisse, D. Sachs, E. A. Variano, F. H. Stillinger, R. Connelly, S. Torquato, P. M. Chaikin, *Science* **2004**, *303*, 990–993.
- [272] M. Niu, T. Akiyama, R. Takahashi, J. Yagi, *AIChE Journal* **1996**, *42*, 1181–1186.
- [273] N. Zobel, T. Eppinger, F. Behrendt, M. Kraume, *Chemical Engineering Science* **2012**, *71*, 212–219.
- [274] J. D. McWhirter, M. E. Crawford, D. E. Kleins, *Transport in Porous Media* **1997**, *27*, 99–118.
- [275] W. M. Visscher, M. Bolsterli, *Nature* **1972**, *239*, 504–507.
- [276] G. T. Nolan, P. E. Kavanagh, *Powder Technology* **1992**, *72*, 149–155.
- [277] A. Yang, C. T. Miller, L. D. Turcoliver, *Physical Review E* **1996**, *53*, 1516–1524.
- [278] H. P. Zhu, Z. Y. Zhou, R. Y. Yang, A. B. Yu, *Chemical Engineering Science* **2008**, *63*, 5728–5770.
- [279] P. A. Cundall, O. D. L. Strack, *Geotechnique* **1979**, *29*, 47–65.
- [280] G. Lu, J. R. Third, C. R. Müller, *Chemical Engineering Science* **2015**, *127*, 425–465.
- [281] S. Zhao, X. Zhou, W. Liu, C. Lai, *Particuology* **2015**, *23*, 109–117.
- [282] M. Kodam, R. Bharadwaj, J. Curtis, B. Hancock, C. Wassgren, *Chemical Engineering Science* **2010**, *65*, 5852–5862.

- [283] M. Kodam, R. Bharadwaj, J. Curtis, B. Hancock, C. Wassgren, *Chemical Engineering Science* **2010**, *65*, 5863–5871.
- [284] Y. Guo, C. Wassgren, W. Ketterhagen, B. Hancock, J. Curtis, *Powder Technology* **2012**, *228*, 193–198.
- [285] J. Zhao, S. Li, P. Lu, L. Meng, T. Li, H. Zhu, *Powder Technology* **2011**, *214*, 500–505.
- [286] Y. Wu, X. AN, A. B. Yu, *Powder Technology* **2017**, *314*, 89–101.
- [287] G. D. Wehinger, C. Fütterer, M. Kraume, *Industrial & Engineering Chemistry Research* **2017**, *56*, 87–99.
- [288] M. V. Tabib, S. T. Johansen, S. Amini, *Industrial & Engineering Chemistry Research* **2013**, *52*, 12041–12058.
- [289] S. Li, J. Zhao, P. Lu, Y. Xie, *Chinese Science Bulletin* **2010**, *55*, 114–119.
- [290] X. Garcia, L. T. Akanji, M. J. Blunt, S. K. Matthai, J. P. Latham, *Physical Review E* **2009**, *80*, 021304.
- [291] R. Caulkin, W. Tian, M. Pasha, A. Hassanpour, X. Jia, *Computers and Chemical Engineering* **2015**, *76*, 160–169.
- [292] R. A. Williams, X. Jia, *Particulate Science and Technology* **2003**, *21*, 195–205.
- [293] X. Jia, M. Gan, R. A. Williams, D. Rhodes, *Powder Technology* **2007**, *174*, 10–13.
- [294] X. Jia, R. A. Williams, *Powder Technology* **2001**, *120*, 175–186.
- [295] A. C. J. de Korte, H. J. H. Brouwers, *Powder Technology* **2013**, *233*, 319–324.
- [296] B. Partopour, A. G. Dixon, *Powder Technology* **2017**, *322*, 258–272.
- [297] G. Boccardo, F. Augier, Y. Haroun, D. Ferré, D. Marchisio, *Chemical Engineering Journal* **2015**, *279*, 809–820.
- [298] J. Fernengel, J. von Seckendorff, O. Hinrichsen, *Proceedings of the 28th European Symposium on Computer Aided Process Engineering* **2018**, 97–102.
- [299] S. Fleischlen, G. D. Wehinger, *ChemEngineering* **2019**, *3*, 52.
- [300] T. Eppinger, K. Seidler, M. Kraume, *Chemical Engineering Journal* **2011**, *166*, 324–331.
- [301] L. W. Rong, K. J. Dong, A. B. Yu, *Chemical Engineering Science* **2013**, *99*, 44–58.
- [302] R. K. Reddy, J. B. Joshi, *Particology* **2010**, *8*, 37–43.
- [303] A. Pavlisic, R. Ceglar, A. Pohar, B. Likozar, *Powder Technology* **2018**, *328*, 130–139.
- [304] R. Mohanty, S. Mohanty, B. K. Mishra, *Journal of the Taiwan Institute of Chemical Engineers* **2016**, *63*, 71–80.
- [305] M. Marek, *Chemical Engineering Science* **2017**, *161*, 382–393.
- [306] P. Magnico, *Chemical Engineering Science* **2003**, *58*, 5005–5024.
- [307] S. Khirevich, A. Hölzel, D. Hlushkou, U. Tallarek, *Analytical Chemistry* **2007**, *79*, 9340–9349.
- [308] L. He, D. K. Tafti, K. Nagendra, *Powder Technology* **2017**, *313*, 332–343.

- [309] H. Freund, T. Zeiser, F. Huber, E. Klemm, G. Brenner, F. Durst, G. Emig, *Chemical Engineering Science* **2003**, *58*, 903–910.
- [310] S. Das, N. G. Deen, J. A. M. Kuipers, *Chemical Engineering Journal* **2018**, *334*, 741–759.
- [311] D. Coelho, J.-F. Thovet, P. M. Adler, *Physical Review E* **1997**, *55*, 1959–1978.
- [312] M. Zhang, H. Dong, Z. Geng, *Chemical Engineering Research and Design* **2018**, *132*, 149–161.
- [313] M. T. Zambon, D. A. Asensio, G. F. Barreta, G. D. Mazza, *Industrial & Engineering Chemistry Research* **2014**, *53*, 19052–19061.
- [314] M. Behnam, A. G. Dixon, M. Nijemeisland, E. H. Stitt, *Industrial & Engineering Chemistry Research* **2013**, *52*, 15244–15261.
- [315] M. E. Taskin, A. G. Dixon, E. H. Stitt, *Numerical Heat Transfer Part A: Applications* **2007**, *52*, 203–218.
- [316] A. Singhal, S. Cloete, S. Radl, R. Quinta-Ferreira, S. Amini, *Chemical Engineering Science* **2017**, *172*, 1–12.
- [317] S. J. P. Romkes, F. M. Dautzenberg, C. M. van den Bleek, H. P. A. Calis, *Chemical Engineering Journal* **2003**, *96*, 3–13.
- [318] S. A. Logtenberg, M. Nijemeisland, A. G. Dixon, *Chemical Engineering Science* **1999**, *54*, 2433–2439.
- [319] Y. Dong, B. Sosna, O. Korup, F. Rosowski, R. Horn, *Chemical Engineering Journal* **2017**, *317*, 204–214.
- [320] A. G. Dixon, G. Walls, H. Stanness, M. Nijemeisland, E. H. Stitt, *Chemical Engineering Journal* **2012**, *200-202*, 344–356.
- [321] G. D. Wehinger, T. Eppinger, M. Kraume, *Chemical Engineering Science* **2015**, *122*, 197–209.
- [322] G. D. Wehinger, T. Eppinger, M. Kraume, *Chemie Ingenieur Technik* **2015**, *87*, 734–745.
- [323] M. Behnam, A. G. Dixon, P. M. Wright, M. Nijemeisland, E. H. Stitt, *Chemical Engineering Journal* **2012**, *s 207-208*, 690–700.
- [324] A. G. Dixon, M. E. Taskin, M. Nijemeisland, E. H. Stitt, *Industrial & Engineering Chemistry Research* **2010**, *49*, 9012–9025.
- [325] A. G. Dixon, *Chemical Engineering Research and Design* **2014**, *92*, 1279–1295.
- [326] B. Partopour, A. G. Dixon, *Computers & Chemical Engineering* **2016**, *88*, 126–134.
- [327] A. H. Mahmoudi, F. Hoffmann, B. Peters, X. Besseron, *International Communications in Heat and Mass Transfer* **2016**, *71*, 20–34.
- [328] G. M. Karthik, V. V. Buwa, *AIChE Journal* **2017**, *63*, 366–377.
- [329] A. G. Dixon, J. Boudreau, A. Rocheleau, A. Troupel, M. E. Taskin, M. Nijemeisland, E. H. Stitt, *Industrial & Engineering Chemistry Research* **2012**, *51*, 15839–15854.
- [330] K. M. Brunner, H. D. Perez, R. P. S. Peguin, J. C. Duncan, L. D. Harrison, C. H. Bartholomew, W. C. Hecker, *Industrial & Engineering Chemistry Research* **2015**, *54*, 2902–2909.
- [331] F. Augier, F. Idoux, J. Y. Delenne, *Chemical Engineering Science* **2010**, *65*, 1055–1064.

- [332] G. E. Mueller, *Powder Technology* **2005**, *159*, 105–110.
- [333] G. W. Delaney, P. W. Cleary, *Europhysics Letters* **2010**, *89*, 34002.
- [334] Z.-Y. Zhou, R.-P. Zou, D. Pinson, A.-B. Yu, *Industrial & Engineering Chemistry Research* **2011**, *50*, 9787–9798.
- [335] W. Nan, Y. Wang, Y. Liu, H. Tang, *Advanced Powder Technology* **2015**, *26*, 527–536.
- [336] E. M. Moghaddam, E. A. Foumeny, A. I. Stankiewicz, J. T. Padding, *Industrial & Engineering Chemistry Research* **2018**, *57*, 14988–15007.
- [337] R. Guises, J. Xiang, J.-P. Latham, A. Munjiza, *Granular Matter* **2009**, *11*, 281–292.
- [338] Z. Yan, S. K. Wilkinson, E. H. Stitt, M. Marigo, *Computational Particle Mechanics* **2015**, *2*, 283–299.
- [339] M. Marigo, E. H. Stitt, *KONA Powder and Particle Journal* **2015**, *32*, 236–252.
- [340] Q. Qian, L. Wang, X. An, Y. Wu, J. Wang, H. Zhao, X. Yang, *Powder Technology* **2018**, *325*, 151–160.
- [341] P. Philippe, D. Bideau, *Physical Review E* **2001**, *63*, 051304.
- [342] L. Pournin, M. Weber, M. Tsukahara, J.-A. Ferrez, M. Ramaioli, T. M. Liebling, *Granular Matter* **2005**, *7*, 119–126.
- [343] D. Gou, X. An, X. Yang, H. Fu, H. Zhang, *Powder Technology* **2017**, *322*, 177–184.
- [344] Z. Xie, X. An, X. Yang, C. Li, Y. Shen, *Powder Technology* **2019**, *344*, 514–524.
- [345] J. Zhao, S. Li, R. Zou, A. Yu, *Soft Matter* **2012**, *8*, 1003–1009.
- [346] A. Wouterse, S. Luding, A. P. Philipse, *Granular Matter* **2009**, *11*, 169–177.
- [347] A. Wouterse, S. R. Williams, A. P. Philipse, *Journal of Physics: Condensed Matter* **2007**, *19*, 406215.
- [348] S. R. Williams, A. P. Philipse, *Physical Review E* **2003**, *67*, 051301.
- [349] J. D. Sherwood, *Journal of Physics A: Mathematical and General* **1997**, *30*, L839–L843.
- [350] W. I. Salvat, N. J. Mariani, G. F. Barreto, O. M. Martínez, *Catalysis Today* **2005**, *107-108*, 513–519.
- [351] P. L. Spedding, R. M. Spencer, *Computers & Chemical Engineering* **1995**, *19*, 43–73.
- [352] K. Schnitzlein, *Chemical Engineering Science* **2001**, *56*, 579–585.
- [353] S. C. Reyes, E. Iglesia, *Chemical Engineering Science* **1991**, *46*, 1089–1099.
- [354] G. E. Mueller, *Powder Technology* **1997**, *92*, 179–183.
- [355] B. Gong, Y. Feng, H. Liao, Y. Liu, X. Wang, K. Feng, *Fusion Engineering and Design* **2017**, *121*, 256–264.
- [356] Q. Qian, X. AN, H. Zhao, K. Dong, X. Yang, *Powder Technology* **2019**, *343*, 79–86.
- [357] S. Zhao, N. Zhang, X. Zhou, L. Zhang, *Powder Technology* **2017**, *310*, 175–186.
- [358] J. Zhao, S. Li, W. Jin, X. Zhou, *Physical Review E* **2012**, *86*, 031307.
- [359] J. Lathan, Y. Lu, A. Munjiza, *Geotechnique* **2001**, *51*, 871–879.

- [360] S. Li, J. Zhao, X. Zhou, *Chinese Physics Letters* **2008**, *25*, 1724–1725.
- [361] P. Niegodajew, M. Marek, *Powder Technology* **2016**, *297*, 193–201.
- [362] W. Nan, Y. Wang, Y. Ge, J. Wang, *Powder Technology* **2014**, *261*, 210–218.
- [363] S. C. McGrother, D. C. Williamson, G. Jackson, *The Journal of Chemical Physics* **1996**, *104*, 6755–6771.
- [364] L. Liu, Z. Li, Y. Jiao, S. Li, *Soft Matter* **2017**, *13*, 748–757.
- [365] A. V. Kyrylyuk, A. P. Philipse, *Physica Status Solidi A* **2011**, *208*, 2299–2302.
- [366] Y. Jiao, S. Torquato, *Physical Review E* **2011**, *84*, 041309.
- [367] Y. Jiao, F. H. Stillinger, S. Torquato, *Physical Review E* **2010**, *81*, 041304.
- [368] J. Q. Gan, A. B. You, Z. Y. Zhou, *Chemical Engineering Science* **2016**, *156*, 64–76.
- [369] K. E. Evans, M. D. Ferrar, *Journal of Physics D: Applied Physics* **1989**, *22*, 354–360.
- [370] K. Dong, C. Wang, A. Yu, *Chemical Engineering Science* **2015**, *126*, 500–516.
- [371] K. Desmond, S. V. Franklin, *Physical Review E* **2006**, *73*, 031306.
- [372] C. Ferreiro-Córdova, J. S. van Duijneveldt, *Journal of Chemical & Engineering Data* **2014**, *59*, 3055–3060.
- [373] P. M. Chaikin, A. Donev, W. Man, F. H. Stillinger, S. Torquato, *Industrial & Engineering Chemistry Research* **2006**, *45*, 6960–6965.
- [374] P. Bolhuis, D. Frenkel, *The Journal of Chemical Physics* **1997**, *106*, 666–687.
- [375] R. Blaak, D. Frenkel, B. M. Mulder, *The Journal of Chemical Physics* **1999**, *110*, 11652–11659.
- [376] A. Baule, R. Mari, L. Bo, L. Portal, H. A. Makse, *Nature Communications* **2013**, *4*, 2194.
- [377] M. Bargiel, *Computational Science - ICCS* **2008**, 126–135.
- [378] A. V. Kyrylyuk, M. A. van de Haar, L. Rossi, A. Wouterse, A. P. Philipse, *Soft Matter* **2011**, *7*, 1671–1674.
- [379] C. R. A. Abreu, F. W. Tavares, M. Castier, *Powder Technology* **2003**, *134*, 167–180.
- [380] J. O. Freeman, S. Peterson, C. Cao, Y. Wang, S. V. Franklin, E. R. Weeks, *Granular Matter* **2019**, *21*, 84.
- [381] Y. Kallus, *Soft Matter* **2016**, *12*, 4123–4128.
- [382] J. Q. Gan, Z. Y. Zhou, A. B. Yu, *Powder Technology* **2017**, *320*, 610–624.
- [383] X. L. Deng, R. N. Davé, *Granular Matter* **2013**, *15*, 401–415.
- [384] F. Dorai, C. M. Teixeira, M. Rolland, E. Climent, M. Marcoux, A. Wachs, *Chemical Engineering Science* **2015**, *180-192*, 129.

3 Experimental Study on the Influence of Filling Method and Particle Material on the Packed-Bed Porosity

Abstract

The reliable prediction of the pressure drop of packed beds requires an accurate estimation of the packed-bed porosity as its error propagation multiplies the occurring errors by a factor of about four. The commonly used correlations to determine porosity depend only on the tube to particle diameter ratio. To improve accuracy, the influence of the filling method and of material properties, in particular surface roughness, density, and restitution coefficient are investigated for random packings of spheres in cylindrical confining walls. Furthermore, statistical methods are applied to identify interconnecting effects between these influencing parameters.

This article was published in:

Chemie Ingenieur Technik, 89, J. Pottbäcker, O. Hinrichsen, Experimental Study on the Influence of Filling Method and Particle Material on the Packed-Bed Porosity, 454-458, Copyright Wiley (2017). DOI: 10.1002/cite.201600151.

Reprint Permission:

If you are the author of a published Wiley article, you have the right to reuse the full text of your published article as part of your thesis or dissertation. In this situation, you do not need to request permission from Wiley for this use.

3.1 Introduction

For the dimensioning of fixed-bed reactors it is essential that fluid dynamic characteristics, especially the pressure drop as well as porosity and the resulting velocity profiles, are predictable and reproducible. There exists a variety of correlations for the prediction of the pressure drop in a fixed bed. A collection can be found by Pešić et al. [1], according to which the pressure drop is influenced by the characteristic diameter, the diameter ratio of the packing elements, the filling height, the superficial velocity, the type of the fluid used, and the porosity (ε) of the bed. In this context, the porosity is the void fraction of the packed bed. Except this global porosity all other parameters can generally be measured or determined in an accuracy sufficient for the prediction of the pressure drop. Unfortunately, the prediction of the porosity of an arbitrary packed bed is often unsatisfactory. Again, numerous correlations for packings of spheres in cylindrical confining walls exist [2–8] though most of them are valid only for a specific set of experimental conditions. The error in pressure drop resulting solely from an error in porosity can be estimated according to error propagation, which is displayed in Eq. (3.1) [9].

$$\left| \frac{\frac{\partial(\Delta P)}{\partial \varepsilon}}{\left(\frac{\Delta P}{\Delta \varepsilon}\right)} \right| = \frac{3 - n \cdot \varepsilon}{1 - \varepsilon} \cdot \frac{\Delta \varepsilon}{\varepsilon} \quad (3.1)$$

Herein, n is 1 for laminar flow and 2 for turbulent flow. For laminar flow ($n = 1$) and a mean porosity of 0.4, a 2.5 % error in the porosity yields about a 10 % error in pressure drop. This is a multiplication by factor four from porosity to pressure drop errors.

The porosity itself is mainly influenced by the tube to particle diameter ratio, the packing mode, the shape as well as the size distribution of the particles and the roughness of the particles surface [5]. Further publications indicate an influence of the particle material density [10], the shape of the container [11] and the filling height to particle diameter ratio, called thickness effect [8, 12].

The aim of the present work is not to develop a new correlation competing already existing ones but to investigate the whole set of parameters including those which are normally kept constant, namely the material properties, in order to develop a much broader guidance to a more predictable and reproducible estimation of the packed-bed porosity.

3.1.1 Wall Effect

It is well known that the local porosity in the packing increases in the near wall region (wall effect). For large tube to particle diameter ratios $\lambda = D/d_p$, this effect of the near wall region plays a minor role on the global porosity, whereas for packed beds of lower λ , this results in an overall increase of the global porosity. Plotting the global porosity versus $\lambda > 2$ gives a decreasing function approaching a constant infinite value ε_{inf} for higher tube to particle diameter ratios [2–8]. For this work, the wall effect correlation

according to Benyahia and O'Neill [7], which is valid for tube to particle diameter ratios between 1.5 and 50, is chosen.

$$\varepsilon = \varepsilon_{\text{inf}} + \frac{1.74}{(\lambda + 1.14)^2} \quad (3.2)$$

It is known that ε_{inf} has to be adjusted to the packing mode used. Benyahia and O'Neill [7] give a correlation for the additional influence of sphericity and de Klerk [5] predicts an influence of surface roughness, without giving further evidence.

3.1.2 Packing Mode

According to Haughey and Beveridge [2, 5] the following packing modes are distinguished for mono-sized spheres: very loose packing ($\varepsilon_{\text{inf}} \geq 0.44$), loose packing ($\varepsilon_{\text{inf}} \geq 0.40$), poured packing ($\varepsilon_{\text{inf}} \geq 0.375$) and densed packing ($\varepsilon_{\text{inf}} \geq 0.36$). The random close packing (RCP) represents the smallest porosity that can be achieved under absence of a global order. In case of spheres this porosity is just below 0.36. The listed packing modes can be achieved by applying respective packing methods: settling down from a fluidized bed, dropping the particles as a loose mass, pouring of particles, and densification of the packing via subsequent vibration, tapping, or shaking. In order to obtain reproducible data it is essential to use certain packing aids such as funnels of specific diameter, slides, vibratory plates, particle meshes as used for snowstorm filling, or specific packing machines [10, 13]. It is desired to keep the relative pressure drop error in terms of reproducibility below 5% [10] by using such packing aids. This correlates to a relative porosity error of about 1%, referring to Eq. (3.1). Unfortunately some packing aids cannot fulfill this requirement [10].

3.1.3 Particle Material

The effect of the particle material is often addressed theoretically though hardly determined experimentally. Generally, the influence of the particle material was not fully clarified yet. On the one hand, e.g., McGeary [14] states that material and shape have no effect on the resulting porosity. On the other hand, Theuerkauf et al. [15] show by DEM simulations that changing the friction factor results in a change of porosity. In this case lowering the friction leads to lower overall porosities with deviations of 0.04, equaling a relative error of 10%. Surface properties such as friction and restitution coefficient are listed by Yang [12] as influencing material parameters without experimental validation.

3.2 Experimental

High precision spheres made of steel with diameter $d = 3$ to 10 mm, aluminum (ALU) with $d = 4$ mm, polyoxymethylene (POM) with $d = 4$ mm and glass with $d = 4$ mm were obtained from KGM Kugelfabrik

GmbH & Co. KG, Germany and VTLG Europe Ltd., Germany. Polyamide (PA) spheres with $d = 3, 4,$ and 5 mm were printed with a Laser Sinter Printer (EOS FORMIGA). The exact particle mass was determined with a sample of 1000 particles for each material and the deviation was less than 0.1% . The density and its deviation, which was about 0.5% , was determined using a pycnometer with a volume of 50 ml as the mean of ten measurements of 50 particles each. Circular plexiglass tubes with an inner diameter of $D = 15$ to 55 mm and a constant height of $H = 100$ mm were used as container. The exact volumes of the tubes were determined by filling them up with a known amount of water. The mean of three measurements was noted. The filling was performed with three different methods using the following packing aids: I) pouring the particles as fast as possible using a funnel with an outlet diameter of 20 mm; II) applying a filling machine consisting of a horizontal tube and a vibrating motor to move the particles slowly to an outlet funnel leading to the plexiglass tubes whereby the filling rate was kept constant at about 500 s m^{-1} filling height; III) utilization of a vibratory plate at constant amplitude to dense the packing produced by slow pouring. The porosity was determined gravimetrically as the water displacement technique [6] was not applicable due to the small density of polyamide. Experiments with the filling machine were performed three times each, experiments with pouring and densification ten times each.

3.3 Results and Discussion

In a first step, a design of experiment (D.o.E) was set up in order to investigate the influences of different parameters on the porosity of mono-sized sphere packings in general. These parameters were the material (factor A), the filling method (factor B) and the size ratio (factor C) of the packing elements. For each parameter, two levels were chosen: rough polyamide vs smooth steel for factor A, pouring vs densification for the filling method and $\lambda = 5$ vs $\lambda = 7$ as diameter ratio. The D.o.E was performed as a fully factorial

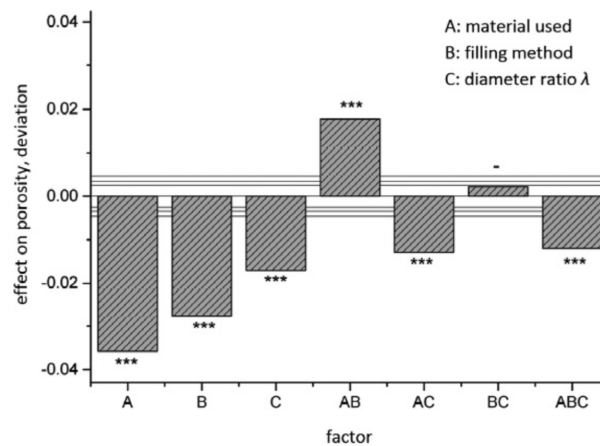


Figure 3.1: Effects of material (A), filling method (B) and diameter ratio (C) on the porosity of a packed bed of spheres.

design, with four runs for each parameter combination, in a randomized form. The results, as displayed in Fig. 3.1, show a considerably large influence of material, a smaller effect for the filling method, and an even smaller effect for the diameter ratio λ .

Furthermore interacting effects between material and filling method (AB), material and diameter ratio (BC) as well as between all three parameters (ABC) could be found. The compilation and evaluation of the D.o.E were performed with Minitab[®] 17 software, the corrected R^2 was determined to be 0.956.

In the second step an in depth parameter study of all three parameter pairs (AB, AC, and BC) was performed.

3.3.1 Diameter Ratio λ and Filling Method

Initially, reproducibility measurements with all three filling methods were performed. Each data point with a specific tube to particle diameter ratio was performed ten times (three in case of machine filling) to gain a mean porosity $\bar{\varepsilon}$. The relative errors ($\Delta\varepsilon/\bar{\varepsilon}$) for each data point were averaged over all data points measured. Depending on the available particle sizes for each material from 27 (aluminum, machine filling) to 970 (steel, pouring) measurements were summed up in this value. The mean relative error of pouring was determined to be about 1.5 %, the filling machine caused an error of about 0.25 % and densification was found to have a mean error of 2 %. This error was slightly dependent on the material used.

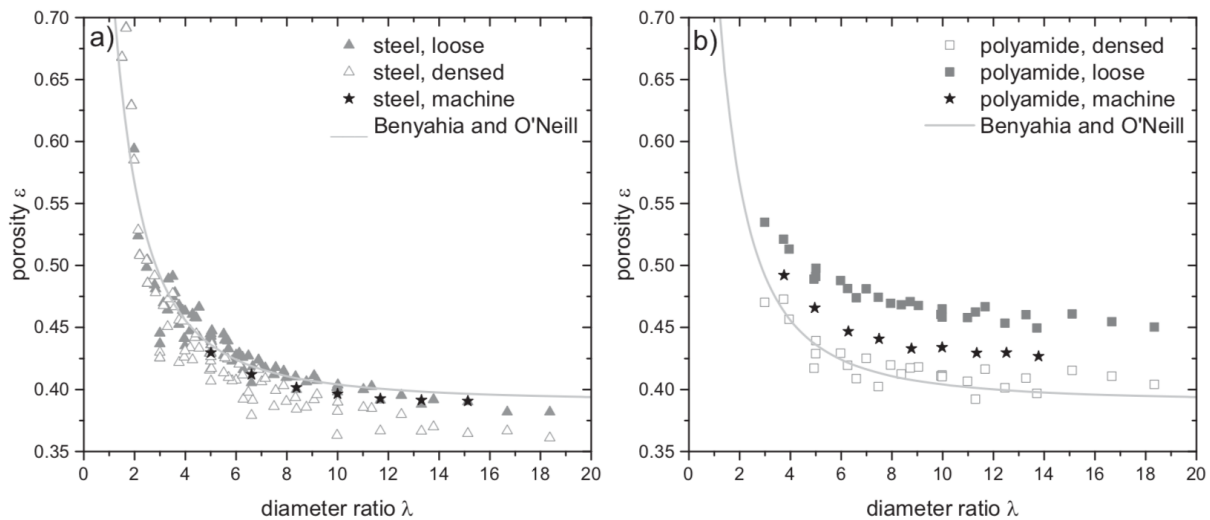


Figure 3.2: Experimental results of the porosity of steel (a) and polyamide (b) spheres varying filling method and diameter ratio. The correlation of Benyahia and O'Neill [7] is given for comparison.

Fig.3.2 exhibits the effect of the filling method for a range of diameter ratios and for two materials, namely for polyamide (Fig. 3.2b) and for steel (Fig. 3.2a). For comparison the correlation of Benyahia and O'Neill is shown.

It can be observed that the absolute values of porosity change with the filling method, though the decline appears to be similar. The obtained data was fitted to the correlation of Benyahia and O'Neill with ε_{inf} being the only fitting parameter.

Table 3.1: Results of fitting data to the correlation of Benyahia and O'Neill [7] for different filling methods.

Filling method	Fig. 3.2b: polyamide			Fig. 3.2a: steel		
	ε_{inf} [-]	corr. R^2 [-]	SSE [-]	ε_{inf} [-]	corr. R^2 [-]	SSE [-]
Pouring	0.448	0.947	0.0010	0.390	0.898	0.0022
Machine	0.418	0.992	0.0006	0.383	0.997	0.0003
Densification	0.393	0.730	0.0020	0.374	0.900	0.0024

The results are displayed in Tab. 3.1, showing a good fit in case of machine filling for both materials and notable deviations in case of pouring and densification. Densification shows the highest errors, which is due to the fact that for certain measurements very ordered packing structures could be gained, resulting in low porosities. This phenomenon was seen before [5].

3.3.2 Filling Method and Material

Varying material and filling method together, it can be found that the difference between the infinite values of the different filling methods change with the material. In case of steel, as can be noticed in Fig. 3.2a and Tab. 3.1, this difference between poured and densified packing is about 0.016. Furthermore, it can be seen that there is hardly any difference between machine filling and pouring as methods. For the polyamide sample, this difference is much higher, namely 0.055, and the machine filling definitely shows an influence on the infinite porosity. This leads to the assumption that the influence of the filling method on the generated packing has different impacts depending on the material. This correlating effect between factor A, material, and factor B, filling method, was predicted in the D.o.E, and can thus be confirmed by experiment.

3.3.3 Material and Diameter Ratio λ

Testing the influence of the particle material, six different materials were tested with machine filling as filling method. It has to be understood that polyamide spheres were very rough having a mean surface roughness depth $R_z = 50 \mu\text{m}$. The sample $\text{steel}_{\text{rust}}$ is exactly the same material as steel, with the only difference that due to small rust production on its surface the roughness was increased. All other samples have smooth surfaces. The material densities are depicted in Tab. 3.2. By comparing the two steel and plastic samples in Fig. 3.3, it can be deduced that the surface roughness seems to have a distinct effect on the porosity by increasing its value significantly.

In terms of density, a general trend with low densities having a tendency to result in higher porosities can be observed. Apparent abnormalities to this trend can be noticed in terms of aluminum, with a porosity much higher than expected, and glass, with a porosity rather less than expected. It is thus assumed that at least a third influencing material parameter overlaps with density and surface roughness. This parameter

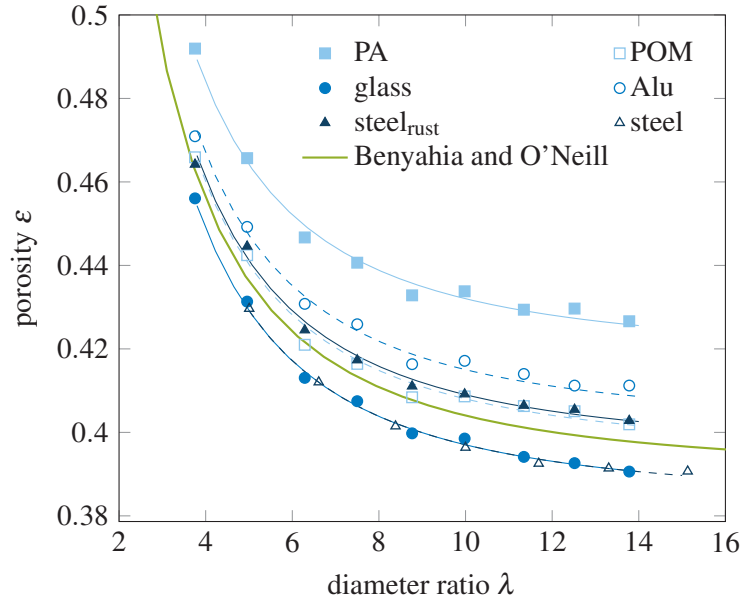


Figure 3.3: Correlation between the material and the diameter ratio on the porosity of a packed bed of spheres using machine filling and the correlation of Benyahia and O'Neill [7] for fitting.

Table 3.2: Properties and results of fitting data to the correlation Benyahia and O'Neill [7] for different materials.

Material	Density [kgm^{-3}]	Restitution k [-] [16–18]	ε_{inf} [-]	corr. R^2 [-]	SSE [-]
Polyamide (PA)	975	n.a.	0.418	0.997	0.0006
Polyoxymethylene (POM)	1354	0.9	0.394	0.989	0.0007
Glass	2550	0.94	0.383	0.998	0.0003
Aluminum	2710	0.6	0.401	0.990	0.0007
Steel (rust)	7780	0.8	0.395	0.992	0.0006
Steel	7780	0.8	0.383	0.997	0.0003

is thought to be the restitution coefficient k proposed by Yang [12]. Using the machine as filling device, single balls fall on top of an already settled packing of balls. In case of high restitution coefficients, the falling ball will make the already settled balls move again, allowing them to find a new, maybe better position. Meanwhile, a ball with a small restitution coefficient falling onto already existing balls will not make them move at all as kinetic energy is transferred to inner energy. Own experiments suppose the following order of restitution coefficients, which are in accordance with literature values as displayed in Tab. 3.2.

$$k_{\text{ALU}} < k_{\text{PA}} < k_{\text{steel}} < k_{\text{POM}} < k_{\text{glass}}$$

It is not known, whether a rusted surface has an impact on the restitution coefficient of steel balls. Own experiments suggest a rather small impact if any. The extraordinary low value for aluminum and high value for glass might explain the deviation to the expected values as described above. The interaction between diameter ratio and material is evaluated by fitting the correlation of Benyahia and O'Neill to the data of Fig. 3.3. Accordingly, their correlation is able to describe the wall effect adequately, only the infinite values have to be adopted to the materials used. The obtained results are displayed in Tab. 3.2.

3.4 Conclusion

In terms of porosity of a packed bed, numerous correlations describing the wall effect only as a function of the tube to particle diameter ratio exist. However, for a general prediction of the packed-bed porosity, these correlations are not sufficient, as they neglect other influencing parameter such as shape [7]. It was found that additional to the influence of the shape, the material, in particular, the roughness, the density, and the restitution coefficient of the packing elements cannot be neglected, nor can the filling method. Both parameters in combination show a huge interconnecting effect as illustrated in D.o.E and experimental studies. The wall effect itself can be well described by the decreasing function of the existing correlation of Benyahia and O'Neill, though the infinite porosity has to be adjusted to the specific cases. According to error propagation, the deviation of the experimental data of the polyamide sample from the correlation in case of pouring, which is 0.06, would, in case of turbulent flow, lead to an error of pressure drop of about 56 %. In case of machine filling, the deviation of 0.026 leads to an error of 24 %. In order to avoid these large errors in the estimation of pressure drop it is therefore not sufficient to only consider the diameter ratio in the determination of porosity. Unfortunately, a specific correlation for the influence of material and filling methods on infinite porosity could not be formulated yet, as material properties overlap and cannot be varied apart from each other in experiment. Numerical methods for packing generation and simulation of fluid dynamics, heat and mass transfer as, e.g., described by Boccardo et al. [19] are therefore needed and currently investigated. Further parameters, not discussed in this paper, that could influence the porosity of a sphere packing are the tube shape, the tube material especially the surface properties, and the size distribution of the particles [10, 12]. It is to be understood, that in this study spheres of nearly ideal sphericity were used and depending on the manufacturing process of the packing particles, size distributions may occur.

Nomenklatur

Latin Symbols

d	sphere diameter	m
d_p	particle diameter	m
D	diameter of tube	m
H	height of tube	m
k	restitution coefficient	-
ΔP	pressure drop	Pa
R_z	mean surface roughness depth	m

Greek Symbols

ε	porosity	-
ε_{inf}	porosity with $\lambda \rightarrow \infty$	-
λ	tube to particle diameter ratio	-

Abbreviations

ALU	aluminum
D.o.E.	design of experiment
PA	polyamide
POM	polyoxymethylene
RCP	random close packing
SSE	sum of squares due to error

References

- [1] R. Pešić, T. K. Radoičić, N. Bošković-Vragolović, Z. Arsenijević, Ž. Grbavčić, *Chemical Industry & Chemical Engineering Quarterly* **2015**, *21*, 419–427.
- [2] D. P. Haughey, G. S. G. Beveridge, *The Canadian Journal of Chemical Engineering* **1969**, *47*, 130–140.
- [3] R. Jeschar, *Archiv für das Eisenhüttenwesen* **1964**, *35*, 91–108.
- [4] G. F. Froment, K. B. Bischoff, *Chemical Reactor Analysis and Design, 2nd ed. Vol.* Wiley New York, **1979**.
- [5] A. de Klerk, *AIChE Journal* **2003**, *49*, 2022–2029.
- [6] A. G. Dixon, *The Canadian Journal of Chemical Engineering* **1988**, *66*, 705–708.
- [7] F. Benyahia, K. E. O'Neill, *Particulate Science and Technology* **2005**, *23*, 169–177.
- [8] E. A. Foumeny, H. A. Moallemi, C. Mcgreavy, J. A. A. Castro, *The Canadian Journal of Chemical Engineering* **1991**, *69*, 1010–1015.
- [9] T. Zeiser, PhD thesis, Universität Erlangen-Nürnberg, **2008**.
- [10] R. Rutgers, *Nature* **1962**, *193*, 465–466.
- [11] G. D. Scott, *Nature* **1960**, *188*, 908–909.
- [12] W.-C. Yang, *Handbook of Fluidization and Fluid-Particle Systems, 1st ed.* CRC Press, Boca Raton, FL, **2003**.
- [13] S. Afandizadeh, E. A. Foumeny, *Applied Thermal Engineering* **2001**, *21*, 669–682.
- [14] R. K. McGeary, *Journal of the American Ceramic Society* **1961**, *44*, 513–522.
- [15] J. Theuerkauf, P. Witt, D. Schwesig, *Powder Technology* **2006**, *165*, 92–99.
- [16] V. Scherer, Untersuchung von Schürung und Mischung auf Rostsystemen, tech. rep., AiF-Projekt 15061, Ruhr-Universität Bochum, Germany, **2010**.
- [17] P. Wriggers, U. Nackenhorst, S. Beuermann, H. Spiess, S. Löhnert, *Technische Mechanik kompakt: Starrkörperstatik-Elastostatik-Kinetik*, 2nd ed., Teubner, Leipzig, **2006**.
- [18] O. V. Kim, P. F. Dunn, *Journal of Aerosol Science* **2007**, *38*, 532–549.
- [19] G. Boccardo, F. Augier, Y. Haroun, D. Ferré, D. Marchisio, *Chemical Engineering Journal* **2015**, *279*, 809–820.

4 Experimental Characterization of Random Packed Spheres, Cylinders and Rings, and their Influence on Pressure Drop

Abstract

The reliable prediction of the pressure drop of packed-beds requires an accurate understanding of the packing characteristics. Therefore, packings of spheres, cylinders and hollow cylinders are studied: firstly, developing a reproducible and easily achievable packing generation method by single dropping; secondly, evaluating and correlating the average bed porosity as a function of the tube-to-particle diameter ratio λ , the diameter-to-height aspect ratio and the inner-to-outer diameter aspect ratio. The packed-bed pressure drop was measured, thoroughly evaluating the influence of particle filling speed, the error propagation from porosity deviations resulting in a multiplication factor of 3.1-3.9 for spheres and 2.4-3.0 for cylinders depending on material characteristics, and the influence of particle surface roughness, with rough particles increasing the packing friction by 17.5%. A novel Carman-type pressure drop correlation for smooth equilateral cylinder packings valid for $Re_p = 10-3000$ is described.

This article was published in:

Chemical Engineering Science, 222, J. von Seckendorff, N. Szesni, R. Fischer, O. Hinrichsen, Experimental characterization of random packed spheres, cylinders and rings, and their influence on pressure drop, 115644, Copyright Elsevier (2020). DOI: 10.1016/j.ces.2020.115644.

Reprint Permission:

As an Elsevier journal author, you have the right to Include the article in a thesis or dissertation (provided that this is not to be published commercially) whether in full or in part, subject to proper acknowledgment; see [the Copyright page](#) for more information. No written permission from Elsevier is necessary.

This right extends to the posting of your thesis to your university's repository provided that if you include the published journal article, it is embedded in your thesis and not separately downloadable.

4.1 Introduction

Random packings of predominantly spherical but also cylindrical particles are deployed in a large range of industrial applications. Thereby, random packed-beds may be investigated in regard to structural characteristics, for instance, the void distribution [1, 2], single- and multi-phase flow aspects [3], the extent of pressure loss along the bed height [4], axial and radial dispersion effects [5] in common with inter- and intra-particle heat [6, 7] and mass transfer properties.

Despite their typically random arrangement, particles in packed beds tend to align with their confining wall's geometry. This alignment evokes an underlying particle order usually named *Wall Effect* reaching some particle diameters into the packing. This not only affects the local void distribution but influences the overall packing characteristics such as average bed porosity. Furthermore, structural packing parameters may be influenced by the particle's material, shape and size distribution, the container's material and shape and the applied deposition and compaction methods [8, 9]. Variations in structural properties are known to result in a significant change of fluid dynamics, heat and mass transfer. For instance, a deviation (error) in average packed-bed porosity results in four times this deviation in regard to bed-normalized pressure drop as predicted by error propagation [10]. While most researchers focus on packed-beds of spheres, random packings of other shapes are only sparsely investigated. The present study aims to fill at least parts of this gap, by investigating average bed porosity and pressure drop variations as a consequence of changed packing particle's shape and material, confinement shape, packing deposition method and tube-to-particle diameter ratio. In the following detailed literature summary, the influences on the packing characteristics are first discussed under theoretical absence of a confining wall, followed by the evaluation of the confining wall's influence. Finally, the relevant state of the art regarding packed bed pressure drop is summarized.

4.1.1 Bulk packing characteristics

At theoretically infinite tube-to-particle diameter ratio $\lambda \rightarrow \infty$, a random packed-bed is characterized by a constant void distribution and the respective bed porosity $\varepsilon_{\text{inf}} = 1 - N \cdot v_p / V_T$. This measure depends on the packing mode and any applied densification processes, the particle's material and the particle's shape [8, 9, 11].

Packing mode

In regard to technically used packed-beds, four packing and compaction methods and their respective porosity values for the well-investigated sphere-shape were identified [1, 2, 12]: very loose random packing ($\bar{\varepsilon} \approx 0.44$) obtained by settling a fluidized bed or by sedimentation; loose random packing ($\bar{\varepsilon} \approx 0.40 - 0.41$) obtained by letting the spheres roll individually into place, individual hand packing or by dropping the spheres as complete loose mass; poured random packing ($\bar{\varepsilon} \approx 0.375 - 0.391$) obtained by

pouring particles into the container; and close random packing ($\bar{\epsilon} \approx 0.359 - 0.375$) obtained by vibrating, shaking or tapping of the container. Thus, technical packings may take on values between 0.36 (Random Close Packing RCP) [13] and 0.44 (Random Loose Packing RLP) [14] in the absence of a confining wall.

Packing densification was addressed in some experimental and numerical studies including the vibration of the packing [15–23], tapping [24–29], sequential addition [30], sock filling [31], air impact densification [32], and snowstorm filling [9, 33]. Optimal vibration conditions have been studied [15–17, 30] others investigate the densifying effect of the smaller particle filling rates (number of particles added per time) [9, 34] where a lower porosity can be gained with fewer particles added at the same time [35–37]. Additional effects of the surrounding fluid are reported [38].

Particle material

Particles of all kinds of material have been used including metal [11], glass [38], ceramics [39], plastic [40] and natural materials [19], however, possible influences of material properties are typically neglected. On contrary, some researches found relevant but in parts inconsistent influences of the particle material on packing properties [11, 34, 41–43], though being hard to evaluate as material parameters can not be independently varied in experiment.

This, however, is easily possible in studying numerically generated packed-beds. A perfect consensus is obtained among different researchers predicting a denser packing when using materials having a lower coefficient of friction [36, 37, 44–51] and a higher coefficient of restitution k [36, 47, 50]. Furthermore, denser packings are gained when the particle material has a lower E-modulus [46, 51] and lower surface energy [47]. Moreover, the packing density seems to be independent from material density.

Particle shape

The particle shape is known to have a significant influence on the bulk packing porosity. To describe a shape in regard to an ideal sphere, the shape factor sphericity Ψ_W as defined by Wadell [52] can be used.

$$\Psi_W = \frac{\pi^{1/3} \cdot (6 \cdot v_p)^{2/3}}{a_p} \quad (4.1)$$

This parameter may be correlated to the average packing porosity at infinite λ , but up to today no universally applicable relation was found. Having no universal descriptive factor available, shapes need to be clustered and separately evaluated. Each cluster has set geometrical parameters, as for instance the solid cylinder, which is characterized by an aspect ratio $a_1 = d/h$ and the equivalent diameters d_p and/or d_v ; or the hollow cylinder cluster having an additional aspect ratio $a_2 = d_i/d$.

Regarding cylinders, some noteworthy experimental studies were performed [27, 40, 53–62]. Accordingly, the packing of equilateral cylinders $a_1 = 1$ gives the densest packings with increasing porosity when increasing or decreasing the aspect ratio from unity, with a stronger effect occurring for elongated cylinders. Numerical studies confirm the general trend [63–67], while absolute values diverge due to different packing modes. Compared to spheres, denser packings can be gained, especially in RCP mode, going down to a porosity around 0.27 [18, 24].

Hollow cylinders were similarly investigated in experiment [56, 57, 59, 68–72] and simulation [73]. They are believed to pack equal to their solid cylinder counterpart, except that the porosity needs to be corrected to the additional inner void caused by the holes [68, 69].

$$(1 - \varepsilon_{sc}) = \frac{1 - \varepsilon}{f \cdot (1 - (a_2)^2)} \quad (4.2)$$

Moreover, an additional correction factor f [68] or f^* [70] is suggested accounting for interpenetration effects occurring for $a_2 < 0.5$.

4.1.2 Confined packed-beds

When packings are confined in a container, the packing is forced to align with the confining walls, resulting in a variation of local structure [1] and an increase of average bed porosity with increasing wall influence λ . As a rule of thumb, packings of spheres are affected by the wall effect when $\lambda < 10$ [1], this extent of wall effect may alter to smaller values for other shapes such as cylinders and rings [56].

Many experimental studies were performed to evaluate the behavior of sphere packings in small containers and many correlations were derived. A summary of correlations can be found elsewhere [74, 75]

Among the displayed wall effect correlations, the ones of Benyahia and O'Neill [56] and Foumeny et al. [20] were selected due to the best fit with our previously presented experimental data [11].

$$\text{Benyahia and O'Neill [56]: } \bar{\varepsilon} = \varepsilon_{inf} + \frac{1.74}{(\lambda + 1.14)^2} \quad \text{for } 1.5 \leq \lambda < 50 \quad (4.3)$$

$$\text{Foumeny et al. [20]: } \bar{\varepsilon} = \varepsilon_{inf} + 0.254 \cdot \frac{\lambda^{-0.923}}{\sqrt{0.723 \cdot \lambda - 1}} \quad \text{for } 1.866 \leq \lambda < 22 \quad (4.4)$$

The variation in packing mode and particle material can be considered by adopting the bulk porosity ε_{inf} to the specific case while keeping the actual wall effect correlation and its parameters constants [11]. On the contrary, investigating packings of shapes other than spheres, ε_{inf} and all pre-parameters are typically adjusted [56, 68].

Confinement shape

Typically, cylindrical confinements are used as packing container but some utilizations of tubes with square ducts are published [76–78]. But when compared, the average bed porosity data of tubes with square duct [77] and those with a circular cross-section [79] appears very similar. Further studies are related to annular packings where the packing is interrupted in the bulk part by one or more introduced tubes [71, 80–82] or spherical containers [83, 84]. A comparison of numerical packings having different confinement shapes including cylinder, half-cylinder, square and rectangle was performed, but only taking one container size into account for each shape [85].

4.1.3 Pressure drop

For many applications, the pressure drop along the bed height is one of the most decisive parameters. Regarding packings of spheres, a large number of correlations have been derived, relating the pressure drop to the packing porosity and the Reynolds number (see [4] for a review). Herein, the pressure drop is incorporated in its non-dimensional form called friction f' :

$$f' = \frac{\Delta P}{H} \cdot \frac{d_p}{\rho \cdot u_0^2} \cdot \frac{\bar{\varepsilon}^3}{1 - \bar{\varepsilon}} = f(\text{Re}_p) \quad \text{with} \quad \text{Re}_p = \frac{\rho \cdot d_p \cdot u_0}{\eta \cdot (1 - \bar{\varepsilon})} \quad (4.5)$$

Despite some exceptions, the friction-Reynolds relation $f(\text{Re}_p)$ is categorized into the Ergun-type [86] and the Carman-type [87]. Both types have a first term with indirect proportionality to Re_p which is dominant for the laminar flow region, and a second term, which relates to the fully turbulent region, where the Ergun-type correlations are independent from Re_p , whereas the Carman-type correlations still considers a small Re-effect. In their review, Erdim et al. [4] strongly prefer the Carman-type description of the turbulent regime. Despite a century of research on pressure drop of packed-beds, Carman's [87] correlation have not changed much since then.

$$\text{Ergun [86]:} \quad f' = \frac{150}{\text{Re}_p} + 1.75 \quad (4.6)$$

$$\text{Carman [87]:} \quad f' = \frac{180}{\text{Re}_p} + \frac{2.871}{\text{Re}_p^{0.1}} \quad (4.7)$$

$$\text{Erdim et al. [4]:} \quad f' = \frac{160}{\text{Re}_p} + \frac{2.81}{\text{Re}_p^{0.096}} \quad (4.8)$$

The effect of the tube-to-particle diameter ratio λ was thoroughly discussed in Erdim et al.'s review [4]. While a lot of correlations include an additional λ -dependency in the friction-Reynolds relation $f(\text{Re}_p, \lambda)$, the implemented effects on the friction are contradictory. Moreover, Erdim et al.'s data [4] of which more than half were gained for $4 \leq \lambda < 10$ were best represented with correlations that did not use an additional λ -relation. It was concluded, that more clarification on this topic is required.

While most research was done using packed-beds of spheres, the effect of particle shape was occasionally discussed. Some researchers suggest the introduction of a universal shape factor such as sphericity Ψ_W [88, 89], others simply adjust the pre-factors for each shape cluster separately [90, 91].

$$\text{Nemec and Levec [89]: } f' = \frac{150}{\Psi_W^{3/2} \cdot \text{Re}_p} + \frac{1.75}{\Psi_W^{4/3}} \quad (4.9)$$

For packed-beds of equilateral cylinders, the pre-factors are slightly larger, 190-216 [90–93] for the first and 1.56 to 2.4 [92, 93] for the second term of the Ergun-type correlation. These factors increase further with decreasing or increasing aspect ratios away from unity [92]. However, the factor adjustment varies much between the research groups and the sphericity inclusion was not tested for a large range of shapes. Consequently, large deviations between data and correlation are seen [94].

Another occasionally discussed parameter is the surface roughness of the particles. While in their review Einfeld and Schnitzlein [90] deny any particle surface effects on pressure drop, there are some examples where an increase in friction is observed for rougher particles [89–91, 93].

4.1.4 Objectives

Although random packings are influenced by a large number of parameters, some are frequently neglected reducing the comparability of literature data. This paper aims to be a guideline on the extent of these influencing factors, especially filling method, material characteristics, shape and size ratios on both, the average porosity and the pressure drop. There is a significant need for standardization of random packing generation, no matter if they are used for pressure drop, heat or mass transport evaluations. The frequently used standard packing procedures random loose and random close packing are experimentally hard to achieve and do not represent industrial reality. Furthermore, literature correlations regarding the tube-to-particle diameter ratio are typically limited to packings of spheres, though packings of cylinders and hollows cylinders are similarly utilized in industry. If correlations are available they neglect the influence of aspect ratios. Additionally, the effect of tube shape is not understood yet. Finally, the propagation of porosity deviations on pressure drop needs to be quantified in order to understand the significance of standardization and delicate parameter selection in terms of packing generation and experimental setups.

4.2 Experimental setup

4.2.1 Experimental packing generation

High precision steel spheres (VTLG Europe Ltd., Germany) with density $\rho = 7780 \text{ kg m}^{-3}$ and restitution $k = 0.8$ [11], high precision spheres made of glass ($\rho = 2550 \text{ kg m}^{-3}$, $k = 0.94$ [11]), aluminum (alu, $\rho = 2710 \text{ kg m}^{-3}$, $k = 0.6$ [11]) and polyoxymethylene (POM, $\rho = 2354 \text{ kg m}^{-3}$, $k = 0.9$ [11]) obtained

from KGM Kugelfabrik GmbH & Co. KG, Germany, 3d printed (selective laser sintering, EOS Formiga, Germany) polyamide spheres, cylinders and hollow cylinders with a rough surface having a mean surface roughness depth $R_z = 50 \mu\text{m}$ and density $\rho = 975 \text{ kg m}^{-3}$, laser cut plexiglass cylinders with a smooth surface ($R_z < 1 \mu\text{m}$) and density $\rho = 1140 \text{ kg m}^{-3}$, and one type of tablet pressed ceramic cylinder with rough surface (approx. $R_z = 20 \mu\text{m}$) and density $\rho = 3020 \text{ kg m}^{-3}$ (all dimensions in Table 4.1), were filled into plexiglass containers. These are of 100 mm height and various diameters, either having a cylindrical ($D = 15\text{-}55 \text{ mm}$), square ($L = 20\text{-}50 \text{ mm}$), rectangular (L, B in Tab. 4.2) or regular polygonal (L in Tab. 4.2) cross-sectional area. The dimensions of the rectangular and regular polygonal cross-sections

Table 4.1: Shape, material, characteristic diameter $d_p = 6 \cdot v_p/a_p$, cylinder aspect ratio $a_1 = d/h$, hole aspect ratio $a_2 = d_i/d$ and true sphericity $\Psi_W = d_p/d_v$ for all particles used in this study.

Shape	Material	Manufacturing method	d_p [mm]	a_1 [-]	a_2 [-]	Ψ_W [-]		
Sphere	Steel	VTLG Europe	3 to 10	-	-	1		
	Polyamide	3d printing	3, 4, 5	-	-	1		
	POM, aluminum, glass	KGM Kugelfabrik	4	-	-	1		
Cylinder	Polyamide	3d printing	3.20	0.75	-	0.866		
			3.57	1.33	-	0.865		
			3.97	1.0	-	0.874		
			4.28	0.8	-	0.869		
			4.59	1.25	-	0.869		
			Ceramics	Tablet press	3.5	1.0	-	0.874
					Acrylic glass	Laser Cutting	2.99	0.5
			3.05	1.0			-	0.874
			3.35	0.75			-	0.868
			3.52	0.6			-	0.852
	3.57	1.33	-	0.866				
	4.05	1.0	-	0.874				
	4.05	1.66	-	0.849				
	4.29	0.8	-	0.869				
	4.47	2.0	-	0.827				
4.74	1.25	-	0.867					
5.01	1.0	-	0.874					
5.25	1.5	-	0.854					
Hollow cylinder	Polyamide	3d printing	3.55	1.33	0.635	0.496		
			3.92	1.0	0.5	0.557		
			3.95	1.0	0.625	0.472		
			4.01	1.0	0.75	0.388		
			4.24	0.8	0.625	0.452		

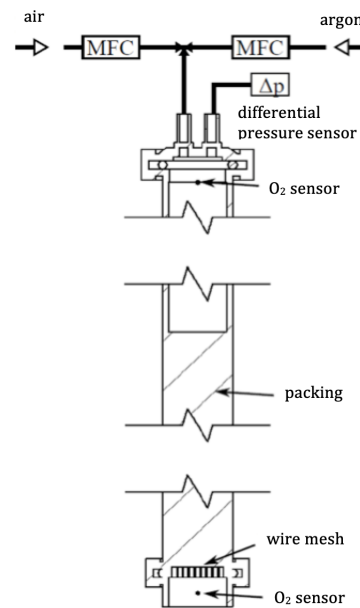
are selected to result in an hydraulic tube diameter $D_h = 4 \cdot A_T/P_T$ of 25 mm. The exact particle mass was determined with a sample of 1000 particles, each, and the deviation was less than 0.1 %. The densities and their deviations, which were about 0.5 %, were determined using a pycnometer with a volume of 50 ml as the mean of ten measurements of 50 particles each. The exact volumes of the tubes were determined by filling them up with a known amount of water. The mean of three measurements was noted.

Particle filling was performed with three different methods using the following packing aids: I) pouring the particles as fast as possible using a funnel with an outlet diameter of 20 mm; II) applying a filling machine consisting of a horizontal tube and a vibrating motor to move the particles slowly to an outlet

Table 4.2: Shape and dimensions of tubes with hydraulic diameter $D_h = 25$ mm.

Shape of cross section	Characteristic length L, B [mm]	Cross sectional area A_T [mm ³]	Circularity $\psi = \frac{\sqrt{4 \cdot \pi \cdot A_T}}{P_T}$ [-]
Regular triangle	$L = 42.2$	771	0.778
Square	$L = 25$	625	0.886
Rectangle	$L = 29, B = 22$	638	0.878
Rectangle	$L = 33.9, B = 20$	678	0.856
Rectangle	$L = 40, B = 18.4$	736	0.823
Rectangle	$L = 57, B = 17$	969	0.746
Regular pentagon	$L = 18.4$	582	0.930
Regular hexagon	$L = 14.2$	524	0.952
Circle	$D = 25$	491	1

funnel leading to the plexiglass tubes whereby the filling time (inverse filling rate) was kept constant at about 0.3 scm^{-3} tube volume by default but was varied for the filling time experiments; III) utilization of a vibratory plate at constant amplitude to dense the packing as much as possible priorly produced by slow pouring. The porosity was determined by the weighing method [68]. Experiments were repeated at least three times each in different orders to exclude systematical errors. The reproducibility of packing generation was discussed earlier [11].

**Figure 4.1:** Schematical drawing of experimental setup for pressure drop measurements.

4.2.2 Experimental determination of pressure drop

Investigating the pressure drop of spherical packed-beds, glass tubes as displayed in Fig. 4.1 with height $H = 500$ mm and various diameters $D = 17$ mm, 20 mm, 23 mm, 25 mm, 27 mm, 35 mm, 45 mm and 55 mm were filled with the above described packing particles using the filling machine. Packings are hold

into place with a wire mesh at the bottom while a metal lid with seal ring closes the top end pressure-tight. Additionally, a 10 mm high monolith is placed on top of the packing to allow even flow distribution. Two differential pressure sensors with different measurement ranges determine the stagnation pressure above the packing against the ambient pressure below. Volume flow of pressurized air can be adjusted using two mass flow controllers operating in the range $0.1\text{-}4\text{ m}^3\text{ h}^{-1}$ and $1\text{-}20\text{ m}^3\text{ h}^{-1}$, respectively.

4.3 Results and discussion

4.3.1 Mean bed porosity and filling method

Spheres

The overall mean of packed-bed porosity for packings of homo-sized, smooth spheres for different tube-to-particle diameter ratios and filling methods was already shown in [11]. These data, extended by some new data for machine filling are again shown in Fig. 4.2.

Due to the reproducibility of single particle dropping (SPD) using the filling machine, an adjustment of the classification of filling methods [1, 2] is proposed:

- i) Random Loose Packing $\bar{\epsilon}_{\text{RLP}} \approx 0.44$: obtained under diminished gravity, such as by settling a fluidized bed or sedimentation.
- ii) Poured Packing: obtained by pouring the particles as a loose mass into the container under influence of gravity.
- iii) Single Particle Dropping $\bar{\epsilon}_{\text{SPD}} \approx 0.383$: obtained by the single placement of particles under influence of gravity.
- iv) Densified Packing: obtained by densification of a poured or single-placed packed-bed by using means such as vibration or tapping.
- v) Random Close Packing $\bar{\epsilon}_{\text{RCP}} \approx 0.359$: highest obtainable bed density.

While RCP, RLP, and SPD represent a distinct and reproducible value, the densified and poured packing comprise all values in between. It is to be noted, that the above-given values vary with material properties such as restitution, and friction [11] and are given for spheres of low friction and high restitution only. In order to account for different material properties, as well as for different shapes, a bed-compactibility parameter is more appropriate than the allocation of distinct values for each case to the above filling procedure classification. Investigating powder beds, the *Hausner Ratio* H_E gives the dependence of densified alias tapped and poured alias apparent bed density. Transferred to packed-beds of spheres, this would

ideally read: $H_{\varepsilon} = (1 - \bar{\varepsilon}_{\text{RCP}})/(1 - \bar{\varepsilon}_{\text{RLP}}) = 1.145$. Unfortunately, especially the RLP is hardly determined as it requires a completely different experimental setup. Consequently, adapting to the industrial reality, the tapped density should be the highest obtainable density by densification of a packed-bed in appropriate time (RCP_{mod}), whereas the apparent density is the lowest density obtained when pouring as many particles in as least time as possible into the respective container (RLP_{mod}). For even more convenience, RCP_{mod} can be replaced by SPD, as densification experiments have a significantly higher uncertainty than single-dropped packed-beds. This results in the following re-definition of the Hausner ratio:

$$H_{\text{mod},1} = \frac{(1 - \bar{\varepsilon}_{\text{RCP,mod}})}{(1 - \bar{\varepsilon}_{\text{RLP,mod}})} \quad \text{and} \quad H_{\text{mod},2} = \frac{(1 - \bar{\varepsilon}_{\text{SPD}})}{(1 - \bar{\varepsilon}_{\text{RLP,mod}})}. \quad (4.10)$$

These two ratios, plotted against λ for smooth and rough homo-sized spheres based on the data of [11] is displayed in Fig. 4.3. Despite a large scattering, for tube-to-particle diameter ratios > 4 , the Hausner ratio

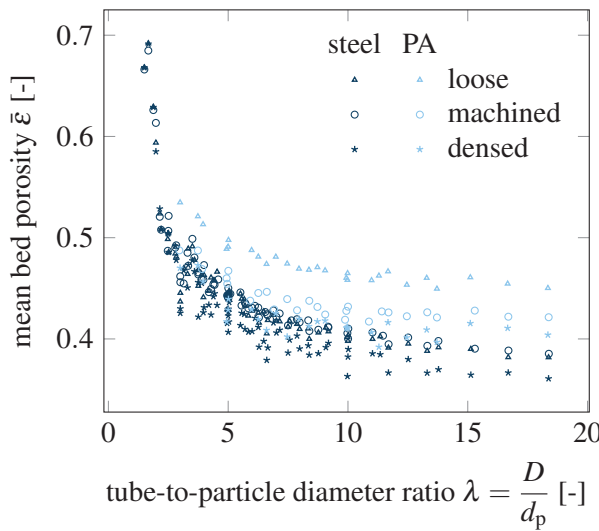


Figure 4.2: Experimental results of the mean bed porosity $\bar{\varepsilon}$ of homo-sized spheres of smooth (steel) and rough (polyamide) surface, plotted against the tube-to-particle diameter ratio λ , for each investigated filling procedure. Parts of the data are same as in [11].

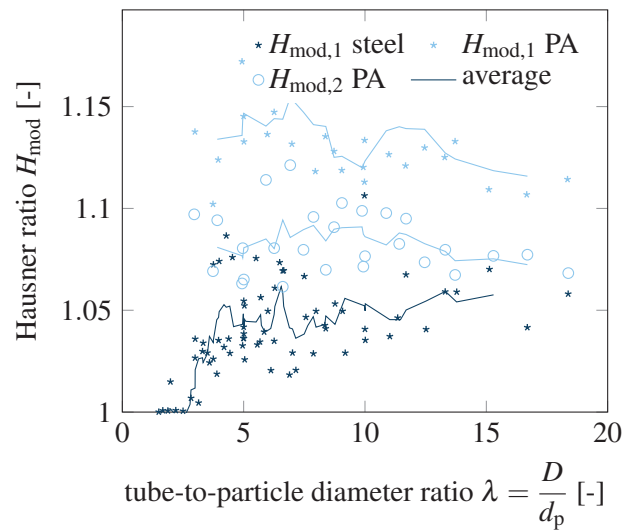


Figure 4.3: Modified Hausner ratio H_{mod} for different materials, plotted against tube-to-particle diameter ratio λ and evaluated with a moving average of 4th order.

is independent of λ , shown by the moving average. For smaller values, the Hausner ratio decreases and reaches 1.00 for $\lambda < 2$. Thus, the compactibility of a sphere packing is superimposed by the effect of the confining wall, however, to a smaller degree compared to the porosity. For containers too small to allow sphere placing next to each other ($\lambda < 2$), the packing is independent of the packing method and probably from the particle material. This is the region, where an analytical solution for the correlation of porosity and container size exists [87]. The mean values of modified Hausner ratio for the region $\lambda > 4$ are displayed in Tab. 4.3. It is to be noted, that the porosity does not change between loose and machine filled steel spheres ($H_{\text{mod},2} \approx 1$) indicating no apparent compaction. Furthermore, The Hausner ratio is larger for polyamide spheres, indicating a larger spectrum of obtainable porosity values when varying the packing method.

Table 4.3: Mean modified Hausner ratios for $\lambda > 4$ and their respective standard errors (SE) for packings of smooth steel and rough polyamide spheres.

Material	Hausner ratio 1 $H_{\text{mod},1}$ [-]	Standard error SE [-]	Hausner ratio 2 $H_{\text{mod},2}$ [-]	Standard error SE [-]
Steel	1.048	0.00250	0.992	0.00262
Polyamide (PA)	1.134	0.00350	1.083	0.00285

Cylinders

Cylindrical particles of two similar materials but with different surface structures due to their production method are compared in regard to their overall packing porosity. Again the three packing modes *loose*, *single drop* and *dense* are evaluated putting some special attention to the cylinders aspect ratio $a_1 = d/h$. Figure 4.4 depicts the wall effect for acrylic glass cylinders with an aspect ratio $a_1 \leq 1$ and Fig. 4.5 depicts

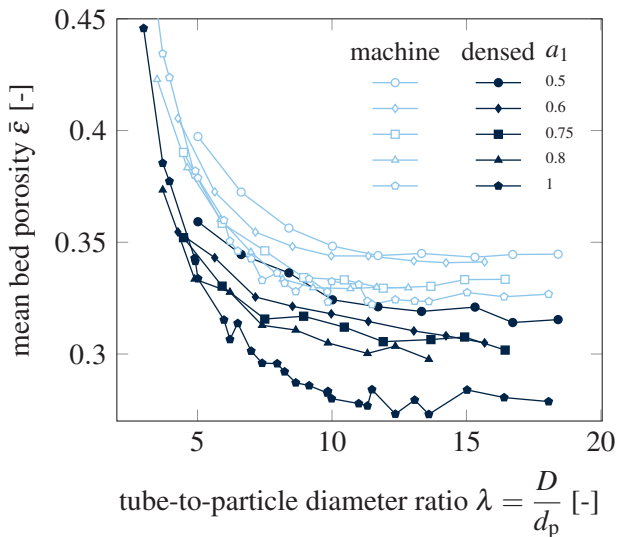


Figure 4.4: Mean bed porosity $\bar{\epsilon}$ as function of tube-to-particle diameter ratio λ for elongated cylinders with an aspect ratio $a_1 \leq 1$, for dense packed (dark) and machine filled (light) packing modes.

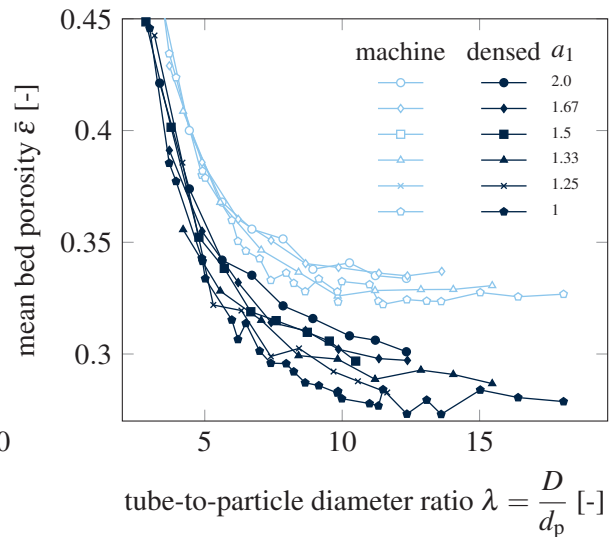


Figure 4.5: Mean bed porosity $\bar{\epsilon}$ as function of tube-to-particle diameter ratio λ for flat cylinders with an aspect ratio $a_1 \geq 1$, for dense packed (dark) and machine filled (light) packing modes.

the respective wall effect for acrylic glass cylinders with aspect ratios $a_1 \geq 1$. In contrary to spheres, when packing cylinders the definition of the tube-to-particle diameter ratio includes the equivalent particle diameter d_p in order to take the particle's height into account. As can be seen, the porosity is lowest for the equilateral cylinder, increasing with increasing and decreasing aspect ratios, however, the increase is more pronounced when using elongated cylinders ($a_1 < 1$). This effect is in accordance with the findings of [55, 95] for bulk cylinder packings. New is, that this porosity difference caused by different aspect ratios is at its maximum in the bulk part of the packing, whereas the different branches merge to a single correlation for lower tube-to-particle diameter ratios. Moreover, this clear behavior is against the findings of [56] neglecting the effects of aspect ratio in their correlation.

In Figs. 4.4 and 4.5 the results for the dense packed packings are highlighted as here, the difference can be seen best. The lighter data represent the machine filled samples, resulting in the very same trend, except

being moved to overall higher values and a smaller actual effect. Consequently, the difference in porosity between the equilateral cylinder and both, the flat and the elongated cylinder were decreased. Besides lucidity, it was renounced to draw the data of poured packings as the experimentation uncertainty was in parts larger than the porosity differences caused by the shape variations and with more repetitions this uncertainty could not be diminished. Consequently, packings of cylindrical particles show a very distinct behavior in small containers when varying the aspect ratio, but the distinctness of the effects increase with a denser packing mode. Furthermore, the equilateral cylinder packs densest among all cylinder variations, reaching values down to 0.273, which is in accordance with literature values [18, 24]. It is to be noted, that this value is significantly smaller than porosities obtained with sphere packings (0.36 [13]), and is just above the densest regular sphere packing with a porosity of 0.26.

The results of the rough polyamide packing are displayed in Fig. 4.6. Here, the experimental results of the poured and machine filled packing methods are displayed as it was impossible to bring the cylinders into a reproducible dense state. Theoretically, the densest state should be similar to the densest state of the smooth acrylic glass cylinders, however, this could not be achieved. For information, the respective porosity values of a sphere packing are added. The data is directly comparable as being made of the same material and the same production method. Basically, the same trend as discussed for the smooth acrylic glass cylinders can be seen, with the exception, that the effects caused by the aspect ratio variation are much more pronounced.

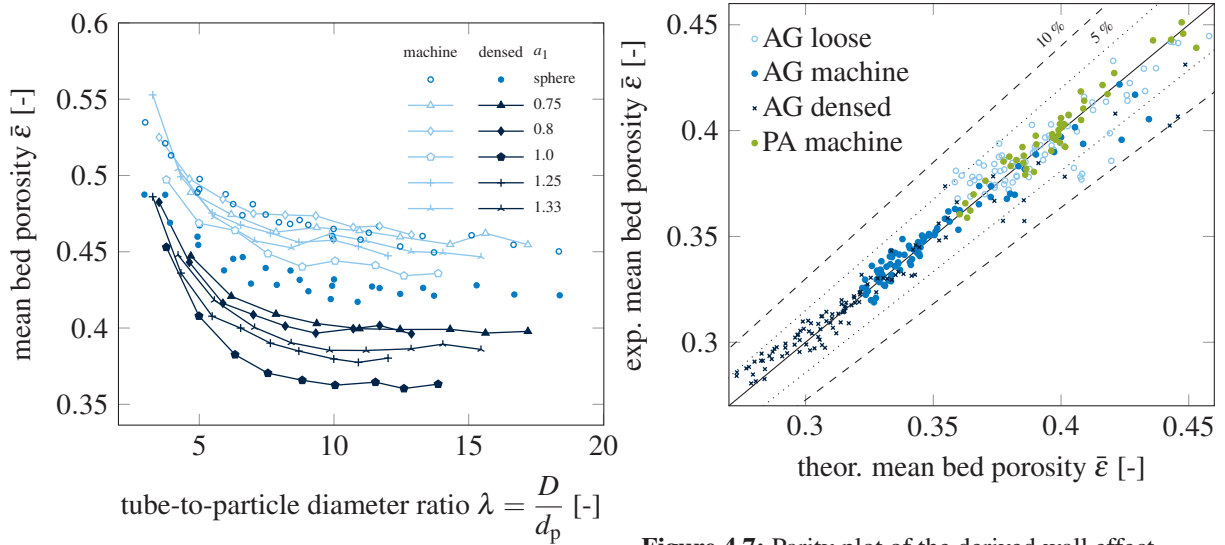


Figure 4.6: Mean bed porosity $\bar{\varepsilon}$ as function of tube-to-particle diameter ratio λ for all polyamide cylinders, highlighting the results for the machine filled packing (dark) and the poured packing (light).

Figure 4.7: Parity plot of the derived wall effect correlation (4.11) together with (4.12) for cylinders of varying aspect ratios, materials and filling method. The respective parameters are displayed in Table 4.4.

In our previous study [11] we showed that porosity variations due to material properties and packing mode can be considered by simply adjusting ε_{inf} to the appropriate value. As a variation of the aspect ratio primarily varies the bulk porosity value, we suggest to correlate the bulk porosity ε_{inf} to the bulk porosity of the equilateral cylinder $\varepsilon_{\text{inf,eq}}$ and the aspect ratio a_1 , weighted with an exponent n :

$$\varepsilon_{\text{inf}} = \varepsilon_{\text{inf,eq}} \cdot a_1^n \quad (4.11)$$

wherein n is case sensitive for $a_1 > 1$ and $a_1 < 1$. As wall effect correlation, Benyahia and O'Neill's [56] is selected due to an overall good fit with experimental data [11].

$$\text{Benyahia and O'Neill [56]:} \quad \bar{\varepsilon} = \varepsilon_{\text{inf}} + \frac{A}{(\lambda + B)^2} = \varepsilon_{\text{inf}} + \frac{1.703}{(\lambda + 0.611)^2} \quad (4.12)$$

The resulting fitting parameters $\varepsilon_{\text{inf,eq}}$ and exponent n , and the corrected R^2 are listed in Table 4.4. The

Table 4.4: Correlation parameter overview for Eq. (4.11).

Material	Filling Method	Infinite porosity $\varepsilon_{\text{inf,eq}}$ [-]	Aspect ratio $a_1 = d/h$ [-]	Shape exponent n [-]	Coefficient of determination R^2 [%]	Hausner ratio H_{mod} [-]
Acrylic glass	Loose	0.363	$a_1 \leq 1$	-0.040	92	$H_{\text{mod},2} = 1.087$
			$a_1 > 1$	0.054	92	
	Machine	0.314	$a_1 \leq 1$	-0.098	91	$H_{\text{mod},1} = 1.13$
			$a_1 > 1$	0.072	99	
Polyamide	Dense	0.276	$a_1 \leq 1$	-0.18	95	$H_{\text{mod},2} = 1.124$
			$a_1 > 1$	0.12	93	
	Loose	0.423	$a_1 \leq 1$	-0.203	83	$H_{\text{mod},2} = 1.124$
			$a_1 > 1$	0.12	94	
Machine	0.357	$a_1 \leq 1$	-0.372	98	$H_{\text{mod},2} = 1.124$	
		$a_1 > 1$	0.212	95		

model was developed with the data of the acrylic glass particles alone and then tested with the polyamide cylinders. The respective parity plot in Fig. 4.7 shows calculated and experimental data points for the acrylic glass (AG) cylinders for each packing mode separately. Furthermore, the model test data of the machine filled polyamide (PA) cylinders is added, showing a perfect fit. Exponent n depends on the packing mode or better on the densification state of the packing and the packing material. As can be seen in Table 4.4, n increases with increased packing density and rougher surface conditions, indicating that in these cases, the effect of a_1 is much more pronounced. A close to linear trend between shape exponent n and the infinite porosity describing the filling method can be derived. The respective correlations are summarized in Eq. (4.13) and Eq. (4.14).

$$n = -0.7401 \cdot \varepsilon_{\text{inf,eq}} + 0.3171 \quad \text{for} \quad a_1 > 1 \quad (R^2 = 0.90) \quad (4.13)$$

$$n = 1.5891 \cdot \varepsilon_{\text{inf,eq}} - 0.6108 \quad \text{for} \quad a_1 < 1 \quad (R^2 = 0.97) \quad (4.14)$$

The Hausner ratio H_{mod} itself describes the effects already discussed for the experimental data, which is a higher Hausner ratio for particles with rough surfaces and a generally higher Hausner ratio compared to packings of spherical particles.

$$H_{\varepsilon} = \frac{1 - \varepsilon_{\text{inf,eq,dense}}}{1 - \varepsilon_{\text{inf,eq}}} \quad (4.15)$$

Consequently, a packing of cylinders can take a wider range of porosity values depending on the packing mode, which is a potential source of experimental uncertainty when not considered appropriate.

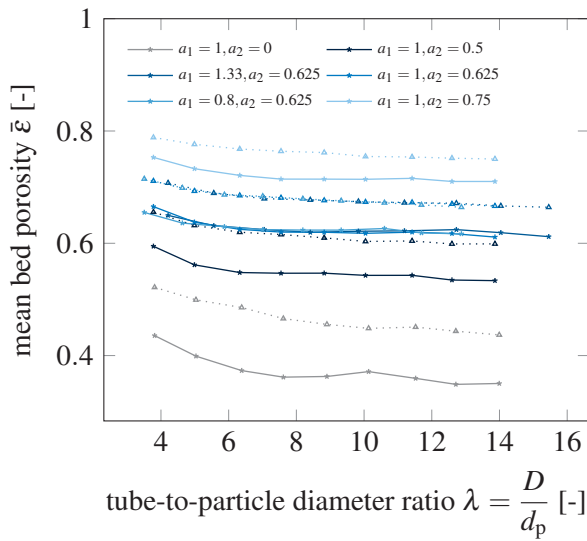


Figure 4.8: Mean bed porosity $\bar{\epsilon}$ as function of tube-to-particle diameter ratio λ for hollow cylinders, for densified (solid line) and poured (dotted line) packing modes.

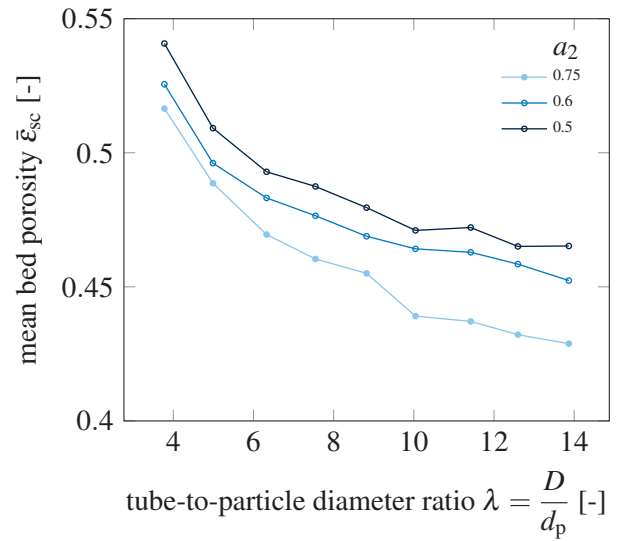


Figure 4.9: Visualization of the hollow cylinder interpenetration with aspect ratio $a_2 = 0.5, 0.625$ and 0.75 , by calculating the respective solid cylinder base porosity $\bar{\epsilon}_{sc}$, here displayed as a function of λ .

Hollow cylinders

The hollow cylinders were evaluated similarly. Figure 4.8 shows the average porosity values obtained by pouring (dotted line) and after densification (solid line), as a function of the tube-to-particle diameter ratio. For the calculation of the equivalent particle diameter d_p in λ , the volume and surface of the holes of the cylinders are neglected as otherwise extreme high λ values are obtained. It is obvious that packings of hollow cylinders have much higher porosities than the solid cylinders, and the average porosities are further increased with increasing hole size alias aspect ratio a_2 . Furthermore, a difference in cylinder aspect ratio a_1 does not have any observable influence. The obtained data was again fitted to Benyahia and O'Neill's [56] correlation, however, the pre-factors needed to be adjusted to $A = 2.167$ and $B = 2.167$. The obtained bulk porosities ϵ_{inf} , R^2 and the Hausner ratio H_{mod} are summarized in Table 4.5. It is remarkable, that the Hausner ratio is not affected by the shape variation taking a constant value of 1.16. This is slightly lower than the respective cylinder and higher than the respective sphere packings.

Furthermore, the interpenetration of the hollow cylinders is evaluated by subtracting the sum of inner hole volumes from the total void, resulting in the solid cylinder base porosity ϵ_{sc} as proposed in [68]. Shown in Fig. 4.9, the solid cylinder base porosity decreases with increasing hole aspect ratio a_2 , indicating an increased particle interpenetration. As the interpenetration is not observed for $a_2 < 0.5$ [68], the differences between the shapes having $a_2 = 0.625$ and $a_2 = 0.75$ with $a_2 = 0.5$ quantifies the amount of overlap.

Table 4.5: Shape and fitting parameter overview of rough polyamide hollow cylinders packed using the pouring and densification methods.

$a_1 = d/h$ [-]	1	1.33	1	0.8	1	Filling method
$a_2 = d_i/d$ [-]	0.5	0.625	0.625	0.625	0.75	
ε_{inf} [-]	0.742	0.659	0.660	0.658	0.594	Loose
R^2 [%]	96	98	99	98	95	
ε_{inf} [-]	0.699	0.606	0.605	0.604	0.529	Dense
R^2 [%]	93	73	91	71	89	
$H_{\text{mod},1}$ [-]	1.167	1.155	1.155	1.162	1.158	

Filling speed

With the filling machine, any desired filling speed could be set by adjusting the angle of the vibrating tube to the reactor. The filling speed is herein measured as the time needed to fill one meter of packing. As the tube dimensions were constant, this can be easily calculated to the actual filling speed which should be defined as the time needed to fill a cubic centimeter of packing. There are some indications in literature [9, 35–37] that bed porosity correlates with the filling speed, these data, however, are mostly unvalidated numerical results. As displayed in Fig. 4.10 there is a clear trend between filling speed and bed porosity according to which, porosity decreases sharply when increasing the filling time starting at around 5 s m^{-1} (pouring) and reaching a plateau at around 150 s m^{-1} (single particle placement). The porosity difference $\Delta \bar{\varepsilon}_f$ between pouring and single particle placement is considered as the maximal possible porosity deviation that is to taken into account when packing mode is not clearly described or constant. Normalized to the plateau porosity $\bar{\varepsilon}_{\text{SPD}}$ (single particle dropping), the relative porosity deviation is obtained, which is displayed in Fig. 4.11 for all investigated shapes and as a function of tube-to-particle diameter ratio λ . Accordingly, spheres are less prone to filling speed influences as cylinders, and rougher shapes are more affected than smooth shapes. Furthermore, packings with higher λ are slightly more affected.

4.3.2 Influence of tube shape

The significant influence of cylindrical confining walls on packed-bed structures gives rise to the question, how this influence changes when the shape of confinement is varied. Therefore, a selection of containers with square (Fig. 4.12a), rectangular (Fig. 4.12c) and regular polygonal (Fig. 4.12d) cross-sections were packed with homo-sized, smooth steel spheres and for comparison with homo-sized spheres of other material (Fig. 4.12b). As can be seen from Fig. 4.12, the container's cross-section has hardly any influence on the wall effect correlation. This is yet valid when the particle material is varied. Changing the particle material results in a shift of mean bed porosity (see herefor [11]). This shift can be perfectly reproduced using square tubes instead of cylindrical as displayed in Fig. 4.12b.

However, having a closer look at Figs. 4.12c and 4.12d a larger, but un-systematical scattering in the low- λ region is revealed, at least compared to a relatively small deviation for higher values. This is contradictory

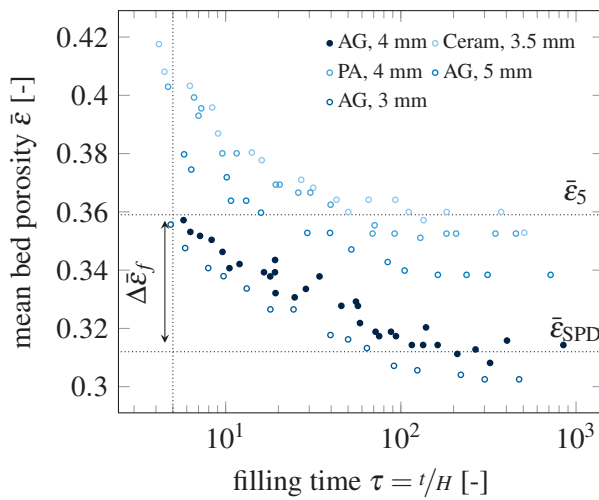


Figure 4.10: Mean bed porosity $\bar{\varepsilon}$ decreases with increasing filling time τ (inverse filling rate) until reaching a constant value ε_{SPD} .

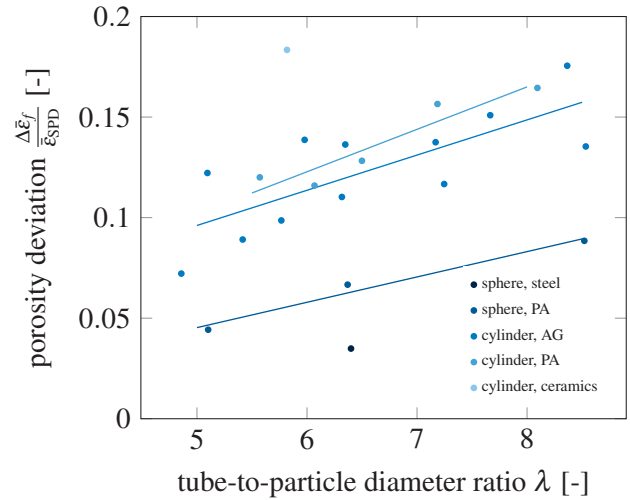


Figure 4.11: Maximal porosity deviation $\Delta\bar{\varepsilon}_f/\bar{\varepsilon}_{SPD}$ obtained from filling time τ (inverse filling rate) variation for packings of cylinders and spheres of different aspect ratio and material.

to the general observation, that the data scattering due to measurement uncertainties increases with λ as can be seen for instance in Fig. 4.2. Moreover, the data scattering is present for only one direction, in particular, to lower porosity values.

According to McGeary [96] and later re-addressed by Klerk [1], wall effect correlations of sphere packings may have additional extrema, indicating tube-to-particle diameter ratios allowing ideal, and thus highly structured packing arrangements. This is of special interest for $2 < \lambda < 5$ and most pronounced for a minimum at $\lambda = 3.0$, where the tube size is optimal to fit a center sphere surrounded by a ring of six spheres in each layer. Having a close look at Fig. 4.2 and Fig. 4.12a this minimum can be seen for densed and machined packings. Changing the tube shape, these discontinuities may persist, but at slightly different λ values.

Packing equilateral cylinders rather than spheres, a clear difference between the tubes with circular and square cross-section can be observed as displayed in Fig. 4.13a. For $\lambda < 8$, the cylinders pack denser in square confinement than in a circular. While there is still some increase in porosity for decreasing λ , the wall effect is significantly reduced. For $\lambda > 8$ similar porosity values are obtained in both types of confinement.

Additionally varying the aspect ratio of the packed cylinders leads to the already discussed increase in porosity with decreasing aspect ratio a_1 in both, circular and square confinement as shown in Fig. 4.13b. The porosity difference between confinement shape for $\lambda < 8$ appears to be less significant when decreasing the aspect ratio.

When packing equilateral cylinders into rectangular tubes with different circularities, as shown in Fig. 4.13c, the obtained porosity values spread much more for $\lambda < 8$, however, a clear correlation to circularity cannot be identified. A mild trend of lower porosities for confinement shapes closer to

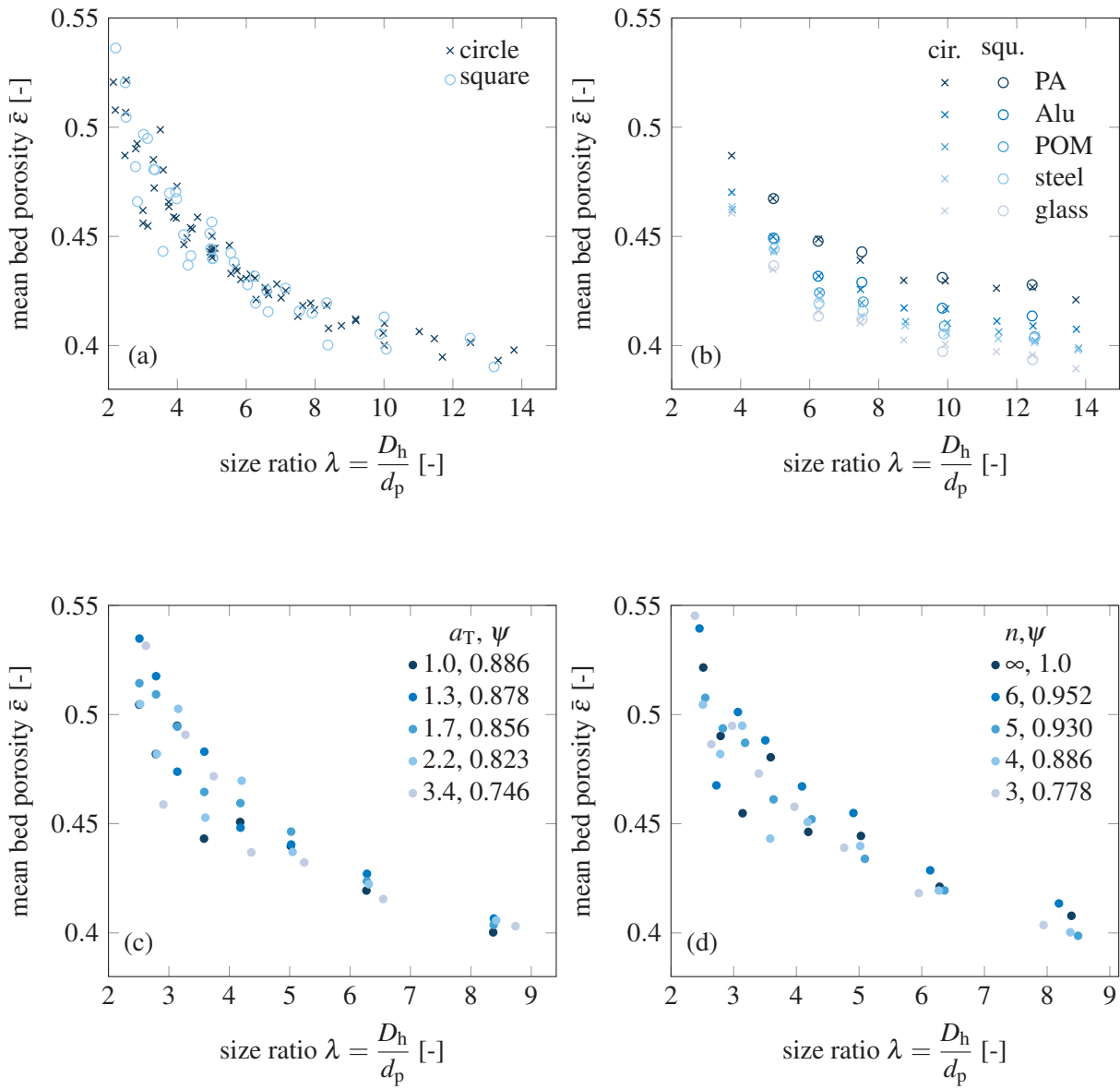


Figure 4.12: Dependence of λ on mean bed porosity for spheres packed into containers of (a) square and circular cross section using only steel spheres, (b) square and circular cross section comparing spheres made of different material, (c) rectangular cross section with varying aspect ratio a_T using steel spheres, and (d) regular polygonal cross section with n sides packed with steel spheres.

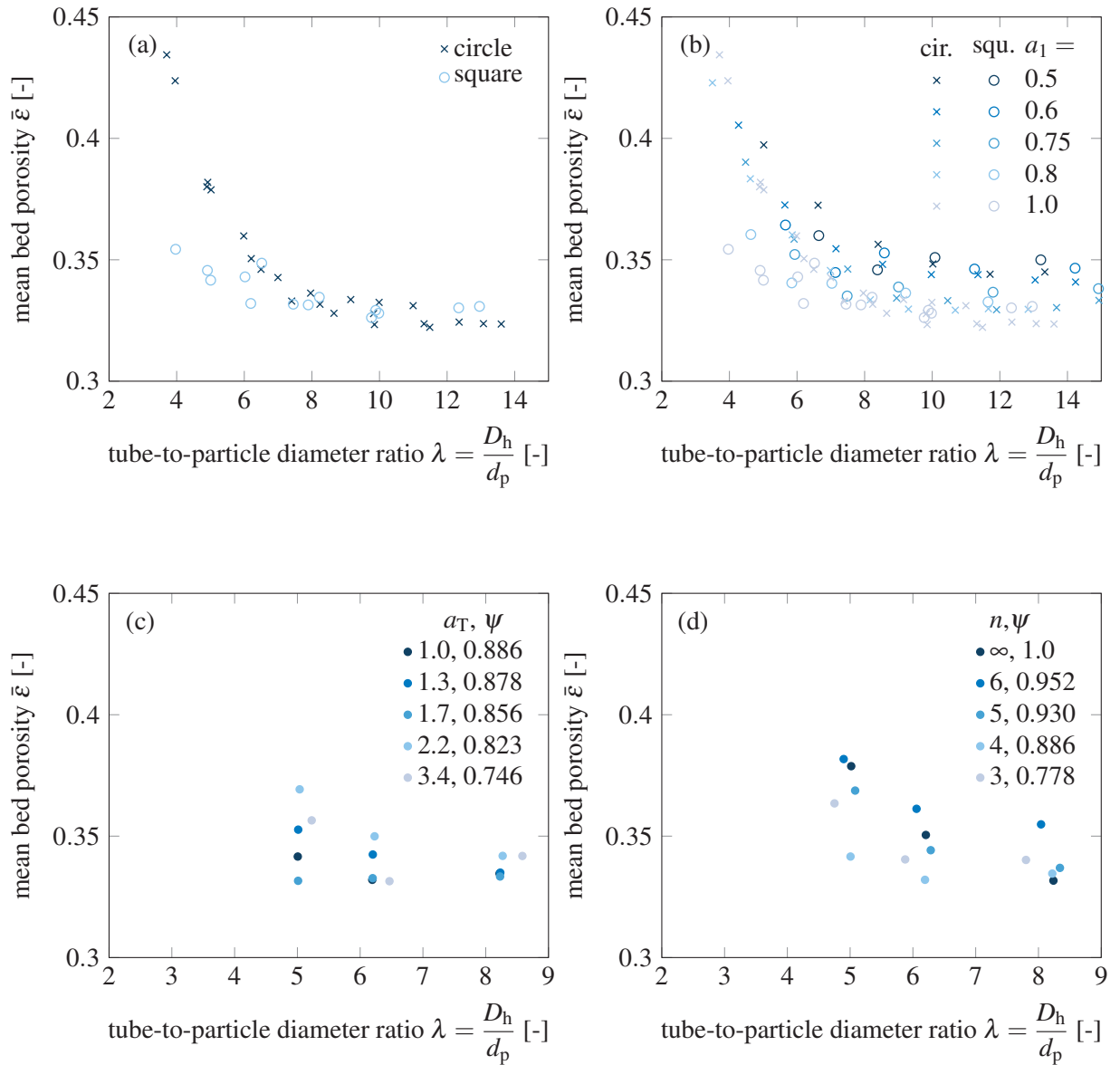


Figure 4.13: Dependence of λ on mean bed porosity $\bar{\epsilon}$ of acrylic glass cylinders packed into containers with (a) square and circular cross section using equilateral cylinders, (b) square and circular cross section packed with cylinders of different aspect ratio a_1 , (c) rectangular cross section with varying aspect ratio a_T packed with equilateral cylinders, and (d) regular polygonal cross section with n sides packed with equilateral cylinders.

the square shape can be interpreted. Same appears to the variation of tube shape for regular n -gons (cf. Fig. 4.13d): there is at least some influence on porosity, however, a clear link to circularity is not possible. In summary, equilateral cylinders appear to pack best in square confinements. Either variation of the particle shape by decreasing the aspect ratio or of confinement shape reduces this influence on porosity.

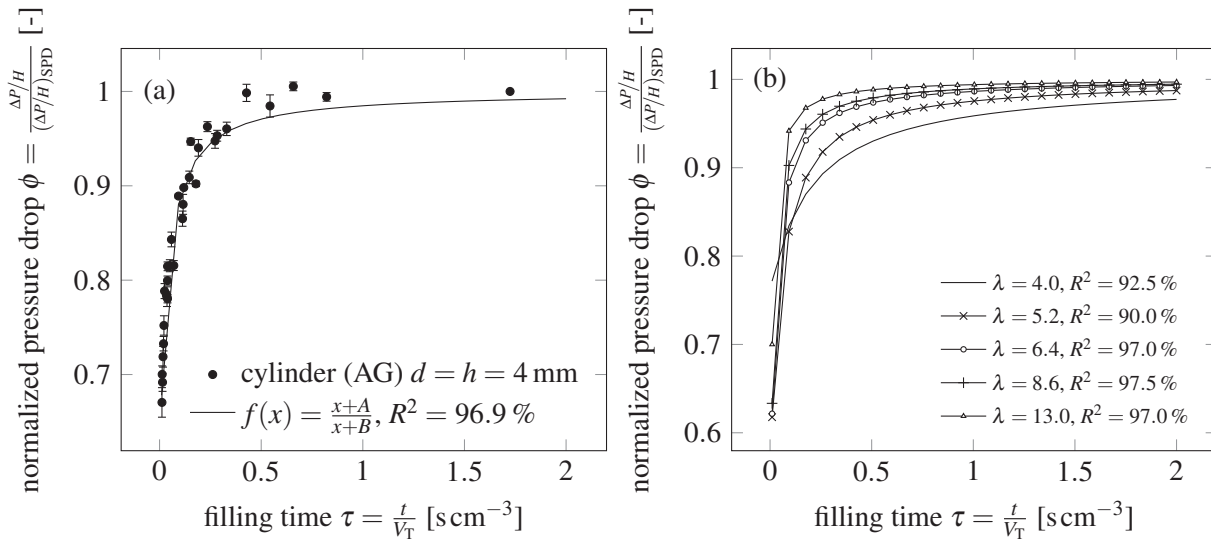


Figure 4.14: Relation of relative pressure drop and filling time τ , depicted for (a) smooth (AG) equilateral cylinders with $\lambda = 6.4$ and (b) rough (PA) equilateral cylinders for various λ . The error bars in (a) are obtained from measurements of different flow velocity; the used cylinders have the dimensions $d = h = 4$ mm.

4.3.3 Pressure drop of cylinder packings

The pressure drop obtained from polyamide (PA, rough) and acrylic glass (AG, smooth) cylinders of different aspect ratios and packed into tubes of different diameters using the filling machine and a large range of filling times, was determined. Additionally, the respective porosity values were noted for each created packing. As a very large data set is obtained, the following results are restricted to the findings of equilateral cylinders. The three major goals of this evaluation include constraints to gain reproducible pressure drop data, the quantification of error propagation of porosity in regard to pressure drop, which also allows an estimation of pressure drop deviation for a known porosity deviation, and the influence of particle material on pressure drop correlations.

Data reproducibility

Early measurements came with a huge experimentation uncertainty which could be related back to inconsistent packing properties, especially the packing porosity. As discussed above, the filling speed of the particles during the tube packing process has a significant effect on the overall bed porosity, unless single-particle packing is performed. Based on this finding, the influence of the filling time (inverse filling rate) on the pressure drop was first evaluated, determining an appropriate filling time allowing reproducible pressure drop data. In Fig. 4.14a, the obtained results for packings of the smooth acrylic glass cylinders with dimensions $d = h = 4$ mm are displayed. Herein, the obtained height normalized pressure drop is normalized to the pressure drop obtained for very high filling times. Error bars indicate the data scatter obtained when varying the flow velocity. As can be seen, for small filling times, only a

tiny increase or decrease in packing speed results in a large change in pressure drop. A couple of seconds of total filling time may increase or decrease the pressure drop by more than 10 %. On the other hand, the pressure drop does not alter at all for higher filling times. Consequently, a minimum filling time was determined, that is required to allow reproducible packing conditions. It was decided to use the filling time when the curve reaches 95 % of its saturation, denoted as τ_{95} .

$$\phi = \frac{(\Delta P/H)}{(\Delta P/H)_{SPD}} = f(\tau) = \frac{\tau + A}{\tau + B} \quad \text{with} \quad \tau_{95} = \frac{A - 0.95 \cdot B}{0.05}, \quad \phi_{0.0122} = \frac{0.0122 + A}{0.0122 + B} \quad (4.16)$$

This value was determined for all available cylinder and sphere packings by fitting the experimental data to Eq. (4.16) and calculating τ_{95} from the obtained pre-factors. Furthermore, the sensitivity of the normalized, relative pressure drop ϕ in regard to the filling time was determined, denoted as $\phi_{0.0122}$. In Table 4.6 selected results for a tube diameter $D = 25$ mm are summarized. Herein, the rows with the general shape and material specification are the averages obtained from all particles in that class, the rows with specific dimensions comprise the specific data of this specific shape. Furthermore, this table lists two values for τ_{95} having different units as it is easier to imagine a filling time of 136 s for 1 m packing height as the value based on the filled volume, however, when varying the tube diameter, the volume based filling time is indispensable.

Figure 4.14b displays the fitted correlations obtained when varying the filling time of the rough polyamide equilateral cylinders. With increasing tube-to-particle diameter ratio, τ_{95} decreases while $\phi_{0.0122}$ increases, except for $\lambda = 4.0$. Consequently, less wall-affected packings are less prone to filling rate influence and thus data inconsistency.

The error propagation of porosity

Table 4.6: Parameter overview of filling time (inverse filling rate) relation and error propagation evaluation for packings of in the $D = 25$ mm tube.

Shape/material	τ_{95} [s m ⁻¹]	τ_{95} [s cm ⁻³]	$\phi_{0.0122}$ [-]	$\epsilon_{\text{err}} = \frac{\Delta \epsilon}{\epsilon_{\text{SPD}}}$ [-]	$P_{\text{err}} = \frac{\Delta(\Delta P/H)}{(\Delta P/H)_{\text{SPD}}}$ [-]	$\frac{P_{\text{err}}}{\epsilon_{\text{err}}}$ [-]	R^2 [%]
Cylinder AG	136	0.277	0.70	0.124	0.321	2.6	97.7
$d = h = 4$ mm	121	0.246	0.70	0.136	0.33	2.4	97.1
Cylinder PA	69.9	0.142	0.63	0.137	0.401	2.9	98.0
$d = h = 4$ mm	77.0	0.157	0.64	0.128	0.387	3.0	98.7
Cylinder ceramic	83.3	0.170	0.61	0.183	0.465	2.5	99.8
Sphere PA	37.8	0.077	0.79	0.052	0.249	3.9	97.6
$d = 4$ mm	41.0	0.084	0.80	0.053	0.252	3.8	96.1
Sphere steel	22.6	0.046	0.89	0.035	0.109	3.1	89.1
$d = 4$ mm							

The error propagation of porosity on pressure drop using the Ergun equation [86] has been determined and discussed theoretically in literature [10]. Accordingly, depending on the fluid state (laminar or turbulent), a deviation in porosity leads to four times this deviation in regard to pressure drop. In order to prove

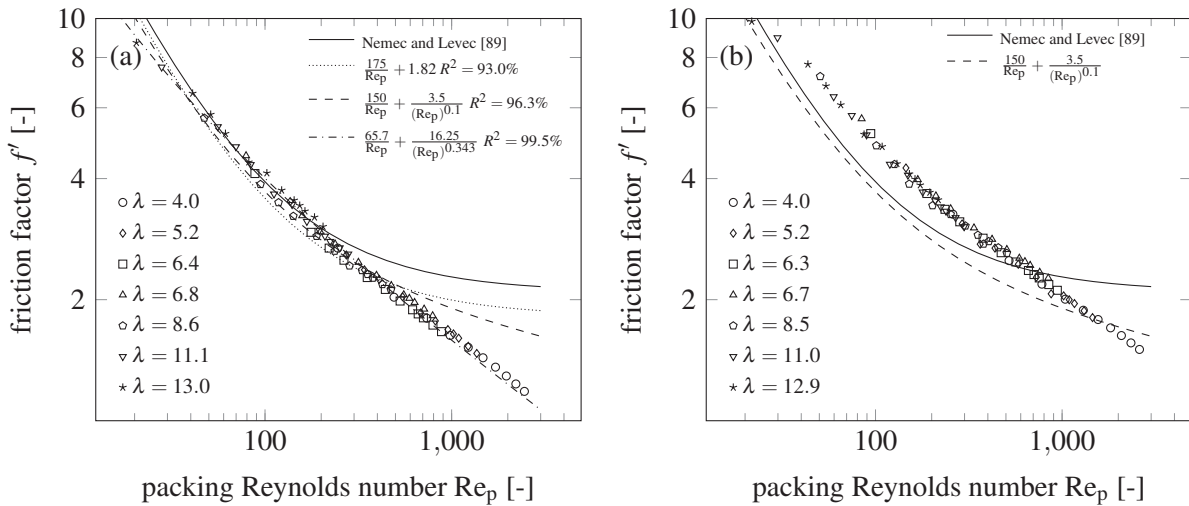


Figure 4.15: Friction factor f' obtained from packings of various tube-to-particle diameter ratios λ when varying Reynolds Re_p by adjusting fluid velocity. Packings of (a) smooth (AG) and (b) rough (PA) equilateral cylinders of dimensions $d = h = 4$ mm were used. The sphericity-based correlation of Nemece and Levec [89] is added as well as curve fitting results using the Ergun-type and the Carman-type correlations.

this with experimental data, the maximal deviation in porosity and pressure drop between the fastest and slowest filling time (inverse filling rate) was determined (see Table 4.6). Regarding rough spheres, the ratio between pressure drop and porosity deviation is very close to the predicted quadruplication. However, cylinders are less affected having a ratio between 2.4 and 3.0. Moreover, rough particles are stronger affected than smooth particles. This is vice versa a proof for an existing influence of particle surface roughness on pressure drop which is frequently denied [90], but is in accordance with some other researchers predicting higher pressure drops for rougher particles [43, 89, 91].

The influence of particle roughness

Finally, Fig. 4.15a and Fig. 4.15b display the determined friction factors of packings of equilateral cylinders with a smooth and rough surface, respectively, obtained for different Reynolds numbers and when varying λ . For comparison, the sphericity-based pressure drop correlation of Nemece and Levec [89] is added. Moreover, the data of Fig. 4.15a is fitted to the Ergun equation (dotted line) [86], and the Carman equation [87], once with set exponent $n = 0.1$ (dashed line) and once with variable exponent (dash dotted line).

It is well known that Ergun-type correlations overpredict the friction factor at high Reynolds numbers for packings of spheres [4], thus it does not surprise, that this is here also the case. The extent of difference between the data and the correlations is, however, unexpected. Even when using the first Carman-type correlation (dotted line in Fig. 4.15a), the overprediction at high Reynolds numbers is still present. On the other hand, due to the very limited selection of flow velocities, the respective data are all obtained from low- λ tubes, where any sort of wall effect may occur and affect the friction factor. We, however, suggest

to use Eq. (4.18) corresponding to the dashdotted line in Fig. 4.15a as a novel pressure drop correlation for equilateral cylinders valid for packing Reynolds numbers 10-3000 and tube-to-particle diameter ratios 4-13.

$$f' = \frac{150}{\text{Re}_p} + \frac{3.5}{(\text{Re}_p)^{0.1}} \quad R^2 = 96.3\% \quad (4.17)$$

$$f' = \frac{65.7}{\text{Re}_p} + \frac{16.25}{(\text{Re}_p)^{0.343}} \quad R^2 = 99.5\% \quad (4.18)$$

Comparing the packing friction of smooth and rough cylinders, a perfect shift of the whole dataset to higher values is observable. The obtained friction is constantly around 17.5 % higher compared to the smooth cylinders of the same dimensions.

In summary, the importance of an appropriate packing method was emphasized in order to allow reproducible and comparable pressure drop data. Herefor, a minimum filling rate is determined. Coping to this minimum filling time (maximum filling rate) is more important investigating pressure drop compared to the sole investigation of packing porosity as the effect is much higher, due to the error propagation. This error propagation is shown to be shape and material dependent, vice versa proving the importance of shape and material influences on the pressure drop. Finally, pressure drop data was fitted to existing correlations originally developed for sphere packings, however concluding, that more data, especially in a wider Reynolds range is required to allow reliable pressure drop predictions.

4.4 Conclusion

A broad experimental study was performed including the evaluation of packed beds of spheres, cylinders, and hollow cylinders. In the first step, the average bed porosity of these shapes as a function of the tube-to-particle diameter ratio was determined. Moreover, the Hausner ratio was utilized as a packing compressibility parameter, describing the sensitivity to packing densification.

With spheres, known correlations could be reproduced, obtaining higher values for rough particle surfaces. Investigating cylinders, the known correlations were fitted to the effect of cylinder aspect ratio. With increasing or decreasing aspect ratio away from unity, higher porosities are obtained, while a stronger effect is observed for elongated cylinders, rougher particle surfaces, and denser packings. Regarding hollow cylinders, the average bed porosity but also particle interpenetration is significantly increased when increasing the hole size. The Hausner ratio is smallest with spheres and considerably larger when packing cylinders. Moreover, the Hausner ratio increases with increasing particle roughness.

Furthermore, it could be shown that the tube shape has hardly any influence on the packing of spheres, even when using tubes with cross-sections of low circularity. Especially between circular and square cross-section a perfect fit of data was obtained. On the contrary, when packing cylinders a considerable effect of confinement shape can be observed, more predominantly at small tube-to-particle diameter

ratios. The densest packings are obtained packing equilateral cylinders into confinements with square cross-sections.

Finally, the packed-bed pressure drop of smooth and rough equilateral cylinders was measured as a function of particle filling speed and as a function of Reynolds number. Regarding the packing of smooth cylinders, available correlations were adjusted. Rough cylinder packings resulted in 17 % higher packing friction compared to the smooth cylinders, proving an influence of particle surface roughness on pressure drop.

As a conclusion it is strongly suggested to use single particle dropping as preferred filling method when packing particles into confinements. If this is not possible or desired, it is suggested to at least list the utilized filling rates and/or densification parameters. It is further suggested to be more precise on material parameters of particles for both, packing and pressure drop experiments.

Future works may include numerical shape development studies and experimental three-dimensional packing analysis studies as for example by x-ray computed tomography for different shapes and the evaluation of the effect of material characteristics and packing methods on the local packing structure.

CRedit authorship contribution statement

Jennie von Seckendorff: Conceptualization, Methodology, Software, Formal analysis, Investigation, Visualization. Normen Szesni: Project administration. Richard Fischer: Project administration, Funding acquisition. Olaf Hinrichsen: Supervision, Funding acquisition.

Declaration of Competing Interest

The authors declare that they have no known competing financial interests or personal relationships that could have appeared to influence the work reported in this paper.

Acknowledgements

The authors would like to thank Benedict Schäfer, Yongqing Lee and Teng Daquan for conducting some of the experiments and Tobias Abstreiter for laser cutting the acrylic glass cylinders.

Financial and substantial support of MuniCat, a strategic alliance between the Technical University of Munich (TUM) and Clariant Produkte (Deutschland) GmbH, Germany is gratefully acknowledged. Jennie von Seckendorff would further like to thank the TUM Graduate School for generous support.

Appendix A. Supplementary material

Supplementary data to this article can be found online at <https://doi.org/10.1016/j.ces.2020.115644>.

Nomenclature

Latin Symbols

a_p	particle surface area	m^2
a_1	cylinder aspect ratio $a_1 = d/h$	-
a_2	hole aspect ratio $a_2 = d_i/h$	-
A, B	pre-factors in correlations	-
A_T	cross-sectional area of tube	m^2
B, L	characteristic length of tube cross-section	m
d	true diameter of sphere, cylinder or hollow cylinder	m
d_i	inner diameter of hollow cylinder	m
d_p	sauter diameter of particle $d_p = 6 \cdot v_p / a_p$	m
d_v	particle volume equivalent sphere diameter $d_v = \sqrt[3]{6 \cdot v_p / \pi}$	m
D	diameter of tube	m
D_h	hydraulic diameter of tube $D_h = 4 \cdot A_T / P_T$	m
f, f^*	hollow cylinder interpenetration factor	-
f'	friction coefficient $f' = \frac{\Delta P}{H} \cdot \frac{d_p}{\rho \cdot u_0^2} \cdot \frac{\bar{\varepsilon}^3}{(1-\bar{\varepsilon})}$	-
h	height of (hollow) cylindrical particle	m
H	height of tube	m
$H_{\text{mod}}, H_\varepsilon$	different versions of the Hausner ratio	-
k	coefficient of restitution	-
n	exponent	-
N	number of particles per packing	-
ΔP	pressure drop	Pa
P_T	perimeter of tube's cross-section	m
P_{err}	relative pressure drop deviation	-
Re_p	packing Reynolds number $Re_p = \frac{\rho \cdot d_p \cdot u_0}{\eta \cdot (1-\bar{\varepsilon})}$	-
R_z	mean surface roughness depth	m
t	filling time	s
u_0	superficial velocity	$m s^{-1}$
V_T	volume of tube	m^3
v_p	volume of particle	m^3

Greek Symbols

ε	local porosity	-
$\bar{\varepsilon}$	mean bed porosity	-
ε_{inf}	porosity with $\lambda \rightarrow \infty$	-
$\varepsilon_{\text{inf,eq}}$	porosity of equilateral cylinder with $\lambda \rightarrow \infty$	-
ε_{err}	porosity deviation	-

ε_{sc}	porosity of solid cylinder base	-
$\Delta\varepsilon_f$	porosity difference between poured and single dropped bed	-
η	fluid viscosity	Pas
λ	tube-to-particle diameter ratio	-
ρ	material density	kg m^{-3}
Ψ_w	sphericity $\Psi_w = \frac{\pi^{1/3} \cdot (6 \cdot v_p)^{2/3}}{a_p}$	-
ψ	circularity $\psi = \frac{\sqrt{4 \cdot \pi \cdot A_T}}{P_T}$	-
τ	filling time (inverse filling rate) $\tau = t/H$ or $\tau = t/V_T$	s m^{-1} , s cm^{-3}
τ_{95}	filling time at $\phi = 0.95$	-
ϕ	normalized pressure drop	-
$\phi_{0.0122}$	normalized pressure drop at $\tau = 6 \text{ s m}^{-1}$ or $\tau = 0.0122 \text{ s cm}^{-3}$	-

Abbreviations

AG	acrylic glass
Alu	aluminum
PA	polyamide
POM	polyoxymethylen
RLP	random loose packing
RCP	random close packing
SE	standard error
SPD	single particle dropping

References

- [1] A. de Klerk, *AIChE Journal* **2003**, *49*, 2022–2029.
- [2] D. P. Haughey, G. S. G. Beveridge, *The Canadian Journal of Chemical Engineering* **1969**, *47*, 130–140.
- [3] B. Einfeld, K. Schnitzlein, *Chemical Engineering Science* **2005**, *60*, 4105–4117.
- [4] E. Erdim, Ö. Akgiray, I. Demir, *Powder Technology* **2015**, *283*, 488–504.
- [5] J. M. P. Q. Delgado, *Heat and Mass Transfer* **2006**, *42*, 279–310.
- [6] W. van Antwerpen, C. G. du Toit, P. G. Rousseau, *Nuclear Engineering and Design* **2010**, *240*, 1803–1818.
- [7] M. Winterberg, E. Tsotsas, *Chemical Engineering Science* **2000**, *55*, 5937–5943.
- [8] W.-C. Yang, *Handbook of Fluidization and Fluid-Particle Systems, 1st ed.* CRC Press, Boca Raton, FL, **2003**.
- [9] S. Afandizadeh, E. A. Foumeny, *Applied Thermal Engineering* **2001**, *21*, 669–682.
- [10] T. Zeiser, PhD thesis, Universität Erlangen-Nürnberg, **2008**.
- [11] J. Pottbäcker, O. Hinrichsen, *Chemie Ingenieur Technik* **2017**, *89*, 454–458.
- [12] S. Roshani, PhD thesis, University of Leeds, **1990**.
- [13] J. D. Bernal, J. L. Finney, *Nature* **1967**, *214*, 265–266.
- [14] G. Y. Onoda, E. G. Liniger, *Physical Review Letters* **1990**, *64*, 2727–2730.
- [15] H. Zhao, X. AN, Q. Qian, Y. Wu, L. Wang, W. Li, X. Yang, *Particulate Science and Technology* **2019**, *37*, 251–260.
- [16] Z. Xie, X. An, Y. Wu, L. Wang, Q. Qian, X. Yang, *Powder Technology* **2017**, *317*, 13–22.
- [17] C. X. Li, X. Z. An, R. Y. Yang, R. P. Zou, A. B. Yu, *Powder Technology* **2011**, *208*, 617–622.
- [18] Q. Qian, X. An, Y. Wang, Y. Wu, L. Wang, *Particuology* **2016**, *29*, 120–125.
- [19] S. Debbas, H. Rumpf, *Chemical Engineering Science* **1966**, *21*, 583–608.
- [20] E. A. Foumeny, H. A. Moallemi, C. Mcgreavy, J. A. A. Castro, *The Canadian Journal of Chemical Engineering* **1991**, *69*, 1010–1015.
- [21] J. Reimann, J. Vicente, E. Brun, C. Ferrero, Y. Gan, A. Rack, *Powder Technology* **2017**, *318*, 471–483.
- [22] Y. Wu, X. AN, A. B. Yu, *Powder Technology* **2017**, *314*, 89–101.
- [23] Q. Qian, L. Wang, X. An, Y. Wu, J. Wang, H. Zhao, X. Yang, *Powder Technology* **2018**, *325*, 151–160.
- [24] S. Sharma, M. D. Mantle, L. F. Gladden, J. M. Winterbottom, *Chemical Engineering Science* **2001**, *56*, 587–595.
- [25] G. Lumay, N. Vandewalle, *Physical Review E* **2004**, *70*, 051314.
- [26] E. Ben-Naim, J. B. Knight, E. R. Nowak, H. M. Jaeger, S. R. Nagel, *Physica D: Nonlinear Phenomena* **1998**, *123*, 380–385.

- [27] E. Caglioti, V. Loreto, H. J. Herrmann, M. Nicodemi, *Physical Review Letters* **1997**, *79*, 1575–1578.
- [28] P. Philippe, D. Bideau, *Physical Review E* **2001**, *63*, 051304.
- [29] L. Pournin, M. Weber, M. Tsukahara, J.-A. Ferrez, M. Ramaioli, T. M. Liebling, *Granular Matter* **2005**, *7*, 119–126.
- [30] J. Baker, A. Kudrolli, *Physical Review E* **2010**, *82*, 061304.
- [31] M. Bazmi, S. H. Hashemabadi, M. Bayat, *Transport in Porous Media* **2013**, *97*, 119–132.
- [32] D. Gou, X. An, X. Yang, H. Fu, H. Zhang, *Powder Technology* **2017**, *322*, 177–184.
- [33] E. Harris, *Patent*, GB 606867, **1946**.
- [34] J. C. Macrae, W. A. Gray, *The British Journal of Applied Physics* **1961**, *12*, 164–172.
- [35] J. Fernengel, J. von Seckendorff, O. Hinrichsen, *Proceedings of the 28th European Symposium on Computer Aided Process Engineering* **2018**, 97–102.
- [36] E. M. Moghaddam, E. A. Foumeny, A. I. Stankiewicz, J. T. Padding, *Industrial & Engineering Chemistry Research* **2018**, *57*, 14988–15007.
- [37] Z. P. Zhang, L. F. Liu, Y. D. Yuan, A. B. Yu, *Powder Technology* **2001**, *116*, 23–32.
- [38] V. Stanek, V. Eckert, *Chemical Engineering Science* **1979**, *34*, 933–940.
- [39] J. J. Lerou, G. F. Froment, *Chemical Reactor Design and Technology* **1986**, 729–736.
- [40] E. A. Foumeny, A. Kulkarni, S. Roshani, A. Vatani, *Applied Thermal Engineering* **1996**, *16*, 195–202.
- [41] J. Schuster, D. Vortmeyer, *Chemie Ingenieur Technik* **1980**, *52*, 848–849.
- [42] H. Susskind, W. Becker, *Nature* **1966**, *212*, 1564–1565.
- [43] C. W. Crawford, O. A. Plumb, *Journal of Fluids Engineering* **1986**, *108*, 343–347.
- [44] C. M. Wensrich, *Powder Technology* **2012**, *219*, 118–127.
- [45] J. Theuerkauf, P. Witt, D. Schwesig, *Powder Technology* **2006**, *165*, 92–99.
- [46] Z.-Y. Zhou, R.-P. Zou, D. Pinson, A.-B. Yu, *Industrial & Engineering Chemistry Research* **2011**, *50*, 9787–9798.
- [47] W. Nan, Y. Wang, Y. Liu, H. Tang, *Advanced Powder Technology* **2015**, *26*, 527–536.
- [48] R. Guises, J. Xiang, J.-P. Latham, A. Munjiza, *Granular Matter* **2009**, *11*, 281–292.
- [49] X. Garcia, L. T. Akanji, M. J. Blunt, S. K. Matthai, J. P. Latham, *Physical Review E* **2009**, *80*, 021304.
- [50] G. Boccardo, F. Augier, Y. Haroun, D. Ferré, D. Marchisio, *Chemical Engineering Journal* **2015**, *279*, 809–820.
- [51] H. Tangri, Y. Guo, J. S. Curtis, *Powder Technology* **2017**, *317*, 72–82.
- [52] H. Wadell, *The Journal of Geology* **1935**, *43*, 250–280.
- [53] J. G. Parkhouse, A. Kelly, *Proceedings of the Royal Society A* **1995**, *451*, 737–746.
- [54] R. P. Zou, A. B. Yu, *Powder Technology* **1996**, *88*, 71–79.

- [55] A. B. Yu, N. Standish, *Powder Technology* **1993**, 74, 205–213.
- [56] F. Benyahia, K. E. O’Neill, *Particulate Science and Technology* **2005**, 23, 169–177.
- [57] M. Giese, K. Rottschäfer, D. Vortmeyer, *AIChE Journal* **1998**, 44, 484–490.
- [58] F. Benyahia, *Particulate Science and Technology* **1996**, 14, 221–237.
- [59] G. Sonntag, *Chemie Ingenieur Technik* **1960**, 32, 317–329.
- [60] J. Blouwolff, S. Fraden, *Europhysics Letters* **2006**, 76, 1095–1101.
- [61] E. A. Foumeny, S. Roshani, *Chemical Engineering Science* **1991**, 46, 2363–2364.
- [62] M. Novellani, R. Santini, L. Tadrist, *The European Physical Journal B* **2000**, 13, 571–578.
- [63] X. Jia, M. Gan, R. A. Williams, D. Rhodes, *Powder Technology* **2007**, 174, 10–13.
- [64] J. Zhao, S. Li, P. Lu, L. Meng, T. Li, H. Zhu, *Powder Technology* **2011**, 214, 500–505.
- [65] Y. Li, D. Wu, J. Zhang, L. Chang, D. Wu, Z. Fang, Y. Shi, *Powder Technology* **2000**, 113, 176–184.
- [66] Q. Qian, X. AN, H. Zhao, K. Dong, X. Yang, *Powder Technology* **2019**, 343, 79–86.
- [67] K. Dong, C. Wang, A. Yu, *Chemical Engineering Science* **2015**, 126, 500–516.
- [68] A. G. Dixon, *The Canadian Journal of Chemical Engineering* **1988**, 66, 705–708.
- [69] O. Bey, G. Eigenberger, *Chemical Engineering Science* **1997**, 52, 1365–1376.
- [70] E. A. Foumeny, F. Benyahia, *Heat Recovery Systems and CHP* **1991**, 11, 127–130.
- [71] R. Caulkin, A. Ahmad, M. Fairweather, X. Jia, R. A. Williams, *Computers and Chemical Engineering* **2009**, 33, 10–21.
- [72] N. Chikhi, R. Clavier, J.-P. Laurent, F. Fichot, M. Quintard, *Annals of Nuclear Energy* **2016**, 94, 422–432.
- [73] P. Niegodajew, M. Marek, *Powder Technology* **2016**, 297, 193–201.
- [74] J. von Seckendorff, O. Hinrichsen, *The Canadian Journal of Chemical Engineering* **2020**, in press.
- [75] G. E. Mueller, *Powder Technology* **2019**, 342, 607–612.
- [76] J. M. Buchlin, M. Riethmuller, J. J. Ginoux, *Chemical Engineering Science* **1977**, 32, 1116–1119.
- [77] G. S. Beavers, E. M. Sparrow, D. E. Rodenz, *Journal of Applied Mechanics* **1973**, 40, 655–660.
- [78] Y. Dong, B. Sosna, O. Korup, F. Rosowski, R. Horn, *Chemical Engineering Journal* **2017**, 317, 204–214.
- [79] G. E. Mueller, *Powder Technology* **1992**, 72, 269–275.
- [80] C. G. du Toit, *Nuclear Engineering and Design* **2008**, 238, 3073–3079.
- [81] F. A. Schneider, D. W. T. Rippin, *Industrial & Engineering Chemistry Research* **1988**, 27, 1936–1941.
- [82] M. Winterberg, E. Tsotsas, *International Journal of Thermal Sciences* **2000**, 39, 556–570.
- [83] A. Donev, I. Cisse, D. Sachs, E. A. Variano, F. H. Stillinger, R. Connelly, S. Torquato, P. M. Chaikin, *Science* **2004**, 303, 990–993.

-
- [84] W. Man, A. Donev, F. H. Stillinger, M. T. Sullivan, W. B. Russel, D. Heeger, S. Inati, S. Torquato, P. M. Chaikin, *Physical Review Letters* **2005**, *94*, 198001.
- [85] S. Khirevich, A. Hölzel, D. Hlushkou, U. Tallarek, *Analytical Chemistry* **2007**, *79*, 9340–9349.
- [86] S. Ergun, *Chemical Engineering Progress* **1952**, *48*, 89–94.
- [87] P. Carman, *Transactions of the Institution of Chemical Engineers* **1937**, *15*, 150–166.
- [88] R. Singh, R. S. Saini, J. S. Saini, *Solar Energy* **2006**, *80*, 760–771.
- [89] D. Nemeč, J. Levec, *Chemical Engineering Science* **2005**, *60*, 6947–6957.
- [90] B. Einfeld, K. Schnitzlein, *Chemical Engineering Science* **2001**, *56*, 4321–4329.
- [91] K. G. Allen, T. W. von Backström, D. G. Kröger, *Powder Technology* **2013**, *246*, 590–600.
- [92] I. F. Macdonald, M. S. El-Sayed, K. Mow, F. A. L. Dullien, *Industrial & Engineering Chemistry Fundamentals* **1979**, *18*, 199–208.
- [93] W. Reichelt, *Chemie Ingenieur Technik* **1972**, *44*, 1068–1071.
- [94] K. Vollmari, T. Oschmann, S. Wirtz, H. Kruggel-Emden, *Powder Technology* **2015**, *271*, 109–124.
- [95] R. P. Zou, A. B. Yu, *Chemical Engineering Science* **1996**, *51*, 1177–1180.
- [96] R. K. McGearry, *Journal of the American Ceramic Society* **1961**, *44*, 513–522.

5 Experimental and Numerical Analysis of Void Structure in Random Packed Beds of Spheres

Abstract

The prediction of the pressure drop of packed beds requires an accurate estimation of the packed-bed porosity as its error propagation multiplies the occurring errors by a factor of about four. For a better understanding of the packed bed's local porosity characteristics, a comprehensive x-ray tomography study was performed investigating and correlating the void structure of packed beds made of smooth, mono-sized spheres in cylindrical confining walls having tube-to-particle diameter ratios $\lambda = 3.0$ to 9.0 reinforced by numerically generated packed beds of $\lambda = 1.1$ to 9.0 . An in-depth analysis of the obtained oscillating void profiles is performed, discussing the locations and heights of porosity extrema. Most importantly, a significant and in parts surprising extrema formation in the tube's center is described, especially present for $\lambda < 6$, which is assumed to have a predominant effect on the packed bed's pressure drop.

This article was published in:

Powder Technology, 380, J. von Seckendorff, K. Achterhold, F. Pfeiffer, R. Fischer, O. Hinrichsen, Experimental and numerical analysis of void structure in random packed beds of spheres, 613-628, Copyright Elsevier (2021). DOI: 10.1016/j.powtec.2020.11.026.

Reprint Permission:

As an Elsevier journal author, you have the right to Include the article in a thesis or dissertation (provided that this is not to be published commercially) whether in full or in part, subject to proper acknowledgment; see [the Copyright page](#) for more information. No written permission from Elsevier is necessary.

This right extends to the posting of your thesis to your university's repository provided that if you include the published journal article, it is embedded in your thesis and not separately downloadable.

5.1 Introduction

Packed beds of homo-sized shapes are studied in a wide range of industrial and scientific applications, ranging from chromatography packed columns [1, 2], packed-bed reactors in heterogeneous catalysis [3], packed columns used in separation processes [4] to nuclear pebble bed reactors [5]. The incorporated shaped bodies are frequently of spherical or cylindrical shape and come in sizes ranging from micrometers for chromatography columns to several centimeters in nuclear pebble bed reactors. It is evident, that shaped bodies of sizes smaller than approximately 0.5 mm behave different to those of larger size, as interparticle forces become dominant with decreasing size, leading to packed beds with increasing void content [6, 7]. Thus, only the packings of particles beyond this value are investigated.

Although called random, packing elements within a random packed bed tend to order along the confining wall. Depending on the particle's shape, this imposed order may reach some particle diameters into the tube. For example in a packing of spheres, this order can be observed up to 4 or 5 sphere diameters away from the confining wall [8] resulting in an increase of average bed porosity for tube-to-particle diameter ratios $\lambda = D/d_p < 10$. Studying catalytic multitubular reactors where $\lambda = 4$ to 7 this typically named *Wall Effect* requires a thorough investigation of local packing structure, as it influences fluid dynamics [9, 10], heat [11] and mass transfer [12, 13].

Besides the Wall Effect, the packing of particles is further influenced by the particle material, shape and size distribution, the container material and shape and the applied deposition and compaction methods [14–16]. In spite of, this work focusses solely on the influence of Wall Effect keeping all other parameters constant. Thus, packed-beds of mono-sized, smooth spheres packed into cylindrical containers of tube-to-particle diameter ratios smaller 10, comparing experimental and numerical approaches are adressed.

5.2 State of the art

5.2.1 Axially- and azimuthally-averaged radial porosity profiles

The local structure of packed beds is typically described using the azimuthally and axially averaged radial porosity profile, giving the porosity $\varepsilon(r)$ at a certain distance from the confining tube wall in particle diameters $z_r = (R-r)/d_p$, with R representing the tube radius and r the radial location. Typical experimental methods comprise the solidification of the packed bed with subsequent slice-cutting on a lathe [17–23], the incremental filling of a centrifuged packed bed with small amounts of liquid [24–27] or the projection of the bed using radiography [28], tomography [29–33], magnetic resonance imaging [34–36] or fluorescence [37, 38]. While the solidification/cutting method is known to struggle with particle loss during machining and the inaccuracy of cutting tools, the incremental filling procedure needs to exclude particle movement during bed centrifugation and a proper determination of very small liquid level increments while considering meniscus influences. Projection methods are advantageous due to their non-destructive nature while giving slices of the packed beds in commonly higher resolution compared to

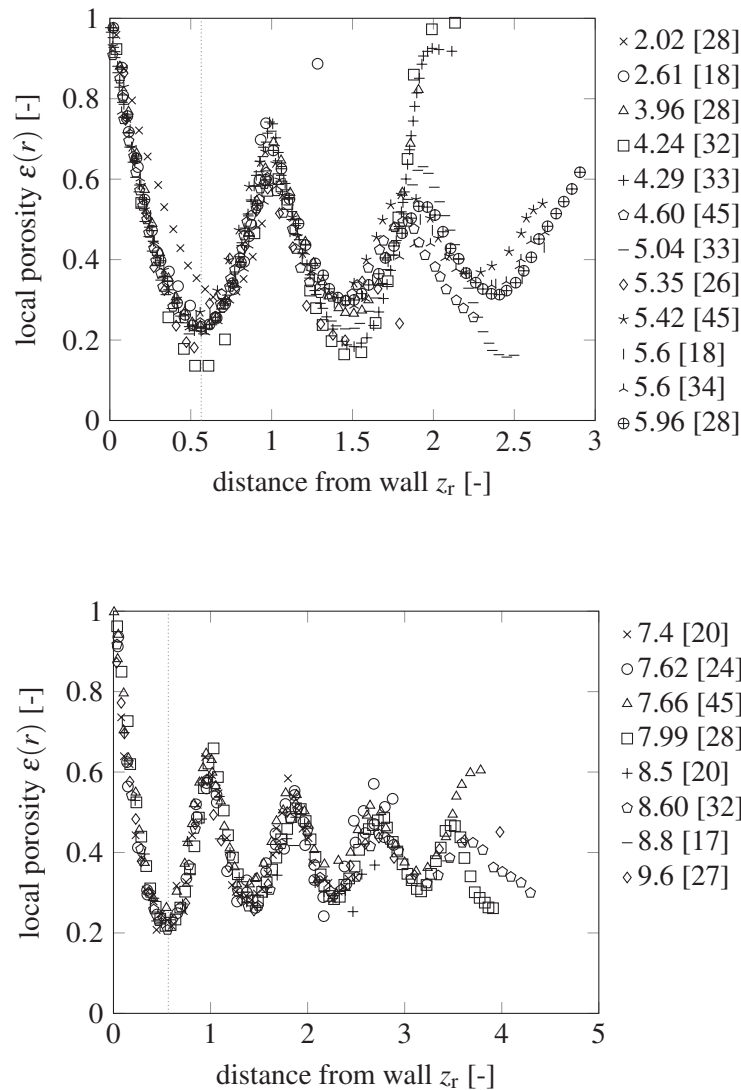


Figure 5.1: Experimental data for radial profiles taken from literature for (a) $\lambda = 1$ to 7 and (b) $\lambda = 7$ to 10. Please consider the maximum wall distance equals $\lambda/2$.

manual machining. However, the consecutive image analysis requires the careful selection of a threshold value for distinguishing between solid and void on typically faded particle edges, leading to general inaccuracies. While most researchers determine the local porosity directly from the packed bed slices by calculating void versus solid content, Mueller [28] selected an approach to determine the sphere centers by radiographic scanning of sphere packings where each sphere has a metal micro-sphere center. Only recently, Reimann et al. [39] adopted this by determining sphere centers from x-ray tomography images. Based on the sphere center locations, the radial porosity profile can be mathematically reconstructed [40–44] and the resulting plots are independent of the selected slicing resolution and threshold values selected for image analysis.

A selection of experimental data is depicted in Figs. 5.1a and 5.1b, sorted into two λ ranges: 1 to 7 and 7 to 10. Data for radial profiles of $\lambda > 10$ are not considered, as a good experimental consensus is already

gained. Some typical properties are generally accepted regarding curve shape: the porosity directly at the tube wall is one; the curve resembles a damped oscillation function with distinct extrema reaching 4 to 5 particle diameters into the tube; the first minimum ε_{\min} is at $z_r \approx 0.5$ and the first maximum ε_{\max} is at $z_r \approx 1.0$. This profile can be explained with the formation of rings of spheres starting with a high degree of order adjacent to the tube wall, reaching 4 to 5 rings into the packing with decreasing distinctness and order until reaching statistical randomness in the bulk part of the packing, presuming a sufficiently high λ . A closer look at Figs. 5.1a and 5.1b reveals the agreement of experimental data for $\lambda > 7$ and some disagreement for smaller values. Here, extreme values of porosity may be gained in the center of the containers. Moreover, higher amplitudes of oscillation can be observed. The phenomena of occurrence and manifestation of these deviations are still unknown and need in-depth investigation on a much broader database.

There are some models trying to describe the radial porosity distribution of sphere packings [46]. These comprise exponential decay functions [47–52], which ignore the oscillation close to the wall, damped oscillation functions with an exponentially damped cosine oscillation [8, 10, 22, 53, 54] or a Bessel function of zero order [28, 55, 56], approaches incorporating λ -specific adaptations [28, 43, 45]; and mathematical sphere center re-estimations derived from experimentally obtained radial porosity profiles with subsequent re-calculation of the radial porosity distribution [57–61]. In Fig. 5.2, selected correlations are plotted along with literature data for tube-to-particle diameter ratios around 4. It can be seen, that a significant deviation between prediction and experiment exists which may need further improvement, especially regarding the prediction of the packings behaviour in the tube's center.

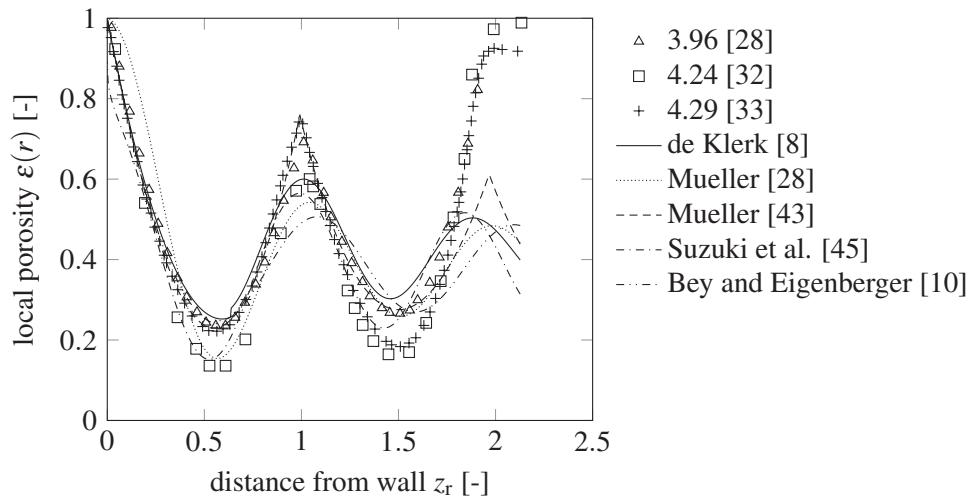


Figure 5.2: Comparison of literature data for $4 \leq \lambda \leq 4.25$ and literature correlations plotted for $\lambda = 4.25$.

5.2.2 Mean bed porosities

Mean bed porosities $\bar{\varepsilon}$ are obtained by experiment or weighted integration of radial porosity profiles. For packings of smooth, mono-sized spheres filled using any measures and intensities of bed densification, a considerable experimental database regarding the λ - $\bar{\varepsilon}$ -interplay is available and depicted in Fig. 5.3.

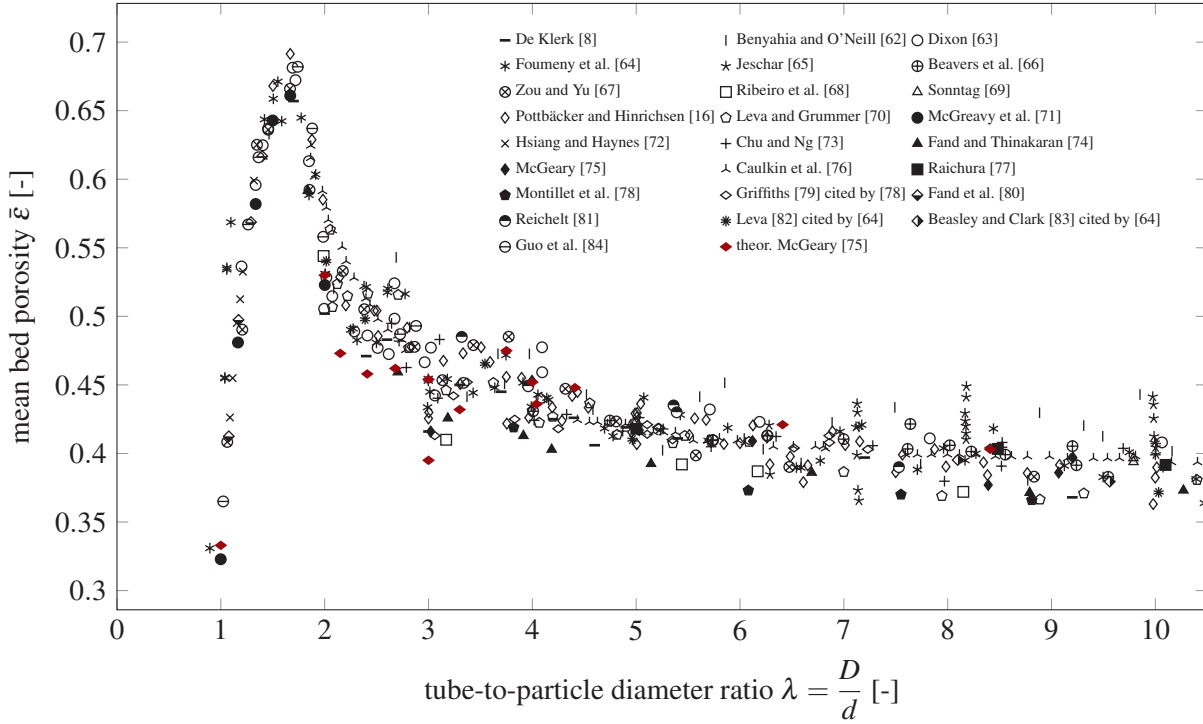


Figure 5.3: Review of experimental results for the mean bed porosity $\bar{\epsilon}$ when varying tube-to-particle diameter λ for mono-sized, smooth, dense packed spheres. Figure taken from [46].

Typically, this curve is divided into two regions: I) $1 \leq \lambda \leq 1.866$ where the mean bed porosity can be analytically determined [85] and II) $\lambda > 1.866$ or 2 where the porosity decreases until reaching a nearly constant value $\bar{\epsilon}_{\text{inf}}$ for $\lambda > 10$. A considerable amount of correlations exist, describing this trend within small deviations [8, 28, 62–69, 74, 79, 86–91]. Among these, only Zou and Yu [67] defined a third intermediate region between $1.866 \leq \lambda \leq 4$, as an additional maximum at $\lambda = 3.95$ was detected, with a preceding minimum around $\lambda = 3$. Further discontinuities were predicted based on theoretical considerations [75] and were observed in experimental studies [8]. However, most frequently abnormal values were explained with typically large measurement uncertainties or not reported at all. Table 5.1 gives an overview of λ locations relating to reported extreme values for mean bed porosity. The existence of

Table 5.1: Review of reported extrema locations.

Source	λ of reported maxima	λ of reported minima	Type
McGeary [75]	2.68, 3.75, 4.41	2.41, 3.00, 4.04	theoretical
Zou and Yu [67]	3.95	≈ 3.0	experimental
De Klerk [8]	-	2.4, 3.0, 4.6	experimental
Figure 5.3	$\approx 2.7, \approx 4.0$	≈ 3.0	reviewed results

extrema in the λ - $\bar{\epsilon}$ plot is explained with favourable and unfavourable particle ring multiples. For instance, at $\lambda = 3.0$ a complete ring of six perfectly fitting spheres encompasses a centrally located sphere stack [75] which in reverse would lead to an extremely low porosity value in the tube center when considering the respective radial porosity profile.

Although a considerable amount of data points exists when merged into one plot, every data source performed measurements under different conditions leading to a certain data scatter that makes it impossible to reliably detect discontinuities. Even without changing conditions, the uncertainties among single data series is quite large [16, 62]. It is thus decided to use numerical packing means for a highly reproducible packing generation untainted by experimental errors in order to study the details of local and mean porosity of slender packed beds of $\lambda < 10$.

5.2.3 Numerical packed bed generation

The numerical packing of spheres into rigid containers itself is well studied since considerable time. Today, a broad selection of commercial and free software packages are available. Typically, packed beds were generated in order to study fluid dynamics, heat and mass transport phenomena [92–97]. Moreover, packed bed studies comprising the influence of particle material properties [98, 99], packed bed compression by vibration [100], tube wall structure [101] and particle shape [95, 102–107] were performed. However, in spite of some constituting works [99, 108] no study exists that explicitly studies the wall effect on local and mean porosity in the herein presented highly resolved manner.

The herein used numerical packing procedure is validated with own results of x-ray tomographically scanned experimental packed beds of mono-sized spheres of different λ . This alone is the most extensive experimental study of this kind for wall affected packed beds which is up to date available in the literature.

5.3 Experimental and numerical setup

5.3.1 Analysis of local packing structure using X-ray CT

Micro x-ray computed tomography scans were performed using 4 mm and 5 mm high precision steel spheres (VTLG Europe Ltd., Germany) with a density $\rho = 7780 \text{ kg m}^{-3}$, filled into 15 mm, 20 mm, 25 mm, 30 mm, 35 mm, 40 mm and 45 mm cylindrical plexiglass containers having a constant height of 100 mm. Thus, the investigated packings have tube-to-particle diameter ratios $\lambda = 3, 4, 6, 6.25, 7, 8$ and 9 and a tube height-to-particle diameter ratio of $\kappa = 20$ and 25. The whole packing height is scanned with a resolution of 0.1 mm, thus resulting in 1000 horizontally sliced images per run.

The exact particle mass was determined with a sample of 1000 particles and the deviation was less than 0.1 %. The density and its deviation, which was about 0.5 %, was determined using a pycnometer with a volume of 50 ml as the mean of ten measurements of 50 particles each. The exact volumes of the tubes were determined by filling them up with a known amount of water. The mean of three measurements was noted. Particle filling was performed applying a filling machine consisting of a horizontal tube and a vibrating motor to move the particles slowly to an outlet funnel leading to the plexiglass tubes whereby the

filling rate was kept constant at about 500 s m^{-1} tube height. The reproducibility of packing generation was discussed earlier [16].

5.3.2 Image analysis

In order to obtain the center position of each sphere, the following procedure was performed: the scans were stacked in FIJI (FIJI Is Just ImageJ, an open source image processing program) to bundles of 250 each and cropped to the inner tube radius. The particle edges are highlighted applying the Build-In find-edges-tool. A black-white threshold is set to binarize the image stacks. Finally, the Hough Circle Transform Plug-In (UCB Vision Science) was used as a circle finding algorithm giving each circles position (x_0 and y_0) and its diameter. In regard to data reduction, only circles with diameters larger than 3 mm were considered. An exemple depiction of the procedure is displayed in Fig.5.4. A Matlab[®] script

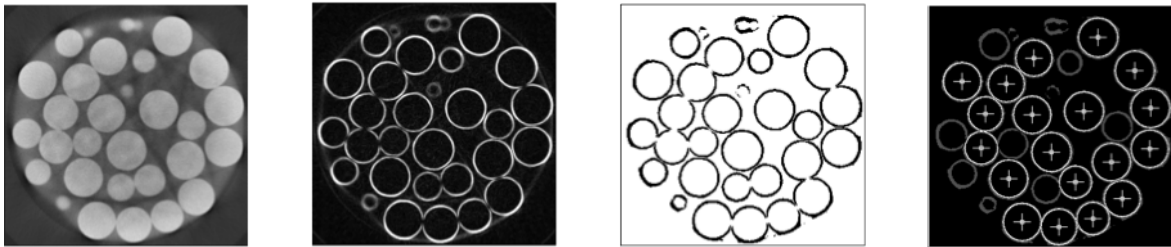


Figure 5.4: Exemplarily depiction of image analysis procedure using FIJI (ImageJ) for detecting circles and their respective centres and diameters comprising (a) the cropped CT-scan, (b) the find-edges-tool, (c) the binarization, and (d) the Hough Circle Transform Plug-In.

is created searching for similar circle positions (x_0 and y_0) in consecutive image counts ($0.1 \cdot z$). The obtained values for x_0 and y_0 are averaged and for the final z_0 -position, the image count of the circle with the largest diameter is sought.

5.3.3 Calculation of axial and radial porosity profiles

Knowing the center positions of each sphere, the axial and radial porosity profiles can be determined by known procedures [40]. Generally, these procedures can be divided into volume and area-based approaches. Here, the volume based solution is selected for the calculation of the axial porosity profile, whereas a simplification is supposed, leading to a pseudo-volume based approach for the determination of the respective radial porosity profiles.

Gaining the axial distribution, horizontal slices are cut forming disk-shaped bins with height Δz . The intersected volume $V_{n,i}$ between a sphere of index i , radius r and axial center position $z_{0,i}$ and a plane at axial position z_n , can be calculated with the formulas known for spherical caps (Eq. (5.1)).

$$V_{n,i} = \frac{\pi \cdot h_i^2}{3} \cdot (3 \cdot r - h_i) \quad \text{with} \quad h_i = r - |(z_{0,i} - z_n)| \quad (5.1)$$

Consequently, regarding disk-shaped bins, each sphere has either no intersection with the upper (z_{n+1}) or lower (z_n) bin limit slice ($\Delta V_{n,i} = V_{n+1,i} - V_{n,i} = 0$), intersects one of them, but not the other ($\Delta V_{n,i} = V_{n,i}$ or $\Delta V_{n,i} = V_{n+1,i}$), or intersects both ($\Delta V_{n,i} = V_{n+1,i} - V_{n,i}$). For each bin, the portion of all containing sphere caps and sphere slices per total bin volume results in the axial voidage distribution $\varepsilon(z_n)$.

$$\varepsilon(z_n) = 1 - \frac{4 \cdot \sum_i \Delta V_{n,i}}{\pi \cdot D^2 \cdot \Delta z} \quad (5.2)$$

The exact determination of the radial porosity distribution is more complex, as cylindrical cuts with spheres resulting in ring-shaped bins with constant thickness Δr need to be solved. Here a simplification is used: with already having sphere fragments of sphere index i sorted into horizontal bins of index n than for a sufficiently small Δz , here $1/300 \cdot d_p$, a cylindrical shape of these fragments based on an averaged radius $r_{n,i}$ may be assumed. A convergence analysis on the selection of Δz has been performed to verify the sufficiency of this approach.

$$r_{n,i} = \sqrt{\frac{\Delta V_{n,i}}{\pi \cdot \Delta z}} \quad (5.3)$$

It is now sufficient to simply determine the 2D cross-section of cutting two circles, in particular of each fragment circle with radius $r_{n,i}$ and each bin circle with radius r_m . Herefor, the radial position $r_{0,i} = \sqrt{x_{0,i}^2 + y_{0,i}^2}$ for each sphere fragment is determined. The cross-section $S_{m,n,i}$ of two intersecting circles is calculated as follows:

$$S_{m,n,i} = r_{n,i}^2 \cdot \arccos\left(\frac{a}{r_{n,i}}\right) - a \cdot \sqrt{r_{n,i}^2 - a^2} + r_m^2 \cdot \arccos\left(\frac{b}{r_m}\right) - b \cdot \sqrt{r_m^2 - b^2} \quad (5.4)$$

with $a = \frac{r_{n,i}^2 - r_m^2 + r_{0,i}^2}{2 \cdot r_{0,i}}$ and $b = \frac{r_m^2 - r_{n,i}^2 + r_{0,i}^2}{2 \cdot r_{0,i}}$.

Consequently, regarding ring-shaped bins, each obtained sphere fragment has either no intersection with the outer (r_{m+1}) or inner (r_m) bin limiting circle ($\Delta S_{m,n,i} = S_{m+1,n,i} - S_{m,n,i} = 0$), intersects one of them, but not the other ($\Delta S_{m,n,i} = S_{m,n,i}$ or $\Delta S_{m,n,i} = S_{m+1,n,i}$), or intersects both ($\Delta S_{m,n,i} = S_{m+1,n,i} - S_{m,n,i}$). For each bin, the portion of all containing sphere fragments with index i, n per total ring-shaped bin volume results in the radial voidage distribution $\varepsilon(r_m)$.

$$\varepsilon(r_m) = 1 - \frac{\sum_n \sum_i (\Delta S_{m,n,i} \cdot \Delta z)}{\pi \cdot H \cdot (r_{m+1}^2 - r_m^2)} \quad (5.5)$$

5.3.4 Numerical packing generation with DigiDEM™

Packing generation is performed incorporating the DigiDEM™ code, a voxelated particle simulation software incorporating a digital packing algorithm based on the *Monte Carlo Approach* whilst explicitly considering physical interaction forces similar to the *Discrete Element Method* and is elsewhere described in more detail [30, 109]. The packing procedure is identical to the one we already described [108]. In a nutshell: spheres with diameters of 100 voxel at resolution 10 voxel mm⁻¹ and set material properties such as density $\rho = 3000 \text{ kg m}^{-3}$, coefficient of restitution $e = 0.3$, coefficient of friction $\mu = 0.7$ and

Poisson's ratio $\nu = 0.3$ are filled into tubes of constant height $H = 3000$ voxel and varying diameter $D = 110$ voxel to 1000 voxel, thus representing packed beds with tube-to-particle diameter ratios $\lambda = 1.1$ to 9 . The final packing is again represented by sphere center coordinates. Regarding reproducibility, the packing of relative tube size $\lambda = 6.25$ was packed ten times and the mean relative standard error regarding the profiles was 1% and the relative standard error regarding the average bed porosity was 0.5% .

5.4 Results an discussion

5.4.1 Experimental results of X-ray study

The packed beds, obtained by x-ray tomography and reconstructed to a 3d packing for all investigated tube-to-particle diameter ratios are displayed in Fig. 5.5.

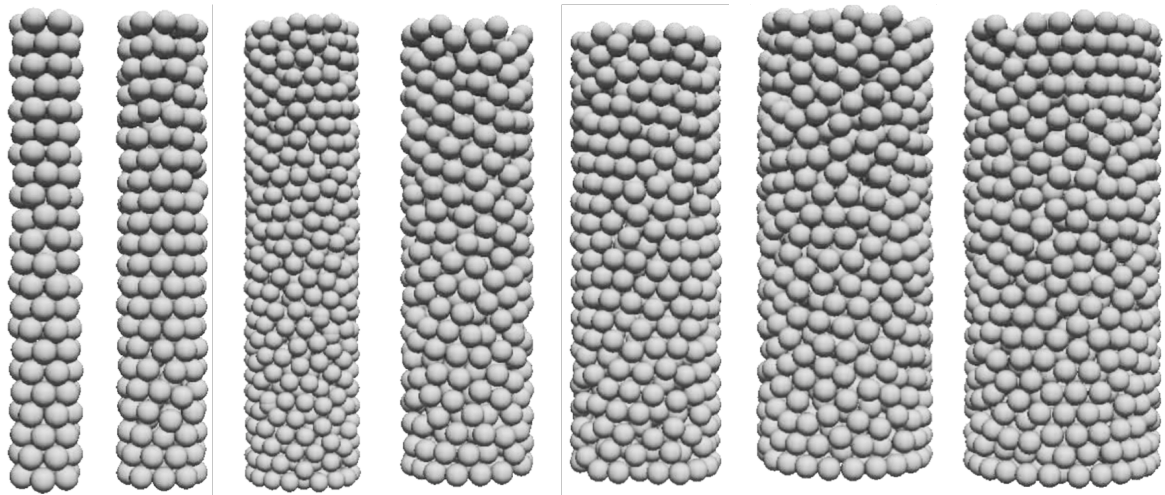


Figure 5.5: Reconstructed 3d packed beds of $\lambda = 3.0, 4.0, 6.25, 6.0, 7.0, 8.0$ and 9.0 based on the determined sphere center positions. The third scan with $\lambda = 6.25$ was the only scan with a packing of 4 mm spheres thus having a different scaling.

From these images, an underlying regular structure can be observed for the packed beds of $\lambda = 3.0$ and 4.0 , based on the fact, that repeating layers of spheres are formed, where the subsequent layer bridges the gaps of the previous, at least for the spheres adjacent to the wall. All other packed beds are significantly more random at first appearance. It is to be emphasized, that these packed beds were not subjected to any means of densification, which is known to significantly increase the packed bed's regularity [39].

Sphere centers

The underlying sphere centers were plotted irrespective their axial location as depicted in Fig. 5.6 for the packed beds of $\lambda = 3, 4, 6, 7, 8$ and 9 . In general, the sphere centers form rings of decreasing order and distinctness when increasing the distance from the wall before reaching complete randomness in the tube center for high λ . This behaviour was described earlier [28]. Furthermore, comparing the sphere center plots obtained with different λ , it appears that the order and distinctness of sphere center rings may depend on λ , as for instance, the second ring is more pronounced for lower λ .

Besides the sphere centers, the circumferences of spheres of two adjacent sphere layers (of distance d_p) were highlighted, depending on their radial position. For instance, regarding Fig. 5.6a, the spheres adjacent to the outer wall were highlighted in yellow for the initial and green for the subsequent layer, and the spheres further away from the wall were highlighted in red and blue, respectively. As already

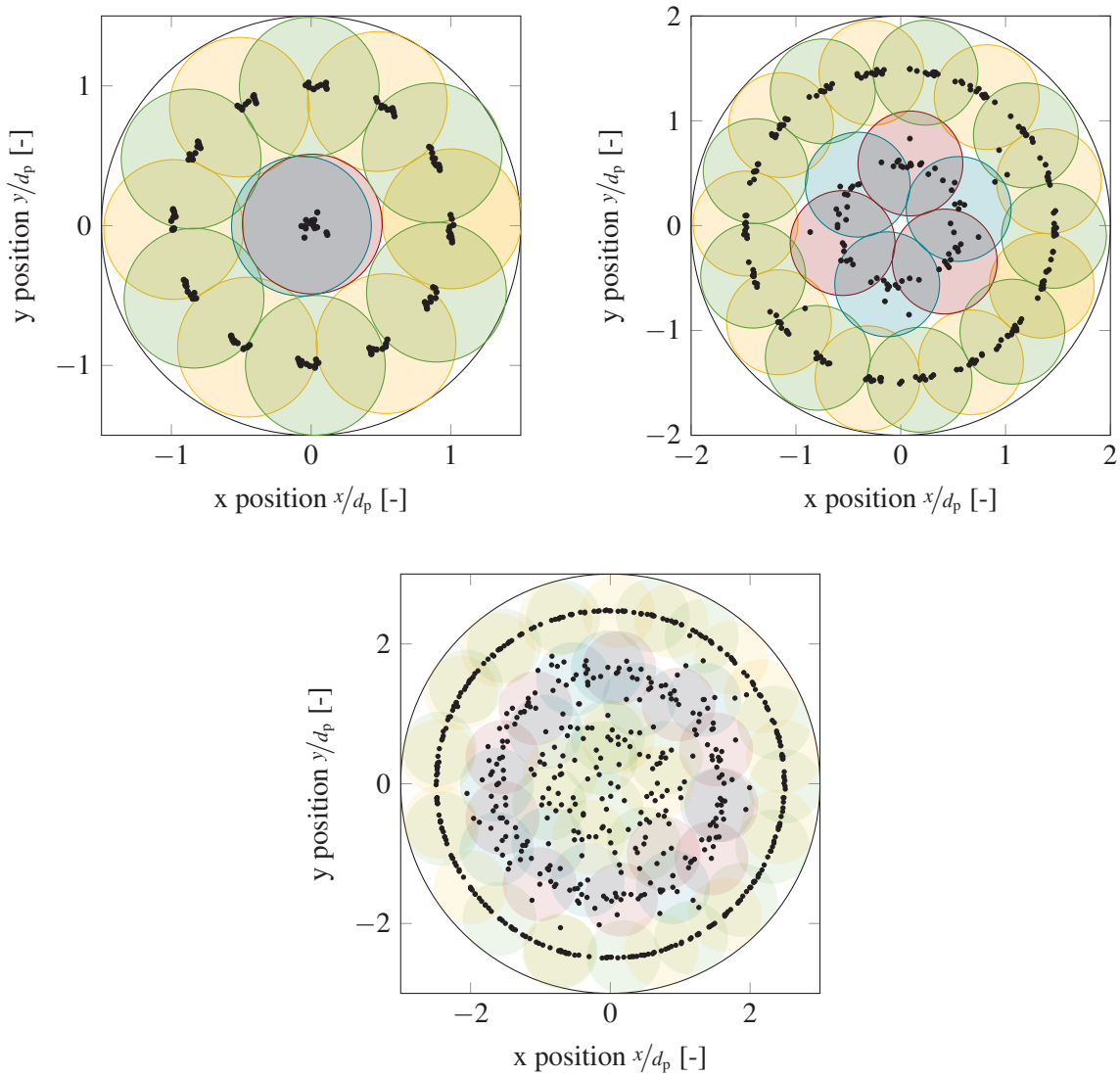


Figure 5.6: Plot of sphere center positions for (a) $\lambda = 3.0$, (b) $\lambda = 4.0$, (c) $\lambda = 6.0$.

addressed, a highly regular structure with an outer ring of six spheres bridging the gaps of the previous layer can be seen, completed with a pile of spheres in the tube center. Consequently, each sphere layer consists of seven spheres.

A similar structure can be identified for the packed bed of $\lambda = 4$ (cf. Fig. 5.6b), with the difference, that the outer ring comprises nine and the inner ring three spheres, totaling 12. In contrary to the packed bed of $\lambda = 3$, the center of the tube has no sphere center resulting in a central void.

No similar structural characteristics can be identified for packed beds of higher λ . Although the sphere circumferences are highlighted in Fig. 5.6c as well, spheres of consecutive layers are not bridging the gaps, and the spheres of the inner rings interfere with the spheres adjacent to the wall, breaking up a strict ring-like placement.

Axially- and azimuthally-averaged radial porosity profiles

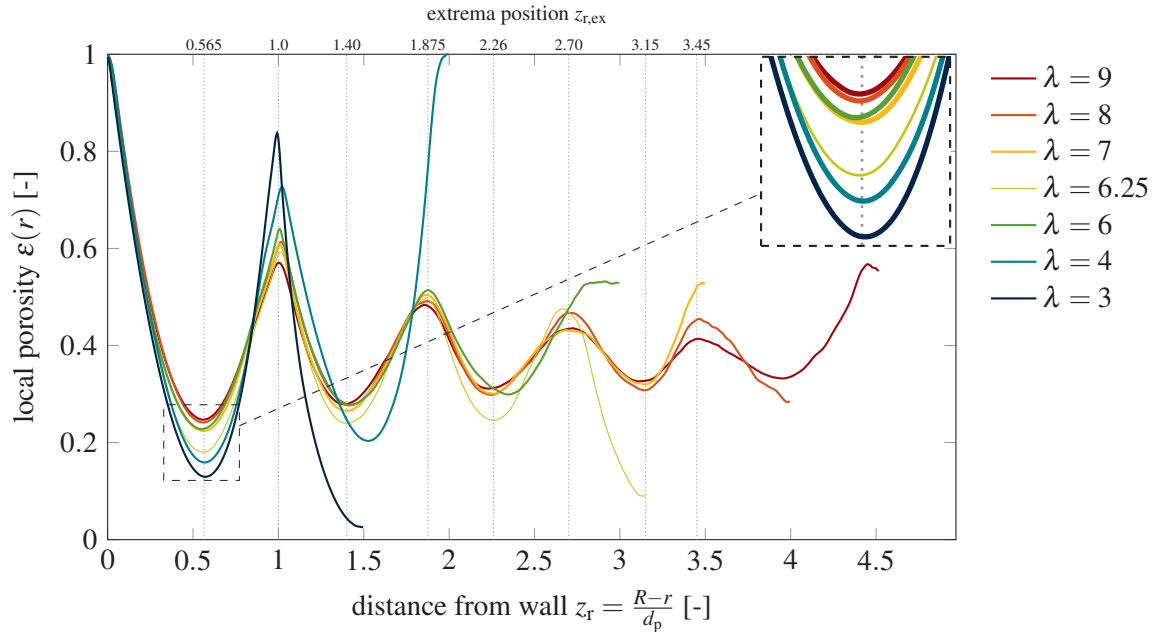


Figure 5.7: Axially- and azimuthally-averaged local porosity distribution in radial direction for $\lambda = 3.0$ to 9.0 .

The radial porosity profiles calculated from CT data are depicted in Fig. 5.7. The general trend is as expected, starting at unity directly at the wall and from there describing an oscillation profile, increasingly damped with increasing distance from the confining wall. However, some special characteristics can be identified:

- i) The first minimum and maximum: The porosity of the first minimum, representing the wall-adjacent ring of sphere centers increases with increasing λ before reaching an infinite value $\varepsilon_{\min 1} \approx 0.25$. This feature is explicitly depicted in the enlargement of Fig. 5.7. Similarly, the consecutive maximum is reduced for larger packed beds. Consequently, the curves representing different λ do intersect in one specific point. This results in a decreasing distinctness of a parabola shape of the first ring of spheres to a more sinusoidal shape for larger packed beds. The sum of these described characteristics proves a decreasing order of the first sphere ring with increasing λ .
- ii) The tube center: The local porosity in the tube center may have the extreme value 0 for $\lambda = 3$ and 1 for $\lambda = 4$. While the existence of packed beds with a central hole, represented by a central value of 1 was already shown in the literature (see Fig. 5.1b and [32, 110]), the existence of a packed bed with a central value of 0 was not experimentally described yet. For larger packed beds, the central values are in all investigated cases more extreme than expected, which is in accordance with results elsewhere published (see Fig. 5.1b). Besides the central value, the locations and values of the one or two previous extrema are affected as well, indicating that interference effects of particle rings occur in the tube center.

iii) The period of oscillation: The position of the extrema are generally accepted to be exactly 0.5 for the first minimum and 1.0 for the corresponding maximum. No information can be found regarding any consecutive extrema position. While the data presented here can confirm the first maximum at exactly 1.0, the first minimum is moved to slightly higher values of around 0.565. However, a close look to the enlargement of Fig. 5.7 reveals, that this may be slightly dependant on λ , as larger values are obtained for $\lambda = 3$ and smaller values for $\lambda = 8$ and 9. The subsequent extrema positions are more or less λ independant at $z_r = 1.40, 1.875, 2.26$ and 2.7 , followed by 3.15 and 3.45 . However, the innermost extremum of a certain packing may differ from this rule, as in the tube center the wall effect from the opposite wall influences the packing. The respective extrema distances starting from the wall are $0.565, 0.435, 0.4, 0.475, 0.385$ and 0.44 between minimum and maximum respectively, and $1.0, 0.835, 0.875, 0.86, 0.825$ between extrema of same kind, the period of oscillation, which is not at all constant.

Data prediction by correlations

With the porosity profiles of $\lambda \geq 6$ being very similar, they are plotted together in Fig. 5.8 along with selected correlations plotted for $\lambda = 8$ including different versions of the exponentially damped cosine function by de Klerk [8], Suzuki et al. [45] and Bey and Eigenberger [10], the Bessel function by Mueller [28] and the approach of parabola chains by Mueller [43]. An insufficient representation of the above described oscillation period characteristics are most prominent in the correlation of Bey and Eigenberger [10], leading to a positive offset of almost half a period in the tube's center. This offset is smaller but still clearly visible when considering the correlation of de Klerk [8] and the Bessel function of Mueller [28]. The porosity of the first minimum is considerably underestimated using Mueller's Bessel

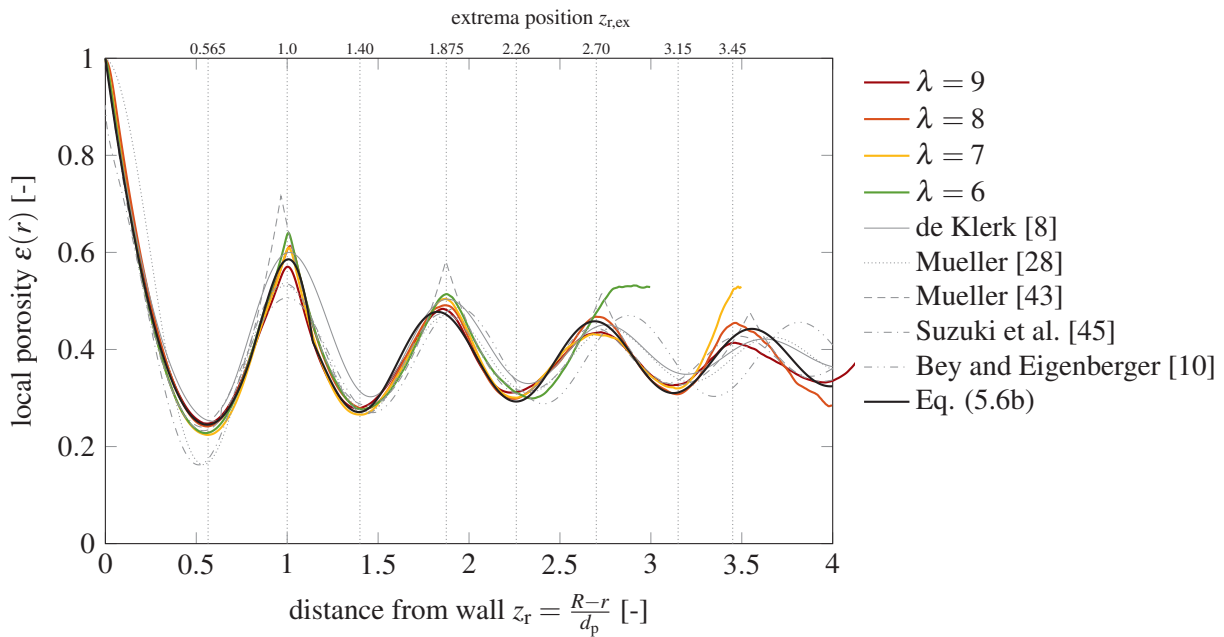


Figure 5.8: Comparison of experimental data with literature correlations and Eq. (5.6b) plotted for $\lambda = 8.0$

function [28] but also Suzuki et al.'s solution [45]. The slightly inconvenient approach of parabola chains by Mueller [43], however, gives a good representation of oscillation period but overestimates all maxima. The Sum of Square Errors (SSE) obtained by using the existing correlations with the given parameters for our data is displayed in Table 5.2. Furthermore, the parameters of the existing correlations are fitted

Table 5.2: Sum of Standard Error (SSE) of selected literature correlations and the correlation of Eq. (5.6a) in regard to the experimental data, and the SSE of the selected literature correlations fitted to the data of $\lambda = 9$.

SSE	$\lambda = 3$	$\lambda = 4$	$\lambda = 6$	$\lambda = 7$	$\lambda = 8$	$\lambda = 9$	$\lambda = 9(\text{fit})$
Bessel function by Mueller [28]	14.39	11.23	2.924	3.002	2.318	4.234	3.105
Parabola approach by Mueller [43]	15.47	6.685	1.346	1.440	0.965	2.231	1.496
Damped cosine function by Suzuki et al. [45]	4.992	10.03	2.106	1.054	1.398	1.964	1.755
Damped cosine function by de Klerk [8]	6.208	9.773	1.439	1.541	1.103	2.932	1.344
Damped cosine function by Bey and Eigenberger [10]	16.45	13.72	2.202	4.090	4.166	5.437	1.074
Damped cosine function as of Eq. (5.6a)	6.418	6.644	0.742	0.888	0.699	1.089	-

to our data set of $\lambda = 9$ to evaluate the potential of each correlation. From the existing correlations, the correlations of Mueller [43] and Suzuki et al. [45] perform best in predicting the experimental data. However, fitting the data to the correlations, the best results are obtained using the correlation of Bey and Eigenberger [10]. Adapting this correlation leads to the development of Eq. (5.6a). Here, a λ -dependent representation of $\varepsilon_{\min,1}$ is introduced. Furthermore, parameters a , b , and c are fitted to the experimental data. A slight λ -dependence of parameter b has been found, with $\bar{\varepsilon}_{\text{inf}} = 0.38$ and $z_{r,\min,1} = 0.56$.

$$\varepsilon_1(r) = \varepsilon_{\min,1} + (1 - \varepsilon_{\min,1}) \cdot \left(\frac{z_r}{z_{r,\min,1}} - 1 \right)^2 \quad \text{for } z_r \leq z_{r,\min,1} \quad (5.6a)$$

$$\varepsilon_2(r) = \bar{\varepsilon}_{\text{inf}} + (\varepsilon_{\min,1} - \bar{\varepsilon}_{\text{inf}}) \cdot \exp \left[-a \cdot \left(\frac{z_r}{b} - 1 \right) \right] \cdot \cos \left[\frac{\pi}{c} \cdot \left(\frac{z_r}{b} - 1 \right) \right] \quad \text{for } z_r > z_{r,\min,1}$$

$$\text{with } a = 0.138, b = 0.652 \cdot \lambda^{-0.094}, c = 0.806$$

$$\text{and } \varepsilon_{\min,1} = -0.0033 \cdot \lambda^2 + 0.0596 \cdot \lambda - 0.0208 \quad \text{for } \lambda \leq 10$$

$$\varepsilon_{\min,1} = 0.24 \quad \text{for } \lambda > 10$$

From Table 5.2 it can be seen that Eq. (5.6a) is capable to give a significantly better representation of all data sets. A further improvement of correlation (5.6a) is obtained when implementing a linear interpolation of both correlation parts. This also results in a continuous equation.

$$\varepsilon(r) = d \cdot \varepsilon_1(r) + (1 - d) \cdot \varepsilon_2(r) \quad \text{with } d = \begin{cases} 1 & \text{for } z_r \leq z_a \\ \frac{z_r - z_e}{z_a - z_e} & \text{for } z_a < z_r < z_e \\ 0 & \text{for } z_r \geq z_e \end{cases} \quad (5.6b)$$

Herein, $z_a = 0.8$ and $z_e = 1.14$ are used. It is further to be noted that parameter a characterizes the damping and is assumed to alter with packing mode and material properties. Thus, a dependence on the infinite porosity $\bar{\varepsilon}_{\text{inf}}$ is expected [16]. However, this influence is yet not investigated in detail and should thus be addressed in future works. In spite of the relatively good fit for the data of $\lambda > 6$, all correlations struggle

to adequately predict the profiles of $\lambda = 3$ and $\lambda = 4$. In order to understand the behaviour of porosity profiles for $\lambda < 6$ a more thorough investigation is needed.

Porosity profile along tube height

Besides the radial porosity profile, the axial porosity profiles along the tube length are displayed in Fig. 5.9. These profiles are only rarely presented as they do not add much structural information except for one thing: to prove the independence of structure from axial location and selected tube height and thus proving a constant packed bed generation procedure. It is generally known, that the tube bottom and top affect the

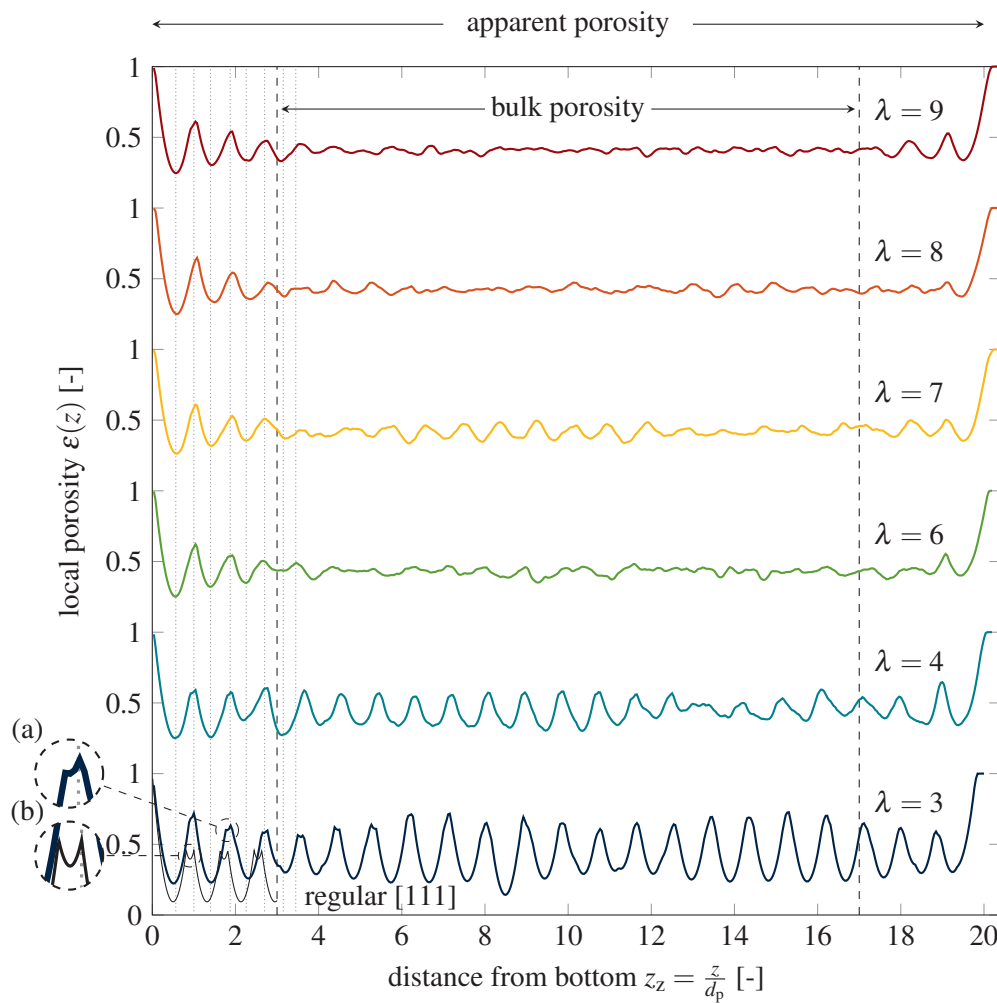


Figure 5.9: Radially averaged porosity distribution in axial direction for $\lambda = 3.0$ to 9.0 and the regular close packed equivalent.

local void structure similar to the circumferential wall, however, as typically packing height is significantly larger than its diameter, these effects are generally neglected. The first and only study regarding this topic named *thickness effect* was performed by Zou and Yu [67] finding an overall increase in mean bed porosity for too low packing heights. From their data it can be followed, that a tube height-to-particle diameter ratio of > 20 , as used herein, should be enough to avoid tube top and bottom effects on the porosity.

As can be seen from Fig. 5.9, the bottom part reaches 3 to 4 particle diameters into the tube, slightly increasing for increasing λ . The shape is again a damped oscillation function, however the damping depends on λ , too. Especially the oscillation for $\lambda = 3$ is hardly damped along the tube height, indicating a highly ordered structure throughout the packing, similar to the one of the first layers adjacent to the flat tube bottom. For comparison, the porosity profile of regular dense packed spheres on a solid flat wall as described by Ridgway and Tarbuck [111] is added. The shape of this profile resembles a string of alternating large and small parabola. The large parabola describe the sphere layers as can be seen in random arrangements as well. The small parabola, which is enlarged in subfigure (b) of Fig. 5.9 describes the regular overlapping of sphere layers. This characteristic detail can be found in some of the peaks for the axial distribution within packed beds of $\lambda = 3$, as displayed in the enlargement of subfigure (a). Furthermore, a significant shift of extrema position can be noted comparing regular and random packed bed arrangements. For comparison, the extrema locations identified for the radial porosity distribution are included in Fig. 5.9, coinciding with the extrema evoked by the plane tube bottom for all investigated random packed beds. Consequently, it appears, that a curved and a flat wall have similar effects on the local porosity.

Compared to the bottom and top fraction, the bulk part of the axial porosity is characterized by a constant mean porosity. Thereby the oscillation is more pronounced, both in terms of amplitude and shape for smaller λ and decreases with increasing bed size. The top fraction is again characterized by the solid cap added to allow constant packing heights. The effect reaches up to three particle diameters into the tube and has a similar, but less pronounced shape as the bottom wall. It is to be noted, that when no cap is used, the top part would look slightly different.

Regarding top and bottom fraction, both result in higher overall porosities compared to the respective bulk porosity. Thus, the relevant question is, if the apparent porosity including the full bed height is significantly different to the bulk porosity, or differently put, if the initial assumption, that a tube height to particle diameter $\frac{H}{d_p} = 20$ is sufficient to neglect the thickness effect is correct. Figure 5.10 displays the estimated porosity error as the difference of apparent $\bar{\epsilon}_a$ and bulk $\bar{\epsilon}_b$ porosity based on the bulk porosity, versus the tube height-to-particle diameter ratio (upper x-axis) and the respective apparent-to-wall packing height.

It was found, that the two cases $\lambda = 3$ and 4 behave similarly and were combined to the darker curve and all others were combined to the lighter curve. The two points where the two curves cross the vertical solid line of $\frac{H}{d_p}$ mark the experimental results. The obtained curves extrapolate these values under the assumption, that when decreasing or increasing the tube height, this solely changes the bulk packing part, not the top and bottom part. As can be seen from Fig. 5.10, a porosity increase of 2.0 % ($\lambda = 3$ and 4) to 3.5 % ($\lambda = 6$ to 9) between bulk and apparent porosity can be measured. A value of below 1 % is typically accepted to be insignificant, higher values should be avoided as they may lead to an erroneous prediction of pressure drop where the porosity error is known to have the fourfold effect [112]. Consequently, the herein selected tube height was not sufficient to neglect the tube bottom and top effects. The presented extrapolation predicts a minimum tube height of 37 and 64 particle diameters, respectively, based on the 1 % error acceptance. Alternatively, the bottom and top part can simply be cut off which is the selected method in this work.

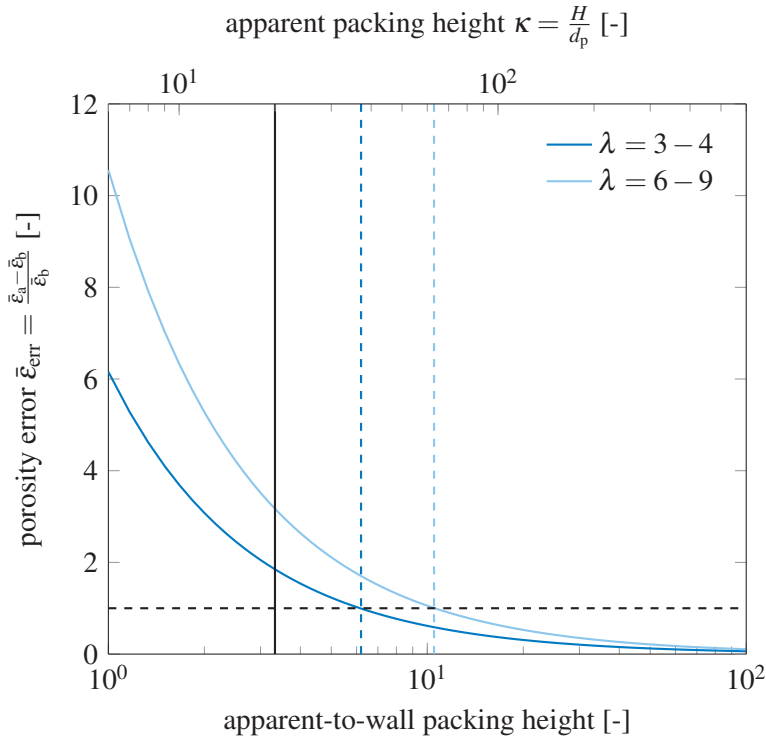


Figure 5.10: Obtained and extrapolated porosity error between apparent and bulk porosity as a function of tube height-to-particle diameter ratio κ .

In summary, the local structure of a considerable amount of non-densed packed beds comprising smooth, mono-sized spheres ranging from $\lambda = 3.0$ to 9.0 are investigated. Structural characteristics regarding sphere center positions, radial and axial porosity profiles could be highlighted and existing knowledge reviewed and enlarged.

5.4.2 Validation of numerical packing generation

Figure 5.11 displays the radial porosity profiles comparing experiment and numerical packing generation. Besides, the herein used packing algorithm DigiDEMTM, the results for another packing procedure using BlenderTM that we published elsewhere [108] is added in terms of completeness. An excellent fit of the experimental data and the two numerical procedures as displayed in Figs. 5.11a to 5.11d could be obtained. The already discussed extreme values in the tube center are similarly obtained in artificial generated packed beds. The attention may be further drawn to the excellent fit of extrema position. The slight difference between experiment and DigiDEMTM simulation can be explained with a slightly more regular structure of the numerically generated packings, especially for larger packed beds. It is known, that a bed densification results in higher amplitudes [39], however, the extent of this amplitude variation due to bed compression is much larger than the small deviations displayed here.

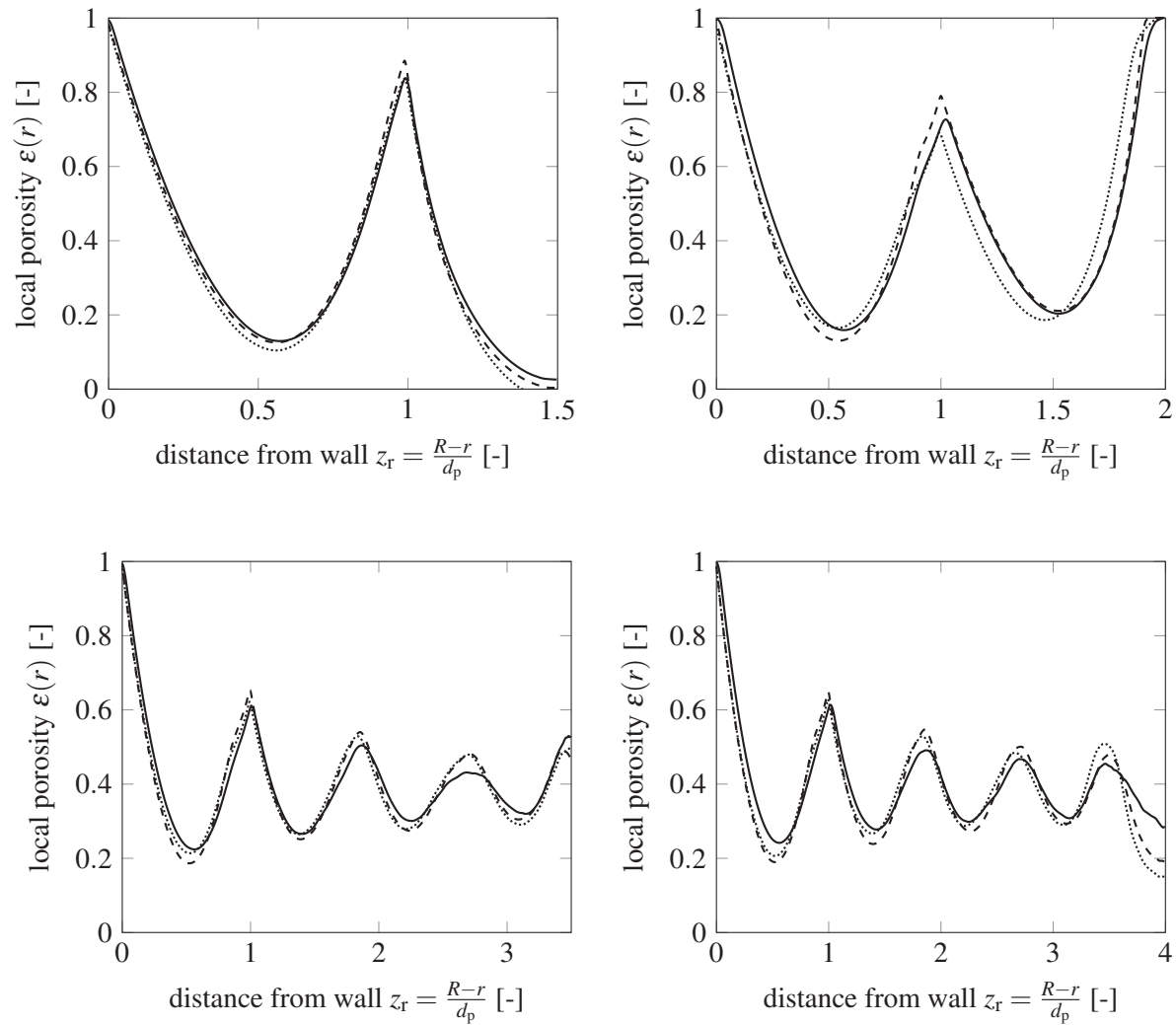


Figure 5.11: Comparison of radial porosity plots obtained by experiment (solid line), DigiDEMTM (dashed line), and BlenderTM [108] (dotted line) for (a) $\lambda = 3.0$, (b) $\lambda = 4.0$, (c) $\lambda = 7.0$, and (d) $\lambda = 8.0$.

5.4.3 Extrapolation of results

With the validated numerical packing procedure, a comprehensive study with packing sizes between $\lambda = 1.1$ and 9.0 is performed. λ is varied in steps of 0.05 between $\lambda = 1.95$ and 4.0 and in steps of 0.1 and 0.2 below $\lambda = 1.95$ and above $\lambda = 4.0$. For $\lambda > 6$, a step size of 0.5 and 1.0 is selected.

Radial porosity distributions

The resulting radial porosity profiles are plotted in Fig. 5.12 for the data of $\lambda < 6.0$. For a more in-depth characterization, Fig. 5.13 displays the porosity in the tube center, Fig. 5.14a displays the local porosity of each curves minima (lower part) and maxima (upper part) and Fig. 5.14b displays the position of each extremum, alternating maxima and minima, each as a function of tube-to-particle diameter ratio λ .

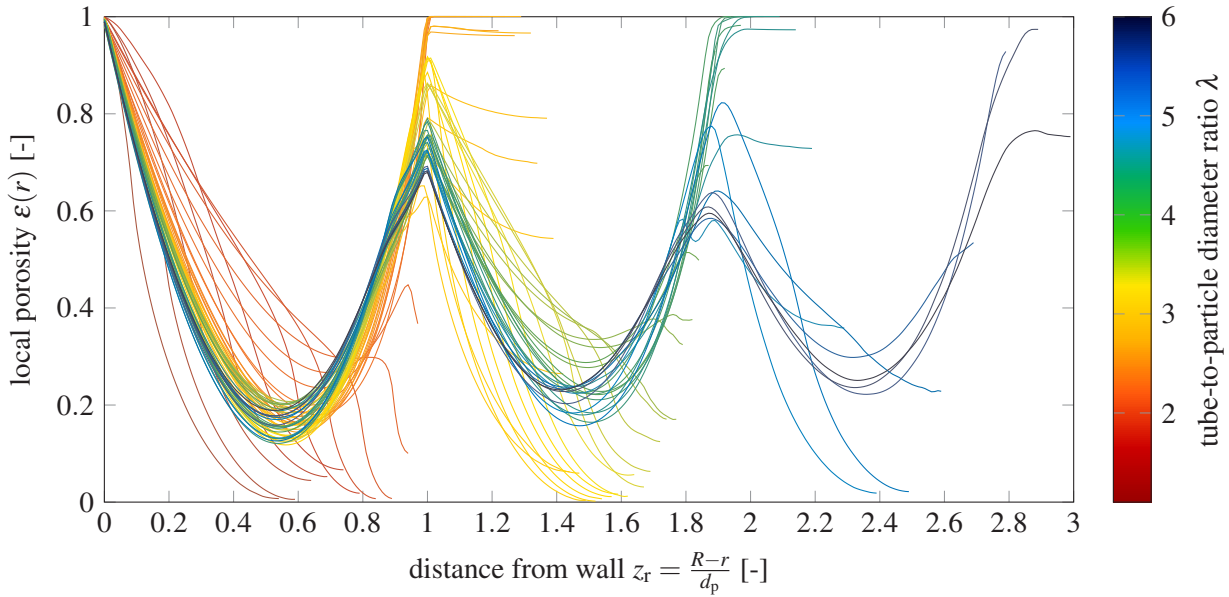


Figure 5.12: Obtained curve family of radial porosity profiles for a large number of numerically generated packed beds using DigiDEMTM for packed bed sizes between $\lambda = 1.1$ and 6.0

From Figs. 5.12 and 5.13 a distinct pattern regarding the tube center porosity can be identified. For $\lambda = 1.0$ the packed bed is characterized as a strictly regular chain of single spheres stacked over another. With increasing λ , the spheres stick to the tube wall while starting to increasingly fit into another until enough space is available to place two spheres next to each other at $\lambda = 2.0$, which also represents the circular link of the first ring of spheres: for more structural details of these packings, refer to [113]. In this λ -range, the porosity in the tube center is always zero due to the perfect fit of the spheres, in spite of the sphere centers are always 0.5 particle diameters away from the tube wall. With the completion of the outermost ring of spheres, the central porosity jumps to unity thus forming a completely empty duct in the tube's center. A further increase in λ increases the size of the central duct but does not break up the complete outer ring of spheres. This behaviour can be seen in Figs. 5.12 and 5.13, as the porosity is constantly one from $z_r = 1.0$ onwards in the respective λ -region. The increase in tube size only affects the organisation of the outer ring with increasingly fitting more spheres per layer but keeping the central duct untouched until the collapse of this system around $\lambda = 2.6$ with the introduction of central spheres. From thereon, the central porosity jumps back down reaching zero for $\lambda \approx 3.0$. Here, a perfect pile of spheres fits into the tube center surrounded by a complete outer ring of spheres. During a further increase of λ , the outer completed ring of spheres is un-affected while forming a quite solid border for the inner spheres, that behave similarly to the single-sphere arrangements of $\lambda < 2.0$ before completing the second ring of spheres around $\lambda = 3.8$. The rings of spheres intertwine so that an expected completion of the second ring at $\lambda = 4.0$ theoretically fitting four sphere spheres aside into the tube diameter is reduced to lower values. From the completion of the second ring onwards, a central empty duct is again formed which increases while untouched the completed ring structure until a certain point of instability, where the first central sphere is added. In summary, the packed bed structure for increasing bed sizes starting at the smallest possible size $\lambda = 1.0$ consists of a repeating alternation of central sphere strings and empty ducts surrounded by complete rings of spheres. However, with each sphere added due to the increased bed size, the randomness of the system is increased, smoothening the initially strict borders between these

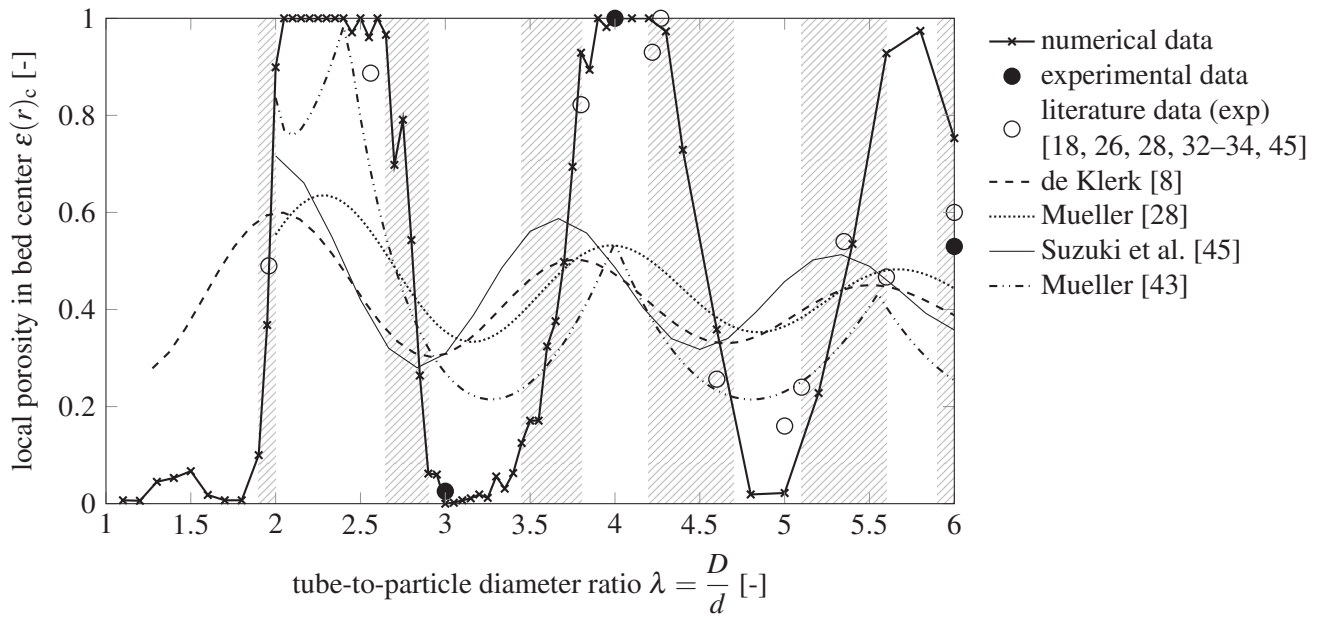


Figure 5.13: Local bed porosity at the tube's center of numerical data for $\lambda = 1.1$ to 6.0, compared to experimental data, literature data and typical correlations for radial porosity profiles.

two states and increasing the respective transition-regions represented by the shaded areas in Fig. 5.13 and all following figures, were intermediate porosity values are obtained.

Besides the numerical data, experimental data points were included in Fig. 5.13 of the above-described experiments and the data found in literature and displayed in Fig. 5.1. Although the experimental database is quite sparse while produced under various experimental conditions and packing procedures, a very good fit of experiment and numerical prediction of the central packing porosity is achieved. Furthermore, the predicted central porosity values of selected correlations officially valid for $\lambda > 2$ is added. Among these, the correlation of de Klerk [8] shall represent all standard cosine-exponential type correlations neglecting any influence of λ on the radial bed porosity, the correlation of Suzuki et al. [45] shall represent all scaled cosine-exponential type correlations including an influence of λ within the fitting constants, the correlation of Mueller [28] shall represent all the variations of the scaled Bessel-function type correlation that include an influence of λ within the fitting constants and Mueller [43] represents a scaling approach of parabola function chains. It is obvious, that none of the known correlations no matter if including λ -scaled constants or not, are capable to sufficiently represent the radial porosity profiles for packed beds of $\lambda < 6.0$. Among the known, the scaling of parabola function chains [43] might be the most promising approach for this region, however, finding a correlation that sufficiently represents the described unsteady behaviour of the curve family depicted in Fig. 5.12 is a challenge. A possible approach might include the combination of completed rings with a case sensitive selection for the tube center region, where the porosity is either constant one (duct), decreases rapidly to zero (string) or is in between (transition).

Some more structural details are clustered in Fig. 5.14. Besides the unsteadiness of the porosity in the tube center, the porosity and location of extrema characterizing the completed rings of spheres are not constant either, however, their overall effect is probably less important. The upper three curves of Fig. 5.14a

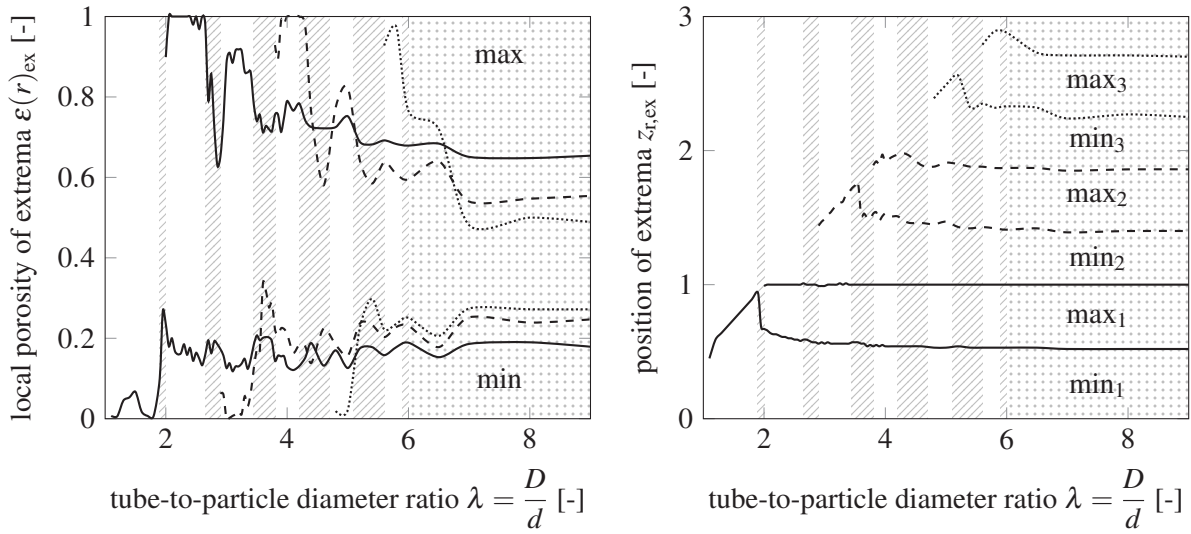


Figure 5.14: (a) Local porosity and (b) position of extrema of the radial porosity distribution for $\lambda = 1.1$ to 9.0 , separately for the first (solid line), the second (dashed line), and the third (dotted line) minimum (lower curve) and maximum (upper curve), respectively.

describe the porosity of the maxima of the radial porosity distributions respectively for the first, second and third one starting at the tube wall. For each maximum, the porosity is unity at the beginning (duct-region) and from that onward is lower in the transition regions as in the consecutive duct/sphere string regions. The lower curve represents the porosity of the minima, which is initially zero, and from there onwards is higher in the transition regions. Regarding the extrema locations displayed in Fig. 5.14b, the location of the minima increases steadily in the sphere string region, decreases sharply with ring completion and slowly decreases hereinafter to a finally constant value. This decrease is not affected by transition regions or the occurrence of further extrema. Compared to that, the location of the first maximum is of surprising unity. In spite of some small deviations in the first transition region, this also accounts for following maxima locations: at $\lambda = 9.0$, the extrema locations are $0.52, 1.0, 1.40, 1.86, 2.25, 2.70$ which is in very well accordance with the values obtained from experiments. The extrema distances are $0.52, 0.48, 0.40, 0.46, 0.39, 0.45$ for all extrema and $1.0, 0.88, 0.86, 0.85, 0.84$ for the extrema of same kind. Consequently, the period of oscillation is around 0.87 and slightly decreasing with increasing peak number.

Correlation approach

Based on the above described findings it can be assumed that for small $\lambda < 6$ the completed rings are not affected by any further increase or decrease of λ . Thus, the tube center is packed independently from the rest of the packing. It is further assumed that this packing order might be similar to the packing order obtained when tubes of $\lambda < 2$ are packed where no ring of spheres is completed yet. For this region, an analytical solution of the porosity profiles exists [113]. The most predominant difference is, that an overlap with the completed sphere rings have to be taken into account. This overlap is assumed to be approximately $0.13z_r$ which corresponds to the difference in oscillation amplitude (ring width) between first and the following oscillations (rings) as earlier discussed. As a hypothesis the porosity profiles

between the completion of the first ring (analytical solution) and the second ring can be described using the by $0.87z_r$ shifted analytical porosity profiles. This approach can also be used for all $\lambda < 6$ having n completed rings of spheres:

$$\text{for } z_r < 1 + (n - 1) \cdot 0.87 : \quad \varepsilon(r, \lambda) \text{ as of existing correlations, e.g. Eq. (5.6b)}$$

$$\text{for } z_r \geq 1 + (n - 1) \cdot 0.87 : \quad \varepsilon(r_s, \lambda_s) \text{ as of analytical solution, e.g. [113]}$$

$$\text{with: } r_s = z_r - n \cdot 0.87, \text{ and } \lambda_s = \lambda - 2 \cdot (1 + (n - 1) \cdot 0.87) + 2 \cdot (1 - 0.87) \quad (5.7)$$

It might be necessary to use linear or quadratic interpolation between these two sections. As an example: when plotting $\lambda = 3$ ($n = 1$), then use existing correlations for $z_r < 1$ and the analytical solution for $\lambda_s = 1.26$ shifted by $\Delta z_r = 0.87$ for $z_r > 1$. The results of selected profiles are displayed in Fig. 5.15. A very well fit of prediction and numerical data can be seen. It shall be noted, that for $\lambda_s < 1$ the analytical solution is $\varepsilon = 1$ (empty tube).

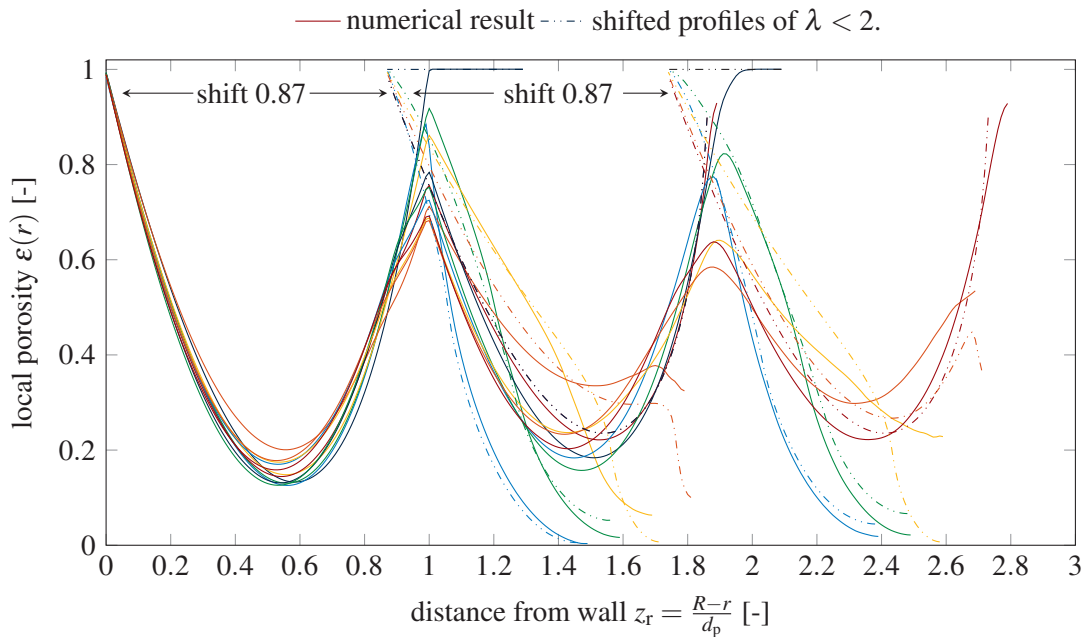


Figure 5.15: Visualization of prediction approach of porosity profiles for packings having tube-to-particle diameter ratios < 6 .

Bulk average porosity

In the last step, the bulk porosity is calculated cutting off three particle diameters from the top and bottom. The resulting values are displayed in Fig. 5.16 versus tube size. Corresponding experimental results of [16] were added to show the validity of the values. Moreover, the values predicted by McGearry [75] based on theoretical considerations regarding complete regular arrangements of ideal packed sphere multiples are added. Although the absolute values are either too low or too high, the general trend can be reproduced. For comparison, the analytical and well accepted correlation of Carman [85] for the region $\lambda = 1.0$ to

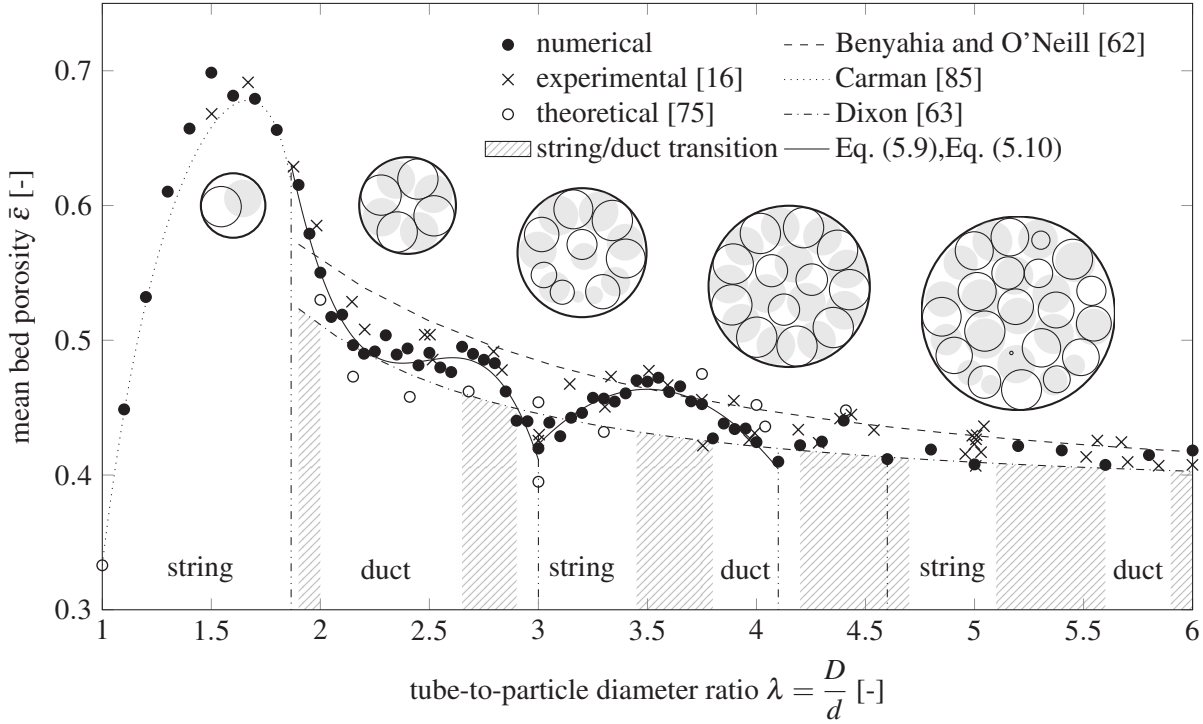


Figure 5.16: Mean bed porosity for $\lambda = 1.1$ to 6.0 of numerical data, compared to experimental and theoretical data points and known correlations.

1.866 is added and fits well with the numerical data points. From the large selection of available empirical correlations to predict the mean bed porosity for a given $\lambda > 2.0$, two correlations were selected roughly marking the upper [62] and lower [63] limit of all correlations. Herein, the porosity value at $\lambda \rightarrow \infty$ was adjusted to the value of 0.383 determined for the added experimental results [16]. While the numerical (and experimental) data points well fit the region spanned by the two limiting correlations, their general steadily decreasing trend can not be confirmed for this λ selection. As already mentioned in the theoretical part of this chapter, the mean bed porosity is rather characterized by attaining extreme values, especially maxima around $\lambda = 3.5$ and 4.4 and minima around $\lambda = 3.0$, 4.1 and 4.6. Moreover, the mean porosity is rather constant in the λ -region 2.2 to 2.7. For $\lambda = 1.0$ to 1.866, the data points follow the already known correlation Eq. (5.8) of Carman [85], for $\lambda = 1.866$ to 3.0, the data can be described using Eq. (5.9) and for $\lambda = 3.0$ to 4.1, the data points are more precisely described by Eq. (5.10).

$$\bar{\varepsilon} = 1 - \frac{2}{3} \cdot \left(\frac{1}{\lambda}\right)^3 \cdot \frac{1}{\sqrt{\frac{2}{\lambda} - 1}} \quad (5.8)$$

$$\text{for } \lambda = 1.0 \text{ to } 1.866$$

$$\bar{\varepsilon} = 0.6622 \cdot \lambda^3 + 4.9493 \cdot \lambda^2 - 12.304 \cdot \lambda + 10.659 \quad R^2 = 0.965 \quad (5.9)$$

$$\text{for } \lambda = 1.866 \text{ to } 3.0$$

$$\bar{\varepsilon} = -0.1639 \cdot \lambda^2 + 1.147 \cdot \lambda - 1.5431 \quad R^2 = 0.853 \quad (5.10)$$

$$\text{for } \lambda = 3.0 \text{ to } 4.1$$

There is at least one more range to be defined, probably ranging from $\lambda = 4.1$ to 4.6 or 5.0, however, the database is too small to properly define respective fitting curves. Subsequently, the data variations are small so that for $\lambda > 5.0$ the existing correlations can be used to estimate the mean bed porosity. As the difference between these is small, no recommendation for a specific correlation shall be given.

The obtained curve of mean porosity versus tube size appears to be independent from the shape of the radial porosity profile and the occurring extrema cannot be allocated to either sphere string arrangements, the existence of empty central ducts or the intermediate transition regions.

Sphere contact number and distribution

Besides the void structure, the contact number distribution [29, 114, 115] of packed spheres, its average [29, 114–116] and the orientation of sphere contacts [11, 39] have been evaluated previously. Typically, this has been done for bulk packings without investigating the influence of the confining wall. Values for average sphere contacts N_c range from about 6 to 7 and depend on the bulk packing porosity, which is altered by particle material and packing method. Recently, an in-depth study evaluated the alteration of the bulk packing contact statistics when approaching the packing's confinement [39]. Close to the wall, especially the orientation of particle contacts showed significant indications for very structured particle arrangements.

With the available numerical packing data, sphere contact statistics have been performed, especially evaluating the effect of tube-to-particle diameter ratio on the average contact number and the standard deviation of its distribution. The obtained results are displayed in Fig. 5.17. Accordingly, the average particle contact number for tube-to-particle diameter ratios equal or smaller 1.8 equals 2. Thereinafter, a drastical increase in average contact number can be observed, flattening to an infinite value for $\lambda > 6.0$. The obtained curve can be fitted to Eq. (5.11):

$$N_c = \begin{cases} 2 & \text{for } \lambda \leq 1.8 \\ \frac{6.2\lambda - 10.9}{\lambda - 1.6} & \text{for } \lambda > 1.8 \end{cases} \quad (5.11)$$

The actual deviation from the fitted curve, however, is quite large for small tube sizes, which is allocated to the unsteadiness of the packing porosity and the small sample size. Besides the average contact number, its deviation, here represented by the standard deviation, shows a similar trend from being very narrow for small λ , rapidly increasing its width before smoothing out to a constant value. Furthermore, bimodal distributions can be observed for most packings between $2 < \lambda < 4$, indicating a large ratio of spheres close to the wall which, obviously, have less contact with other spheres, but with the confining wall.

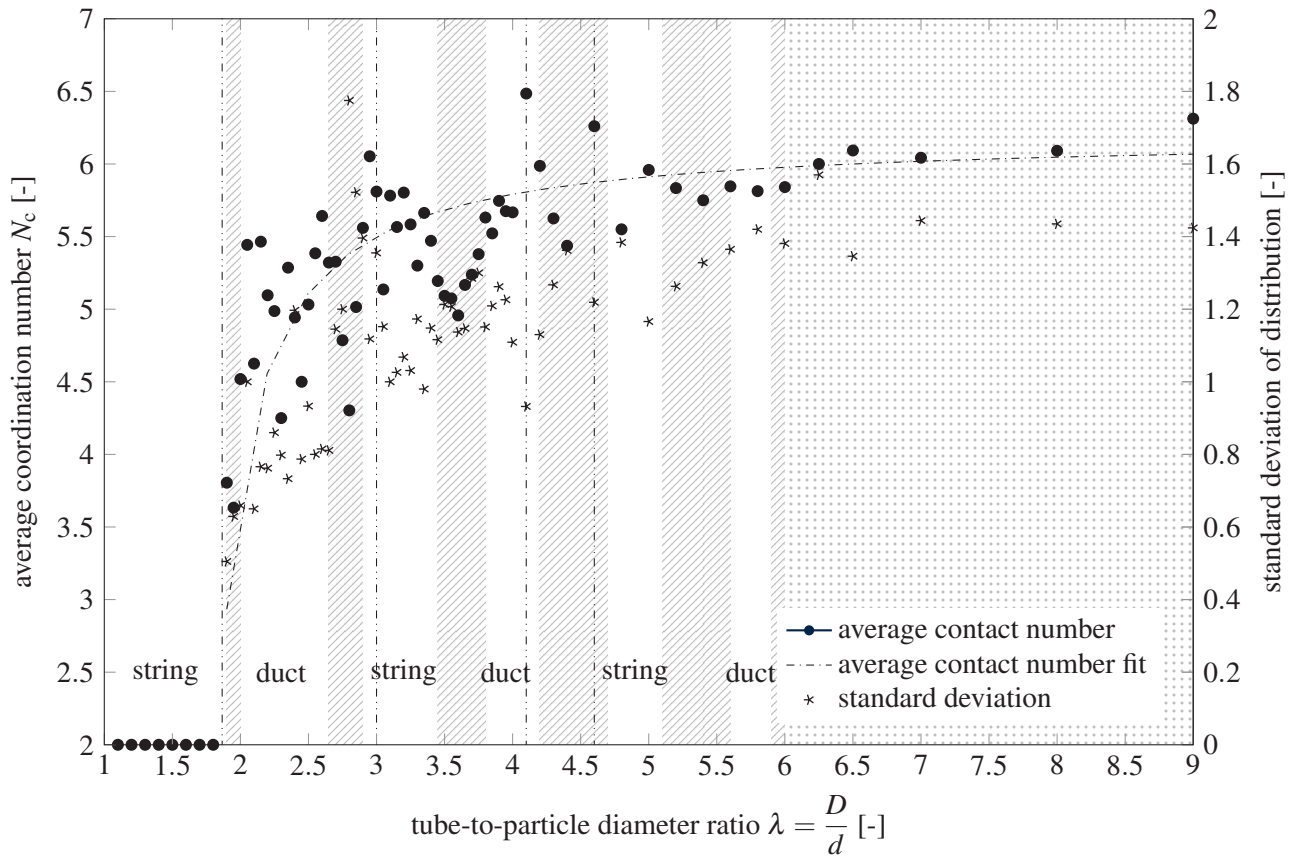


Figure 5.17: Average particle contact number and the standard deviation of its distribution for sphere packings of $\lambda = 1.1$ to 9.0..

5.5 Conclusion

A comprehensive study was conducted to fill the gap of understanding and predicting slender packed beds of mono-sized, smooth spheres in cylindrical confining walls of $\lambda < 10$. The experimental determination of local porosity profiles using x-ray computed tomography was expanded with the analysis of numerically generated packed beds in order to enlarge the available database to a substantial resolution. Furthermore, a general correlation predicting the radial porosity profile has been derived.

Based on this, some remarkable details regarding the shape of the radial and axial porosity profiles as a function of λ are detected and described. These comprise the variation of location and height of the first minimum and maximum and the subsequent modulation of amplitude and period of the present damped oscillation. While the first peak is clearly sharp as obtained by parabola, this can not be seen for the consecutive peaks that may be well described by a cosine term. Most predominantly, it was found that for small λ the values in the center of the tube may take extreme values which in this extent was not described before. This comprises the classification of the central tube part into an empty duct center, a sphere string-ordered center, and the transition between these two states. Depending on which class is apparent, the local porosity values may take the extreme values one and zero. In order to predict this behaviour a correlation is derived based on analytical solutions capable to predict this behaviour. It is to be noted, that these characteristics may be more or less pronounced when using different material properties or packing modes. However, the herein described configuration is probably the best compromise regarding packed bed influencing factors.

It was further noted, that the described structural details of packed beds for small λ do not correlate in clear manner with differences found for the overall mean bed porosity. Again, the generally accepted steadily decreasing trend for $1.866 \leq \lambda$ is an oversimplification for $\lambda < 5$ as occurring extrema are not considered although leading to a significant difference in mean bed porosity, e.g. at $\lambda = 3.0$ the porosity equals 0.42 and at $\lambda = 3.45$ it is 0.47. Depending on the selected correlation, this may lead to an error of $>10\%$ between correlation and reality, which is a multiple of the generally accepted 1% error tolerance regarding mean bed porosity. This boundary level relates back to the error propagation for pressure drop, where a deviation in porosity results in approximately the fourfold deviation in pressure drop. Consequently, new correlations were presented for the λ -region 1.866 to 4.1 that well fit the obtained data. Additionally, sphere contact statistics have been evaluated and related to the tube-size.

The proper and validated description of numerically generated packed beds is required for subsequent simulations of fluid dynamics, heat or mass transport. It is questionable if and to what extent the described structural characteristics of packed beds transfer to the flow profile and deduced parameters, depending on λ .

CRedit authorship contribution statement

Jennie von Seckendorff: Conceptualization, Methodology, Software, Formal analysis, Investigation, Visualization. Klaus Achterhold: Investigation. Franz Pfeiffer: Investigation. Richard Fischer: Supervision, Project administration, Funding acquisition. Olaf Hinrichsen: Supervision, Project administration, Funding acquisition.

Declaration of Competing Interest

The authors declare that they have no known competing financial interests or personal relationships that could have appeared to influence the work reported in this paper.

Acknowledgements

The authors would like to thank Johanna Fernengel for providing the BlenderTM script. Financial and substantial support of MuniCat, a strategic alliance between the Technical University of Munich (TUM) and Clariant AG is gratefully acknowledged. Jennie von Seckendorff would further like to thank the TUM Graduate School for generous support.

Nomenclature

Latin Symbols

a, b	variables in Eq. (5.4)	m
a, b, c, d	variables in Eq. (5.6b)	-
d_p	particle/sphere diameter	m or voxel
D	diameter of tube	m or voxel
e	coefficient of restitution	-
h	height of sphere cap	m
H	height of tube	m or voxel
n	number of complete rings	-
r	radial position from tube center	m
r	sphere radius	m
R	radius of the tube	m
S	(bin) cross section	m ²
V	(bin) volume	m ³
x	x coordinate	m
y	y coordinate	m
z	axial position from tube bottom	m
z_a	begin of interpolation region	-
z_e	end of interpolation region	-
z_r	non-dimensional distance from tube wall in particle diameters	-
$z_{r,min,1}$	non-dimensional distance of the first minimum from tube wall	-
z_z	non-dimensional distance from tube bottom in particle diameters	-

Greek Symbols

ε	local porosity	-
$\bar{\varepsilon}$	mean bed porosity	-
$\varepsilon_{min,1}$	local porosity of the first minimum adjacent to the wall	-
ε_{inf}	porosity with $\lambda \rightarrow \infty$	-
λ	tube-to-particle diameter ratio	-
κ	tube height-to-particle diameter ratio	-
ρ	material density	kg m ⁻³
μ	coefficient of friction	-
ν	Poisson's ratio	-

Indices

0	sphere center value
a	apparent variable
b	bulk variable
c	tube center variable
ex	value or location of extrema
i	control variable, sphere index
n	control variable, axial bin
m	control variable, radial bin
max	maximum
min	minimum
s	shifted value

References

- [1] M. Dorn, F. Eschbach, D. Hekmat, D. Weuster-Botz, *Journal of Chromatography A* **2017**, *1516*, 89–101.
- [2] K. K. Unger, R. Skudas, M. M. Schulte, *Journal of Chromatography A* **2008**, *1184*, 393–415.
- [3] G. Eigenberger in *Handbook of Heterogeneous Catalysis, 2nd ed.* (Eds.: C. Ertl, H. Knözinger, F. Schüth, J. Weitkamp), Wiley-VCH, Weinheim, **2008**.
- [4] A. Mersmann, M. Kind, J. Stichlmair, *Thermal Separation Technology: Principles, Methods, Process Design*, Springer-Verlag Berlin Heidelberg, **2011**.
- [5] A. Koster, H. D. Matzner, D. R. Nicholsi, *Nuclear Engineering and Design* **2003**, *222*, 231–245.
- [6] A. B. Yu, J. Bridgwater, A. Burbidge, *Powder Technology* **1997**, *92*, 185–194.
- [7] C. L. Feng, A. B. Yu, *Powder Technology* **1998**, *99*, 22–28.
- [8] A. de Klerk, *AIChE Journal* **2003**, *49*, 2022–2029.
- [9] E. Erdim, Ö. Akgiray, I. Demir, *Powder Technology* **2015**, *283*, 488–504.
- [10] O. Bey, G. Eigenberger, *Chemical Engineering Science* **1997**, *52*, 1365–1376.
- [11] W. van Antwerpen, C. G. du Toit, P. G. Rousseau, *Nuclear Engineering and Design* **2010**, *240*, 1803–1818.
- [12] R. W. Fahien, J. M. Smith, *AIChE Journal* **1955**, *1*, 28–37.
- [13] J. M. P. Q. Delgado, *Heat and Mass Transfer* **2006**, *42*, 279–310.
- [14] W.-C. Yang, *Handbook of Fluidization and Fluid-Particle Systems, 1st ed.* CRC Press, Boca Raton, FL, **2003**.
- [15] S. Afandizadeh, E. A. Foumeny, *Applied Thermal Engineering* **2001**, *21*, 669–682.
- [16] J. Pottbäcker, O. Hinrichsen, *Chemie Ingenieur Technik* **2017**, *89*, 454–458.
- [17] L. H. S. Roblee, R. M. Baird, J. W. Tierney, *AIChE Journal* **1958**, *4*, 460–464.
- [18] R. F. Benenati, C. B. Brosilow, *AIChE Journal* **1962**, *8*, 359–361.
- [19] M. Propster, J. Szekely, *Powder Technology* **1977**, *17*, 123–138.
- [20] J. S. Goodling, R. I. Vachon, W. S. Stelpflug, S. J. Ying, M. S. Khader, *Powder Technology* **1983**, *35*, 23–29.
- [21] M. C. Thadani, F. N. Peebles, *Industrial & Engineering Chemistry Process Design and Development* **1966**, *5*, 265–268.
- [22] R. Küfner, H. Hofmann, *Chemical Engineering Science* **1990**, *45*, 2141–2146.
- [23] W. Du, N. Quan, P. Lu, J. Xu, W. Wei, L. Zhang, *Chemical Engineering Research and Design* **2016**, *106*, 115–125.
- [24] K. Ridgway, K. J. Tarbuck, *Journal of Pharmacy and Pharmacology* **1966**, *18*, 168S–175S.
- [25] M. R. Shaffer, MA thesis, Perdue University, Lafayette, **1953**.
- [26] J. J. Lerou, G. F. Froment, *Chemical Reactor Design and Technology* **1986**, 729–736.

- [27] M. Giese, K. Rottschäfer, D. Vortmeyer, *AIChE Journal* **1998**, *44*, 484–490.
- [28] G. E. Mueller, *Powder Technology* **1992**, *72*, 269–275.
- [29] G. J. Auwerda, J.-L. Kloosterman, D. Lathouwers, T. H. J. J. van der Hagen, *Nuclear Technology* **2013**, *183*, 272–286.
- [30] R. Caulkin, X. Jia, C. Xu, M. Fairweather, R. A. Williams, H. Stitt, M. Nijemeisland, S. Aferka, M. Crine, A. Léonard, D. Toye, P. Marchot, *Industrial & Engineering Chemistry Research* **2009**, *48*, 202–213.
- [31] F. Al-Falahi, M. Al-Dahhan, *Nuclear Engineering and Design* **2016**, *310*, 231–246.
- [32] C. M. Wensrich, *Powder Technology* **2012**, *219*, 118–127.
- [33] N. J. Mariani, W. I. Salvat, M. A. Campesi, G. F. Barreto, O. M. Martinez, *International Journal of Chemical Reactor Engineering* **2009**, *7*, A82.
- [34] A. J. Sederman, P. Alexander, L. F. Gladden, *Powder Technology* **2001**, *117*, 255–269.
- [35] R. Balzan, A. L. Sellerio, D. Mari, A. Comment, G. Gremaud, *Granular Matter* **2013**, *15*, 873–879.
- [36] R. Balzan, A. L. Sellerio, D. Mari, A. Comment, *Applied Magnetic Resonance* **2015**, *46*, 633–642.
- [37] J. M. Buchlin, M. Riethmuller, J. J. Ginoux, *Chemical Engineering Science* **1977**, *32*, 1116–1119.
- [38] F. A. Schneider, D. W. T. Rippin, *Industrial & Engineering Chemistry Research* **1988**, *27*, 1936–1941.
- [39] J. Reimann, J. Vicente, E. Brun, C. Ferrero, Y. Gan, A. Rack, *Powder Technology* **2017**, *318*, 471–483.
- [40] C. G. du Toit, *Powder Technology* **2019**, *342*, 475–485.
- [41] N. J. Mariani, O. M. Martínez, G. F. Barreto, *Chemical Engineering Science* **2001**, *56*, 5693–5707.
- [42] N. J. Mariani, G. D. Mazza, O. M. Martinez, G. F. Barreto, *The Canadian Journal of Chemical Engineering* **2000**, *78*, 1133–1137.
- [43] G. E. Mueller, *Powder Technology* **2010**, *203*, 626–633.
- [44] G. E. Mueller, *Powder Technology* **2012**, *229*, 90–96.
- [45] M. Suzuki, T. Shinmura, K. Iimura, M. Hirota, *Advanced Powder Technology* **2008**, *19*, 183–195.
- [46] J. von Seckendorff, O. Hinrichsen, *The Canadian Journal of Chemical Engineering* **2020**, in press.
- [47] M. Giese, PhD thesis, Technische Universität München, **1998**.
- [48] D. Vortmeyer, J. Schuster, *Chemical Engineering Science* **1983**, *38*, 1691–1699.
- [49] B. C. Chandrasekhara, D. Vortmeyer, *Wärme- und Stoffübertragung* **1979**, *12*, 105–111.
- [50] P. Cheng, C. T. Hsu, *International Journal of Heat and Mass Transfer* **1986**, *29*, 1843–1853.
- [51] J. R. Sodr e, J. A. R. Parise, *Experimental Thermal and Fluid Science* **1998**, *17*, 265–275.
- [52] M. L. Hunt, C. L. Tien, *Chemical Engineering Science* **1990**, *45*, 55–63.
- [53] H. Martin, *Chemical Engineering Science* **1978**, *33*, 913–919.
- [54] Y. Cohen, A. B. Metzner, *AIChE Journal* **1981**, *27*, 705–715.

- [55] G. E. Mueller, *Powder Technology* **2019**, *342*, 607–612.
- [56] G. E. Mueller, *Chemical Engineering Science* **1991**, *46*, 706–708.
- [57] V. M. H. Govindarao, G. F. Froment, *Chemical Engineering Science* **1986**, *41*, 533–539.
- [58] V. M. H. Govindarao, K. V. S. Ramrao, *Chemical Engineering Science* **1988**, *43*, 2544–2545.
- [59] V. M. H. Govindarao, M. Subbanna, A. V. S. Rao, K. V. S. Ramrao, *Chemical Engineering Science* **1990**, *45*, 362–364.
- [60] J. Kubie, *Chemical Engineering Science* **1988**, *43*, 1403–1405.
- [61] N. J. Mariani, W. I. Salvat, O. M. Martínez, G. F. Barreto, *The Canadian Journal of Chemical Engineering* **2002**, *80*, 186–193.
- [62] F. Benyahia, K. E. O’Neill, *Particulate Science and Technology* **2005**, *23*, 169–177.
- [63] A. G. Dixon, *The Canadian Journal of Chemical Engineering* **1988**, *66*, 705–708.
- [64] E. A. Foumeny, H. A. Moallemi, C. Mcgreavy, J. A. A. Castro, *The Canadian Journal of Chemical Engineering* **1991**, *69*, 1010–1015.
- [65] R. Jeschar, *Archiv für das Eisenhüttenwesen* **1964**, *35*, 91–108.
- [66] G. S. Beavers, E. M. Sparrow, D. E. Rodenz, *Journal of Applied Mechanics* **1973**, *40*, 655–660.
- [67] R. P. Zou, A. B. Yu, *Chemical Engineering Science* **1995**, *50*, 1504–1507.
- [68] A. M. Ribeiro, P. Neto, C. Pinho, *International Review of Chemical Engineering* **2010**, *2*, 40–46.
- [69] G. Sonntag, *Chemie Ingenieur Technik* **1960**, *32*, 317–329.
- [70] M. Leva, M. Grummer, *Chemical Engineering Progress* **1947**, *43*, 713–718.
- [71] C. McGreavy, E. A. Foumeny, K. H. Javed, *Chemical Engineering Science* **1986**, *41*, 787–797.
- [72] T. C. S. Hsiang, H. W. Haynes, *Chemical Engineering Science* **1977**, *32*, 678–681.
- [73] C. F. Chu, K. M. Ng, *AIChE Journal* **1989**, *35*, 148–158.
- [74] R. M. Fand, R. Thinakaran, *Journal of Fluids Engineering* **1990**, *112*, 84–88.
- [75] R. K. McGearry, *Journal of the American Ceramic Society* **1961**, *44*, 513–522.
- [76] R. Caulkin, M. Fairweather, X. Jia, N. Gopinathan, R. A. Williams, *Computers and Chemical Engineering* **2006**, *30*, 1178–1188.
- [77] R. C. Raichura, *Experimental Heat Transfer* **1999**, *12*, 309–327.
- [78] A. Montillet, E. Akkari, J. Comiti, *Chemical Engineering and Processing: Process Intensification* **2007**, *46*, 329–333.
- [79] N. B. Griffiths, PhD thesis, University of Cambridge, **1986**.
- [80] R. M. Fand, M. Sundaram, M. Varahasamy, *Journal of Fluids Engineering* **1993**, *115*, 169–172.
- [81] W. Reichelt, *Chemie Ingenieur Technik* **1972**, *44*, 1068–1071.
- [82] M. Leva, *Chemical Engineering* **1949**, *55*, 115–117.
- [83] D. E. Beasley, J. A. Clark, *International Journal of Heat and Mass Transfer* **1984**, *27*, 1659–1669.
- [84] Z. Guo, Z. Sun, N. Zhang, M. Ding, J. Wen, *Chemical Engineering Science* **2017**, *173*, 578–587.

- [85] P. Carman, *Transactions of the Institution of Chemical Engineers* **1937**, *15*, 150–166.
- [86] M. E. Aerov, PhD thesis, Moscow, **1951**.
- [87] J. E. Ayer, F. E. Soppet, *Journal of the American Ceramic Society* **1965**, *48*, 180–183.
- [88] G. F. Froment, K. B. Bischoff, *Chemical Reactor Analysis and Design, 2nd ed. Vol. Wiley New York*, **1979**.
- [89] A. S. Puschnov, *Khim. Neft. Mashinostr.* **2005**, *6*, 10.
- [90] A. S. Puschnov, *Chemical and Petroleum Engineering* **2006**, *42*, 14–17.
- [91] N.-S. Cheng, *Powder Technology* **2011**, *210*, 261–266.
- [92] M. Zhang, H. Dong, Z. Geng, *Chemical Engineering Research and Design* **2018**, *132*, 149–161.
- [93] G. D. Wehinger, C. Fütterer, M. Kraume, *Industrial & Engineering Chemistry Research* **2017**, *56*, 87–99.
- [94] M. E. Taskin, A. G. Dixon, E. H. Stitt, *Numerical Heat Transfer Part A: Applications* **2007**, *52*, 203–218.
- [95] M. V. Tabib, S. T. Johansen, S. Amini, *Industrial & Engineering Chemistry Research* **2013**, *52*, 12041–12058.
- [96] A. Singhal, S. Cloete, S. Radl, R. Quinta-Ferreira, S. Amini, *Chemical Engineering Science* **2017**, *172*, 1–12.
- [97] H. Freund, T. Zeiser, F. Huber, E. Klemm, G. Brenner, F. Durst, G. Emig, *Chemical Engineering Science* **2003**, *58*, 903–910.
- [98] Z. P. Zhang, L. F. Liu, Y. D. Yuan, A. B. Yu, *Powder Technology* **2001**, *116*, 23–32.
- [99] J. Theuerkauf, P. Witt, D. Schwesig, *Powder Technology* **2006**, *165*, 92–99.
- [100] Q. Qian, L. Wang, X. An, Y. Wu, J. Wang, H. Zhao, X. Yang, *Powder Technology* **2018**, *325*, 151–160.
- [101] N. Zobel, T. Eppinger, F. Behrendt, M. Kraume, *Chemical Engineering Science* **2012**, *71*, 212–219.
- [102] A. Wouterse, S. R. Williams, A. P. Philipse, *Journal of Physics: Condensed Matter* **2007**, *19*, 406215.
- [103] H. Tangri, Y. Guo, J. S. Curtis, *Powder Technology* **2017**, *317*, 72–82.
- [104] J. D. Sherwood, *Journal of Physics A: Mathematical and General* **1997**, *30*, L839–L843.
- [105] S. R. Williams, A. P. Philipse, *Physical Review E* **2003**, *67*, 051301.
- [106] B. Partopour, A. G. Dixon, *Powder Technology* **2017**, *322*, 258–272.
- [107] G. Boccoardo, F. Augier, Y. Haroun, D. Ferré, D. Marchisio, *Chemical Engineering Journal* **2015**, *279*, 809–820.
- [108] J. Fernengel, J. von Seckendorff, O. Hinrichsen, *Proceedings of the 28th European Symposium on Computer Aided Process Engineering* **2018**, 97–102.
- [109] R. A. Williams, X. Jia, *Particulate Science and Technology* **2003**, *21*, 195–205.
- [110] Z. Guo, Z. Sun, N. Zhang, M. Ding, X. Cao, *Powder Technology* **2017**, *319*, 445–451.

- [111] K. Ridgway, K. J. Tarbuck, *Chemical Engineering Science* **1968**, *23*, 1147–1155.
- [112] T. Zeiser, PhD thesis, Universität Erlangen-Nürnberg, **2008**.
- [113] V. M. H. Govindarao, K. V. S. Ramrao, A. V. S. Rao, *Chemical Engineering Science* **1992**, *47*, 2105–2109.
- [114] D. Pinson, R. P. Zou, A. B. Yu, P. Zulli, M. J. McCarthy, *Journal of Physics D: Applied Physics* **1998**, *31*, 457–462.
- [115] M. Oda, *Soils and Foundations* **1977**, *17*, 29–42.
- [116] T. Aste, M. Saadatfar, T. J. Senden, *Physical Review E* **2005**, *061302*, 71.

Part III

Shape Matters - Numerical Study on Shape Optimization

6 Numerical Shape Development Study in View of Random Packed Beds. Part I: The Yo-Yo Shape

Abstract

A huge variety of shaped bodies geometries to be used in catalytic fixed bed reactors is available in industry. However, only sparsely shapes other than spheres, cylinders and hollow cylinders are systematically investigated by scientific institutions. As a starting point, the known geometries typically published in patents and patent applications are reviewed and classified regarding fabrication methods and shape characteristics. It is well known that even small variations of these shapes may have a major impact on fluid dynamics as well as in heat and/or mass transfer of the reaction system. An arbitrary selected Yo-Yo shape being a sphere with an equatorial duct of variable width, deepness and rounding radius is evaluated in regard to packing structure, flow field, pressure drop and residence time distribution. This study marks the first attempt to utilize the steadily increasing possibilities of numerical packing generation and computational fluid dynamics, for an in-deep understanding of shape impact and its potential for future automated shape optimization procedures.

This article was published in:

Chemical Engineering Journal, 404, J. von Seckendorff, P. Scheck, M. Tonigold, R. Fischer, O. Hinrichsen, Numerical Shape development study in view of random packed beds - The Yo-Yo shape, 126468, Copyright Elsevier (2021). DOI: 10.1016/j.cej.2020.126468.

Reprint Permission:

As an Elsevier journal author, you have the right to Include the article in a thesis or dissertation (provided that this is not to be published commercially) whether in full or in part, subject to proper acknowledgment; see [the Copyright page](#) for more information. No written permission from Elsevier is necessary.

This right extends to the posting of your thesis to your university's repository provided that if you include the published journal article, it is embedded in your thesis and not separately downloadable.

6.1 Introduction

Heterogeneously catalyzed reactions require the presence of solid catalyst material, in industrial-scale application typically shaped to distinct bodies in order to reduce the pressure loss along the reactor. Nonetheless, the shaped bodies randomly stacked into the reactor need to ensure uniform reactant distribution and catalyst contact in common with an appropriate heat transport characteristic. The optimization of these parameters by simply varying the geometry of the catalyst body has an impressive economic impact proven by the sheer amount of existing patents and patent applications in this field. Despite, the systematically scientific description of shape effects on fluid dynamics, heat and mass transport are frequently restricted to the well-investigated random packing of spheres [1–3]. A much smaller experimental database is available regarding the utilization of random packings of cylinders and hollow cylinders [4–6], sometimes also called Raschig rings. Despite minor exceptions, hardly any experimental study goes beyond these three shapes, which is justified with the strongly increasing complexity of the whole system making a scientific evaluation be a challenge. While the shape of a sphere is easily described with its radius as the only unambiguous parameter, a cylinder comes in various diameter-to-height aspect ratios, a certain orientation expressed by a rotation matrix or angle and a large set of selectable definitions for characteristic diameters, most frequently the Sauter diameter or the diameter of the sphere with equal volume. Besides its increasing structural complexity, the availability of test bodies possesses another problem. While spherical shapes can be easily obtained in sufficient accuracy and number (marbles, ball bearings, beads), accurate cylindrical shapes are less easy to find especially in varying aspect ratios and researchers tend to machine them from wood [7], metal [8], plastic [8] or even vegetables [9] and spaghetti [10]. It is obvious that this technique can not be used for manufacturing more complex test bodies. In industry, methods such as tablet pressing are used to form the catalyst bodies. This forming procedure requires punch and press die sets that are typically too expensive to obtain for a designed shaped study. It is thus, that researchers accommodate with nature's products such as lentils, all sorts of beans and rice [8, 9] to name but a few if shapes other than spheres and cylinders shall be evaluated. Unfortunately, these products are not accurately formed and a significant experimental uncertainty needs to be considered. With upcoming 3d printing capabilities, uniform packing particles can be produced, that differ significantly from anything known before. Though to the actual catalyst production by 3d printing is probably still a long way off, this technique is highly appreciated for prototyping packed bed shapes to be incorporated into systematical, experimental shape evaluation studies.

With developing numerical techniques, the virtual creation of single, arbitrary shaped elements is not a problem anymore, however, the numerical generation of random packings of these arbitrary shapes still is a compromise. While the complete physical description of the randomly packing of particles, called the Discrete Element Method [11, 12], is basically only valid for spheres, efforts were undertaken, to create the desired arbitrary shapes using certain workarounds [13, 14]. Besides the limitations of packing generation, some studies exist, comparing fluid dynamics [15, 16], heat [17, 18] and mass transfer [19, 20] within packed beds of typically simple shapes, but also more complex ones. But despite the impressive capability, numerical studies offer the required validation with experimental data remains the main issue.

In this study, shape variations of a sphere with a circumferential duct, the Yo-Yo shape, are evaluated numerically. This shape is simple enough to still be comparable to the frequently evaluated sphere but with cutting a surrounding channel, a higher geometric surface area and a lower packed bed pressure drop is expected. While the final shape will be producible by traditional tablet pressing techniques, the previous numerical evaluation significantly decreases development costs while being capable to find the optimal geometry.

6.2 Theory

6.2.1 Packing structure

Important geometric parameters are the geometric surface area a_{geo} , the axially averaged radial porosity distribution $\varepsilon(r)$ and the average bed porosity $\bar{\varepsilon}$. The geometric surface area can be calculated according to Eq. (6.1).

$$a_{\text{geo}} = \frac{N \cdot a_p}{V_T} = 6 \cdot \frac{1 - \bar{\varepsilon}}{d_p} \quad (6.1)$$

The average bed porosity can be easily determined experimentally by water displacement [21–23] or weighing method [4, 24] and numerically by determining the number of void cells in the calculation grid. The parameter is known to depend on the tube-to-particle diameter ratio λ and on the particle's material, shape and size distribution, the container's material and shape and the applied deposition and compaction methods [25, 26]. In this study, a standardized packing is used incorporating smooth, homo-sized ideal particles, a standard packing mode and constant tube characteristics.

For low tube-to-particle diameter ratios $\lambda < 10$, an increase in average bed porosity with decrease of λ can be observed due to the confining influence of the tube's wall (see [4, 21, 27–30] for experimental studies and [4, 21, 22, 27, 29, 31–36] for derived correlations). In this study, λ varies between 5 and 5.8, which is inside the wall effected range. This wall effect causes the particles to align to a wall-induced ring-like pattern, which eases out 4 to 5 particle diameters away from all surrounding confinements [27]. The radial porosity distribution expresses this particle order, with a local porosity of one directly at the tube wall and for spheres describing a damped oscillating trend reaching into the packing's bulk region [27]. Experimentation methods to determine radial porosity profiles include bed solidification and incremental machining techniques [9, 37–42] as well as bed projection methods including x-ray tomography [43–47] and magnetic resonance imaging [48–52]. A selection of derived correlations were presented by Antwerpen et al. [1].

While spheres are well studied, only sparsely shapes other than spheres are investigated as complex geometries require a hand full of aspect ratios and characteristic diameters. Moreover, simple shape factors as for instance sphericity were proven incapable to universally describe bed characteristics [53]. Consequently, there is no rule and no correlation that can predict the average and local void distribution

for a packed bed of arbitrary shaped particles. Due to availability problems of shaped particle packings, studies on geometrical variations are prone to be performed numerically. In this context, computational packing generation can be performed by the Discrete Element Method (DEM) [11, 12, 54] or similar tools [55–57]. But as the original DEM was only defined for ideal spheres, compromises have to be accepted in order to use this technique with arbitrary shapes. These compromises include the time consuming enlargement of the actual DEM code bit-by-bit to other shapes [58–61], the computational expensive assembly of the desired shape by a large enough number of overlapping spheres [16, 62–68], the transfer of the DEM-algorithm and underlying physics to voxels (cubes) and the subsequent assembly of the desired shape by voxels [69–73], or, by ignoring certain physical conditions, shapes can be represented by a surface grid [13, 74]. A good comparison of some methods in regard to packing generation was presented by Fernengel et al. [14] for spheres and Caulkin et al. [68] for cylinders.

6.2.2 Fluid dynamics

The fluid dynamical evaluation of a packed bed comprises the pressure loss of the packing and the flow field analysis, most predominantly the axially averaged radial profile of the axial velocity component $u_z(r)$, but also the radial profile of the radial velocity component $u_r(r)$. The importance of the latter was only recently emphasized in regard to heat transfer [75]. Many pressure loss experiments have been performed in regard to sphere packings, and many correlations have been derived (see [3] for a review) relating the non-dimensional pressure loss called friction f' to the fluid state indicated by the packing Reynolds number Re_p , but again, a broad understanding of the effects of any other packed shape is still virtually absent.

$$f' = \frac{\Delta P}{H} \cdot \frac{d_p}{\rho \cdot u_0^2} \cdot \frac{\bar{\varepsilon}^3}{1 - \bar{\varepsilon}} = f'(\text{Re}_p) \quad \text{with} \quad \text{Re}_p = \frac{\rho \cdot d_p \cdot u_0}{\eta \cdot (1 - \bar{\varepsilon})} \quad (6.2)$$

$$\text{Ergun [76] :} \quad f' = \frac{150}{\text{Re}_p} + 1.75 \quad (6.3)$$

$$\text{Eisfeld and Schnitzlein [77] :} \quad f' = \frac{K_1 \cdot \left(1 + \frac{2}{3 \cdot \lambda \cdot (1 - \bar{\varepsilon})}\right)^2}{\text{Re}_p} + \frac{1 + \frac{2}{3 \cdot \lambda \cdot (1 - \bar{\varepsilon})}}{\left(\frac{k_1}{\lambda^2} + k_2\right)^2} \quad (6.4)$$

$$\text{Erdim et al. [3] :} \quad f' = \frac{160}{\text{Re}_p} + \frac{2.81}{\text{Re}_p^{0.096}} \quad (6.5)$$

While the correlation of Ergun [76] is the most known correlation, for instance Eisfeld and Schnitzlein [77] additionally considered the influence of the wall by introducing λ , and to a certain degree the particle shape by listing pre-parameters K_1 , k_1 , and k_2 for a small shape selection. Despite, Erdim et al. [3] reviewed a large number of correlations finding the least experimentation error for a packed bed of spheres in their version of the original Carman [34] equation, being valid for all λ .

The experimental validation of flow profiles is still a major area of concern, as obtainable data is typically not representative or too vague. This predominates the evaluation of flow fields by numerical means such as computational fluid dynamics (CFD). Despite, scattered experimental studies have been performed, including the determination of the flow profile underneath a packing by anemometers [78] or specially

designed collectors [79], by incorporating electrochemical sensors into packing elements [80] or by using projection methods such as magnetic resonance imaging [52, 81], laser doppler anemometry [82] or particle image velocimetry [83]. While some details are still unveiled, it is generally accepted, that the radial flow pattern is somewhat equivalent to the radial porosity distribution. Consequently, large inhomogeneities in the local porosity distribution results in equivalent flow inhomogeneities and should thus be avoided. In a packing of spheres, the terms *channeling* and *wall channeling* were established describing the by-passing of flow in the high porosity regions between ordered sphere layers and between the outermost sphere layer and the confining wall, respectively.

6.3 Methods

The herein performed general simulation procedure consists of the steps of i) shape design, ii) numerical packing generation, iii) mesh creation, iv) steady-state flow simulation, v) dynamic flow simulation with tracer, and vi) post-processing of the data (cf. Fig. 6.1). Each step, except the very first one, requires an

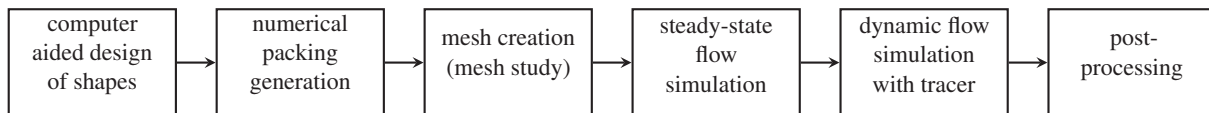


Figure 6.1: General simulation procedure.

accurate validation with experimental data or generally accepted correlations. As for this specific shape, no experimental data nor generally accepted correlations exist, the whole procedure is validated first using a reference sphere packing.

6.3.1 Shape design

The herein selected shape comprises a spherical base shape of diameter d from which a circumferential duct is cut. The cross-section of the whole shape and the details of the duct are displayed in Fig. 6.2. Along a wedge-shape selection of angle-width β , a linear cut is made of deepness a . At the end of this cut and pointing to the sphere center, a circle fragment is drawn where the radius is automatically adjusted to allow tangential connection between sphere fragment and linear cut a . The sharp edge of this duct is rounded-off with radius R . The whole shape is unambiguously described by these four parameters sphere diameter d , duct deepness a , duct width β and rounding radius R .

For the following shape variations, the sphere diameter is kept constant at $d = 10$ mm, duct deepness a was selected to vary among 0 mm, 0.5 mm, 1.0 mm and 1.5 mm, duct width β was selected to vary among 20°, 30°, 40° and 50°, and rounding radius R was selected to vary between 0 mm, 0.5 mm and 1 mm. A total of 28 slightly different shapes were thus obtained, for illustration purposes listed in Table 6.1. The shapes were designed with Autodesk[®] Inventor[®] providing the exact volumes and surface areas for each modification.

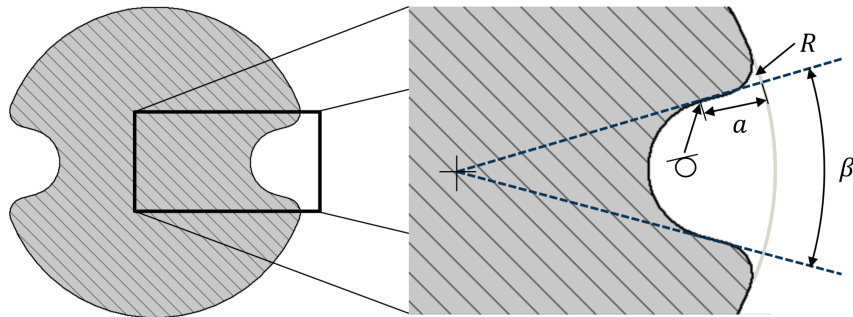


Figure 6.2: Shape details of sphere with circumferential duct.

Table 6.1: Overview of designed shapes incorporated in this study.

Angle β	rounding radius $R = 0.5$ mm				duct deepness $a = 1.0$ mm		
	$a = 0$ mm	$a = 0.5$ mm	$a = 1.0$ mm	$a = 1.5$ mm	$R = 0$ mm	$R = 0.5$ mm	$R = 1.0$ mm
50°							
40°							
30°							
20°							

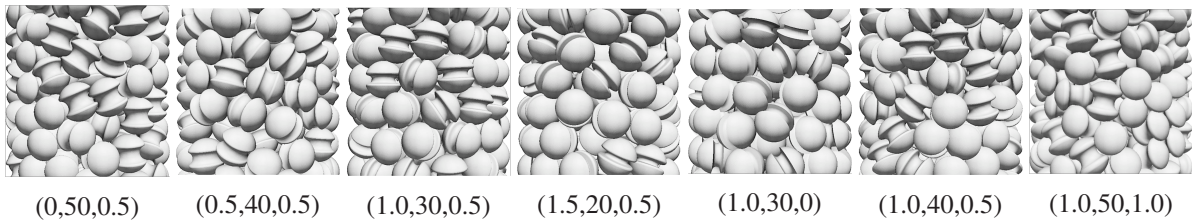


Figure 6.3: Selection of packed tubes with shapes of dimension (a, β, R) .

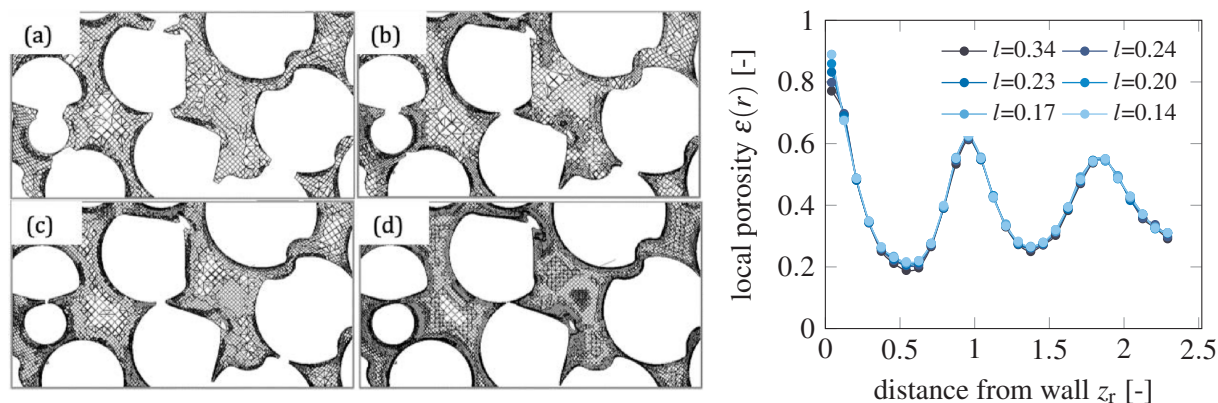
6.3.2 Numerical packing generation

Packing generation is performed utilizing the DigiDEMTM code, a voxelated particle simulation software incorporating a digital packing algorithm based on the *Monte Carlo Approach* whilst explicitly considering physical interaction forces similar to the *Discrete Element Method* and is elsewhere described in more detail [44, 69]. The packing procedure is identical to the one we already described [14]. Hereby, the 3d objects were digitized to a resolution of 10 voxel mm^{-1} , thus 100 voxel define the shapes diameter. The material properties were set as follows: density $\rho = 3000 \text{ kg m}^{-3}$, coefficient of restitution $e = 0.3$, coefficient of friction $\mu = 0.7$ and Poisson's ratio $\nu = 0.3$. The objects are filled into tubes of constant height $H = 3000 \text{ voxel}$ (300 mm) and diameter $D = 500 \text{ voxel}$ (50 mm), thus representing packed beds with a tube-to-particle diameter ratio $\lambda = 5.0$ when considering the reference sphere. The packing mode was selected to be damping and the stop criterion is a pre-set time of 3 s. Figure 6.3 displays extracts of the packed beds for a selection of shapes.

The herein used packing procedure is identical to the one presented and validated with literature data in [14], despite that ideal spheres were used instead. It is also identical to the one described and validated with computer-tomography scans in [84], again for ideal spheres. As no experimental data is available for the herein used shapes, the validity of packing procedure and the adequacy of voxel resolution are assumed based on the perfect fit of numerical results and experimental data in regard to spheres. For spheres, the reproducibility as the mean relative standard error of packing generation was found to be one percent for the radial porosity profiles and 0.5 percent for the averaged bed porosity, based on ten identical packing repetitions (see [84]).

6.3.3 Mesh creation and mesh study

The location vector and the rotation matrix of each particle in a packing are obtained from the numerical packing generation tool. Based on this information, the packing is reconstructed in combination with an .stl-file of the intended shape having the respective size using a LINUX bash script. The meshing of the void space of the reconstructed packed bed is performed using *snappyHexMesh*, a build-in meshing tool of computational fluid dynamics freeware OpenFOAM[®] that generates castellated irregular shaped mesh cells. This allows a mesh refinement where a higher resolution is needed, typically close to the contact points. Here, The mesh is refined in three steps close to each true and near contact point and additionally, five layers of layered mesh cells are introduced to smoothly represent the round sphere's surface.



(a) Exemplarily cut through meshes of size $l = 0.34$ mm, 0.23 mm, (b) Comparison of radial porosity distribution. 0.20 mm and 0.14 mm (left to right).

Figure 6.4: Comparison of different mesh resolutions of shape (0.5,30,0.5), where l represents the mean cell size in mm. The fine grid convergence index [85] was just below 1 % for $l = 0.20$ mm and 0.15 % for $l = 0.14$ mm.

No effort was done regarding a specialized treatment of contact points, as for instance the creation of bridges, cutting of caps, the shrinkage or inflation of all spheres, as at times described in the literature. A mesh study (cf. Fig. 6.4) with decreasing mesh sizes is performed, and the mesh resulting in a *fine grid convergence index* [85] in regard to porosity, velocity and pressure drop of just below 1 % was asserted to sufficiently fulfill the requirements.

6.3.4 Steady-state and dynamic flow simulation

Computational fluid dynamics using open source code OpenFOAM[®] is performed on all numerically generated packed beds including the reference sphere packing. Simulation of the steady-state flow of air at ambient conditions is performed incorporating the *SIMPLE* (Semi- Implicit Method for Pressure Linked Equations [86]) algorithm. The convergence criteria is 0.001 for all parameters. The standard superficial velocity is selected to be $u_0 = 1.132 \text{ m s}^{-1}$. The incompressibility of the fluid is assumed and justified with excess pressure being significantly below 1 bar. Moreover, a broad selection of turbulence models is tested with the reference sphere packing. These comprise for instance the *Wall-Adapting Local Eddy-viscosity model* (WALE) [87], the *Spalart-Allmaras Detached-Eddy-Simulation* (DES) [88, 89], the *k - kl - ω Reynolds-Averaged Simulation* (RANS) [90] and the *Launder-Sharma k-ε model* [91]. The differences in resulting pressure drop simulated for $\text{Re} = 10$ to 10000 is negligible small among all tested models and when compared to the theoretical solutions using the pressure drop correlation of Einfeld and Schnitzlein [77] and Erdim et al. [3] as displayed in Fig. 6.5. The *Launder-Sharma k-ε model* is finally selected to be utilized as turbulence model.

The dynamic flow simulations using the *scalarTransportFoam* solver available in OpenFOAM[®] is based on the velocity field u created using steady-state conditions, except that at time $t = 0$ s a tracer (scalar T) is added just above the packing and distributed over the tube cross-section, performing a step experiment with its normalized concentration ranging from 0 to 1. Eq. (6.6) shows the incompressible form of the

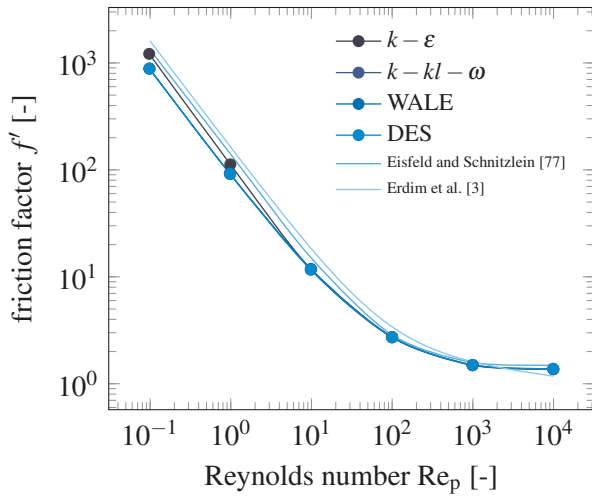


Figure 6.5: Friction factors f' obtained for a large range of Reynolds numbers Re_p and various turbulence models for the reference packing of spheres. A very good agreement of simulation results and empirical correlations can be identified, especially for the intended range of $Re_p > 10$.

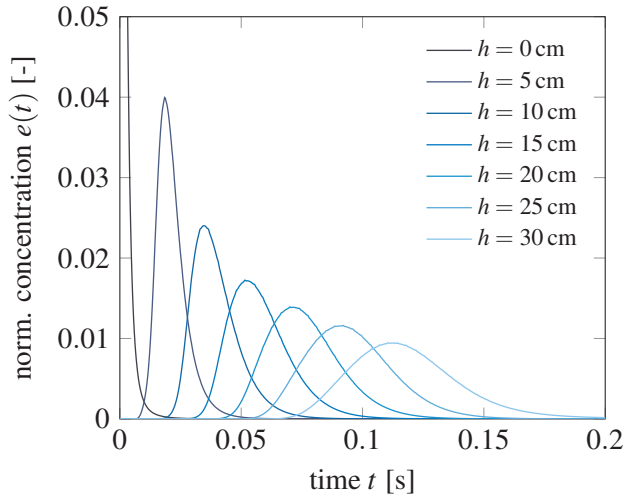


Figure 6.6: Residence time distribution curves obtained at various heights along the packed bed performing a step experiment with tracer injection at $t = 0$ s and $h = -0.25$ cm.

scalar transport ans is hence devided by the density.

$$\frac{\partial}{\partial t}(T) + \nabla \cdot (u \cdot T) - \nabla \cdot (D_T \cdot \nabla T) = S_T \quad (6.6)$$

The numerical time step Δt is determined so that the Courant number $Co = \Delta t \cdot \tau_c$ is below 1. Herein, the characteristic time scale of a local cell $\tau_c = \frac{1}{2 \cdot V_c} \cdot \sum(\phi_i)$ depends on the cell volume V_c and the face volumetric fluxes ϕ_i . The distribution of the tracer is numerically measured at a certain time interval and at different height positions along the packing. This is exemplarily depicted in Fig. 6.6. The simulation is stopped when the average tracer concentration at the measuring point directly below the packing reaches unity.

6.3.5 Post-processing

A comprehensive PythonTM script incorporating the pandas' library is developed for the data analysis of the resulting pressure drop and velocity fields. This script comprises the sorting of cells and their values to horizontal and ring-shaped bins to calculate the axial and radial distributions, respectively. Moreover, the velocity field is sorted in sphere shell shaped bins starting from the particle's center and averaged over all investigated packing particles. This allows the visualization of flow fields within the circumferential ducts of the previously described Yo-Yo shape, particle's overlapping due to these ducts and the separate evaluation of bulk flow away from the shapes ducts. In order to neglect top (inflow) and bottom (outflow) effects, both in regard to porosity and flow distribution, a section of three particle diameters is cut off from the top and the bottom of the packing. Due to the varying cell size, all values are related to the respective cell volume. An exemplary depiction of all three distributions is displayed in Fig. 6.7, whereof the axial

distribution is shown to prove an evenly packing structure along with the tube height and will not be evaluated any further.

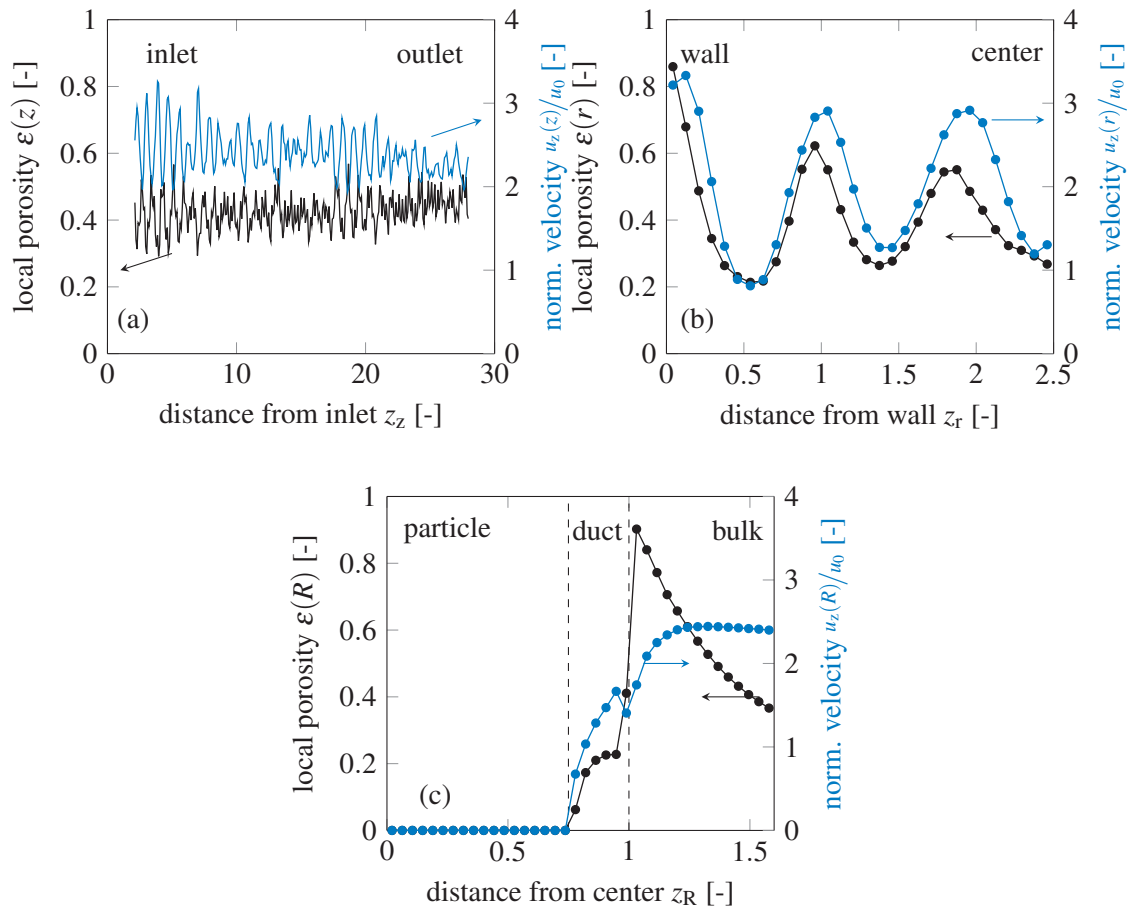


Figure 6.7: Distributions of local porosity $\epsilon(x)$ and normalized axial velocity component $u_z(x)/u_0$ as obtained by the post-processing procedure displayed for a packing of the (0.5,30,0.5) Yo-Yo shape as (a) axial distribution with $x = z$, (b) radial distribution with $x = r$, and (c) spherical distribution with $x = R$.

6.4 Results and discussion

The obtained results are clustered into geometrical considerations, flow field features, pressure drop characteristics and residence time properties.

6.4.1 Geometrical considerations

Regarding geometric packing characteristics, the axially averaged local porosity distribution in radial direction $\epsilon(r)$, hereinafter the radial porosity distribution, as a function of the dimensionless distance from the wall $z_r = (R_1 - r)/d$ is the typically used parameter. Figure 6.8 displays the radial porosity distribution

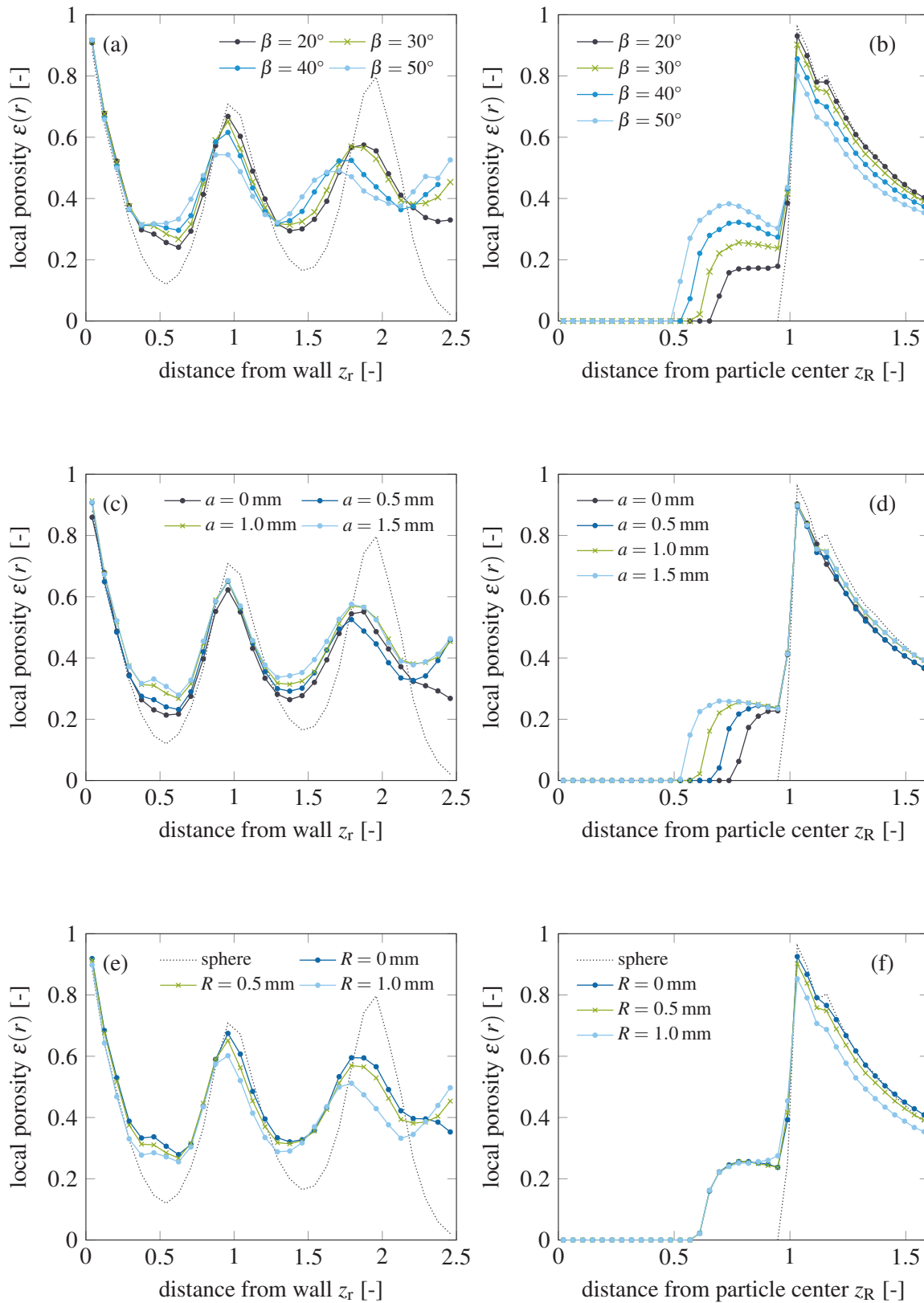


Figure 6.8: Comparison of radial (left) and spherical (right) porosity distributions of selected shape families (a,b) (1.0, β ,0.5), (c,d) (a ,30,0.5), and (e,f) (1.0,30, R), based on reference shape (1.0,30,0.5) [green cross marks] and compared with a reference sphere packing [black dotted line].(For interpretation of the references to colour in this figure legend, the reader is referred to the web version of this article.)

for a selected reference Yo-Yo shape specification with dimensions (1.0,30,0.5) as a green curve with cross marks. From this reference, the obtained results for Yo-Yo shapes where only one parameter is varied are added. This comprises the variation of duct width β in Fig. 6.8a, duct deepness a in Fig. 6.8c and rounding radius R in Fig. 6.8e. For comparison, the radial porosity distribution of the reference sphere is added as a dotted line. The oscillatory behavior typically obtained for packed beds of spheres describing an accumulation of sphere centers in a ring-like structure starting from the tube wall is visible. While this oscillatory behavior can be generally seen for the new Yo-Yo shapes, too, the distinctness of the ring formation, however, is significantly reduced, discernible in a smaller oscillation amplitude. It is suspected, that this may drastically reduce flow channeling effects.

Comparing the various shape parameters, an increase in duct width β reduces the overall oscillation amplitude, an increase in duct deepness a increases the porosity minima (particle ring centers) but does only sparsely effect the maxima (inter-particle ring void) and an increase in rounding radius R moves the whole porosity distribution to lower values.

The overall decrease of amplitude in case of increasing β can be explained with increased particle overlap and interpenetration. While spheres can't overlap by any means, the introduction of circumferential ducts allows particle interpenetration in this region. With increasing duct width, this interpenetration increases, both in the axial and radial direction. This randomizes the particle placements away from the formation of clearly distinctive ring structures. Still, the confining wall causes the formation of some order, especially directly adjacent to it. It is to be noted, that the oscillation period is moving to smaller values as well. This can be explained again with the particle interpenetration, but may additionally be caused by the slight decrease of the volume-based particle size.

While the increase of duct width increases the particle interpenetration and thus reduces maxima and increases minima, the increase in duct deepness only affects the minima porosities with again decreasing the overall oscillation amplitude. This effect may be explained, that with increasing duct deepness, no increase in particle interpenetration can be obtained, but the mere solid volume reduction causes the minima to increase. Additionally, the formation of an intermediate mini-maximum at the original minima position can be observed with increasing duct deepness. This intermediate maximum is known from packed beds with packing particles having one or more through-cut holes [92].

The increase in rounding radius evokes a shift of the radial porosity distribution without significantly changing its appearance. Consequently, particles simply pack slightly denser when edges are smoothed. It is assumed that the overall packing structure is however not affected.

For a better understanding of particle interpenetration, the shell-volume-averaged porosity distribution starting at a particle center to the bulk of a packing, averaged over all packing particles and hereinafter called spherical distribution is plotted and displayed in Figs. 6.8b, 6.8d and 6.8f. For comparison, the data of the reference sphere packing is added. Regarding spheres, the porosity is zero until reaching the sphere's surface at $z_R = R/(d/2) = 1$. Here, a sharp increase in porosity marks the transition between solid particle and packing void. In contrary, regarding spheres with equatorial ducts a third region, the duct-region is obtained, after which the sharp transition to the bulk of the packing occurs. Any particle

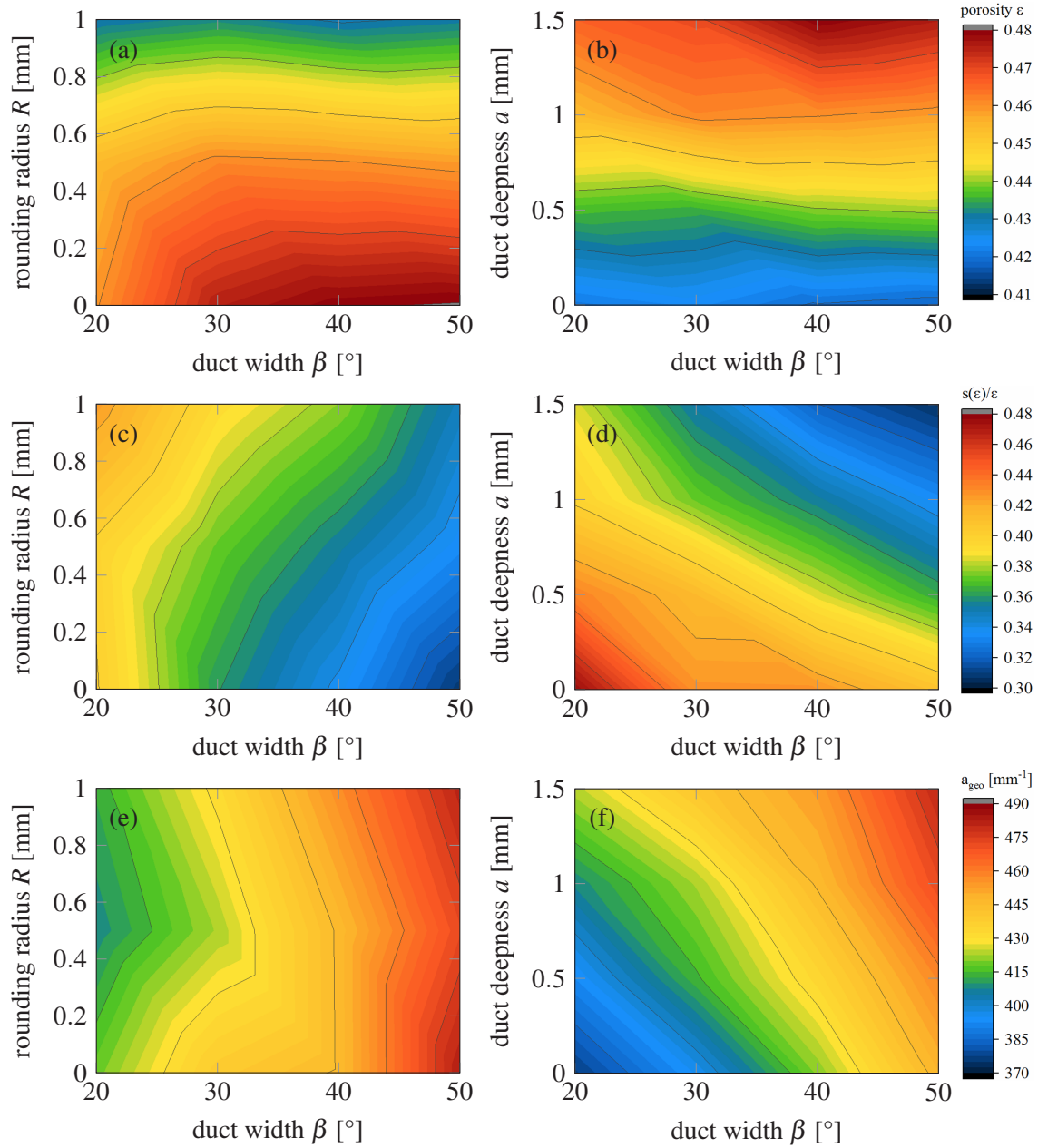


Figure 6.9: Contour plot of geometric characteristics: (a,b) average bed porosity $\bar{\epsilon}$, (c,d) normalized standard deviation $s^{(\epsilon)}/\bar{\epsilon}$, and (e,f) geometric surface area a_{geo} , for the rounding radius (left) and the duct deepness (right) against duct width, respectively.

interpenetration should be visible in this intermediate region of the sphericle distribution as a reduction in porosity especially close to $z_R = 1$.

This phenomenon can be clearly seen in Fig. 6.8b when varying the duct width, as with increasing β , the formation of a minimum just below $z_R = 1$ is more pronounced. Moreover, it can be seen, that the variation of β affects the duct and the bulk packing structure. In contrary, when varying the duct deepness, all curves merge just below $z_R = 1$, indicating no change in particle penetration. Moreover, the bulk packing porosity is not affected at all by varying a , thus an increase in duct deepness only increases inner-particle void without affecting the surrounding packing structure. Last but not least, when changing the rounding radius, the particle penetration and inner-particle void remain untouched, while the bulk packing structure is in a more condensed state. In summary, the observations based on radial and spherical porosity distributions draw the same conclusions regarding the effect of shape properties on packing structure.

Besides these local packing structure properties, averaged values are typically used for a quick parameter overview and later processing regarding for instance pressure drop considerations. These comprise the average bed porosity $\bar{\varepsilon}$ which is calculated as the total cell volume per tube volume after removing inflow and outflow regions, the geometric surface area a_{geo} and the characteristic diameters d_p and d_v . The results for all investigated Yo-Yo shapes are displayed in the contour plots of Fig. 6.9 and Fig. 6.S1. From these plots, it is observable, that a higher average porosity can be obtained with increasing duct deepness a and lower rounding radius R while being only sparsely effected by the duct width β . Regarding the geometric surface area, higher values are obtained with increasing duct width β and duct deepness a , while being less affected by the rounding radius R . It is to be noted, that all values of the average porosity and the geometric surface area are significantly larger than those of the reference sphere packing (see Table 6.2).

In order to have a single parameter for the evaluation of packing structure, especially in terms of oscillation amplitude, the relative weighted standard deviation of the radial porosity distribution $s(\bar{\varepsilon})/\bar{\varepsilon}$ is introduced, which describes the mean normalized amplitude height. A smaller value is favored, indicating a smaller oscillation amplitude. As displayed in Fig. 6.9, a smoother void distribution is obtained with increasing duct deepness a and duct width β and with decreasing rounding radius R .

In summary, regarding only the geometric packing characteristics, Yo-Yo shapes with large a and β and small R should be preferred, emphasizing that without exception all shape variations are meliorated in regard to the reference sphere.

6.4.2 Flow field features

Similar to the porosity profiles, velocity profiles of the axial velocity component u_z as defined in Fig. 6.10 normalized to the superficial velocity $u_0 = 1.132 \text{ m s}^{-1}$ are plotted and displayed in Fig. 6.11. Again, the

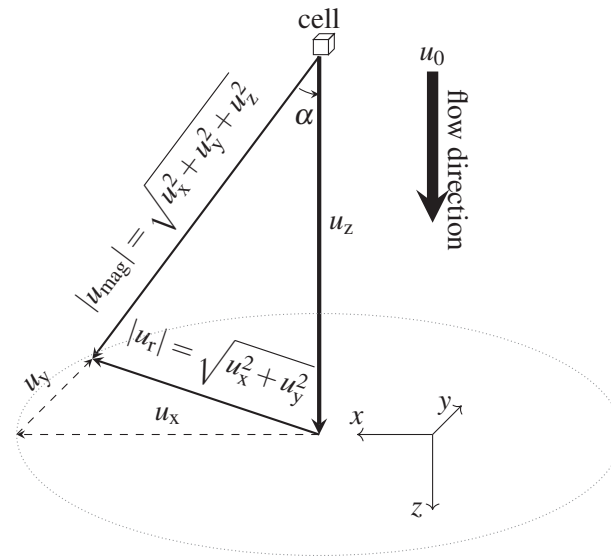


Figure 6.10: Schematic drawing of relevant velocity components of the flow vector $|u_{\text{mag}}|$ with an angle α to the flow direction of superficial velocity u_0 and packing velocity $u_z = u_0/\bar{\epsilon}$.

results of the reference sphere packing are added as dotted line and the shape selection is equal to the porosity profile discussion.

Regarding the radial velocity $u_z(r)$ distribution, a general significant reduction of oscillation can be seen for all Yo-Yo shapes in regard to the reference sphere packing. The alternating occurrence of low flow and high flow regions (channels) are equivalent to the respective porosity profiles. Without going into great detail, Yo-Yo shapes with large duct width β and large duct deepness a should be selected for less channeling. The selection of rounding radius R is less significant. For exploratory reasons, the spherical velocity distributions are added.

Besides the axial velocity distribution, the radial and spherical distribution of the normalized radial velocity component u_r (see Fig. 6.10) is displayed in Fig. 6.S2 in the Supplementary information. Again, the distribution is much smoother compared to packings of spheres. Furthermore, the radial and spherical distributions of flow vector angle α as defined in Fig. 6.10 are plotted in Fig. 6.S3 in the Supplementary information. The flow vector angle describes the relationship between axial and radial velocity component. Small values $\alpha < 20^\circ$ indicate non-distracted channel flow, whereas large values, especially $\alpha > 90^\circ$ indicate backflow. Both are not favoured in terms of residence time distribution, as backflow regions increase the residence time and channel flow regions reduce it. A closer look to Fig. 6.S3 reveals averaged flow vector angles, that attain very large mean values even above 90° at positions of low flow/low porosity when regarding packed beds of spheres. This describes the occurrence of significant dead zones with high back flow portion at the locations where the spheres form high density rings. This undesired characteristic is significantly reduced when shapes with circumferential ducts are utilized. Additionally, these ducts are assumed to allow a better radial dispersion of fluid flow, based on these findings.

The interaction of structural characteristics and resulting flow profiles are displayed in Fig. 6.12 for the afore mentioned reference Yo-Yo shape with dimensions (1.0,30,0.5). For comparison, the respective curves of the reference sphere are added as dotted lines. As can be seen, the axial velocity and the flow

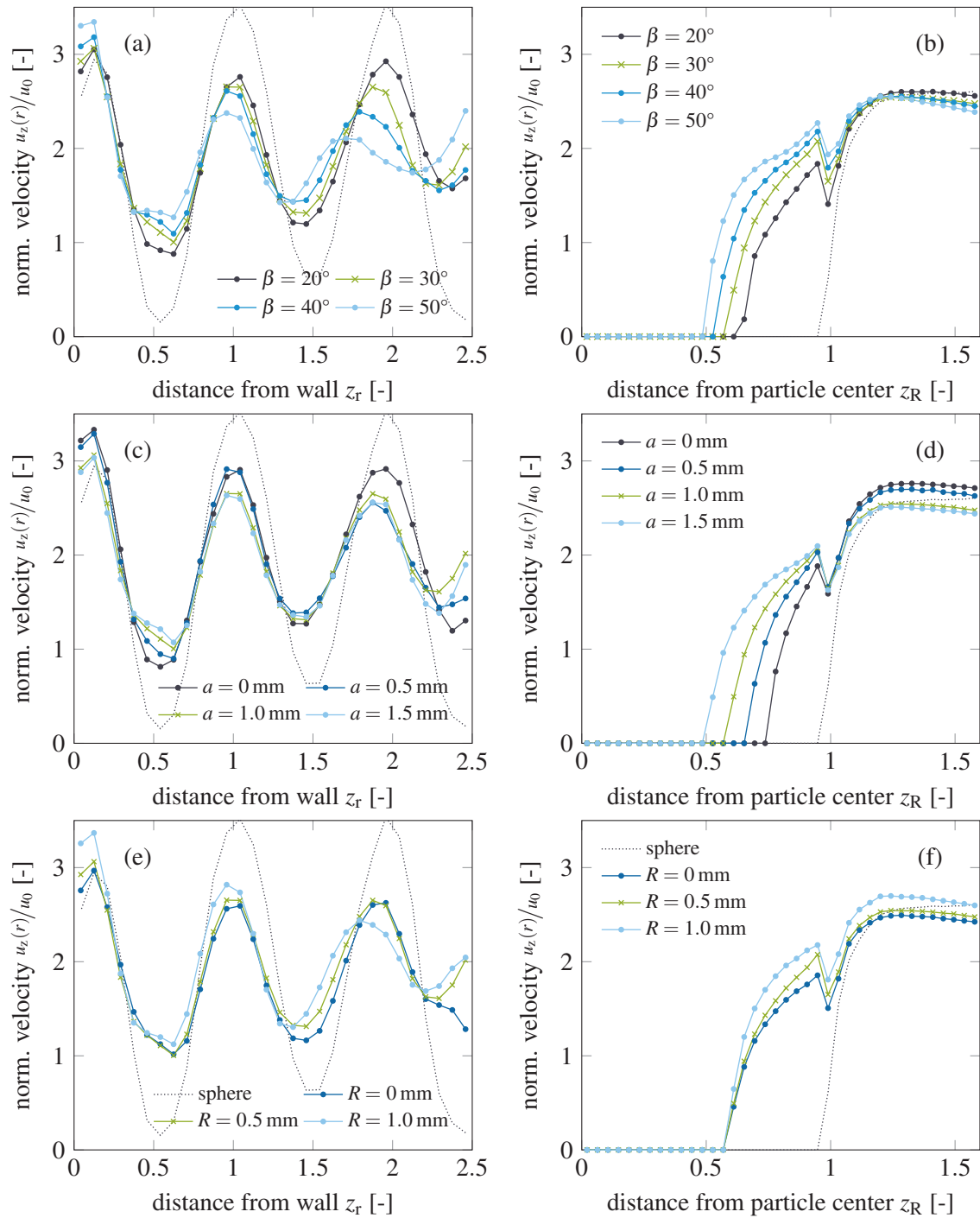


Figure 6.11: Comparison of radial (left) and spherical (right) distributions of the axial velocity component u_z of selected shape families (a,b) $(1.0, \beta, 0.5)$, (c,d) $(a, 30, 0.5)$, and (e,f) $(1.0, 30, R)$, based on reference shape $(1.0, 30, 0.5)$ [green cross marks] and compared with a reference sphere packing [black dotted line]. (For interpretation of the references to colour in this figure legend, the reader is referred to the web version of this article.)

vector angle follow strictly the pattern predetermined by the packing porosity. Consequently, in regions with high porosity, the axial velocity is high and the flow vector angle is low. This channel formation is significantly more pronounced when regarding spheres. In contrary, the radial velocity component does not follow this pattern, neither for the herein discussed Yo-Yo shape nor for the reference sphere.

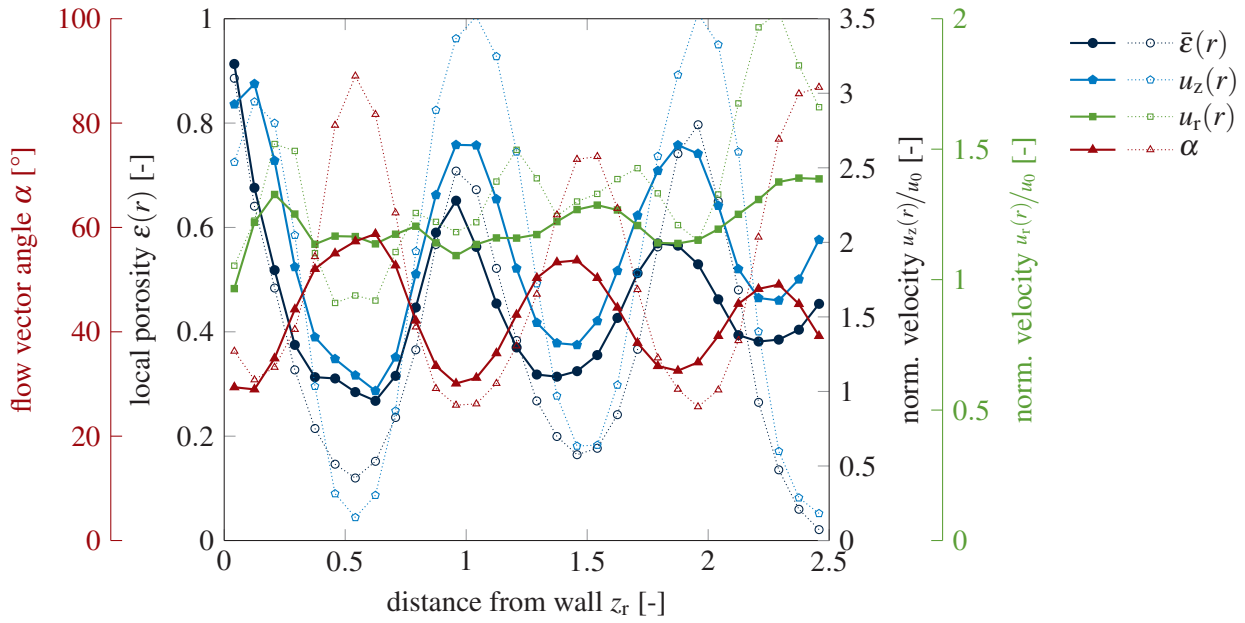


Figure 6.12: Comparison of flow vector angle α , local porosity $\epsilon(r)$ and normalized axial $u_z(r)$ and radial $u_r(r)$ velocity component in radial packing direction, exemplarily shown for reference shape (1.0,30,0.5) with solid and reference sphere with empty symbols.

The mean values for all discussed flow parameters as well as the respective relative weighted standard deviation of the radial distributions are displayed for all investigated shapes as contour plots in the Supplementary Figs. 6.S4 and 6.S5. A selection of underlying values as well as the reference sphere values are listed in Table 6.2. In all parameters the herein described Yo-Yo shapes are preferred to the reference sphere.

Table 6.2: Overview of flow field parameters of selected shapes and the reference sphere packing.

parameter	Sphere	(0,50,0.5)	(0.5,40,0.5)	(1.0,30,0.5)	(1.5,20,0.5)
a_{geo} [mm^{-1}]	354.7	447.4	433.7	423.0	424.1
$\bar{\epsilon}$ [-]	0.4089	0.4178	0.4394	0.4612	0.4657
$\frac{s(\bar{\epsilon})}{\bar{\epsilon}}$ [-]	0.5687	0.4084	0.3848	0.3725	0.3849
$\bar{u}_z(r)$ [-]	2.451	2.4027	2.2850	2.1768	2.1552
$\frac{u_0}{s(\bar{u}_z(r)/u_0)}$ [-]	0.4972	0.3633	0.3211	0.3054	0.3196
$\bar{u}_r(r)$ [-]	1.249	1.340	1.279	1.164	1.214
$\frac{u_0}{s(\bar{u}_r(r)/u_0)}$ [-]	0.1542	0.04506	0.04803	0.06259	0.08106
$\bar{\alpha}(r)$ [°]	48.81	41.65	40.79	39.43	38.54
$\frac{s(\bar{\alpha}(r))}{\bar{\alpha}(r)}$ [-]	0.4126	0.2357	0.2245	0.2348	0.2523

In a further step, the superficial velocity was varied to cover Reynolds numbers from $Re = 10$ to 3000. As depicted in figure Fig. 6.13 an increase of oscillation amplitude is obtained with decreasing superficial flow velocity, which is especially predominant in the channel flow region.

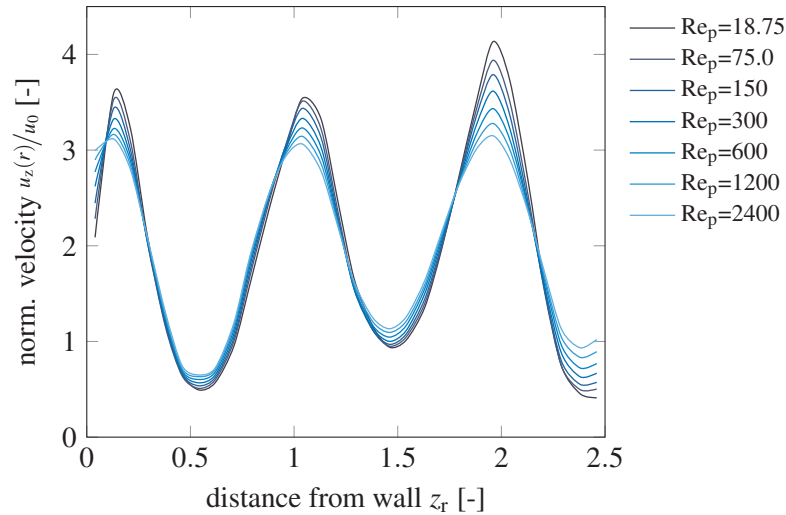


Figure 6.13: Variation of normalized flow velocity $u_z(r)$ with the packing Reynolds number Re_p , exemplarily shown for shape (0,20,0.5).

6.4.3 Pressure drop characteristics

The obtained friction factors for all investigated Yo-Yo shape variations using the base case of superficial velocity $u_0 = 1.132 \text{ ms}^{-1}$, are summarized in Fig. 6.14. For comparison, the correlations of Erdim

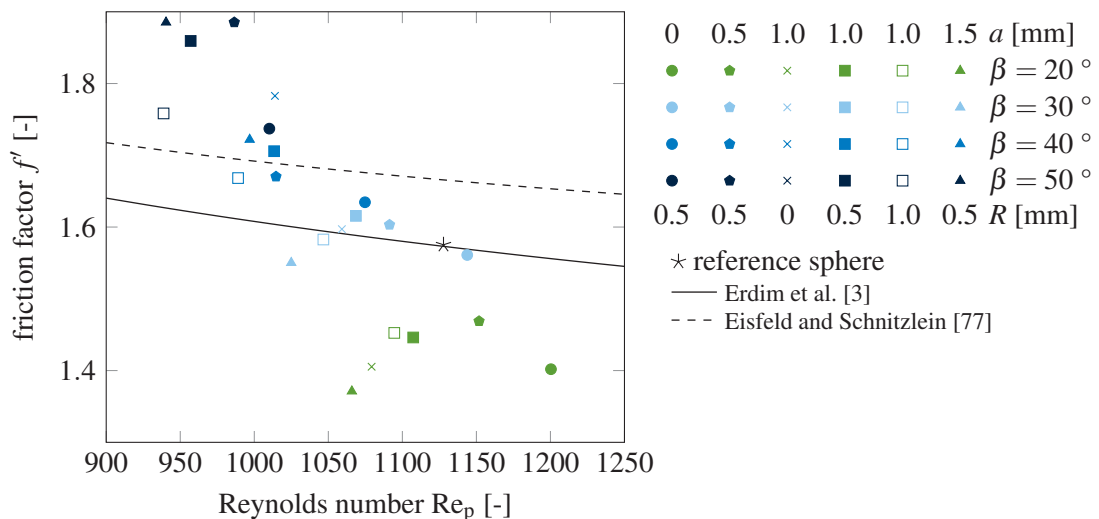


Figure 6.14: Comparison of friction factors f' for all investigated shape variations and the reference sphere packing for the respective Reynolds numbers obtained with superficial velocity $u_0 = 1.132 \text{ ms}^{-1}$ and the case sensitive porosity and size values. The literature correlations of Erdim et al. [3] and Einfeld and Schnitzlein [77] obtained for sphere packings are added as reference.

et al. [3] and Einfeld and Schnitzlein [77] are plotted, representing the reference sphere case. The different Reynolds numbers are obtained as the shape sensitive porosity and Sauter diameter are included in this number. It can be seen, that the largest influence on the friction factor (non-dimensional pressure drop) is obtained by varying the duct width β . In contrary to the preferred flow characteristics of large β , the friction factor is smaller for lower values of β . No linear trend can be observed for the shape variation of duct deepness a and rounding radius R in regard to friction factor. There are probably overlapping shape effects that could be investigated in a separate statistical based setup using design of experiment tools.

Besides, the influence of Reynolds number by varying the superficial velocity was investigated and the obtained friction factors are displayed in Fig. 6.15 for eight selected Yo-Yo shape cases. It is clearly

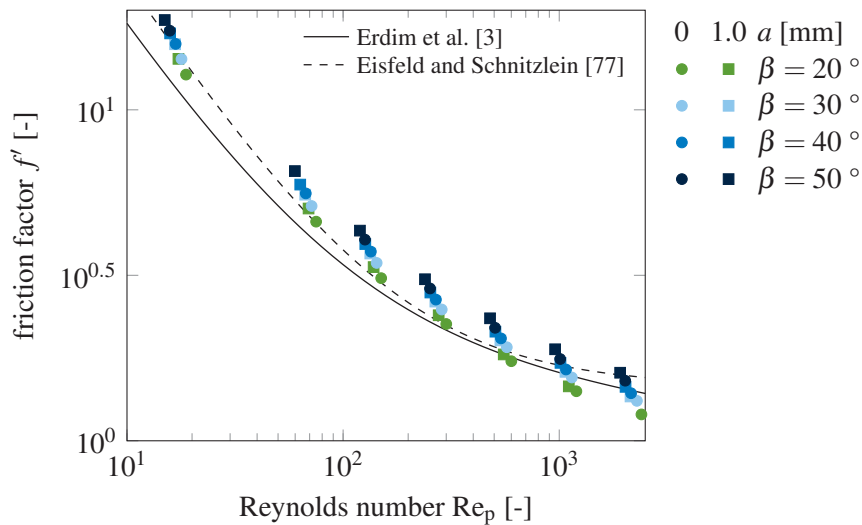


Figure 6.15: Comparison of friction factors f' for eight selected shapes with constant rounding radius $R = 0.5$ mm but varying superficial velocity, resulting in a Reynolds number range of around 10 to 2000. The literature correlations of Erdim et al. [3] and Einfeld and Schnitzlein [77] obtained for sphere packings are added as reference.

visible, that the variation of the Reynolds number does not alter the shape influence, with shapes having a low β being preferred in regard to friction. Moreover, friction is slightly larger for a larger duct deepness a . Moreover, the overall friction factor trend is closer to Einfeld and Schnitzlein's correlation for low Re_p and closer to Erdim et al.'s correlation at high Re_p values. However, in general, the given trend for spheres is met quite well using the herein investigated spherical Yo-Yo shapes with equatorial ducts. It is to be noted, that a lower friction factor does not necessarily result in lower bed pressure drop, as shape sensitive parameters such as porosity and Sauter diameter are included in this parameter. It is further noted, that the small shift in Reynolds number comes as well from individual values of porosity and characteristic diameter for each investigated packing.

In summary, Yo-Yo shapes with small duct widths β are preferred in regard to pressure drop. This is in contrary to the findings for fluid field and structural characteristics.

6.4.4 Residence time properties

Due to the high processing time and CPU requirements of dynamic flow simulations, only selected cases were incorporated in the residence time distribution study. The obtained data for average residence time $\bar{\tau}$ and the square root of its variance $\sqrt{\sigma^2}$ (so called statistical dispersion) are listed in Table 6.3. Moreover, the theoretical average residence time $\bar{\tau}_{\text{theo}} = V_T/\dot{V}$ is given which can be calculated from the

Table 6.3: Overview of residence time distribution characteristics for selected investigated shapes.

	(1.0,20,0.5)	(1.0,30,0.5)	(1.0,40,0.5)	(1.0,50,0.5)	(0,30,0.5)	(0.5,30,0.5)	(1.5,30,0.5)	(1.0,30,1.0)
$\bar{\tau}$ [s]	0.1267	0.1291	0.1286	0.1279	0.1186	0.1217	0.1309	0.1213
$\sqrt{\sigma^2}$	0.02346	0.02297	0.02327	0.02348	0.02332	0.02283	0.02223	0.02274
Bo [-]	56.3	61.2	59.1	57.4	49.7	54.9	67.4	54.9
$E(\theta)_{\text{max}}$	2.42	2.50	2.40	2.35	2.25	2.35	2.63	2.42
$\bar{\epsilon}_0$	0.4738	0.4819	0.4819	0.4794	0.4412	0.4558	0.49	0.4537
$\bar{\tau}_{\text{theo}}$ [s]	0.126	0.128	0.128	0.127	0.117	0.121	0.130	0.120

average bed porosity. However, as the residence time is determined for the whole packing length, the porosity value $\bar{\epsilon}_0$ needs to be taken, which is obtained before cutting off inflow and outflow regions. It was unfortunately not possible to exclude the inflow region ranging three particle diameters into the packing when performing tracer step experiments. Theoretically, this can be done by determining the residence time distribution at the end of the inflow region and mathematically subtract this curve from the overall residence time distribution. This, however, requires mathematically complex deconvolution algorithms. As this inflow-uneffected residence time distribution can most probably not be measured in experiment, it was decided to accept possible minor errors by tracking the residence time distribution along with the full packing height. Here, theoretically calculated and numerically obtained average residence time show a perfect fit for all investigated cases.

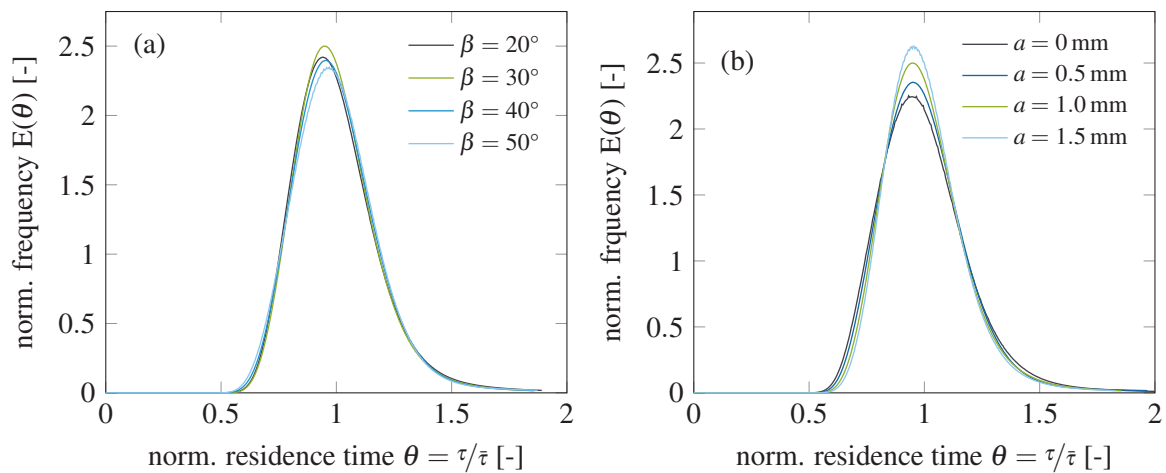


Figure 6.16: Residence time distributions obtained with a superficial velocity $u_0 = 1.132 \text{ ms}^{-1}$.

The obtained curves are displayed in Fig. 6.16. Herein, the maxima position, as well as the average residence time, only depend on the porosity of the packing. A lower porosity decreases the residence time as it increases the average flow velocity. The breadth of distribution is expressed with the square root of the variance. Regarding the investigated shape selection, a steeper residence time distribution and thus a larger Bodenstein number is obtained with increasing duct deepness. The channel width, however, does not result in a clear trend, with a maximal Bodenstein number at 30°. Moreover, a larger rounding radius resulted in a decrease of the Bodenstein number.

6.5 Conclusion

Regarding the shape development of catalyst shaped bodies, a novel shape called Yo-Yo, based on a sphere but having one circumferential duct is presented and numerically evaluated regarding its packing structure and flow characteristics. For an in-depth study, duct parameters duct width, duct deepness and rounding radius are varied. In regard to DEM-generated packing structure, high average porosities with small oscillation in the radial direction and a high geometric surface area are favored. These could be obtained with deep, wide ducts having no rounded edges. All shape variations show significantly improved parameters in regard to spheres. The numerically obtained flow fields were separately investigated concerning the distribution and the average of the axial velocity component, the radial velocity component, and the flow vector angle. Moreover, the deviation from the respective average values in the radial direction is examined which characterizes the tendency of channel formation. In general, all shape variations showed a better performance than the reference sphere, and among the investigated duct parameters, high duct width and deepness show even more preferred behavior, similar to the packing structure. No clear trend could be detected regarding the rounding radius. Investigating the friction factor as a non-dimensional number for packed bed pressure drop an opposite trend could be found. Here, ducts with smaller duct width and deepness and higher rounding radius resulted in lower, more preferred values. Moreover, only some shapes are preferred compared to the reference sphere shape. Concerning the residence time distribution, no clear trends could be found, but the broadest distribution was obtained with low duct width and the thinnest when using a high rounding radius.

In summary, novel shapes are presented, that show highly improved behavior compared to spheres. However, it was found that packings of shapes having preferred structural characteristics and consequently flow distributions lead to unfavorable friction parameters. The lower the tendency of flow channel formation, the higher is the resulting friction of the packing. This can be easily explained as flow channels are formed at locations where low structural renitency is present. Consequently, it is not surprising when packings with an evenly distributed void structure possesses a higher renitency to the flow and thus results in higher bed friction and pressure drop. It is up to the applicant whether a lower pressure drop is the major optimization parameter or structural considerations shall be taken into account as well, most probably leading to a compromise of both parameters. Unfortunately, the positive effect of more evenly distributed packing structures and flow profiles on parameters of interest, such as heat and mass transfer or dispersion is not yet studied in detail, which makes a quantified assessment of advantages a challenge and a task to be solved in the future.

Regarding the original intention of the Yo-Yo shape, to both, increase the geometric surface area and simultaneously decrease the pressure drop compared to a packing of spheres, the Yo-Yo shape variations with a narrow, deep duct offer the best compromise. Further steps include the experimental evaluation of this Yo-Yo shape incorporating either prototyped shapes obtained by 3d printing or the direct manufacturing of the shapes by tablet pressing. It, however, remains questionable if this preferred Yo-Yo shape version may not come with significant disadvantages regarding its mechanical stability.

CRedit authorship contribution statement

Jennie von Seckendorff: Conceptualization, Methodology, Software, Formal analysis, Investigation, Visualization. Peter Scheck: Conceptualization. Markus Tonigold: Project administration. Richard Fischer: Funding acquisition. Olaf Hinrichsen: Supervision, Funding acquisition.

Declaration of Competing Interest

The authors declare that they have no known competing financial interests or personal relationships that could have appeared to influence the work reported in this paper.

Acknowledgements

The authors would like to thank Julian Thomas for performing the turbulence model study, Florian Habla for his general guidance on OpenFOAM and Johanna Fernengel for providing a script to process residence time distribution curves at arbitrary packing heights.

Financial and substantial support of MuniCat, a strategic alliance between the Technical University of Munich (TUM) and Clariant AG is gratefully acknowledged. Jennie von Seckendorff would further like to thank the TUM Graduate School for generous support.

Appendix A. Supplementary data

Supplementary data to this article can be found online at <https://doi.org/10.1016/j.cej.2020.126468>.

Nomenclature

Latin Symbols

a	duct deepness, shape parameter	m^{-1}
a_{geo}	geometric surface area $a_{\text{geo}} = N \cdot a_p / V_T$	m^{-1}
a_p	particle surface area	m^2
Bo	Bodenstein number $\text{Bo} \approx 2 \cdot \left(\frac{\bar{v}^2}{\sigma^2} - 1 \right)$	-
Co	Courant number $\text{Co} = \Delta t \cdot \tau_c$	-
d	sphere diameter	m
d_p	Sauter diameter of particle $d_p = 6 \cdot v_p / a_p$	m
d_v	volume equivalent diameter of particle $d_v = \sqrt[3]{6 \cdot v_p / \pi}$	m
D	diameter of tube	m or voxel
D_T	diffusion coefficient	$m^2 s^{-1}$
e	coefficient of restitution	-
$E(\theta)$	non-dimensional residence time distribution	-
f'	friction coefficient $f' = \frac{\Delta P}{H} \cdot \frac{d_p}{\rho \cdot u_0^2} \cdot \frac{\bar{\varepsilon}^3}{1 - \bar{\varepsilon}}$	-
h	axial location	m
H	height of tube	m or voxel
K_1, k_1, k_2	pre-factors of Einfeld and Schnitzlein's [77] correlation	-
l	average mesh size	m
N	number of particles per packing	-
ΔP	pressure drop	Pa
r, z, R	control variable in radial, axial and spherical direction	m
R	rounding radius	m
R_T	radius of the tube	m
Re_p	packing Reynolds number $\text{Re}_p = \frac{\rho \cdot d_p \cdot u_0}{\eta \cdot (1 - \bar{\varepsilon})}$	-
$s(x)$	standard deviation of measure x	-
t	time	s
T	tracer scalar	-
Δt	time step of dynamic flow simulation	s
u_x, u_y, u_z	velocity component in coordinate directions	$m s^{-1}$
u_r	velocity component in radial direction $u_r = \sqrt{u_x^2 + u_y^2} $	$m s^{-1}$
u_{mag}	velocity vector magnitude $u_{\text{mag}} = \sqrt{u_x^2 + u_y^2 + u_z^2} $	$m s^{-1}$
V_T	volume of tube	m^3
v_p	volume of particle	m^3
\dot{V}	volumetric flow rate	$m^3 s^{-1}$
z_r	non-dimensional distance from tube wall in particle diameters $z_r = \frac{R_T - r}{d}$	-
z_R	non-dimensional distance from particle center in particle diameters $z_R = \frac{2 \cdot R}{d}$	-

Greek Symbols

α	flow vector angle in regard to main flow direction	$^{\circ}$
β	duct width, shape parameter	$^{\circ}$
ε	local porosity	-
$\bar{\varepsilon}$	mean bed porosity	-
η	fluid viscosity	Pa s
θ	non-dimensional residence time $\theta = \frac{t}{\tau_c}$	-
λ	tube-to-particle diameter ratio	-
ρ	material density	kg m^{-3}
μ	coefficient of friction	-
ν	Poisson's ratio	-
σ^2	variance	-
$\bar{\tau}$	average residence time	-
τ	local residence time	-
τ_c	characteristic local cell time scale $\tau_c = \frac{1}{2 \cdot V_c} \cdot \sum(\phi_i)$	s^{-1}
ϕ	face volumetric flux	$\text{m}^3 \text{s}^{-1}$

Appendix

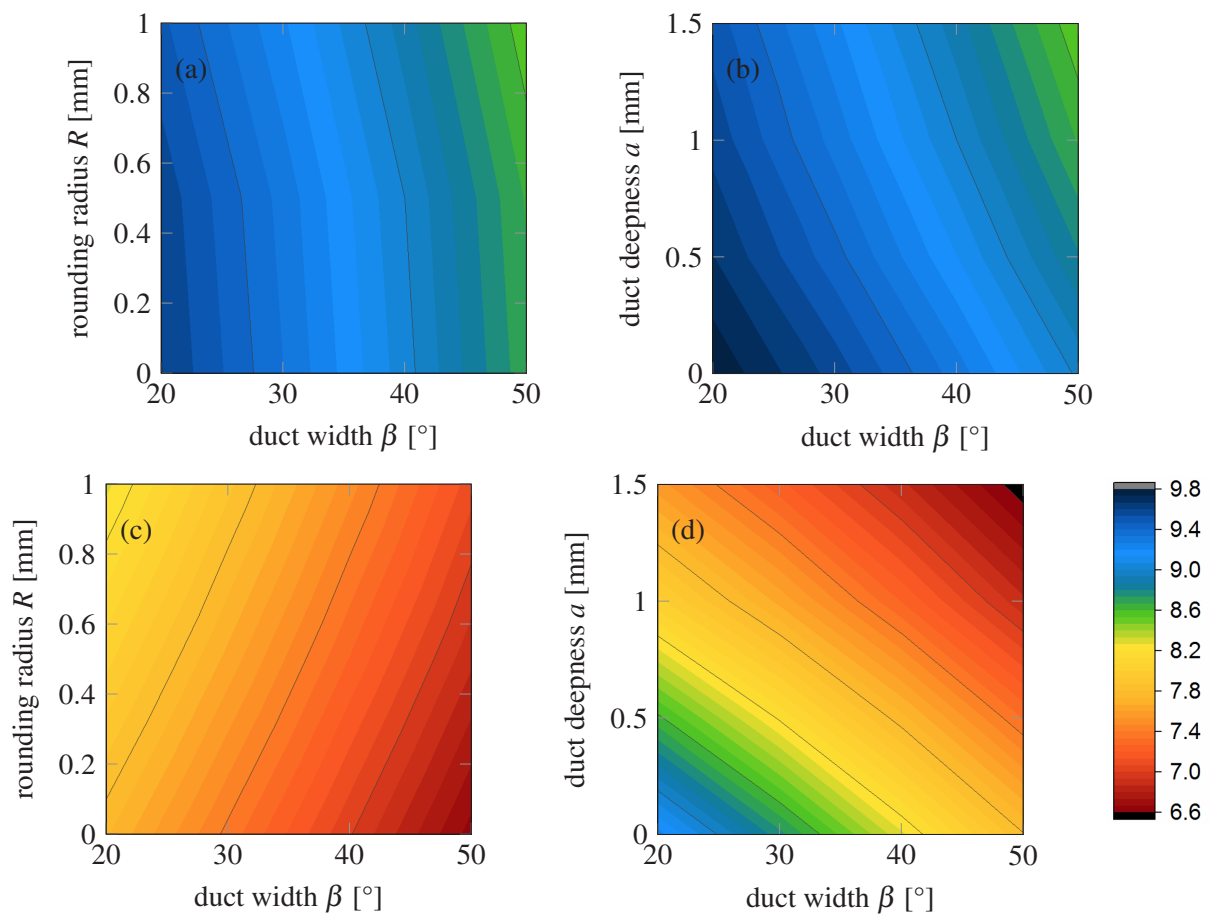


Figure 6.S1: Contour plot of (a,b) volume equivalent diameter d_v and (c,d) Sauter diameter d_p for the rounding radius and the duct depth against duct width, respectively.

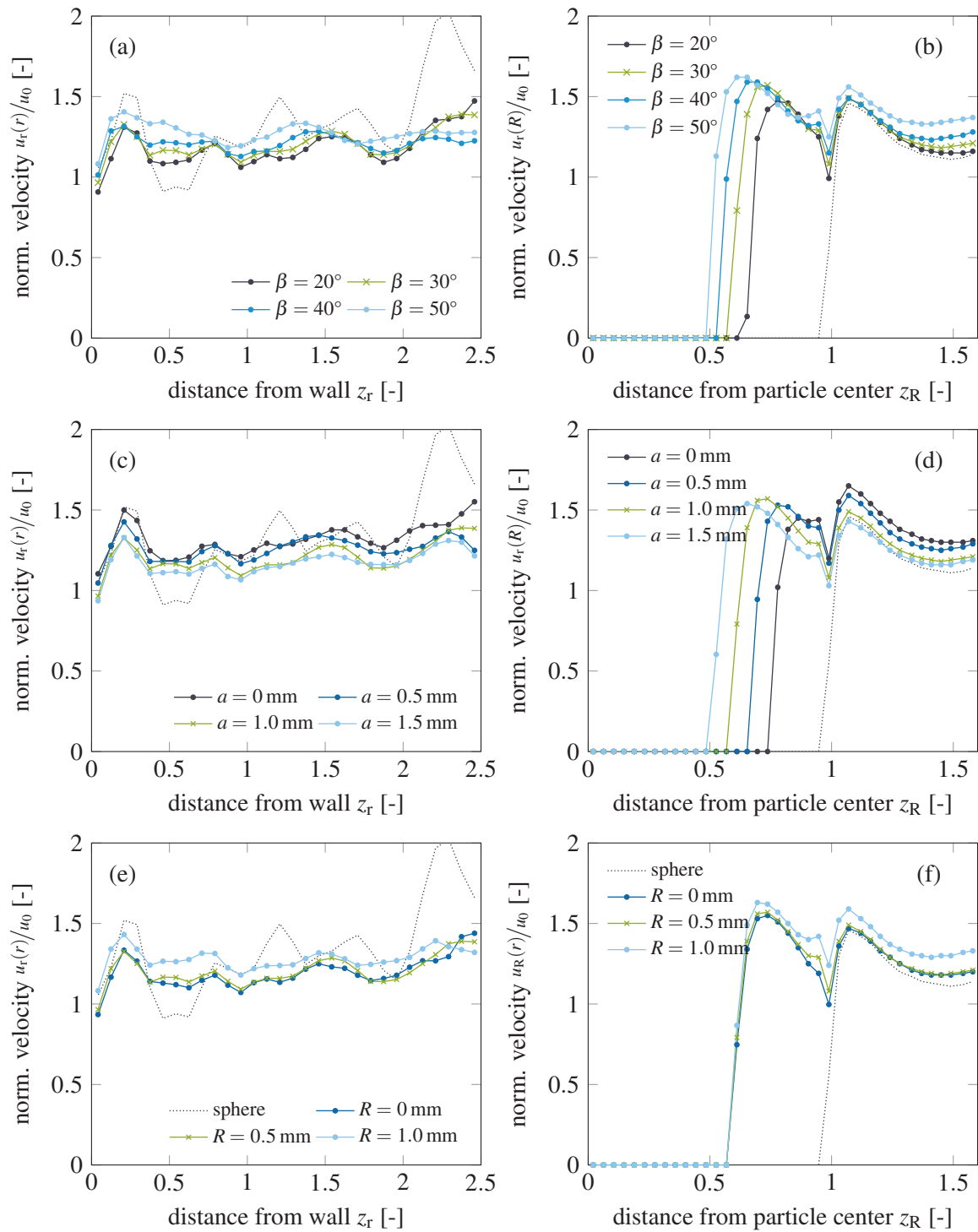


Figure 6.S2: Comparison of radial (left) and spherical (right) distributions of the radial velocity component u_r of selected shape families (a,b) $(1.0, \beta, 0.5)$, (c,d) $(a, 30, 0.5)$, and (e,f) $(1.0, 30, R)$ based on reference shape $(1.0, 30, 0.5)$ [green cross marks] and compared with a reference sphere packing [black dotted line].

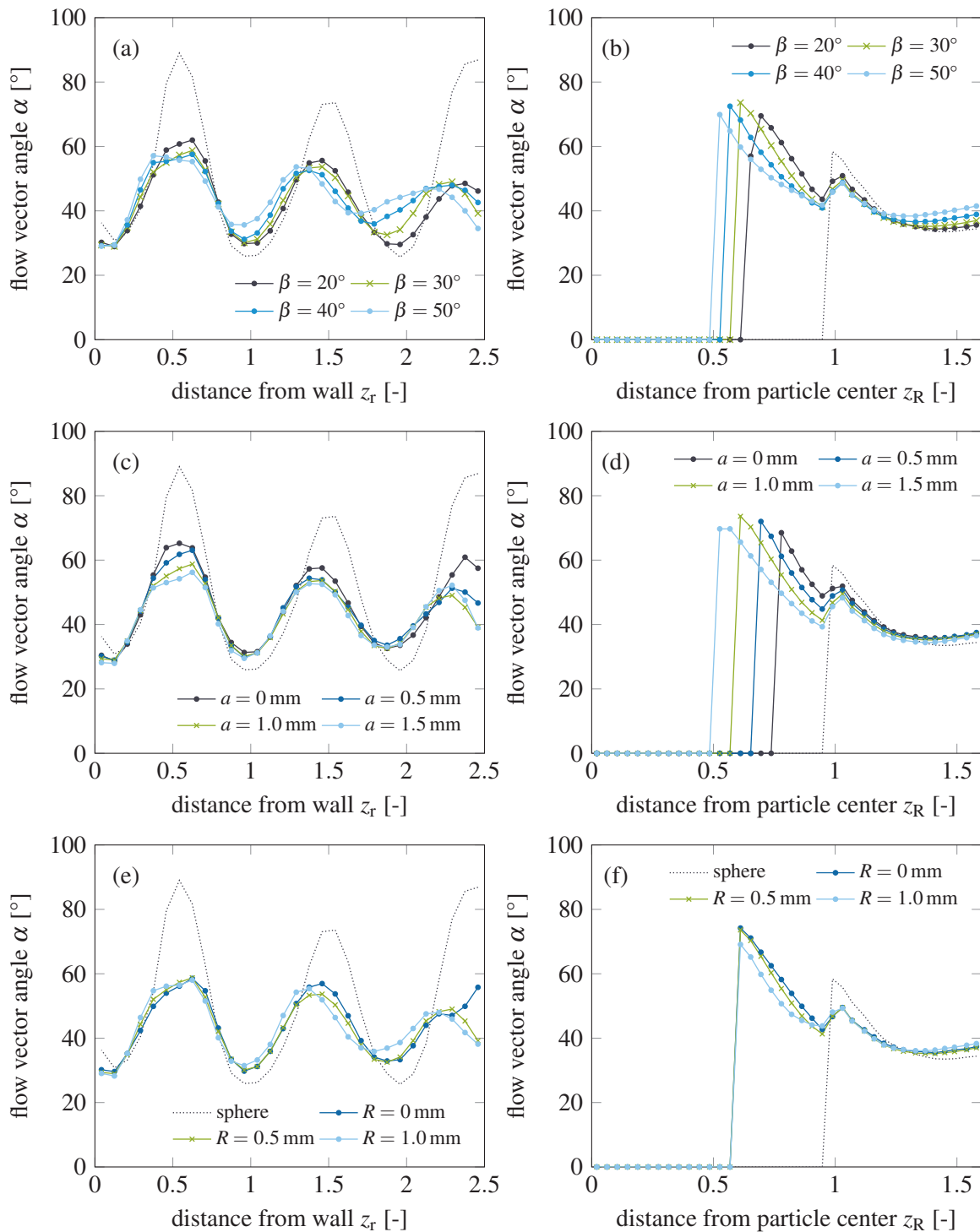


Figure 6.S3: Comparison of radial (left) and spherical (right) distributions of the flow vector angle component α of selected shape families (a,b) (1.0, β ,0.5), (c,d) (a ,30,0.5), and (e,f) (1.0,30, R) based on reference shape (1.0,30,0.5) [green cross marks] and compared with a reference sphere packing [black dotted line].

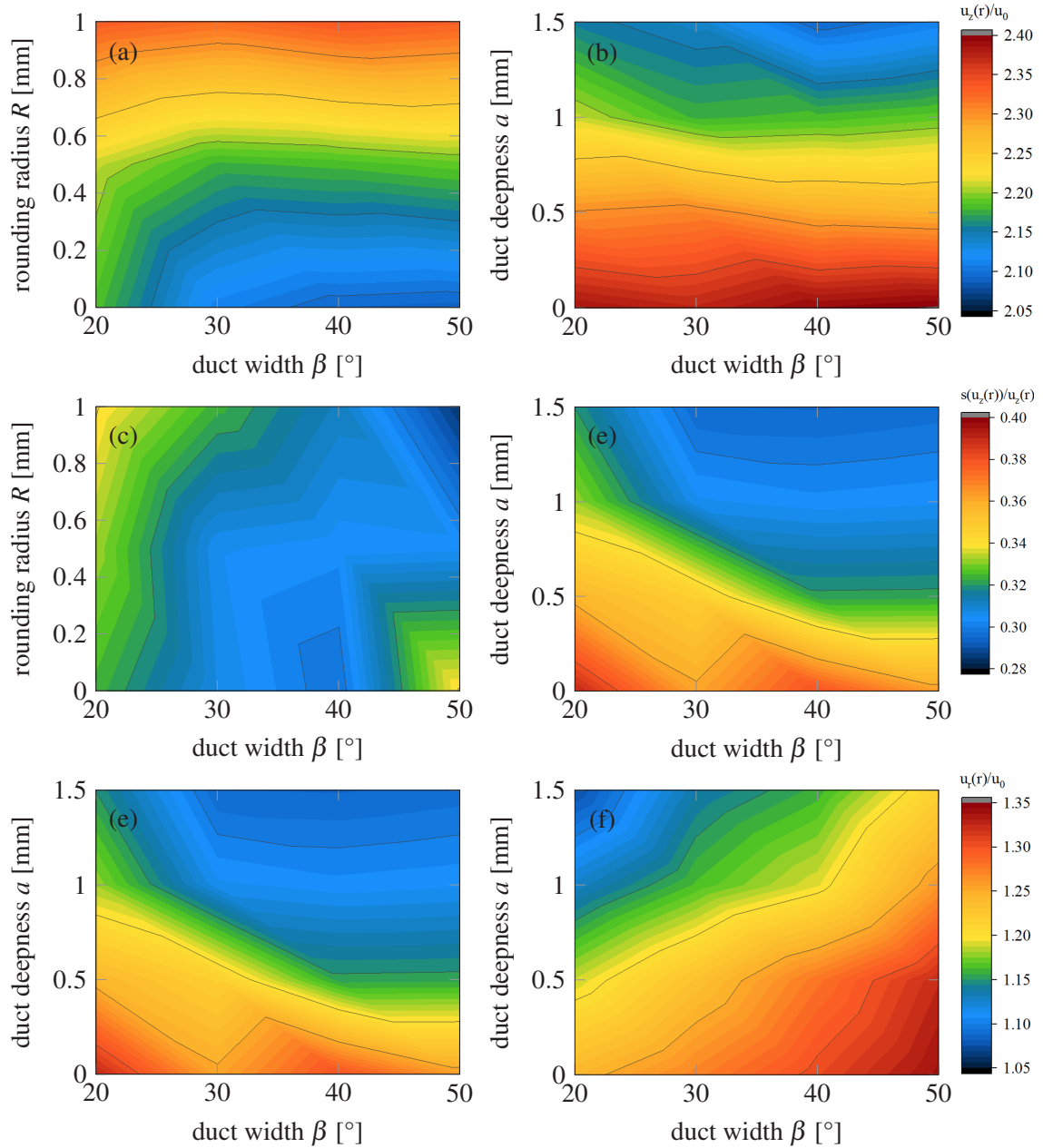


Figure 6.S4: Contour plot of flow field characteristics: (a,b) normalized axial velocity $u_z(r)/u_0$, (c,d) normalized standard deviation of axial velocity $s(u_z(r))/u_z(r)$, and (e,f) normalized radial velocity $u_r(r)/u_0$, for the rounding radius (left) and the duct deepness (right) against duct width, respectively.

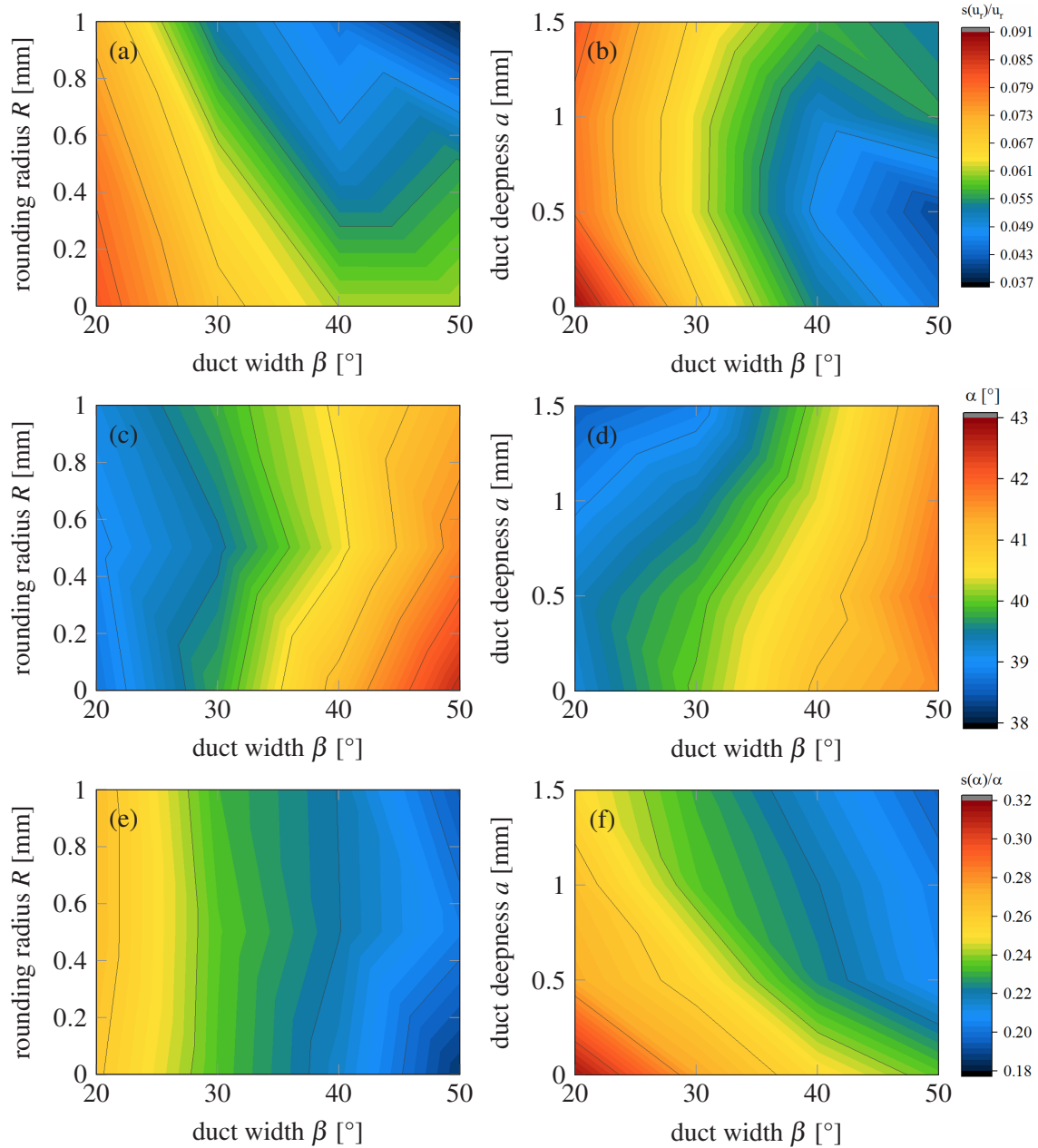


Figure 6.S5: Contour plot of geometric characteristics: (a,b) normalized standard deviation of radial velocity $s(u_r(r))/u_r(r)$, (c,d) flow vector angle α , and (e,f) normalized standard deviation of flow vector angle $s(\alpha)/\alpha$ for the rounding radius (left) and the duct deepness (right) against duct width, respectively.

References

- [1] W. van Antwerpen, C. G. du Toit, P. G. Rousseau, *Nuclear Engineering and Design* **2010**, *240*, 1803–1818.
- [2] J. M. P. Q. Delgado, *Heat and Mass Transfer* **2006**, *42*, 279–310.
- [3] E. Erdim, Ö. Akgiray, I. Demir, *Powder Technology* **2015**, *283*, 488–504.
- [4] A. G. Dixon, *The Canadian Journal of Chemical Engineering* **1988**, *66*, 705–708.
- [5] F. Benyahia, *Particulate Science and Technology* **1996**, *14*, 221–237.
- [6] Q. Qian, X. An, Y. Wang, Y. Wu, L. Wang, *Particology* **2016**, *29*, 120–125.
- [7] K. G. Allen, T. W. von Backström, D. G. Kröger, *Powder Technology* **2013**, *246*, 590–600.
- [8] R. P. Zou, A. B. Yu, *Powder Technology* **1996**, *88*, 71–79.
- [9] W. Du, N. Quan, P. Lu, J. Xu, W. Wei, L. Zhang, *Chemical Engineering Research and Design* **2016**, *106*, 115–125.
- [10] J. G. Parkhouse, A. Kelly, *Proceedings of the Royal Society A* **1995**, *451*, 737–746.
- [11] P. A. Cundall, O. D. L. Strack, *Geotechnique* **1979**, *29*, 47–65.
- [12] W. Zhong, A. Yu, X. Liu, Z. Tong, H. Zhang, *Powder Technology* **2016**, *302*, 108–152.
- [13] G. Boccardo, F. Augier, Y. Haroun, D. Ferré, D. Marchisio, *Chemical Engineering Journal* **2015**, *279*, 809–820.
- [14] J. Fernengel, J. von Seckendorff, O. Hinrichsen, *Proceedings of the 28th European Symposium on Computer Aided Process Engineering* **2018**, 97–102.
- [15] T. Eppinger, K. Seidler, M. Kraume, *Chemical Engineering Journal* **2011**, *166*, 324–331.
- [16] G. D. Wehinger, C. Fütterer, M. Kraume, *Industrial & Engineering Chemistry Research* **2017**, *56*, 87–99.
- [17] M. Zhang, H. Dong, Z. Geng, *Chemical Engineering Research and Design* **2018**, *132*, 149–161.
- [18] A. G. Dixon, G. Walls, H. Stanness, M. Nijemeisland, E. H. Stitt, *Chemical Engineering Journal* **2012**, *200-202*, 344–356.
- [19] G. D. Wehinger, T. Eppinger, M. Kraume, *Chemical Engineering Science* **2015**, *122*, 197–209.
- [20] A. G. Dixon, *Chemical Engineering Research and Design* **2014**, *92*, 1279–1295.
- [21] F. Benyahia, K. E. O’Neill, *Particulate Science and Technology* **2005**, *23*, 169–177.
- [22] E. A. Foumeny, H. A. Moallemi, C. Mcgreavy, J. A. A. Castro, *The Canadian Journal of Chemical Engineering* **1991**, *69*, 1010–1015.
- [23] E. A. Foumeny, A. Kulkarni, S. Roshani, A. Vatani, *Applied Thermal Engineering* **1996**, *16*, 195–202.
- [24] J. E. Ayer, F. E. Soppet, *Journal of the American Ceramic Society* **1965**, *48*, 180–183.
- [25] W.-C. Yang, *Handbook of Fluidization and Fluid-Particle Systems, 1st ed.* CRC Press, Boca Raton, FL, **2003**.

- [26] S. Afandizadeh, E. A. Foumeny, *Applied Thermal Engineering* **2001**, *21*, 669–682.
- [27] A. de Klerk, *AIChE Journal* **2003**, *49*, 2022–2029.
- [28] J. Pottbäcker, O. Hinrichsen, *Chemie Ingenieur Technik* **2017**, *89*, 454–458.
- [29] R. P. Zou, A. B. Yu, *Chemical Engineering Science* **1995**, *50*, 1504–1507.
- [30] C. McGreavy, E. A. Foumeny, K. H. Javed, *Chemical Engineering Science* **1986**, *41*, 787–797.
- [31] R. M. Fand, R. Thinakaran, *Journal of Fluids Engineering* **1990**, *112*, 84–88.
- [32] R. Jeschar, *Archiv für das Eisenhüttenwesen* **1964**, *35*, 91–108.
- [33] M. E. Aerov, PhD thesis, Moscow, **1951**.
- [34] P. Carman, *Transactions of the Institution of Chemical Engineers* **1937**, *15*, 150–166.
- [35] G. E. Mueller, *Powder Technology* **1992**, *72*, 269–275.
- [36] N.-S. Cheng, *Powder Technology* **2011**, *210*, 261–266.
- [37] L. H. S. Roblee, R. M. Baird, J. W. Tierney, *AIChE Journal* **1958**, *4*, 460–464.
- [38] R. F. Benenati, C. B. Brosilow, *AIChE Journal* **1962**, *8*, 359–361.
- [39] J. S. Goodling, R. I. Vachon, W. S. Stelpflug, S. J. Ying, M. S. Khader, *Powder Technology* **1983**, *35*, 23–29.
- [40] C. G. du Toit, *Nuclear Engineering and Design* **2008**, *238*, 3073–3079.
- [41] R. Kufner, H. Hofmann, *Chemical Engineering Science* **1990**, *45*, 2141–2146.
- [42] A. Montillet, L. le Coq, *Powder Technology* **2001**, *121*, 138–148.
- [43] G. J. Auwerda, J.-L. Kloosterman, D. Lathouwers, T. H. J. J. van der Hagen, *Nuclear Technology* **2013**, *183*, 272–286.
- [44] R. Caulkin, X. Jia, C. Xu, M. Fairweather, R. A. Williams, H. Stitt, M. Nijemeisland, S. Aferka, M. Crine, A. Léonard, D. Toye, P. Marchot, *Industrial & Engineering Chemistry Research* **2009**, *48*, 202–213.
- [45] N. J. Mariani, W. I. Salvat, M. A. Campesi, G. F. Barreto, O. M. Martinez, *International Journal of Chemical Reactor Engineering* **2009**, *7*, A82.
- [46] J. Reimann, J. Vicente, E. Brun, C. Ferrero, Y. Gan, A. Rack, *Powder Technology* **2017**, *318*, 471–483.
- [47] X. Gan, M. Kamlah, J. Reimann, *Fusion Engineering and Design* **2010**, *85*, 1782–1787.
- [48] R. Balzan, A. L. Sellerio, D. Mari, A. Comment, G. Gremaud, *Granular Matter* **2013**, *15*, 873–879.
- [49] R. Balzan, A. L. Sellerio, D. Mari, A. Comment, *Applied Magnetic Resonance* **2015**, *46*, 633–642.
- [50] R. Stannarius, *Review of Scientific Instruments* **2017**, *88*, 051806.
- [51] A. J. Sederman, P. Alexander, L. F. Gladden, *Powder Technology* **2001**, *117*, 255–269.
- [52] N. L. Nguyen, V. van Buren, R. Reimert, A. von Garnier, *Magnetic Resonance Imaging* **2005**, *23*, 395–396.
- [53] R. P. Zou, A. B. Yu, *Chemical Engineering Science* **1996**, *51*, 1177–1180.
- [54] H. P. Zhu, Z. Y. Zhou, R. Y. Yang, A. B. Yu, *Chemical Engineering Science* **2008**, *63*, 5728–5770.

- [55] A. S. Clarke, H. Jónsson, *Physical Review E* **1993**, *47*, 3975–3984.
- [56] G. T. Nolan, P. E. Kavanagh, *Powder Technology* **1992**, *72*, 149–155.
- [57] A. Yang, C. T. Miller, L. D. Turcoliver, *Physical Review E* **1996**, *53*, 1516–1524.
- [58] G. Lu, J. R. Third, C. R. Müller, *Chemical Engineering Science* **2015**, *127*, 425–465.
- [59] S. Zhao, X. Zhou, W. Liu, C. Lai, *Particuology* **2015**, *23*, 109–117.
- [60] M. Kodam, R. Bharadwaj, J. Curtis, B. Hancock, C. Wassgren, *Chemical Engineering Science* **2010**, *65*, 5852–5862.
- [61] Y. Guo, C. Wassgren, W. Ketterhagen, B. Hancock, J. Curtis, *Powder Technology* **2012**, *228*, 193–198.
- [62] J. Zhao, S. Li, P. Lu, L. Meng, T. Li, H. Zhu, *Powder Technology* **2011**, *214*, 500–505.
- [63] Y. Wu, X. AN, A. B. Yu, *Powder Technology* **2017**, *314*, 89–101.
- [64] H. Tangri, Y. Guo, J. S. Curtis, *Powder Technology* **2017**, *317*, 72–82.
- [65] M. V. Tabib, S. T. Johansen, S. Amini, *Industrial & Engineering Chemistry Research* **2013**, *52*, 12041–12058.
- [66] S. Li, J. Zhao, P. Lu, Y. Xie, *Chinese Science Bulletin* **2010**, *55*, 114–119.
- [67] X. Garcia, L. T. Akanji, M. J. Blunt, S. K. Matthai, J. P. Latham, *Physical Review E* **2009**, *80*, 021304.
- [68] R. Caulkin, W. Tian, M. Pasha, A. Hassanpour, X. Jia, *Computers and Chemical Engineering* **2015**, *76*, 160–169.
- [69] R. A. Williams, X. Jia, *Particulate Science and Technology* **2003**, *21*, 195–205.
- [70] X. Jia, M. Gan, R. A. Williams, D. Rhodes, *Powder Technology* **2007**, *174*, 10–13.
- [71] X. Jia, R. A. Williams, *Powder Technology* **2001**, *120*, 175–186.
- [72] A. C. J. de Korte, H. J. H. Brouwers, *Powder Technology* **2013**, *233*, 319–324.
- [73] R. Caulkin, M. Fairweather, X. Jia, N. Gopinathan, R. A. Williams, *Computers and Chemical Engineering* **2006**, *30*, 1178–1188.
- [74] B. Partopour, A. G. Dixon, *Powder Technology* **2017**, *322*, 258–272.
- [75] M. Behnam, A. G. Dixon, P. M. Wright, M. Nijemeisland, E. H. Stitt, *Chemical Engineering Journal* **2012**, *s 207-208*, 690–700.
- [76] S. Ergun, *Chemical Engineering Progress* **1952**, *48*, 89–94.
- [77] B. Einfeld, K. Schnitzlein, *Chemical Engineering Science* **2001**, *56*, 4321–4329.
- [78] O. Bey, G. Eigenberger, *Chemical Engineering Science* **1997**, *52*, 1365–1376.
- [79] R. Mohanty, S. Mohanty, B. K. Mishra, *Journal of the Taiwan Institute of Chemical Engineers* **2016**, *63*, 71–80.
- [80] S. Bu, J. Yang, Q. Dong, Q. Wang, *Applied Thermal Engineering* **2014**, *73*, 1525–1532.
- [81] P. Lovreglio, S. Das, K. A. Buist, E. A. J. F. Peters, L. Pel, J. A. M. Kuipers, *AIChE Journal* **2018**, *64*, 1896–1907.

- [82] M. Giese, K. Rottschäfer, D. Vortmeyer, *AIChE Journal* **1998**, *44*, 484–490.
- [83] Y. A. Hassan, E. E. Dominguez-Ontiveros, *Nuclear Engineering and Design* **2008**, *238*, 3080–3085.
- [84] J. von Seckendorff, K. Achterhold, F. Pfeiffer, R. Fischer, O. Hinrichsen, *Powder Technology* **2021**, *380*, 613–628.
- [85] I. B. Celik, U. Ghia, P. J. Roache, C. J. Freitas, H. Coleman, P. E. Raad, *Journal of Fluids Engineering* **2008**, *130*, 078001.
- [86] L. Caretto, A. Gosman, S. Patankar, D. Spalding in *Lecture Notes in Physics, Vol. 19*, Springer, **1972**, pp. 60–68.
- [87] F. Nicoud, F. Ducros, *Flow Turbulence and Combustion* **1999**, *62*, 183–200.
- [88] P. R. Spalart, W.-H. Jou, M. Strelets, S. R. Allmaras, *Advances in DNS/LES Columbus USA Greyden Press* **1997**, 137–147.
- [89] P. R. Spalart, S. Deck, M. L. Shur, K. D. Squires, M. K. Strelets, A. Travin, *Theoretical and Computational Fluid Dynamics* **2006**, *20*, 181–195.
- [90] K. Walters, D. Cokljat, *Journal of Fluids Engineering* **2008**, *130*, 121401.
- [91] B. E. Launder, B. I. Sharma, *Letters in Heat and Mass Transfer* **1974**, *1*, 131–137.
- [92] R. Caulkin, A. Ahmad, M. Fairweather, X. Jia, R. A. Williams, *Computers and Chemical Engineering* **2009**, *33*, 10–21.

7 Numerical Shape Development Study in View of Random Packed Beds. Part II: The Design of Experiment

Abstract

Shape variations of random catalyst packings incorporated in heterogeneously catalyst reaction setups are known to come with significant improvements in regard to pressure drop, dispersion, heat and mass transfer. But as studies evaluating packed-beds are generally based on simple shapes, especially spheres, cylinders and hollow cylinders, shape developments in industry remain a matter of trial and error or long-time experience. In a previous study, an in-depth shape parameter study was presented, combining numerical packing generation and computational fluid dynamics to evaluate shape impacts on packing structure, fluid flow and pressure drop characteristics. This study is herein enlarged incorporating the statistical Design of Experiment tool, to allow a broader and more systematic shape evaluation.

7.1 Introduction

Packed-bed reactors are frequently used in chemical technology, especially in heterogeneously catalyzed reactions, where incorporation of the solid catalyst in its powder form results in an undesirably large pressure drop. A substantial number of models and procedures have been performed simulating the fluid dynamics [1–5], heat [6–10] and mass transfer [11–15] of catalytic and inert packed-bed reactors. Due to the availability of large amounts of validation data, spheres are generally selected for these packed bed simulations. Up to date, numerical tools have only sparsely been used for systematic shape variations and the study of its influence of fluid dynamics, heat and mass transfer.

In Chapter 6 the numerical investigation of spherical shapes having a circumferential duct was presented. Compared to a reference packing of spheres, the packings obtained from this novel geometry had significantly improved structural and flow properties and some improvement regarding the friction coefficient. However, the presented study neglected some influencing factors such as the particle size, expressed as the tube-to-particle diameter ratio λ . In regard to a packing of spheres, the influence of tube-to-particle diameter ratio on packing structure [16–18] and pressure drop [19, 20] have been studied and significant influences and variations can be observed for $\lambda < 10$. These influences are evoked by the confining cylindrical wall, forcing the particles to form a distinct particle arrangement in ring-like patterns [21–23]. Moreover, in the previous study, shape parameters were randomly varied, allowing a first assessment of their influence without allowing statistically profound conclusions. Therefore, a statistical profound parameter selection based on the knowledge of the Design of Experiment (DoE) is made and evaluated as an add-on to the previous study.

7.1.1 Target Parameter

In the previous study, a large selection of target parameters were investigated including axially-averaged radial porosity and velocity distributions, shell-and-particle averaged spherical distributions of porosity and velocity, average porosity and velocity values, the friction factor as a function of Reynolds number and the residence time distribution. It was found, that preferred porosity and velocity distributions do not necessarily lead to a preferred friction factor. Thus it was concluded, that one has to select either the minimization of the pressure drop as the major goal, which has a direct impact on the reactor performance or a compromise with improved flow fields needs to be made leading to positive influences on heat transfer [24]. In this study, the two targeted parameter shall be the pressure drop, that typically needs to be as small as possible, and the geometric surface area which is preferably high. These two parameters have a proven impact on the reactor performance, the other parameters including the flow field features, are hereinafter neglected. More specific, it shall be investigated if it is possible with any parameter selection of this new shape to form a packing allowing a geometric surface area of smaller spheres ($d = 5$ mm, $\lambda = 6.6$) and the pressure drop of larger ones ($d = 7$ mm, $\lambda = 4.7$).

In order to evaluate the DoE with ideally a single target parameter, the ratio of geometric surface area and pressure drop shall be investigated. Both parameters depend linearly on the packing height, consequently,

this ratio is constant for a specific packing assuming a constantly packing procedure. The non-dimensional version of this ratio is hereinafter called *bed effectivity* η_{eff} and is defined as:

$$\eta_{\text{eff}} = \frac{a_{\text{geo}}}{\Delta P} \cdot \rho \cdot u_0^2 \cdot H. \quad (7.1)$$

However, fluid density ρ , superficial velocity u_0 and packing height H are kept constant. The bed effectivity can be directly related to the friction factor f' with:

$$\eta_{\text{eff}} = \frac{6 \cdot \bar{\epsilon}^3}{f'}. \quad (7.2)$$

Consequently, in order to solve the given task to find a packing with $a_{\text{geo}} = a_{\text{geo}}(d = 5 \text{ mm})$ and $\Delta P = \Delta P(d = 7 \text{ mm})$, starting from a packing of 7 mm spheres the desired target (t) and starting (s) parameter are:

$$\eta_{\text{eff,t}} = \frac{a_{\text{geo}}(d = 5 \text{ mm})}{\Delta P(d = 7 \text{ mm})} \cdot \rho \cdot u_0^2 \cdot H \quad \text{and} \quad \eta_{\text{eff,s}} = \frac{a_{\text{geo}}(d = 7 \text{ mm})}{\Delta P(d = 7 \text{ mm})} \cdot \rho \cdot u_0^2 \cdot H. \quad (7.3)$$

The task is solved if the degree of achievement ϕ equals one or larger.

$$\phi = \frac{\eta_{\text{eff}} - \eta_{\text{eff,s}}}{\eta_{\text{eff,t}} - \eta_{\text{eff,s}}}. \quad (7.4)$$

The hereinafter described Design of Experiment is evaluated in regard to this parameter.

7.2 Numerical Setup

The herein performed general simulation procedure consists of the steps of i) shape design, ii) numerical packing generation, iii) mesh creation, iv) steady-state flow simulation and vi) post-processing of the data. The general procedure is identical as in the previous study. The validation of each step, especially the

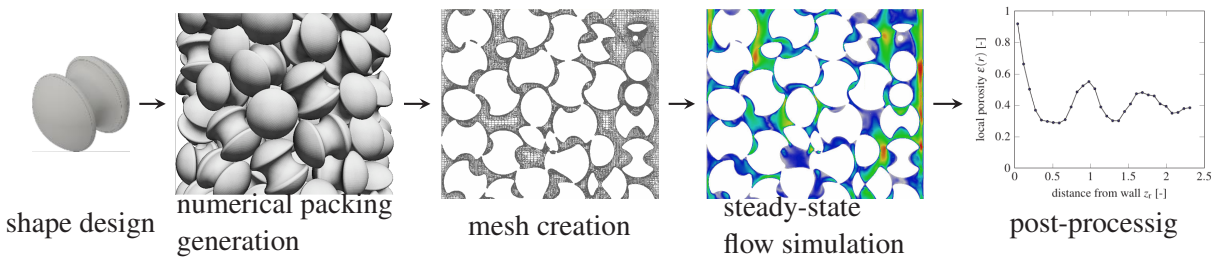


Figure 7.1: General simulation procedure.

validity and reproducibility of the numerical packing generation, the mesh size selection based on a mesh study similar to the validation of flow simulation and the respective selection of an appropriate turbulence model were discussed in detail in the previous study and will be briefly repeated here by pointing out some minor differences.

7.2.1 Shape Design and Design of Experiment

The herein investigated shapes have a spherical base shape, from which cavities of the same cross-section are cut out. These cavities may be cut all along the circumference of the sphere resulting in a circumferential duct, so-called *orbital cut* or these cavities may be cut straight on two opposing positions, the so-called *straight cut*. A third type comprises a twice interrupted orbital cut, the so called *half orbital cut*. As in the previous study, the cut cross-section has a certain deepness a and a certain width β . The edges are rounded with a constant 0.5 mm radius. An overview of the obtained shapes is depicted in Table 7.1.

A fully factorial DoE is selected with four parameters attaining two different states each, and a separate central point. All simulations were randomized but performed only once. The selected parameters are the duct width β , attaining a value of 20° and 50° , the duct deepness a attaining the values 0.5 mm and 1.5 mm, the cut shape, being *straight* and *orbital*, and the particle size selected so that the tube-to-particle diameter equals $\lambda = 4.7$ and $\lambda = 6.6$, whereas the tube diameter is kept constant. The separate central point has the parameters: $\beta = 35^\circ$, $a = 1$ mm, *half orbital* cut and $\lambda = 5.65$. The parameter selection is depicted in Table 7.1.










For comparison and the calculation of the target parameter ϕ , reference sphere packings are generated and simulated having respective tube-to-particle diameter ratios $\lambda = 4.7$, 5.65 and 6.6.

7.2.2 Numerical Packing Generation

Packing generation is performed incorporating the DigiDEMTM code, a voxelated particle simulation software incorporating a digital packing algorithm based on the *Monte Carlo Approach* whilst explicitly considering physical interaction forces similar to the *Discrete Element Method* and is elsewhere described in more detail [25, 26]. The packing procedure is identical to the one we already described [27]. Hereby, the 3d objects were digitized at a resolution of 10 voxel mm^{-1} . The material properties were set as follows: density $\rho = 3000 \text{ kg m}^{-3}$, coefficient of restitution $e = 0.3$, coefficient of friction $\mu = 0.7$ and Poisson's ratio $\nu = 0.3$. The objects are filled into tubes of constant height $H = 3000 \text{ voxel}$ (300 mm) and diameter $D = 470 \text{ voxel}$ (47 mm). The packing mode was selected to be damping and the stop criterion is a pre-set time of 3 s.

The packing procedure was validated using ideal spheres both with literature data [27] and experimental CT-scans Chapter 5. In regard to spheres, the reproducibility as the mean relative standard error of packing generation was found to be one percent for the radial porosity profiles and 0.5 percent for the bed averaged porosity, based on ten identical packing repetitions (see Chapter 5).

Table 7.1: Overview of designed shapes and their parameter selections incorporated in this study.

No.	β [°]	a [mm]	cut shape	λ [-]	straight	orbital
1	50	0.5	straight	4.7		
9	50	0.5	straight	6.6		
2	50	0.5	orbital	4.7		
10	50	0.5	orbital	6.6		
3	20	0.5	straight	4.7		
11	20	0.5	straight	6.6		
4	20	0.5	orbital	4.7		
12	20	0.5	orbital	6.6		
5	50	1.5	straight	4.7		
13	50	1.5	straight	6.6		
6	50	1.5	orbital	4.7		
14	50	1.5	orbital	6.6		
7	20	1.5	straight	4.7		
15	20	1.5	straight	6.6		
8	20	1.5	orbital	4.7		
16	20	1.5	orbital	6.6		
17	35	1.0	half orbital	5.65		

7.2.3 Computational Fluid Dynamics

The numerically generated packings were meshed using OpenFOAM[®] tool *snappyHexMesh* creating a castellated mesh with higher resolution at particle contact points. The mesh size was refined until reaching a Fine Grid Convergence Index [28] $< 1\%$. The steady-state flow of an incompressible fluid was simulated in OpenFOAM incorporating the SIMPLE algorithm in solver *simpleFoam*. The *Launder-Sharma* $k - \varepsilon$ model was utilized as the turbulence model. The validation of the simulations and the selection of the turbulence model were discussed in the previous study in detail. Air was selected as fluid, having a density $\rho = 1.2 \text{ kg m}^{-3}$ and a viscosity $\eta = 0.018 \text{ mPas}$. A superficial velocity $u_0 = 1.0 \text{ ms}^{-1}$ was selected and a parabolic tube flow profile defined at the inflow boundary.

Post-processing was performed incorporating a comprehensive Python[™] script, determining the averages and radial and axial distributions of porosity, fluid field characteristics, and pressure drop. For this, the inflow and outflow region lasting three particle diameters into the tube were excluded, allowing the sole investigation of the bulk packing part.

7.3 Results

7.3.1 Packing Structure

The axially averaged radial porosity distributions of selected shapes are displayed in Fig. 7.2 as a function of the non-dimensional distance from the confining wall $z_r = R-r/d$. For comparison, the respective reference distributions for an ideal sphere are added as dotted ($\lambda = 4.7$) or dashed ($\lambda = 6.6$) line. The reference sphere packing is known to form an underlying structure of ordered particle rings starting from the confining wall and leading to an oscillating radial porosity profile [16, 21]. Herein, each minimum represents the center of these ordered particle rings, and each maximum represents the increased void space between two ring arrangements. It is further known, that the order decreases with increasing distance to the confining wall and with increasing λ . In Fig. 7.2a shapes of same duct dimensions but a different cutting method and particle size are compared. The oscillation amplitude is slightly decreased with higher λ and significantly decreased when having a circumferential cut rather than a straight. All four displayed shapes show a smoother curve than the reference sphere. As explained in the previous study, the cutting of cavities allows particle overlap in this region leading to a reduced particle ring formation. The influence of duct width β and duct deepness a at constant particle size ($\lambda = 6.6$) and cut shape is presented in Fig. 7.2b. A decrease of oscillation amplitude is obtained with increasing a and β . The same effect though with significantly less distinctness can be seen for the smaller particle size ($\lambda = 4.7$) and straight cut as displayed in Fig. 7.2d. Furthermore, a lower oscillation amplitude is obtained with a high a and orbital cut shape keeping β and λ constant as displayed in Fig. 7.2c.

In summary, a smoother porosity profile is obtained with higher λ , duct deepness a and duct width β while generally preferring the orbital cut shape.

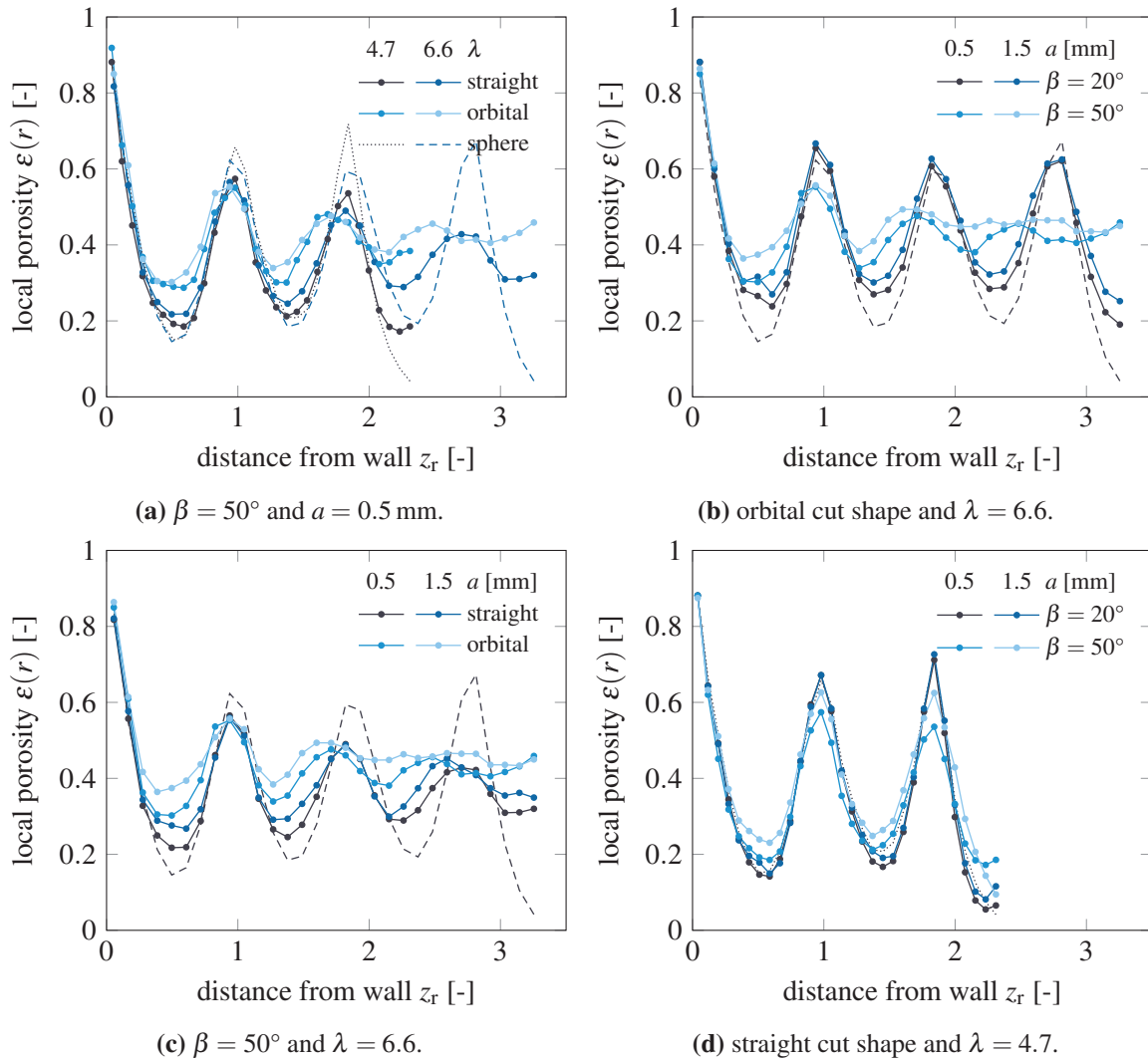


Figure 7.2: Comparison of the radial porosity distribution $\epsilon(r)$ for a selection of shapes. In each figure, two parameters selected from the tube-to-particle diameter ratio λ , the cut shape, the duct deepness a and duct width β were varied and two kept constant. For comparison, the respective data for packings of spheres is added.

7.3.2 Design of Experiment

The effects of shape variation obtained when evaluating the design of experiment are displayed in Fig. 7.3. A positive effect on the degree of achievement representing the ratio of geometric surface area and pressure drop is obtained for lower duct width β , higher duct deepness a and orbital cut shape.

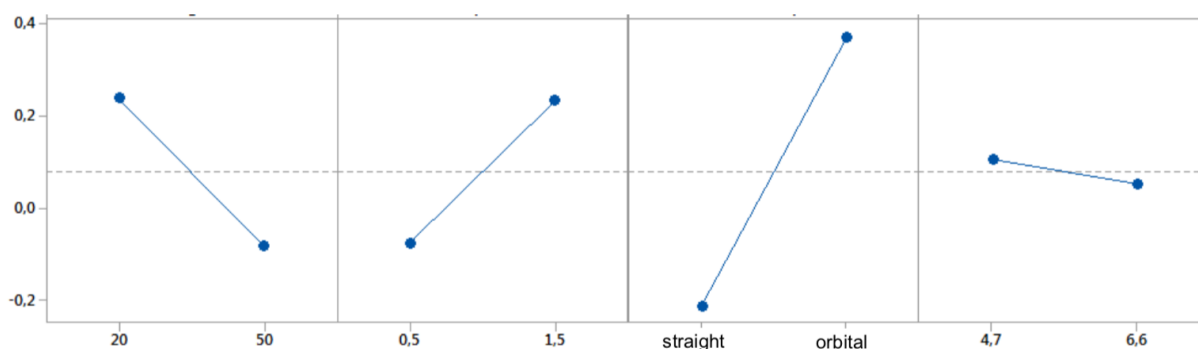


Figure 7.3: Effects of parameter variations including duct width β , duct deepness a , cut shape and tube-to-particle diameter ratio λ (from right to left), on the degree of achievement ϕ .

The effect of particle size represented as the tube-to-particle diameter ratio λ is not significant. Moreover, effect interaction is only significant for the combination of duct deepness a and cut shape. In this evaluation, the originally defined center point was not considered, as its results did not fit to all others. This is explained with the significantly different shape that this center point is based on.

The absolute values of the obtained degree of achievement are displayed in Fig. 7.4. The reference sphere has a value of zero, negative values indicate a worse geometric surface area to pressure drop ratio compared to spheres, a value between zero and one indicates an improvement but not enough to fulfill the target and values larger than one are desired.

In general, all shape variations with a straight cut are worse than the reference sphere, all shape variations having an orbital cut are better. As already mentioned, a higher duct deepness and a reduced duct width increase the degree of achievement, whereas the particle size has hardly any influence. In summary, the best shape has a small, deep, orbital duct. Unfortunately, the targeted value could not be attained.

7.3.3 Extrapolation of Results

Based on the learnings of the Design of Experiment, the results are extrapolated to create a shape that fulfills the targeted requirements regarding the geometric surface area to pressure drop ratio. It is thought, that this further increase can be obtained by decreasing duct width β and/or increasing duct deepness a . As the duct width is already very small, it is decided to increase the duct deepness to $a = 2.0$ mm forming the shape depicted in Fig. 7.5, where $\lambda = 4.7$ and $\beta = 20^\circ$ are kept constant. A packing of this shape is generated similar to the other herein used packings, and the fluid dynamics are simulated equally to the above-described method. Finally, a packing of this extrapolated shape reaches a degree

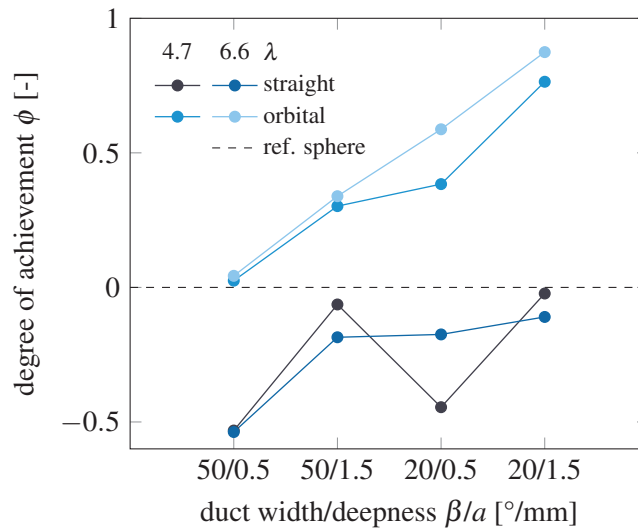


Figure 7.4: Absolute values of the degree of achievement ϕ for all parameter combinations tested in this DoE, which the reference sphere marking the horizontal line at $\phi = 0$.

of achievement $\phi = 1.11$ which is significantly above the targeted value. Consequently, the herein



Figure 7.5: One of presumably a range of possible shapes capable to fulfill the requirements in regard to geometric surface area and pressure drop.

investigated sphere-based shapes having circumferential cavities are capable to replace a sphere packing having an improved geometric surface area to pressure drop ratio larger than the desired value. It is however questionable if such a shape having a very narrow deep duct is actually producible using the known production methods such as tablet pressing. Up-coming knew production methods such as additive manufacturing (3d printing) might be required to allow the accurate production of this shape. It is furthermore questionable if such a shape has enough mechanical stability to withstand the reactor filling procedure as a narrow, deep duct should significantly decrease the particles mechanical stability, most probably evoking breakage along the duct circumference.

7.3.4 Packing Structure and Resulting Pressure Drop

As already in the previous study mentioned, an intuitively preferred packing structure having a smooth radial porosity distribution and in consequence, a reduced tendency to flow channel formation is not equal

to the packings preferred regarding pressure drop and geometric surface area. As previously discussed, it is assumed that a more evenly packing structure leads automatically to a higher pressure drop, due to the increased renitency this packing opposes to the flow especially compared to high-void channels. It is to be discussed in future, if the channel formation tendency should be included in the list of targeted parameters which in industrial applications is up to date frequently solely devoted to a low pressure drop and a high geometric surface area as the positive effects of improved flow profiles are not sufficiently proven, yet.

7.4 Conclusion

Using the statistically based Design of Experiment approach, a selection of the so-called Yo-yo shape variations are investigated in regard to improved pressure drop and geometric surface area characteristics. It was found that spherical based shapes having circumferential cut cavities come with improved properties, especially when these ducts are of narrow, deep shape. It was further shown, that the particle size, expressed as the non-dimensional tube-to-particle diameter ratio has only a small, if not at all negligible influence on the investigated parameters. It is, however, to be noted, that in regard to spheres the influence of this ratio λ is not linear and increases with decreases λ -values. Consequently, no definite conclusion can be drawn regarding the influence of small λ -values.

More precisely, it was to be investigated, if any parameter variation of this novel Yo-Yo shape is capable to generate a packing having the pressure drop of a reference sphere packing of $\lambda = 4.7$ and the much larger geometric surface area of a packing of $\lambda = 6.6$. This task could be fulfilled using a Yo-Yo shape having an orbital duct and parameters duct width $\beta = 20^\circ$ and duct deepness $a = 2.0$ mm. It is however questionable if such a shape can be produced or is mechanically stable enough to withstand reactor conditions.

Nomenclature

Latin Symbols

a	duct deepness, shape parameter	m^{-1}
a_{geo}	geometric surface area $a_{\text{geo}} = N \cdot a_p / V_T$	m^{-1}
a_p	particle surface area	m^2
d	sphere diameter	m
D	diameter of tube	m or voxel
e	coefficient of restitution	-
f'	friction coefficient $f' = \frac{\Delta P}{H} \cdot \frac{d_p}{\rho \cdot u_0^2} \cdot \frac{\bar{\varepsilon}^3}{1 - \bar{\varepsilon}}$	-
H	height of tube	m or voxel
N	number of particles per packing	-
ΔP	pressure drop	Pa
r	control variable in radial direction	m
R_T	radius of the tube	m
u_0	superficial velocity	m s^{-1}
V_T	volume of tube	m^3
v_p	volume of particle	m^3
z_r	non-dimensional distance from tube wall in particle diameters $z_r = \frac{R_T - r}{d}$	-

Greek Symbols

β	duct width, shape parameter	$^\circ$
ε	local porosity	-
$\bar{\varepsilon}$	mean bed porosity	-
η	fluid viscosity	Pa s
η_{eff}	bed effectivity $\eta_{\text{eff}} = \frac{a_{\text{geo}}}{\Delta P} \cdot \rho \cdot u_0^2 \cdot H$	-
λ	tube-to-particle diameter ratio	-
ρ	material density	kg m^{-3}
μ	coefficient of friction	-
ν	Poisson's ratio	-
ϕ	degree of achievement	-

References

- [1] T. Eppinger, K. Seidler, M. Kraume, *Chemical Engineering Journal* **2011**, *166*, 324–331.
- [2] G. D. Wehinger, C. Fütterer, M. Kraume, *Industrial & Engineering Chemistry Research* **2017**, *56*, 87–99.
- [3] P. Lovreglio, S. Das, K. A. Buist, E. A. J. F. Peters, L. Pel, J. A. M. Kuipers, *AIChE Journal* **2018**, *64*, 1896–1907.
- [4] S. Khirevich, A. Hölzel, D. Hlushkou, U. Tallarek, *Analytical Chemistry* **2007**, *79*, 9340–9349.
- [5] H. Freund, T. Zeiser, F. Huber, E. Klemm, G. Brenner, F. Durst, G. Emig, *Chemical Engineering Science* **2003**, *58*, 903–910.
- [6] M. Zhang, H. Dong, Z. Geng, *Chemical Engineering Research and Design* **2018**, *132*, 149–161.
- [7] M. Behnam, A. G. Dixon, M. Nijemeisland, E. H. Stitt, *Industrial & Engineering Chemistry Research* **2013**, *52*, 15244–15261.
- [8] M. E. Taskin, A. G. Dixon, E. H. Stitt, *Numerical Heat Transfer Part A: Applications* **2007**, *52*, 203–218.
- [9] B. Partopour, A. G. Dixon, *Powder Technology* **2017**, *322*, 258–272.
- [10] A. G. Dixon, G. Walls, H. Stanness, M. Nijemeisland, E. H. Stitt, *Chemical Engineering Journal* **2012**, *200-202*, 344–356.
- [11] G. D. Wehinger, T. Eppinger, M. Kraume, *Chemical Engineering Science* **2015**, *122*, 197–209.
- [12] G. D. Wehinger, T. Eppinger, M. Kraume, *Chemie Ingenieur Technik* **2015**, *87*, 734–745.
- [13] A. G. Dixon, *Chemical Engineering Research and Design* **2014**, *92*, 1279–1295.
- [14] B. Partopour, A. G. Dixon, *Computers & Chemical Engineering* **2016**, *88*, 126–134.
- [15] F. Augier, F. Idoux, J. Y. Delenne, *Chemical Engineering Science* **2010**, *65*, 1055–1064.
- [16] A. de Klerk, *AIChE Journal* **2003**, *49*, 2022–2029.
- [17] F. Benyahia, K. E. O’Neill, *Particulate Science and Technology* **2005**, *23*, 169–177.
- [18] J. Pottbäcker, O. Hinrichsen, *Chemie Ingenieur Technik* **2017**, *89*, 454–458.
- [19] B. Eisfeld, K. Schnitzlein, *Chemical Engineering Science* **2001**, *56*, 4321–4329.
- [20] E. Erdim, Ö. Akgiray, I. Demir, *Powder Technology* **2015**, *283*, 488–504.
- [21] G. E. Mueller, *Powder Technology* **1992**, *72*, 269–275.
- [22] W. van Antwerpen, C. G. du Toit, P. G. Rousseau, *Nuclear Engineering and Design* **2010**, *240*, 1803–1818.
- [23] M. Suzuki, T. Shinmura, K. Iimura, M. Hirota, *Advanced Powder Technology* **2008**, *19*, 183–195.
- [24] M. Behnam, A. G. Dixon, P. M. Wright, M. Nijemeisland, E. H. Stitt, *Chemical Engineering Journal* **2012**, *s 207-208*, 690–700.
- [25] R. A. Williams, X. Jia, *Particulate Science and Technology* **2003**, *21*, 195–205.

- [26] R. Caulkin, X. Jia, C. Xu, M. Fairweather, R. A. Williams, H. Stitt, M. Nijemeisland, S. Aferka, M. Crine, A. Léonard, D. Toye, P. Marchot, *Industrial & Engineering Chemistry Research* **2009**, *48*, 202–213.
- [27] J. Fernengel, J. von Seckendorff, O. Hinrichsen, *Proceedings of the 28th European Symposium on Computer Aided Process Engineering* **2018**, 97–102.
- [28] I. B. Celik, U. Ghia, P. J. Roache, C. J. Freitas, H. Coleman, P. E. Raad, *Journal of Fluids Engineering* **2008**, *130*, 078001.

8 Numerical Shape Development Study in View of Random Packed Beds. Part III: Sphere Feature Evaluation

Abstract

With up-coming additive manufacturing techniques being utilized in the production of shaped heterogeneous catalysts, the existing strict geometrical constraints concerning shape design may shift or even vanish in the near future. However, the influence of shape on fluid dynamics, heat and mass transfer is largely unknown. An exclusively numerical study unique in the literature was performed, investigating a range of comparable shapes designed from simple spheres in regard to packing structure, fluid field, and packed-bed pressure drop. Results include a clearly visible disparity between packing structure and fluid profiles caused by clogged or unavailable voids for selected shapes resulting in unrealistic high friction factor values. Moreover, shapes tending to result in more even radial flow profiles come with increased packed-bed pressure drops at comparable average bed porosities. Thus, optimizing the shaped catalysts geometry requires a compromise between at least these two parameters which have been combined to a novel characteristic and dimensionless number.

8.1 Introduction

In the chemical industry, packed-bed reactors are the universally applicable work horses, especially for heterogeneously catalyzed reactions. Herefor, the catalytic material is shaped into distinct particles by means such as tablet pressing and extrusion, and subsequently packed randomly into the reactor tubes. Besides chemical engineering, many other industrial applications of packed-beds are known, ranging from nuclear technology [1] over solar energy storage systems [2] to pharmaceutical processing [3].

Decisive parameters of packed-beds have been largely investigated by numerical and experimental means. However, up to today, experimental techniques struggle to resolve parameters that require the determination of localized variations as for instance the flow field and heat profiles. Computational fluid dynamics has been performed over some decades now, but with increasing computer power is capable to simulate highly resolved and expanded random packings. These simulations include the determination of fluid dynamics [4–17], heat [18–28] and mass transfer [29–39]. As catalyst shapes obtained from traditional manufacturing processes only come in a small selection of simple shapes, experimental and numerical studies have not been performed investigating arbitrary shapes that are beyond the manufacturing geometry constraints. But with upcoming additive manufacturing techniques [40], almost any imaginable shape might be available in the near future. It is thus required to investigate novel shapes that have not been possible before to evaluate the potential 3d printing techniques can unfold in regard to catalytical packed-bed reactors.

In a previous study, a numerical procedure was described for the simulation of fluid dynamics of packed beds, as was similarly done dozens of times before [4, 20, 22, 25, 27, 41]. This procedure has been thoroughly validated using a packing of smooth homo-sized spheres with experimental literature data. It was then utilized to investigate the influence of parameter variations regarding the novel, so-called Yo-Yo shape, a sphere with a circumferential duct of certain deepness, width and edge rounding. In contrary to this previous study, the present investigation comprises shapes that differ from their features, having ducts, holes, bellies, drops, cavities of different numbers, or combinations thereof. The detailed-shape parameters, such as hole diameter, rounding radius, drop length, belly width and so on is not varied. In order to allow comparability between these shapes, they are designed to have the same final volume and the same feature volume. The presented study is first of its kind, investigating the effect of shape feature variation on packing structure and fluid dynamics of packed beds.

8.1.1 Packing Structure

Important structural parameters include the geometric surface area a_{geo} , the axially averaged radial porosity distribution $\varepsilon(r)$ and the average bed porosity $\bar{\varepsilon}$. The water displacement [42–44] and weighing method [45, 46] are typically used experimental procedures to determine the average bed porosity, which itself depends on the tube-to-particle diameter ratio λ , the particle's material, shape and size distribution, the container's material and shape and the applied deposition and compaction methods [47, 48]. Except

the shape, everything else is kept constant in this study, including the tube-to-particle diameter ratio which is fixed at $\lambda = 5.0$.

The confining wall of a packing causes the packing particles to align to this wall's shape creating a ring-like pattern easing out 4 to 5 particle diameters into the tube [49]. Especially when packing spheres, this results in a radial porosity distribution describing roughly a damped oscillating trend [49] often seen in experiments [50–67]. For packings of spheres, respective correlations are derived [68].

In contrary to spheres, packings of other shapes are only sparsely investigated. These more complex geometries require a handful of aspect ratios and characteristic diameters. The attempt to find a universal shape factor as for instance sphericity could not be completed up to today [69]. Consequently, it is not possible to predict packing structure parameters of arbitrary shapes. Compared to experimental methods, numerical tools can be used to distinctively evaluate single parameters. These numerical tools comprise the Discrete Element Method (DEM) [70–72] or similar ones [41, 73–75]. Advantages and limitations of these tools, especially in the context of shape representation were compared by Fernengel et al. [76] for spheres and Caulkin et al. [77] for cylinders.

8.1.2 Fluid Dynamics

Fluid dynamics comprises the evaluation of the pressure loss along with the packing and flow field parameters, including the axially averaged radial profile of the axial velocity component $u_z(r)$ and the radial profile of the radial velocity component $u_r(r)$. The importance of the latter was only recently emphasized in regard to heat transfer [31]. Over about a century, pressure loss experiments have been performed resulting in a large selection of correlations at least for sphere packings (see [78] for a review). These relate the non-dimensional pressure loss called friction f' to the fluid state indicated by the packing Reynolds number Re_p .

$$f' = \frac{\Delta P}{H} \cdot \frac{d_p}{\rho \cdot u_0^2} \cdot \frac{\bar{\varepsilon}^3}{1 - \bar{\varepsilon}} = f(\text{Re}_p) \quad \text{with} \quad \text{Re}_p = \frac{\rho \cdot d_p \cdot u_0}{\eta \cdot (1 - \bar{\varepsilon})} \quad (8.1)$$

$$\text{Eisfeld and Schnitzlein [79]:} \quad f' = \frac{K_1 \cdot \left(1 + \frac{2}{3 \cdot \lambda \cdot (1 - \bar{\varepsilon})}\right)^2}{\text{Re}_p} + \frac{1 + \frac{2}{3 \cdot \lambda \cdot (1 - \bar{\varepsilon})}}{\left(\frac{k_1}{\lambda^2} + k_2\right)^2} \quad (8.2)$$

$$\text{Erdim et al. [78]:} \quad f' = \frac{160}{\text{Re}_p} + \frac{2.81}{\text{Re}_p^{0.096}} \quad (8.3)$$

Available experimental methods for the flow field evaluation including magnetic resonance imaging [12, 66, 80], laser doppler anemometry [81], particle image velocimetry [82], and some others [9, 83, 84] still struggle in determining flow profiles in high resolution as required for a decent model evaluation in computational fluid dynamics (CFD). While certain details still remain unveiled, the equivalence of radial porosity and velocity profiles and thus packing structure and fluid field cannot be overseen, at least for packings of spheres. Consequently, terms like *channeling* and *wall channeling* were established describing

the by-passing of flow close to the wall and between sphere rings, where high porosities systematically occur.

8.2 Simulation Procedure

The herein performed general simulation procedure consists of the steps of i) shape design, ii) numerical packing generation, iii) mesh creation, iv) steady-state flow simulation and vi) post-processing of the data. The general procedure is identical as in the previous studies.

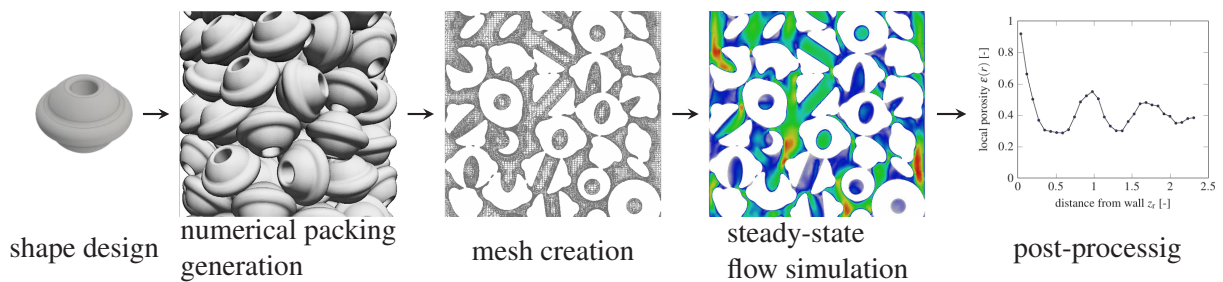






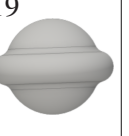





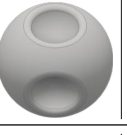


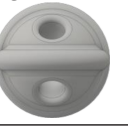
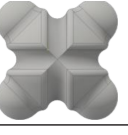






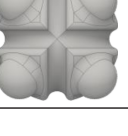



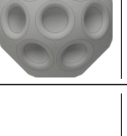
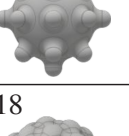
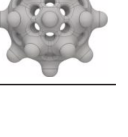
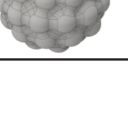

Figure 8.1: General simulation procedure.

8.2.1 Shape Design

The herein investigated shapes are developed from an ideal spherical base shape. This base sphere comes in three dimensions, having a diameter of $d_1 = 10.6$ mm, $d_2 = 9.3$ mm and $d_3 = 10.0$ mm. In case 1, internal features summing up to a total feature volume $v_{\text{sub}} = 102.4$ mm³ are removed symmetrically from the larger sphere's (d_1) interior. In case 2, external features having a total added feature volume $v_{\text{add}} = 102.4$ mm³ are constructed and symmetrically distributed over the smaller sphere's (d_2) exterior. Finally, case 3 represents the combination of external addition and internal subtraction of features, each having $v_{\text{add}} = v_{\text{sub}} = 102.4$ mm³, from the mean sized sphere (d_3). For this last case, features designed for case 1 and 2 are explicitly used and combined. These features comprise holes, ducts, cavities, drops and bellies in different numbers one to multi, and their combinations where possible. Table 8.1 displays an overview of the shapes designed and incorporated in this study. It is to be emphasized, that all shapes come with the same final particle volume v_p and consequently the same sphere-volume-based characteristic particle diameter $d_v = 10$ mm.

Additionally, the influence of a spherical void space in the center as introduced in [85, 86] of a sphere is investigated. Herefor, additional versions of the shapes multi-hole, three-hole-drop and multi-hole-drop are created having a central void space.

Table 8.1: Overview of designed shapes incorporated in this study.

No.	case 1:			case 2:		case 3:		
	hole	duct	cavity	drop	belly	hole'n' belly	duct'n' drop	hole'n' drop
one	1 	6 	10 	14 	19 	22 	25 	29 
two	2 	7 	11 	15 	20 	23 	26 	
three	3 	8 	12 	16 	21 	24 	27 	30/31 
multi	4/5 	9 	13 	17 				32/33 
extra				18 			28 	

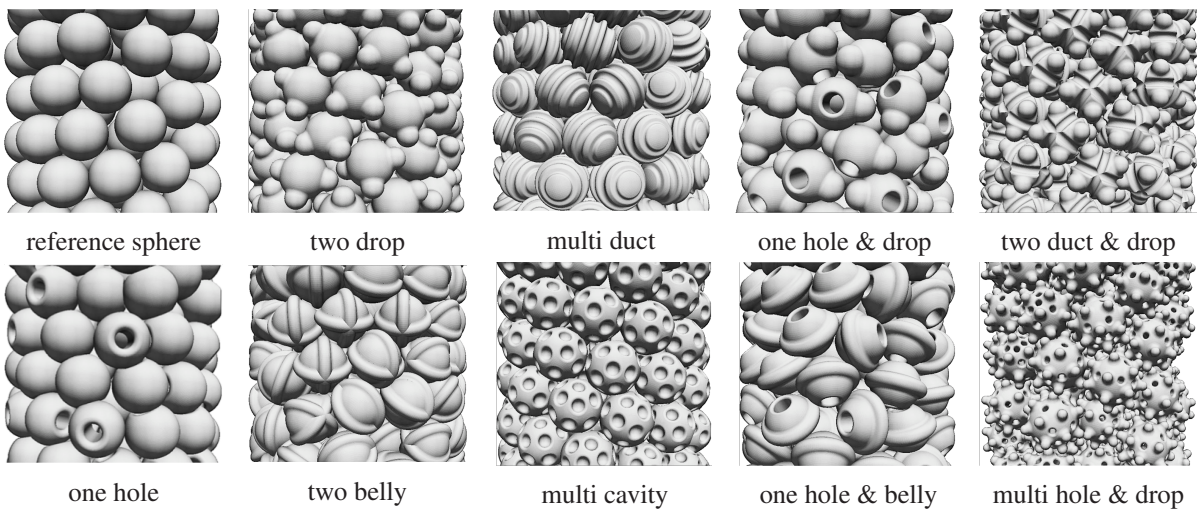


Figure 8.2: Selection of packed tubes with shapes incorporated in this study.

8.2.2 Numerical Packing Generation

Packing generation is performed incorporating the DigiDEMTM code, a voxelated particle simulation software incorporating a digital packing algorithm based on the *Monte Carlo Approach* whilst explicitly considering physical interaction forces similar to the *Discrete Element Method* and is elsewhere described in more detail [58, 87]. The packing procedure is identical to the one we already described [76]. Hereby, the 3d objects were digitized at a resolution of 10 voxel mm⁻¹. The material properties were set as follows: density $\rho = 3000 \text{ kg m}^{-3}$, coefficient of restitution $e = 0.3$, coefficient of friction $\mu = 0.7$ and Poisson's ratio $\nu = 0.3$. The objects are filled into tubes of constant height $H = 3000$ voxel (300 mm) and diameter $D = 500$ voxel (50 mm). The packing mode was selected to be damping and the stop criterion is a pre-set time of 3 s.

The packing procedure was validated using ideal spheres both with literature data [76] and experimental CT-scans Chapter 5. In regard to spheres, the reproducibility as the mean relative standard error of packing generation was found to be one percent for the radial porosity profiles and 0.5 percent for the bed averaged porosity, based on ten identical packing repetitions (see Chapter 5).

8.2.3 Numerical Fluid Dynamics

The numerically generated packings were meshed using OpenFOAM tool *snappyHexMesh* creating a castellated mesh with higher resolution at particle contact points. The mesh size was refined until reaching a Fine Grid Convergence Index [88] $< 1\%$. Steady-state flow of an incompressible fluid was simulated in OpenFOAM incorporating the SIMPLE algorithm in solver *simpleFoam*. The *Launder-Sharma $k - \epsilon$* model was utilized as the turbulence model. The validation of the simulations and the selection of the turbulence model is discussed in the previous study in detail. Air was selected as fluid, having a density $\rho = 1.2 \text{ kg m}^{-3}$ and a viscosity $\eta = 0.018 \text{ mPas}$. A superficial velocity $u_0 = 1.0 \text{ m s}^{-1}$ was selected and a parabolic tube flow profile defined at the inflow boundary.

Post-processing was performed incorporating a comprehensive PythonTM script, determining the averages as well as the radial and axial distributions of porosity, flow components, and pressure drop. For this, the inflow and outflow region lasting three particle diameters into the tube were excluded, allowing the sole investigation of the bulk packing part.

8.3 Results and Discussion

8.3.1 Geometrical Considerations

The packing structure is typically analyzed plotting the axially average local porosity in radial direction from the tube wall to the center. In the theory section, the characteristics of the radial porosity distribution

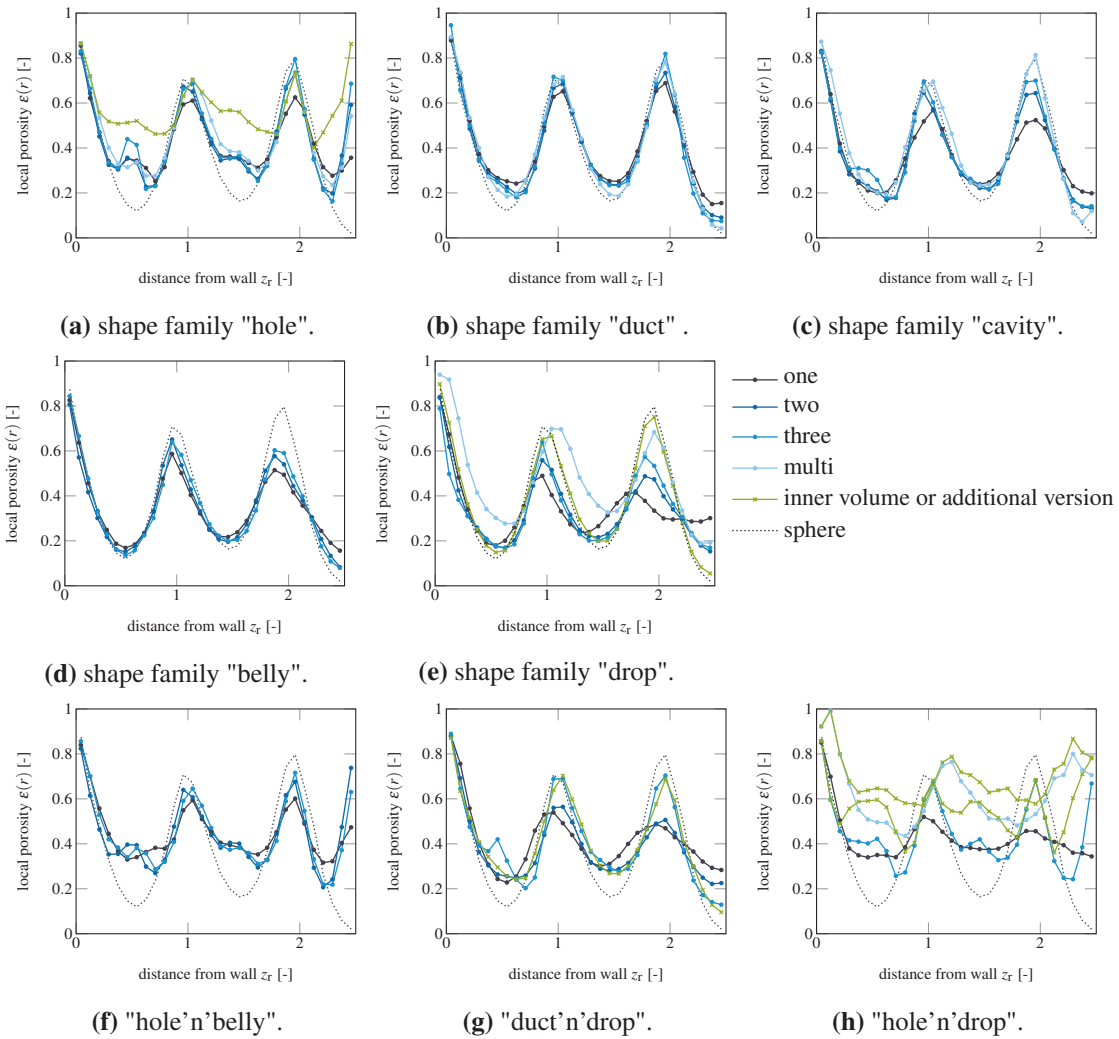


Figure 8.3: Comparison of the radial porosity distribution $\varepsilon(r)$ obtained from the investigated packings made of particles with certain features as a function of the dimensionless distance from the tube wall in particle diameters $z_r = \frac{D/2-r}{d_v}$. In all subfigures, the data of the reference sphere packing is added as dotted line, the green cross data indicates shapes with additional inner volume (a), and (h), or those of extra version (e), and (g).

of a packing of spheres have been discussed, including the wall-induced ring-like pattern spheres are ordered in, expressed as a damped oscillation function [49, 67]. Starting from this reference packing, the herein presented shapes may influence the tendency or distinctness of ring-shaped particle arrangement, the horizontal overlap between these rings and/or the damping of packing order with increasing distance to the wall. The radial porosity distributions of all investigated shape variations are clustered to their respective feature family and are depicted in the subfigures of Fig. 8.3.

Focussing on the effect of holes (Fig. 8.3a), a significant smoothening of the porosity minima can be observed. As the introduction of holes decreases the solid content at the particle centers and as the particles tend to stack one over another, an overall void increase can be observed at the center of the ring-shaped particle arrangements. It can be further seen, that hardly any difference is obtained when increasing the number of holes while keeping the total hole volume constant. Despite, a small increase of horizontal particle overlap can be observed as maxima are smoothed as well to a certain degree. This is majorly the case for the one-hole shape. When introducing a central void volume into the geometry represented by the green curve, the void is again increased at the locations with cumulated particle centers.

Compared to that, shapes with circumferential ducts (Fig. 8.3b) result in smoothed porosity minima and maxima with decreasing manifestation when increasing the number of elements from one to multi. Shapes having circular cavities (Fig. 8.3c) lead to a packing with significantly reduced porosity maxima similar to shapes having bellies (Fig. 8.3d) or drops (Fig. 8.3e). In all cases, the smoothening is decreased with an increasing element number. Only the one-drop case results in a shift of extrema location and thus the overall ring-arrangement of the particles. This is probably due to the more prolate spheroid appearance. The additional multi-drop version with the long narrow drops results in a shift of the porosity profile away from the wall. This can be explained with the drops creating a distance between the wall and the shape's solid body.

Combining two of these aforementioned features leads to combined effects. It can be concluded, that smoother radial porosity profiles can be obtained in general, when the outer appearance resembles more a prolate (one drop and combos) or an oblate (one belly, two drops and combos) spheroid appearance rather than an ideal spherical. Holes and inner volumes decrease the packing density where particle centers accumulate. Other features such as duct and cavity reduce the overall ring formation tendency and shapes such as belly, drop and cavity increase the damping toward the center of the tubes.

The averaged bed porosity relative to the reference sphere is displayed in Fig. 8.4. The shape variations are numbered top-down and left-right based on the order of Table 8.1. Neglecting the cases, where an additional inner volume is added (case 5, 31 and 33), the loosest packings are obtained with the multi-drop and multi-drop'n'hole shapes. Generally, packed bed elements with holes and most variations of the combos result in at least a 10 % higher porosity as the reference sphere. Despite some exceptions packings with drops and bellies result in a denser packing arrangement. The packing porosity trend with increasing feature number is not clear, in some cases (e.g. holes, cavity, hole'n'drop) a general increase can be observed, in others (duct, belly, hole'n'belly, duct'n'drop) is the porosity roughly constant. Comparing shape variations of same shape family and feature number (17/18 and 26/27) indicate that a slight variation of geometry may have a significant effect or none at all.

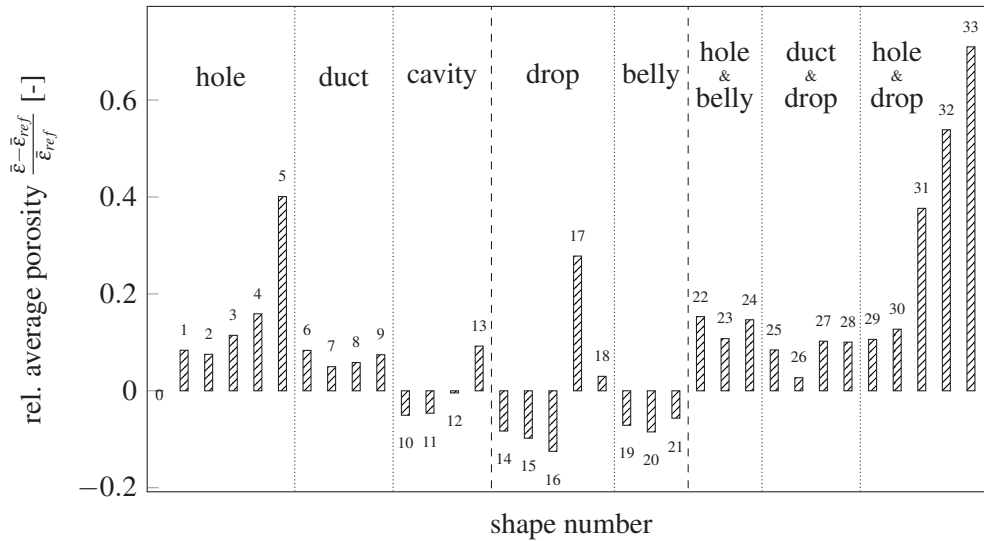


Figure 8.4: Relative deviation of average porosity $\bar{\epsilon}$ in regard to the reference sphere packing $\bar{\epsilon}_{ref}$.

A geometry variation starting from the reference sphere increases in all cases the geometric surface area a_{geo} of the packing of up to 70 % as displayed in Fig. 8.5. The highest surface areas can be obtained with the three-duct'n'drop variation (28) followed by the multi-hole (4/5) and three-hole'n'drop (30/31) shape. The geometric surface area is influenced by the shapes surface-to-volume ratio which is smallest in case of the reference spheres and largest in the multi-hole'n'drop (32/33) shape, and the number of particles in the packing or rather the packing porosity. Good geometric surface areas can be obtained with holes, hole'n'bellies and hole'n' drops. A general trend of increasing geometric surface area with increasing feature number can be observed.

8.3.2 Flow Field Analysis

The flow field is analyzed by splitting the obtained velocity vector with x, y, and z-dimension for each mesh cell into its components axial u_z (in main flow direction), radial $u_r = \sqrt{u_x^2 + u_y^2}$ (perpendicular to main flow direction) and the flow vector angle α , defined as the angle between velocity vector and main flow direction. All obtained distribution plots of these parameters as well as the respective average values are depicted in the appendix as Figs. 9.A2 to 9.A9 and shall not be discussed in detail hereinafter.

Instead, the focus is laid to evaluate whether an intuitively preferred smooth radial porosity distribution leads to a comparable smoothing of the radial velocity distribution, or easy put, if a certain radial porosity profile induces a certain velocity field, which should be intuitively the case. For that, the weighted standard deviation of the radial profiles of both parameters normalized to their respective weighted average value is plotted against each other in the parity-plot style diagram of Fig. 8.6. In this diagram, the bisectrix and their percental deviation are given and additionally the standard deviations to the reference sphere are highlighted. For instance, shape 13 (multi-cavity) has a porosity standard deviation of 15 % less than a sphere, a velocity standard deviation of 11 % more than a sphere and the parity of both parameters is 25 % imbalanced.

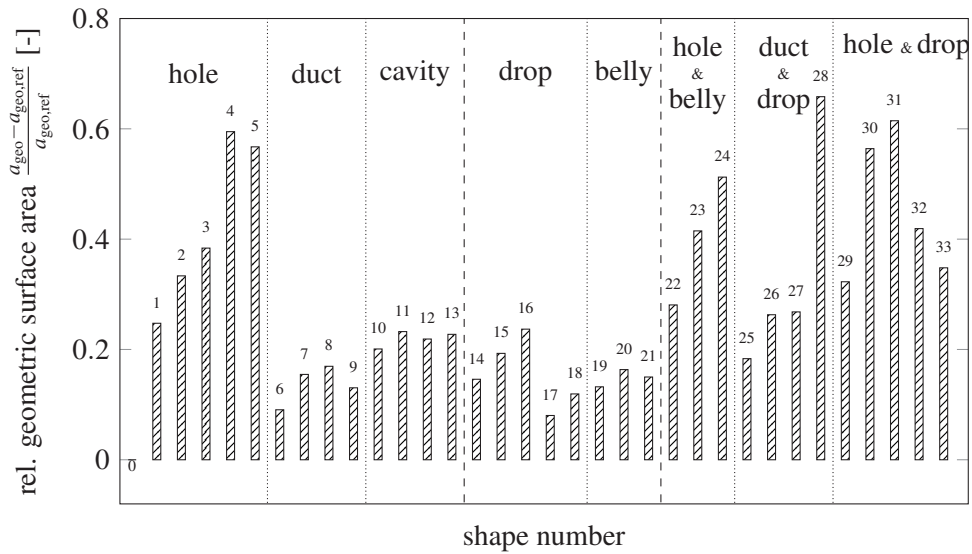


Figure 8.5: Relative deviation of geometric surface area a_{geo} in regard to the reference packing of spheres $a_{\text{geo,ref}}$.

Despite some exceptions, the investigated shapes can be clustered to certain regions in this plot. The reference sphere is well on the parity line. Except shape 13, all shapes have a smaller standard deviation of both, velocity and porosity distribution. In general, shapes having holes or cavities are located above the parity line while drop and belly shapes are typically below, except the multi-drop variation. Shapes with ducts and the duct'n'drop combos do well fit the parity. Shapes having an inner void (5,31 and 33) show the largest imbalance between porosity profile and respective velocity field.

This imbalance of porosity and velocity distribution is thought to be majorly evoked by the occurrence of void zones that by any reason are not flown through effectively alias dead zones, and the occurrence of strong radial velocity components that distract the basically axial flow pattern. In order to evaluate the latter, the average radial velocity is given in Fig. 8.7. It can be seen, that drop and belly shapes come with a very high radial flow component, except the multi-drop variation. This feature leads to a respective placing on the parity plot below the parity line except for the multi-drop case. In contrary, very large positive deviations from the parity can be observed for shapes having holes. Comparing the actual radial profiles of velocity and porosity indicate, that a significant part of these holes is not effectively part of the velocity field. Some explicit examples shall emphasize the reasons.

- **one hole (1):** The single-holed spheres have a significantly smoothed porosity distribution, however the resulting velocity profile is quite similar to the one of the reference sphere. Consequently, most of the holes are either blocked by other particles or are oriented perpendicular to the flow direction. This phenomenon can be also observed in Fig. 8.2.
- **one hole-combos (22 & 29):** The effectivity of the one-holed spheres can be significantly improved by adding drops or a belly to the shapes. The additional feature breaks up the packing pattern and thus prevents hole blockage by other particles. Moreover, the particle orientation is more favorable with the holes not being perpendicular to the main flow direction (Fig. 8.2). These two shapes are among the best regarding the fluid field.

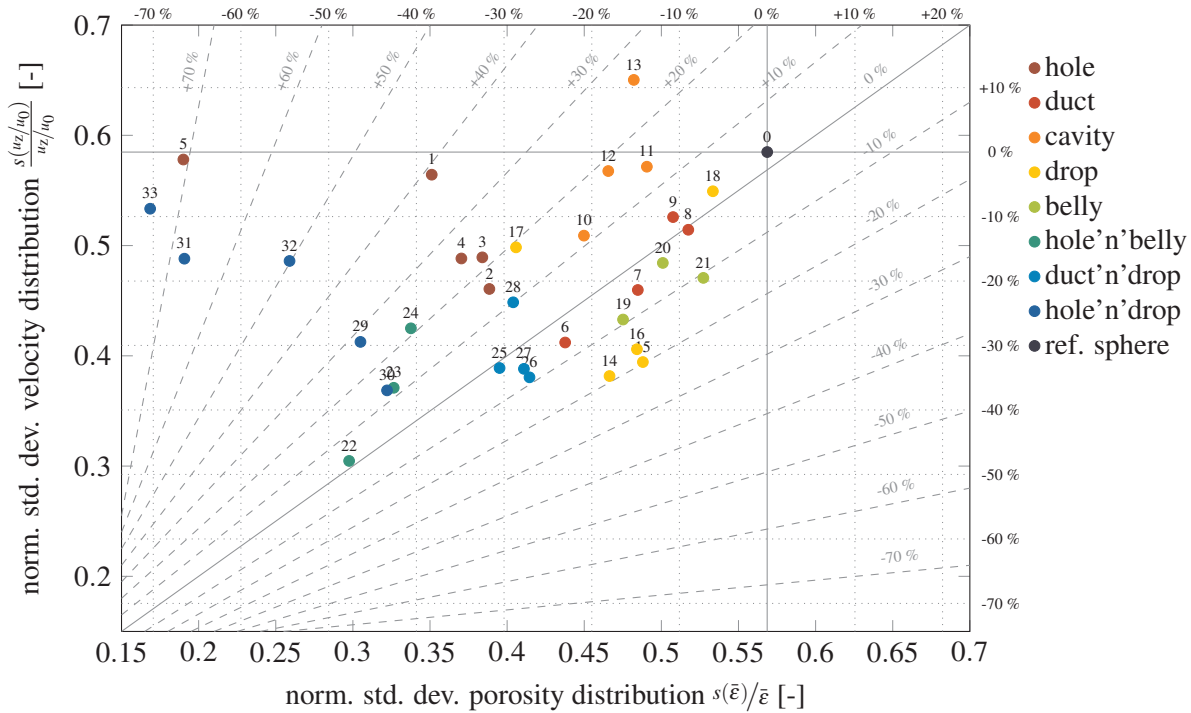


Figure 8.6: Parity plot of the standard deviation of normalized average flow $\frac{s(u_z/u_0)}{u_z/u_0}$ and porosity $s(\bar{\varepsilon})/\bar{\varepsilon}$.

- **two/three/multi-hole (2, 3 & 4):** Increasing the number of channels through the particle decreases the chance of hole blockage. Still, some of the holes are blocked but others are for sure open. Same accounts for the orientation problem. If one hole is perpendicular to the fluid direction, most others are not. Thus the parity of porosity and velocity profiles are much better as at least some holes are open to fluid perfusion.
- **the inner voids (5, 31 & 33):** Comparing the shapes having an inner void with their respective counterparts (4, 30 & 32) leads to the conclusion that the enlargements of inner voids do not contribute at all to the fluid field and thus leading to very large parity deviations.

Regarding the absolute values of the normalized standard deviation, the one-hole'n'belly shape gives the smallest values and thus the most evenly distributed velocity field. Other very good shapes are the duct'n'drop shapes, the one/two/tree-drop shapes, the one-duct shape, the hole'n'belly shapes and the one/two hole'n'drop shapes. In general and with some exceptions it can be concluded that a smoother profile is obtained for combos and for small feature numbers, especially the one-feature shapes.

8.3.3 Packing Friction

Typically, the flow field is not predominantly considered, but the packing friction as a non-dimensional pressure drop characteristic. When keeping the fluid properties (superficial velocity u_0 , density ρ , and viscosity μ) constant, the packing friction depends majorly on the packing porosity but also on the

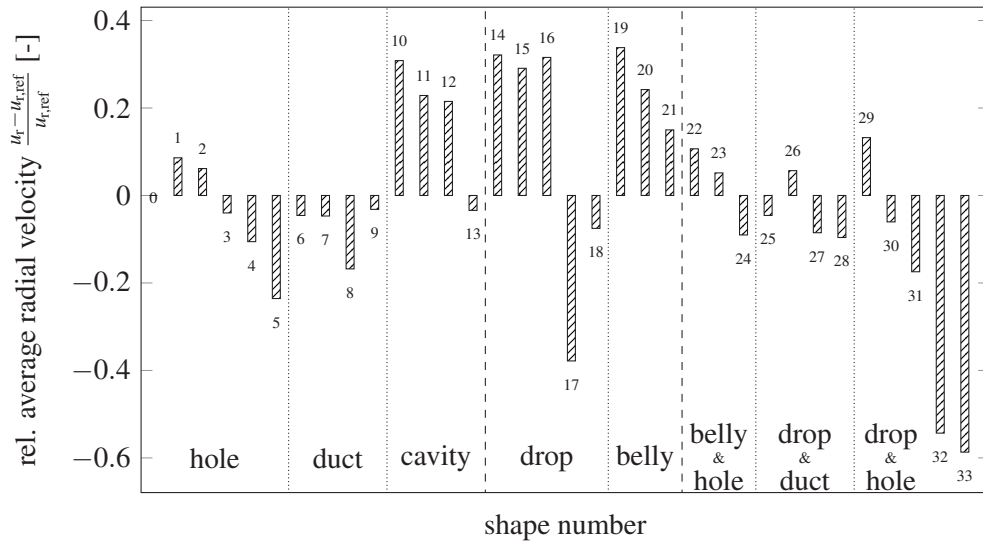


Figure 8.7: Relative deviation of average radial velocity u_r in regard to the reference sphere packing $u_{r,ref}$.

characteristic diameter and the height normalized pressure drop. The friction factors obtained for a certain Reynolds number for all investigated cases are summarized in Fig. 8.8. Additionally, the theoretical correlations of Erdim et al. [78] and Einfeld and Schnitzlein [79] are added. Their validity was proven with spheres including packings with small tube-to-particle diameter ratios.

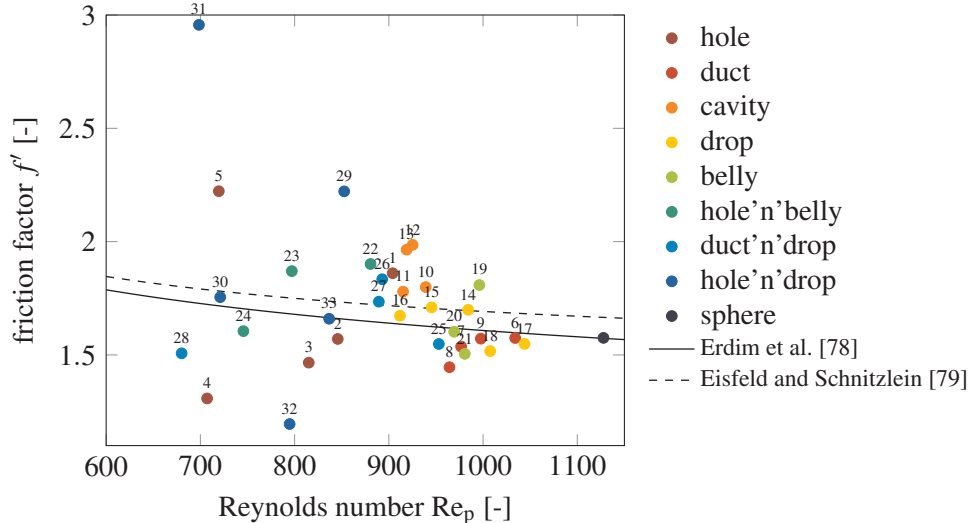


Figure 8.8: Obtained friction factors f' for all shapes at constant fluid properties as a function of the Reynolds number Re_p . Reference correlations for packings of spheres are displayed as solid and dashed line.

The herein investigated shapes can roughly be divided into two groups in regard to friction: group one comprises all shapes having at least one hole or cavity and the other group comprises the remaining shapes having drops, ducts, and bellies. Regarding group two, the obtained friction values are in the order of the already known correlations. Shapes having ducts result in a friction value slightly below the reference correlation of spheres, with a tendency to even lower friction values when having more ducts. Shapes

having one/two/three drops are situated between the two correlations, the multi-drop alternatives come with a slightly reduced friction. Shapes with bellies are again situated in the range of the correlations with the one-belly alternative being slightly above and the three-belly version slightly below. The one-duct'n'belly combo is slightly below the correlation and the two/three duct'n'belly combos are slightly above. The only more significant variation from the correlations can be determined for the second version of the three-duct'n'belly combo (28) which is significantly below the given correlation. In summary, the friction factor of the shapes clustered to group two does vary slightly from the given correlation for spherical particles. Especially the three-duct (8), three-belly (21) and the three-duct'n'belly2 (28) shape result in preferred packing friction factors in regard to spheres.

The shapes of group one, however, show a large spread of friction values that are intuitively rather unrealistic. Especially when comparing the virtually identical shapes with and without added inner void (4/5, 30/31 and 32/33). Here, the shapes with an additional inner void have a friction factor that is approximately doubled compared to the very same shape just without the inner void. And when comparing a sphere with one hole (1) with the solid reference sphere (0), the friction of the first turns out to lay significantly above the second. Thus, these significant deviations in friction can be identified for the same shapes that are very prone to dead zones in the fluid field as discussed above. And it is reasonable, that when a significant part of the packing void does not effectively contribute to the fluid field, why should it have any effect on the pressure drop. Thus, the obtained pressure drop depends on the effectively flown through porosity rather than the total existing void. But as the total existing void is included in the friction factor with power three, a present difference between effective and existing porosity has a major effect on the obtained friction values. This effect can even be extrapolated into absurdity when considering a spherical shell with infinitesimal shell thickness. A packing of these shells will have a porosity close to one, but the fluid field and pressure drop characteristics of a respective solid sphere. Per definition of the friction factor including the solid spheres pressure drop, but the shells porosity the friction will be irrationally high.

As the presence of large deviations between effective porosity and real porosity is now obvious for some shapes, it can not be excluded for all other shapes. It is even more realistic, that all different shape variations have a very specific tendency to dead zone formation. Thus the friction factor in its generally accepted form can neither be used as a predictive number nor as a comparative shape characteristic. The friction factor is probably a great tool to compare and predict the pressure drop of an isolated, well-researched shape such as the sphere, but for comparison or even prediction of pressure drop for different shape variations, an upgraded friction factor definition is required.

8.3.4 Effective Porosity

One concept to cope with the above-detected problem is to introduce a shape-dependent effective porosity parameter $\bar{\epsilon}_{\text{eff}}$. According to the concept, the effective parameter is defined to only include void spaces of a packing that actually contribute to the fluid dynamics and exclude "dead" voids as inner volumes or clogged holes. These "dead" voids may be detected numerically, where the velocity magnitude undercuts

a certain value. Here, the velocity magnitude should be used to include voids having a strong radial but weak axial component as an actively contributing void. In order to find this limiting velocity value, a designed shape study needs to be drafted, that allows different amounts of "dead" voids while keeping the particles outer friction more or less constant.

A possible problem with this approach may be, that "dead" voids do not only occur within particles but also in the fluid bulk especially close to particle contact points. It is to be investigated if the effective porosity is based on the void reduction due to inner "dead" voids solely, or to include bulk dead zones as well. If the latter is chosen, this will also influence the effective porosity of the well-investigated reference sphere case. If the first option is chosen, it is going to be a challenge to define the border between inner and outer voids, which gets more complicated the more complex geometries are investigated. The best example to emphasize this problem are the herein presented cavity shapes, that seem to produce extra "dead" voids without having a true inner volume.

Another problem is, that this effective porosity is most probably be determined for each shape version separately. This makes it hardly impossible to estimate a new shapes pressure drop without decent numerical methods. Moreover, this parameter is probably dependent on the packing method and the tube-to-particle diameter ratio. For instance, a loose packing of single-holed spheres is presumably less prone to hole clogging as a completely densified packing structure. Despite, some shapes, such as those having an internal void responsible for the dead voids may not be affected at all from the packing procedure. It is further known, that, especially for low tube-to-particle diameter ratios, very ordered packing structures can be observed, that may increase hole clogging effects. On the contrary, packings having a very large size ratio may be less prone to dead void formation.

8.3.5 Upgraded Bed Effectivity Parameter

Another possibility is, to define a new shape parameter, that is capable to quantify shape improvements in regard to pressure drop, without using the strongly porosity-dependent friction factor. This parameter, however, is not capable to predict the pressure drop of a packing comprising an arbitrary shape depending on the flow characteristics, but it shall allow at least a comparison.

The first possibility is to use the bed effectivity parameter introduced in our previous study.

$$\eta_{\text{eff}} = \frac{a_{\text{geo}}}{\Delta P} \cdot H \cdot u_0^2 \cdot \rho \quad (8.4)$$

This parameter gives a ratio of the basic parameters of a packed bed that are of technical interest: the geometric surface area, the pressure drop, and the superficial velocity. This parameter was developed based on the fact that the ratio of geomteric surface area and pressure drop is constant for a specific packing when varying the packing height and is thus a practical comparison parameter. Moreover, this parameter can be rearranged to the friction factor by including the porosity $\bar{\epsilon}^3$.

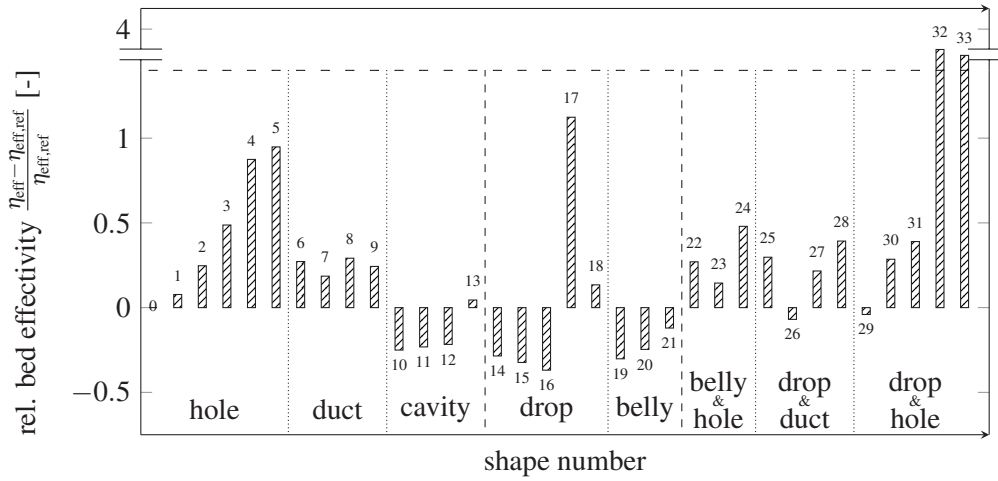


Figure 8.9: Relative deviation of bed effectivity η_{eff} in regard to the reference sphere packing $\eta_{\text{eff,ref}}$.

For a more extensive comparison parameter, this bed effectivity can be weighted with the fluid field characteristics resulting in η_{flow} , especially the inverse of the relative standard deviation of the axial flow component describing the smoothness of velocity distribution and the normalized average radial velocity component describing the radial dispersion of the fluid field.

$$\eta_{\text{flow}} = \eta_{\text{eff}} \cdot \left(\frac{s(u_z/u_0)}{u_z/u_0} \right)^{-1} \cdot \frac{u_r}{u_0} \quad (8.5)$$

Both parameters can be used for the shape comparison, and the selection of one of them depends on the actual requirements of the system. Both parameters are intended to prefer higher values and both parameters have no dimensions. Regarding the second parameter, depending on the system requirements, the three included parts: bed effectivity, smoothness of velocity distribution and radial dispersion can be separately weighted. Here, all three parameters are assigned equal importance. All in this study investigated shapes are compared based on these two parameters and their results are displayed in Fig. 8.9 and Fig. 8.10.

Regarding the original bed effectivity η_{eff} , the multi-hole, multi-drop, and the multi-hole'n'drop shapes are especially preferred. Further good shapes are the three-hole, one and three-duct, three belly'n'hole, one and extra-three-duct'n'drop, and three hole'n'drop. Not preferred are the one-hole shape, all cavity shapes, the one/two/three-drop shapes, all belly shapes, the two duct'n'drop, and the one drop'n'hole. A combination of shapes such as hole and belly does not necessarily result in a better bed effectivity. The easiest way to improve the geometric surface area to pressure drop ratio is to cut at least three holes into the shape in perpendicular directions.

When additionally considering smooth flow profiles and large radial flow components, the best shapes are the one-hole'n'belly shape, the multi-hole'n'drop shape, and the multi-hole shape. Very good results are obtained with almost all combo shapes, two/three-hole shapes and the one-duct shape. Except the cavity shapes, all remaining shapes are classified as being good compared to the reference sphere.

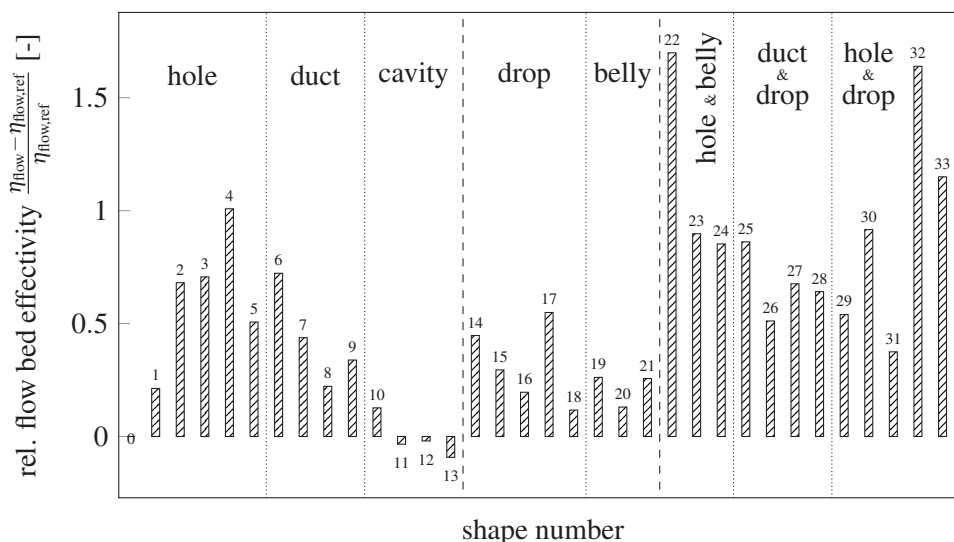


Figure 8.10: Relative deviation of bed effectivity η_{flow} in regard to the reference sphere packing $\eta_{\text{flow,ref}}$.

In summary, independent from the selected comparison parameter, the multi-hole/hole'n'drop shape gives very good results. When considering the geometric surface area and pressure drop solely, the multi-drop shape has favored characteristics, and when including flow properties, the one-hole'n'belly shape is best. In contrary, the cavity shapes are throughout not recommended. Furthermore, these results are well in accordance with previous studies regarding the Yo-Yo shape with perpendicular cut (similar to one duct shape) and straight cut (similar to one cavity shape), where the first performed much better than the second.

8.4 Conclusion

The herein presented numerical shape study was designed in order to utilize modern numerical methods to describe and compare random packed bed elements of complex geometries and to develop a selection guide based on fluid dynamic characteristics. Therefore, shapes were designed with special attention to comparability based on a spherical reference shape. Packed beds were obtained by numerical packing means and the fluid flow was simulated in OpenFOAM. It could be found, that the actual geometry has a high impact on radial void and velocity distribution. The intuitive assumption that a certain radial porosity distribution results in a corresponding velocity field could be proven wrong. Due to the blockage of shape features, especially holes, and adverse particle orientation, a certain part of the void structure does not contribute to the resulting velocity field. This also results in irrational friction factor values, as the friction factor is inherently based on the total void, whereas the included pressure drop appears to be solely affected by the actually accessible voids. Thus, the generally accepted friction factor correlations that are frequently used to predict the pressure drop of simple shaped packings appear un-capable to predict and/or compare shapes of more complex geometries. In order to improve the existing correlations, the concept of an effective porosity parameter is suggested. However, this parameter is assumed to be highly dependent on the shape's geometry, the packing method and the tube-to-particle size ratio, making this

parameter quite inconvenient. Additionally, a non-dimensional shape comparison parameter called bed effectivity is introduced in two versions. The basic definition comprises only the major fluid dynamic and geometric packing characteristics and the upgraded definition additionally includes flow field parameters. Comparing all investigated shapes and depending on the selected bed effectivity version, geometries having lots of holes perform best, followed by the novel one-hole'n'drop and the novel multi-drop shape. An increase of more than 100 % based on the reference sphere packing could be gained with the best of these shapes in terms of bed effectivity.

The herein presented study can be easily transferred to other shape families especially comprising cylindrical particles. Moreover, based on the findings in regard to the friction factor correlations it could be of significant interest to develop a method to determine the effective porosity parameter. It may be of interest to start a respective study with well-researched simple shapes, were validation is already available to a certain degree. Especially in regard to the friction factor correlations, it is frequently addressed to find an appropriate shape factor, which allows the prediction of the pressure drop of unknown shapes. Independently from the question if the friction factor correlation itself needs some decent review, it is assumed to be rather unrealistic to find a single shape factor capable to describe the influence of packed bed geometries.

Finally, it is to be noted, that all herein presented data was not validated by experiment. As the manufacturing of large numbers of differently shaped particles is actually possible when using modern additive manufacturing techniques but at a significant cost, so that a comprehensive validation was renounced. The whole simulation process, however, was validated with respect to the reference sphere. Furthermore, the herein presented results depend on a single packing mode which is known to lead to rather densely packed particle arrangements. It can not be excluded, that packings that are packed more loosely for instance by simple pouring result in different flow characteristics.

Nomenclature

Latin Symbols

a_{geo}	geometric surface area $a_{\text{geo}} = N \cdot a_p / V_T$	m^{-1}
a_p	particle surface area	m^2
d_1, d_2, d_3	sphere diameter	m
d_p	Sauter diameter of particle $d_p = 6 \cdot v_p / a_p$	m
d_v	volume equivalent diameter of particle $d_v = \sqrt[3]{6 \cdot v_p / \pi}$	m
D	diameter of tube	m or voxel
e	coefficient of restitution	-
f'	friction coefficient $f' = \frac{\Delta P}{H} \cdot \frac{d_p}{\rho \cdot u_0^2} \cdot \frac{\bar{\varepsilon}^3}{1 - \bar{\varepsilon}}$	-
H	height of tube	m or voxel
K_1, k_1, k_2	pre-factors of Einfeld and Schnitzlein's [79] correlation	-
N	number of particles per packing	-
ΔP	pressure drop	Pa
r, R	control variable in radial and spherical direction	m
Re_p	packing Reynolds number $\text{Re}_p = \frac{\rho \cdot d_p \cdot u_0}{\eta \cdot (1 - \bar{\varepsilon})}$	-
$s(x)$	standard deviation of measure x	-
u_x, u_y, u_z	velocity component in coordinate directions	m s^{-1}
u_r	velocity component in radial direction $u_r = \sqrt{u_x^2 + u_y^2} $	m s^{-1}
u_0	superficial velocity	m s^{-1}
V_T	volume of tube	m^3
v_p	volume of particle	m^3
$v_{\text{add}}, v_{\text{add}}$	added or subtracted feature volume	m^3
z_r	non-dimensional distance from tube wall in particle diameters $z_r = \frac{D/2 - r}{d_v}$	-
z_R	non-dimensional distance from particle center in particle diameters $z_R = \frac{2 \cdot R}{d_v}$	-

Greek Symbols

α	flow vector angle in regard to main flow direction	$^\circ$
ε	local porosity	-
$\bar{\varepsilon}$	mean bed porosity	-
$\bar{\varepsilon}_{\text{eff}}$	effective average porosity	-
η	fluid viscosity	Pa s
$\eta_{\text{eff}}, \eta_{\text{flow}}$	bed effectivity without or with flow properties	-
λ	tube-to-particle diameter ratio	-
ρ	material density	kg m^{-3}
μ	coefficient of friction	-
ν	Poisson's ratio	-

Indices

ref reference sphere packing value

Appendix

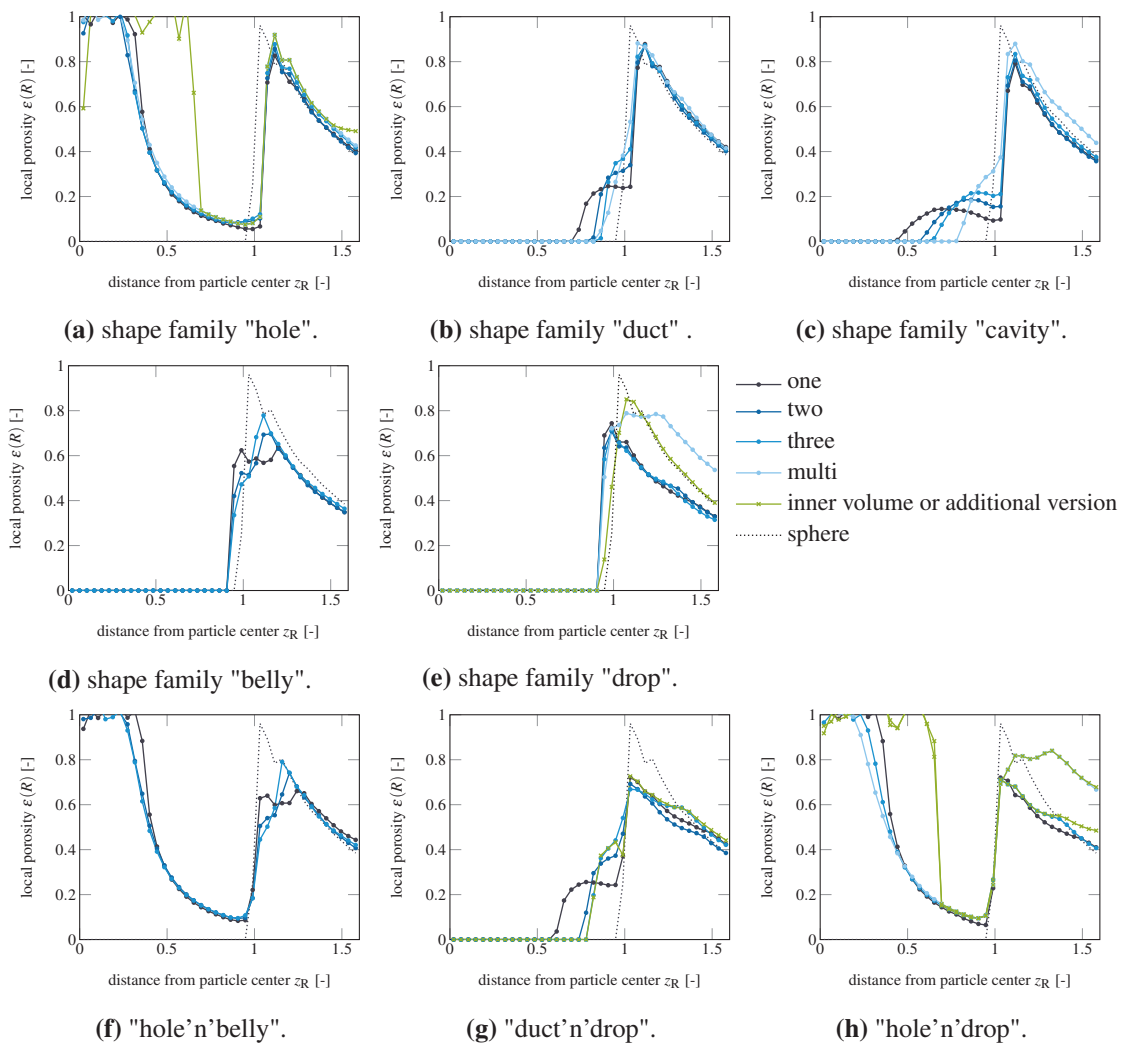


Figure 9.A1: Comparison of spherical porosity distribution $\varepsilon(R)$ of the investigated packings made of particles with certain features as a function of the dimensionless distance from the particle centers in particle diameters $z_R = \frac{2 \cdot R}{d_v}$.

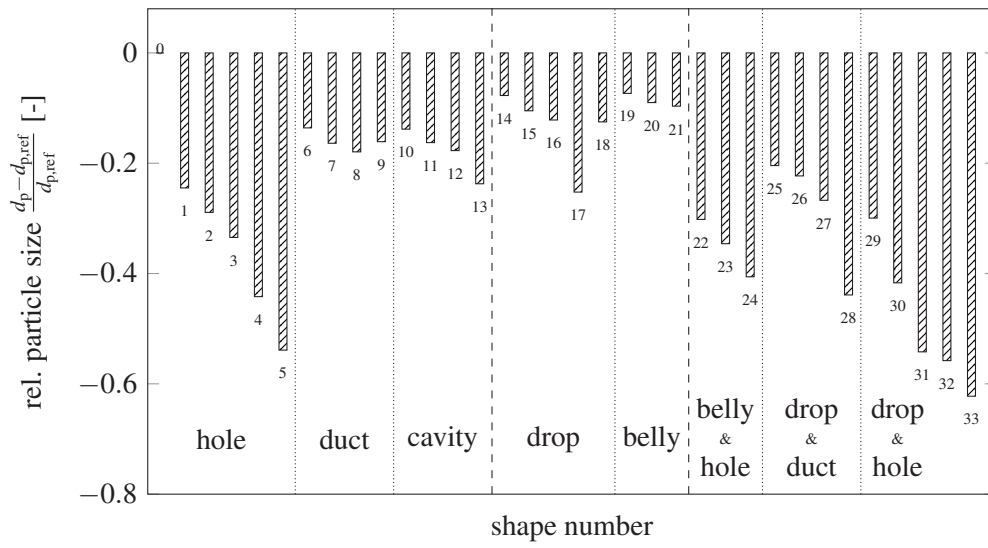


Figure 9.A2: Relative deviation of sauter diameter d_p in regard to a reference sphere $d_{p,ref}$.

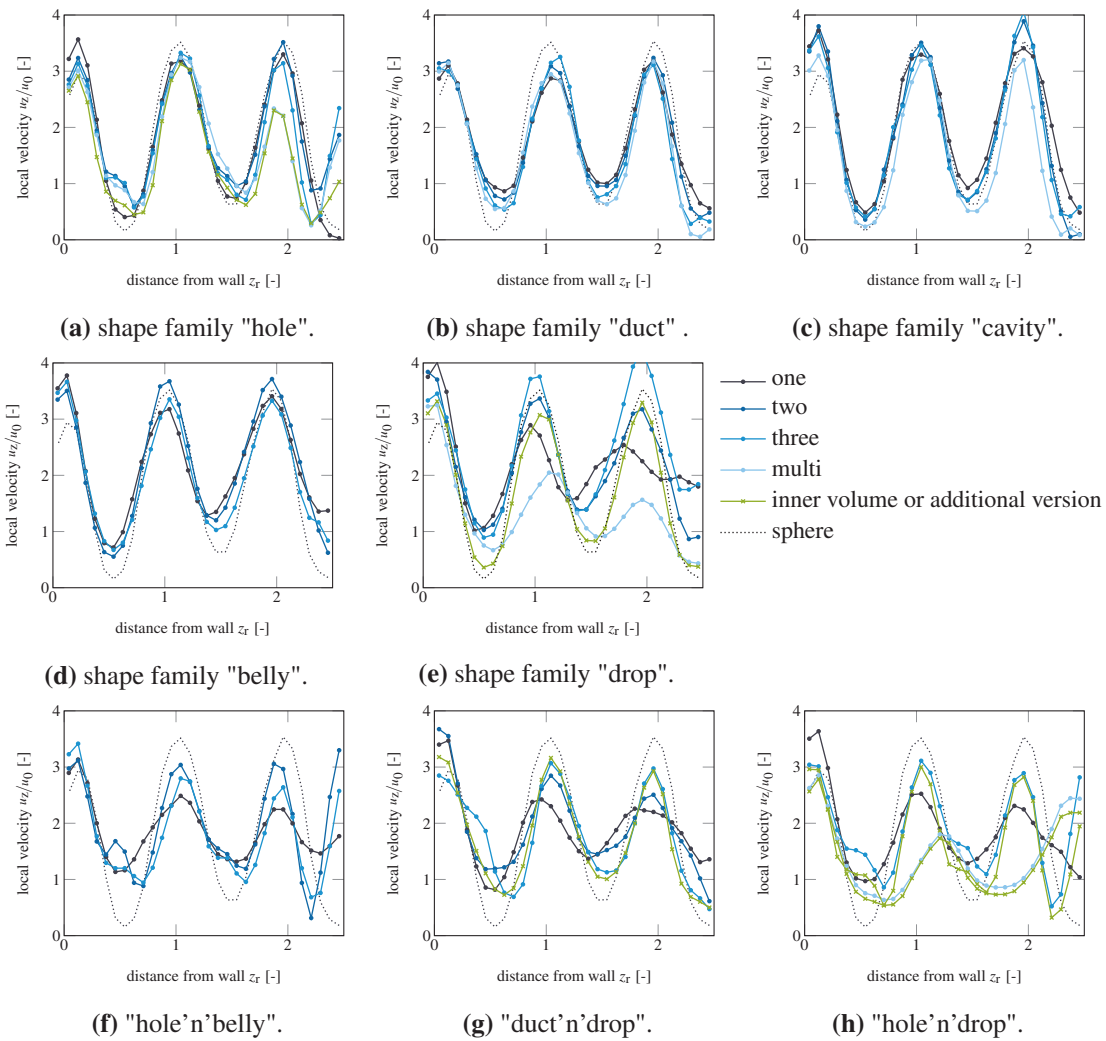


Figure 9.A3: Comparison of the radial distribution of the axial velocity component u_z/u_0 of the investigated packings made of particles with certain features as a function of the dimensionless distance from the tube wall in particle diameters z_r .

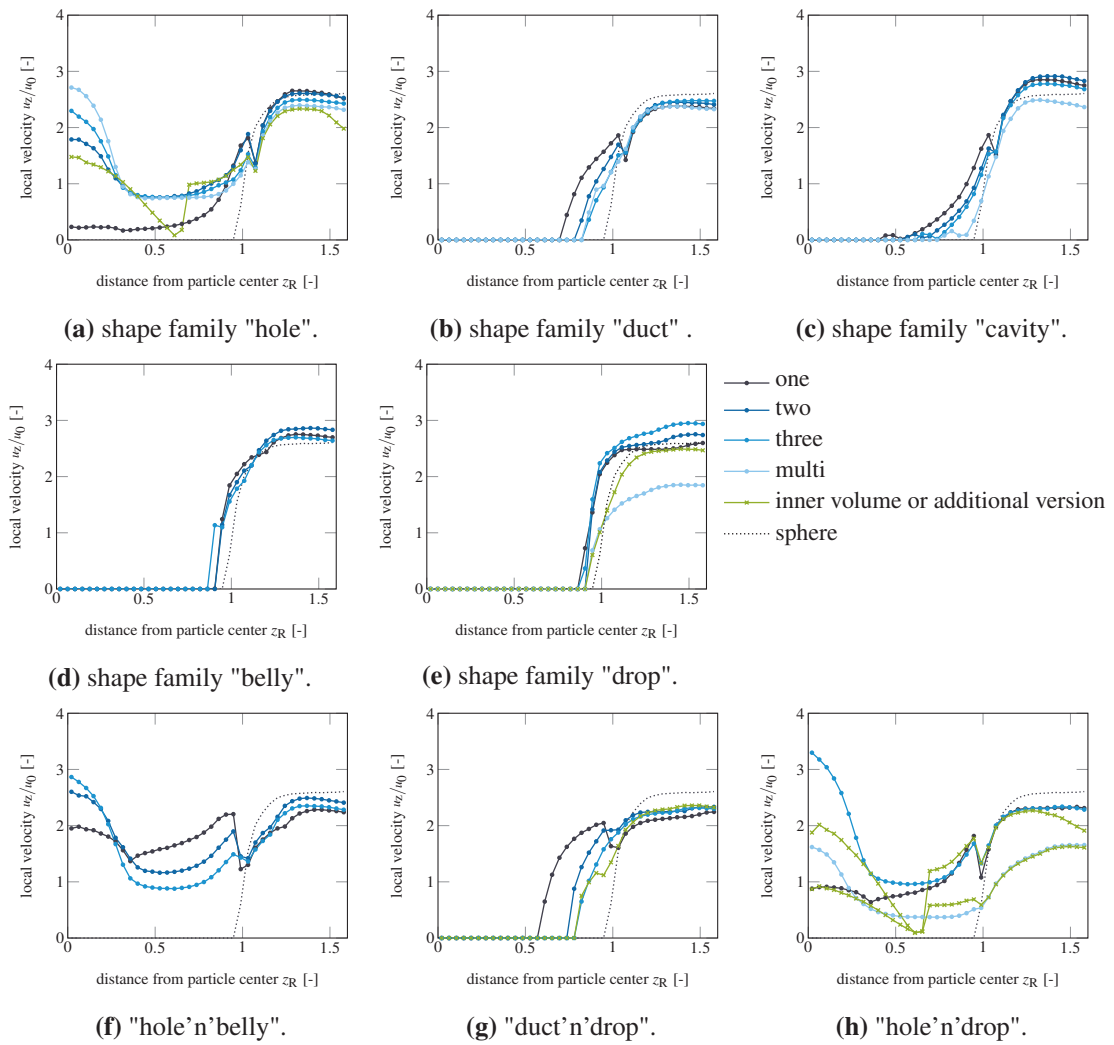


Figure 9.A4: Comparison of the spherical distribution of the normalized axial velocity component $u_z(R)/u_0$ of the investigated packings made of particles with certain features as a function of the dimensionless distance from the particle centers in particle diameters z_R .

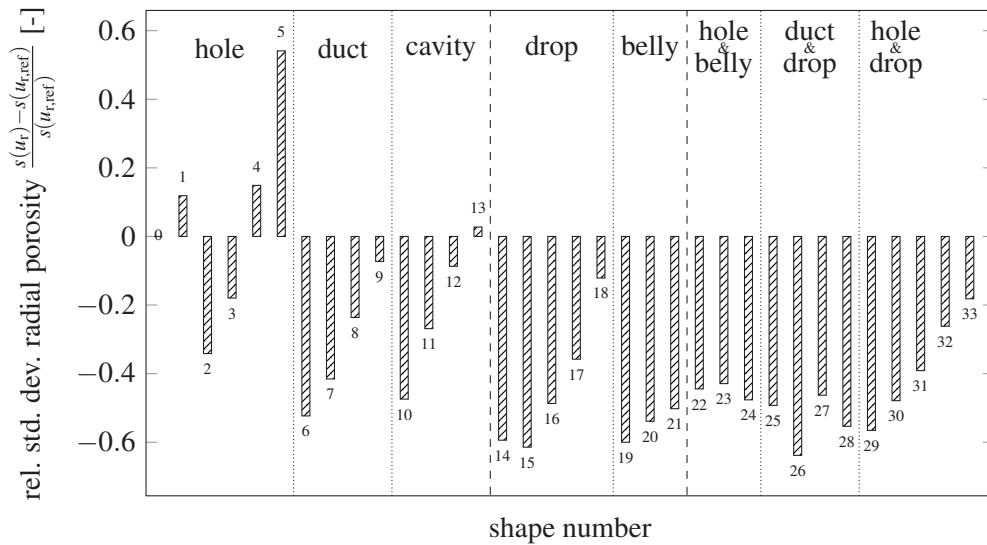


Figure 9.A5: Relative deviation of average radial velocity u_r in regard to a reference sphere $u_{r,ref}$.

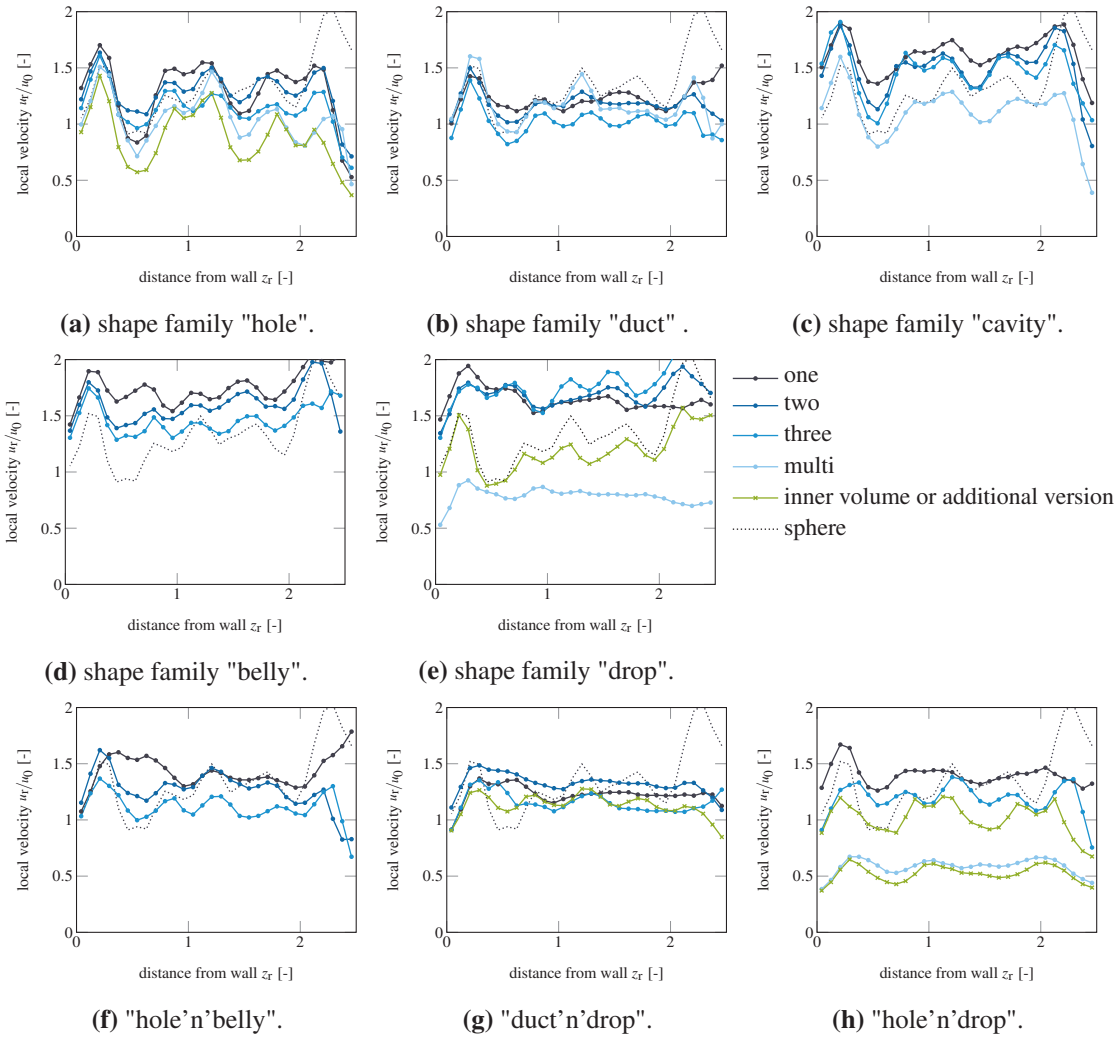


Figure 9.A6: Comparison of the radial distribution of the normalized radial velocity component $u_r(r)/u_0$ of the investigated packings made of particles with certain features as a function of the dimensionless distance from the particle centers in particle diameters z_r .

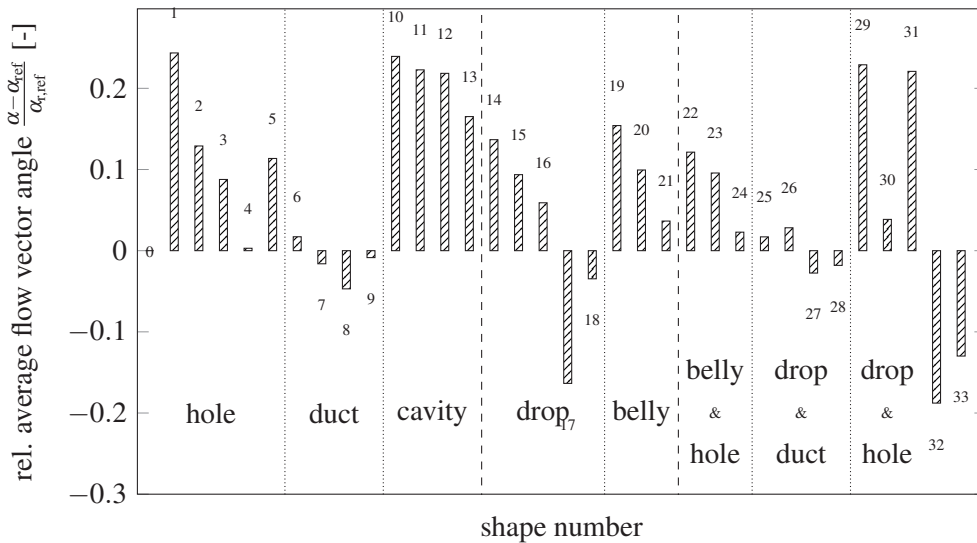


Figure 9.A7: Relative deviation of flow vector angle α in regard to a reference sphere α_{ref} .

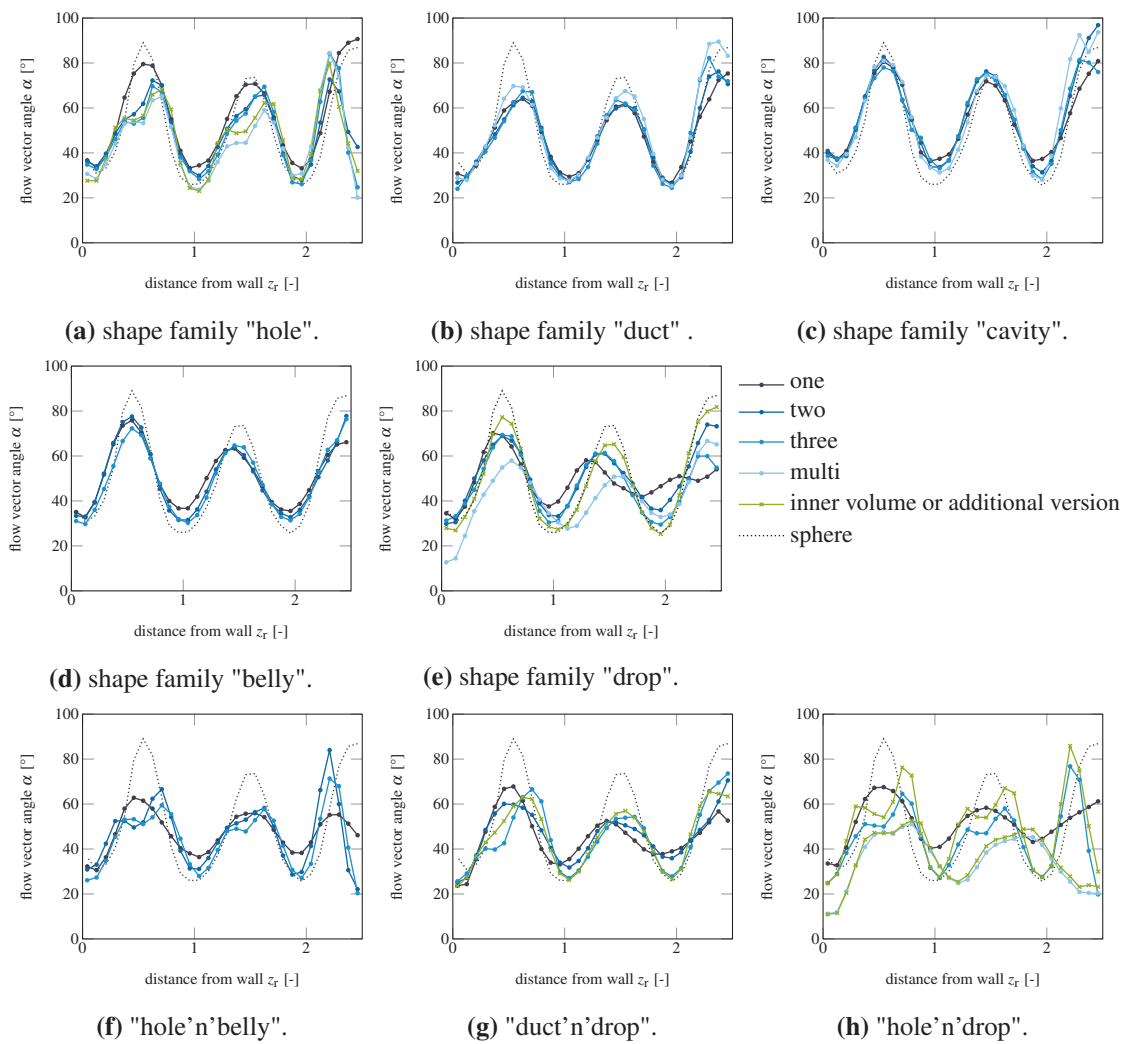


Figure 9.A8: Comparison of radial distribution of flow vector angle $\alpha(r)$ of the investigated packings made of particles with certain features as a function of the dimensionless distance from the particle centers in particle diameters z_r .

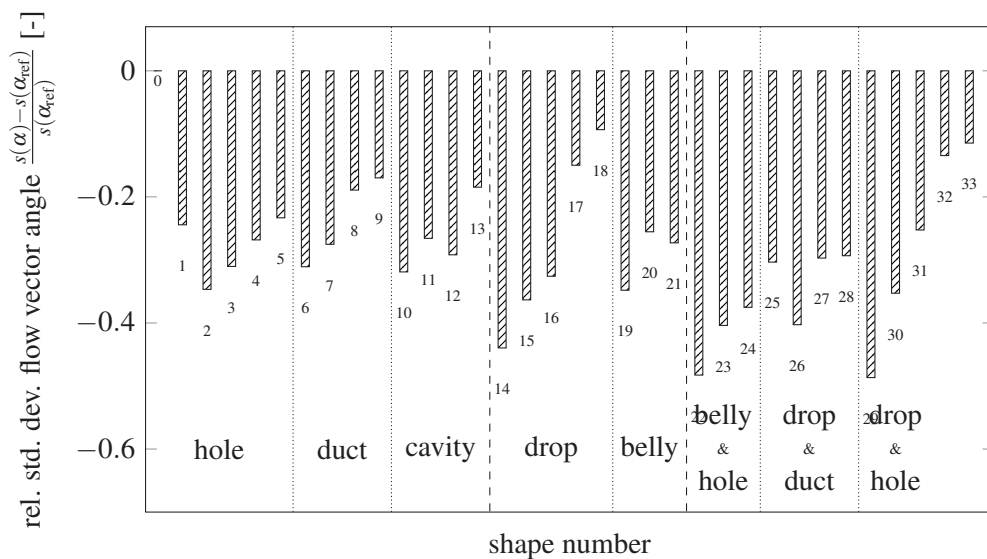


Figure 9.A9: Relative deviation of standard deviation of flow vector angle $s(\alpha)$ in regard to a reference sphere $s(\alpha_{ref})$.

References

- [1] A. Koster, H. D. Matzner, D. R. Nicholisi, *Nuclear Engineering and Design* **2003**, 222, 231–245.
- [2] H. Singh, R. P. Saini, J. S. Saini, *Renewable and Sustainable Energy Reviews* **2010**, 14, 1059–1069.
- [3] A. I. Rodarte-Morales, G. Feijoo, M. T. Moreira, J. M. Lema, *Biochemical Engineering Journal* **2012**, 66, 38–45.
- [4] T. Eppinger, K. Seidler, M. Kraume, *Chemical Engineering Journal* **2011**, 166, 324–331.
- [5] G. D. Wehinger, C. Fütterer, M. Kraume, *Industrial & Engineering Chemistry Research* **2017**, 56, 87–99.
- [6] L. W. Rong, K. J. Dong, A. B. Yu, *Chemical Engineering Science* **2013**, 99, 44–58.
- [7] R. K. Reddy, J. B. Joshi, *Particuology* **2010**, 8, 37–43.
- [8] A. Pavlisic, R. Ceglar, A. Pohar, B. Likozar, *Powder Technology* **2018**, 328, 130–139.
- [9] R. Mohanty, S. Mohanty, B. K. Mishra, *Journal of the Taiwan Institute of Chemical Engineers* **2016**, 63, 71–80.
- [10] M. Marek, *Chemical Engineering Science* **2017**, 161, 382–393.
- [11] P. Magnico, *Chemical Engineering Science* **2003**, 58, 5005–5024.
- [12] P. Lovreglio, S. Das, K. A. Buist, E. A. J. F. Peters, L. Pel, J. A. M. Kuipers, *AIChE Journal* **2018**, 64, 1896–1907.
- [13] S. Khirevich, A. Hölzel, D. Hlushkou, U. Tallarek, *Analytical Chemistry* **2007**, 79, 9340–9349.
- [14] L. He, D. K. Tafti, K. Nagendra, *Powder Technology* **2017**, 313, 332–343.
- [15] H. Freund, T. Zeiser, F. Huber, E. Klemm, G. Brenner, F. Durst, G. Emig, *Chemical Engineering Science* **2003**, 58, 903–910.
- [16] S. Das, N. G. Deen, J. A. M. Kuipers, *Chemical Engineering Journal* **2018**, 334, 741–759.
- [17] D. Coelho, J.-F. Thovert, P. M. Adler, *Physical Review E* **1997**, 55, 1959–1978.
- [18] M. Zhang, H. Dong, Z. Geng, *Chemical Engineering Research and Design* **2018**, 132, 149–161.
- [19] M. T. Zambon, D. A. Asensio, G. F. Barreta, G. D. Mazza, *Industrial & Engineering Chemistry Research* **2014**, 53, 19052–19061.
- [20] M. Behnam, A. G. Dixon, M. Nijemeisland, E. H. Stitt, *Industrial & Engineering Chemistry Research* **2013**, 52, 15244–15261.
- [21] M. E. Taskin, A. G. Dixon, E. H. Stitt, *Numerical Heat Transfer Part A: Applications* **2007**, 52, 203–218.
- [22] M. V. Tabib, S. T. Johansen, S. Amini, *Industrial & Engineering Chemistry Research* **2013**, 52, 12041–12058.
- [23] A. Singhal, S. Cloete, S. Radl, R. Quinta-Ferreira, S. Amini, *Chemical Engineering Science* **2017**, 172, 1–12.
- [24] S. J. P. Romkes, F. M. Dautzenberg, C. M. van den Bleek, H. P. A. Calis, *Chemical Engineering Journal* **2003**, 96, 3–13.

- [25] B. Partopour, A. G. Dixon, *Powder Technology* **2017**, *322*, 258–272.
- [26] S. A. Logtenberg, M. Nijemeisland, A. G. Dixon, *Chemical Engineering Science* **1999**, *54*, 2433–2439.
- [27] Y. Dong, B. Sosna, O. Korup, F. Rosowski, R. Horn, *Chemical Engineering Journal* **2017**, *317*, 204–214.
- [28] A. G. Dixon, G. Walls, H. Stanness, M. Nijemeisland, E. H. Stitt, *Chemical Engineering Journal* **2012**, *200-202*, 344–356.
- [29] G. D. Wehinger, T. Eppinger, M. Kraume, *Chemical Engineering Science* **2015**, *122*, 197–209.
- [30] G. D. Wehinger, T. Eppinger, M. Kraume, *Chemie Ingenieur Technik* **2015**, *87*, 734–745.
- [31] M. Behnam, A. G. Dixon, P. M. Wright, M. Nijemeisland, E. H. Stitt, *Chemical Engineering Journal* **2012**, *s 207-208*, 690–700.
- [32] A. G. Dixon, M. E. Taskin, M. Nijemeisland, E. H. Stitt, *Industrial & Engineering Chemistry Research* **2010**, *49*, 9012–9025.
- [33] A. G. Dixon, *Chemical Engineering Research and Design* **2014**, *92*, 1279–1295.
- [34] B. Partopour, A. G. Dixon, *Computers & Chemical Engineering* **2016**, *88*, 126–134.
- [35] A. H. Mahmoudi, F. Hoffmann, B. Peters, X. Besseron, *International Communications in Heat and Mass Transfer* **2016**, *71*, 20–34.
- [36] G. M. Karthik, V. V. Buwa, *AIChE Journal* **2017**, *63*, 366–377.
- [37] A. G. Dixon, J. Boudreau, A. Rocheleau, A. Troupel, M. E. Taskin, M. Nijemeisland, E. H. Stitt, *Industrial & Engineering Chemistry Research* **2012**, *51*, 15839–15854.
- [38] K. M. Brunner, H. D. Perez, R. P. S. Peguin, J. C. Duncan, L. D. Harrison, C. H. Bartholomew, W. C. Hecker, *Industrial & Engineering Chemistry Research* **2015**, *54*, 2902–2909.
- [39] F. Augier, F. Idoux, J. Y. Delenne, *Chemical Engineering Science* **2010**, *65*, 1055–1064.
- [40] T. Ludwig, J. von Seckendorff, C. Troll, R. Fischer, M. Tonigold, B. Rieger, O. Hinrichsen, *Chemie Ingenieur Technik* **2018**, *90*, 703–707.
- [41] G. Boccardo, F. Augier, Y. Haroun, D. Ferré, D. Marchisio, *Chemical Engineering Journal* **2015**, *279*, 809–820.
- [42] F. Benyahia, K. E. O’Neill, *Particulate Science and Technology* **2005**, *23*, 169–177.
- [43] E. A. Foumeny, H. A. Moallemi, C. Mcgreavy, J. A. A. Castro, *The Canadian Journal of Chemical Engineering* **1991**, *69*, 1010–1015.
- [44] E. A. Foumeny, A. Kulkarni, S. Roshani, A. Vatani, *Applied Thermal Engineering* **1996**, *16*, 195–202.
- [45] A. G. Dixon, *The Canadian Journal of Chemical Engineering* **1988**, *66*, 705–708.
- [46] J. E. Ayer, F. E. Soppet, *Journal of the American Ceramic Society* **1965**, *48*, 180–183.
- [47] W.-C. Yang, *Handbook of Fluidization and Fluid-Particle Systems, 1st ed.* CRC Press, Boca Raton, FL, **2003**.
- [48] S. Afandizadeh, E. A. Foumeny, *Applied Thermal Engineering* **2001**, *21*, 669–682.

- [49] A. de Klerk, *AIChE Journal* **2003**, *49*, 2022–2029.
- [50] L. H. S. Roblee, R. M. Baird, J. W. Tierney, *AIChE Journal* **1958**, *4*, 460–464.
- [51] R. F. Benenati, C. B. Brosilow, *AIChE Journal* **1962**, *8*, 359–361.
- [52] J. S. Goodling, R. I. Vachon, W. S. Stelpflug, S. J. Ying, M. S. Khader, *Powder Technology* **1983**, *35*, 23–29.
- [53] C. G. du Toit, *Nuclear Engineering and Design* **2008**, *238*, 3073–3079.
- [54] R. Kűfner, H. Hofmann, *Chemical Engineering Science* **1990**, *45*, 2141–2146.
- [55] A. Montillet, L. le Coq, *Powder Technology* **2001**, *121*, 138–148.
- [56] W. Du, N. Quan, P. Lu, J. Xu, W. Wei, L. Zhang, *Chemical Engineering Research and Design* **2016**, *106*, 115–125.
- [57] G. J. Auwerda, J.-L. Kloosterman, D. Lathouwers, T. H. J. J. van der Hagen, *Nuclear Technology* **2013**, *183*, 272–286.
- [58] R. Caulkin, X. Jia, C. Xu, M. Fairweather, R. A. Williams, H. Stitt, M. Nijemeisland, S. Aferka, M. Crine, A. Léonard, D. Toye, P. Marchot, *Industrial & Engineering Chemistry Research* **2009**, *48*, 202–213.
- [59] N. J. Mariani, W. I. Salvat, M. A. Campesi, G. F. Barreto, O. M. Martinez, *International Journal of Chemical Reactor Engineering* **2009**, *7*, A82.
- [60] J. Reimann, J. Vicente, E. Brun, C. Ferrero, Y. Gan, A. Rack, *Powder Technology* **2017**, *318*, 471–483.
- [61] X. Gan, M. Kamlah, J. Reimann, *Fusion Engineering and Design* **2010**, *85*, 1782–1787.
- [62] R. Balzan, A. L. Sellerio, D. Mari, A. Comment, G. Gremaud, *Granular Matter* **2013**, *15*, 873–879.
- [63] R. Balzan, A. L. Sellerio, D. Mari, A. Comment, *Applied Magnetic Resonance* **2015**, *46*, 633–642.
- [64] R. Stannarius, *Review of Scientific Instruments* **2017**, *88*, 051806.
- [65] A. J. Sederman, P. Alexander, L. F. Gladden, *Powder Technology* **2001**, *117*, 255–269.
- [66] N. L. Nguyen, V. van Buren, R. Reimert, A. von Garnier, *Magnetic Resonance Imaging* **2005**, *23*, 395–396.
- [67] G. E. Mueller, *Powder Technology* **1992**, *72*, 269–275.
- [68] W. van Antwerpen, C. G. du Toit, P. G. Rousseau, *Nuclear Engineering and Design* **2010**, *240*, 1803–1818.
- [69] R. P. Zou, A. B. Yu, *Chemical Engineering Science* **1996**, *51*, 1177–1180.
- [70] P. A. Cundall, O. D. L. Strack, *Geotechnique* **1979**, *29*, 47–65.
- [71] W. Zhong, A. Yu, X. Liu, Z. Tong, H. Zhang, *Powder Technology* **2016**, *302*, 108–152.
- [72] H. P. Zhu, Z. Y. Zhou, R. Y. Yang, A. B. Yu, *Chemical Engineering Science* **2008**, *63*, 5728–5770.
- [73] A. S. Clarke, H. Jónsson, *Physical Review E* **1993**, *47*, 3975–3984.
- [74] G. T. Nolan, P. E. Kavanagh, *Powder Technology* **1992**, *72*, 149–155.
- [75] A. Yang, C. T. Miller, L. D. Turcoliver, *Physical Review E* **1996**, *53*, 1516–1524.

-
- [76] J. Fernengel, J. von Seckendorff, O. Hinrichsen, *Proceedings of the 28th European Symposium on Computer Aided Process Engineering* **2018**, 97–102.
- [77] R. Caulkin, W. Tian, M. Pasha, A. Hassanpour, X. Jia, *Computers and Chemical Engineering* **2015**, 76, 160–169.
- [78] E. Erdim, Ö. Akgiray, I. Demir, *Powder Technology* **2015**, 283, 488–504.
- [79] B. Einfeld, K. Schnitzlein, *Chemical Engineering Science* **2001**, 56, 4321–4329.
- [80] T. Zeiser, PhD thesis, Universität Erlangen-Nürnberg, **2008**.
- [81] M. Giese, K. Rottschäfer, D. Vortmeyer, *AIChE Journal* **1998**, 44, 484–490.
- [82] Y. A. Hassan, E. E. Dominguez-Ontiveros, *Nuclear Engineering and Design* **2008**, 238, 3080–3085.
- [83] O. Bey, G. Eigenberger, *Chemical Engineering Science* **1997**, 52, 1365–1376.
- [84] S. Bu, J. Yang, Q. Dong, Q. Wang, *Applied Thermal Engineering* **2014**, 73, 1525–1532.
- [85] D. Coupland, S. Winfield, *Patent Application*, WO 2016166526, **2016**.
- [86] M. Erfan, *Patent*, US 8946117, **2015**.
- [87] R. A. Williams, X. Jia, *Particulate Science and Technology* **2003**, 21, 195–205.
- [88] I. B. Celik, U. Ghia, P. J. Roache, C. J. Freitas, H. Coleman, P. E. Raad, *Journal of Fluids Engineering* **2008**, 130, 078001.

List of Figures

1.1	Schematic drawing of the standard alumina printing procedure.	11
1.2	Wall effect considerations concerning the application of a new powder layer onto various substrates.	16
1.3	Schematics of the custom printer setup developed and used for Binder Jetting material development studies.	23
1.4	Particle size distribution of investigated powders.	26
1.5	Representative scanning electron microscopy images of investigated powders.	27
1.6	Influence of temperature treatment on microstructure of investigated powders.	29
1.7	Printer setup validation with different powders and binders.	30
1.8	Droplet test for powder-binder interplay evaluation.	31
2.1	Experimental results obtained from the literature for the mean coordination number \bar{N}_c as a function of porosity $\bar{\epsilon}$	57
2.2	Experimental results obtained from the literature for the cumulative frequency distribution of the mean coordination number \bar{N}_c	58
2.3	Comparison plot of known correlations regarding the relation of mean coordination number \bar{N}_c and mean packed-bed porosity $\bar{\epsilon}$ for random packings and abstract arrangements of mono-sized spheres	60
2.4	Gathered experimental literature data of radial porosity distributions $\epsilon(r)$ oobtained by using various experimental methods and packing procedures and containing spheres of different materials enclosed by a cylindrical confining wall	64
2.5	Comparison of anonymized experimental radial void distribution data $\epsilon(r)$ obtained with $\lambda > 5.0$ and a selection of empirical and semi-analytical correlations as presented in the literature	66
2.6	Influence of packing hight-to-particle diameter ratio κ on the overall bed porosity $\bar{\epsilon}$	69
2.7	Influence of both λ and κ on the overall bed porosity $\bar{\epsilon}$ for a dense packing arrangement.	69
2.8	Summary of experimental literature results for the average bed porosity $\bar{\epsilon}$ when varying the tube-to-particle diameter ratio λ for smooth spheres	70
2.9	Anonymized experimental literature data as displayed in Fig. 2.8 and known correlations regarding the influence of tube-to-particle diameter ratio λ on the mean bed porosity $\bar{\epsilon}$ of smooth spheres	72
2.10	Experimental literature data regarding the sphericity Ψ_w dependent evaluation of packed-bed bulk porosity ϵ_{inf}	76

2.11	Radial porosity distribution $\varepsilon(r)$ for A, equilateral cylinders; C, non-equilateral cylinders; E, hollow cylinders, and average packing porosity $\bar{\varepsilon}$ for B, equilateral cylinders; D, non-equilateral cylinders; F, hollow cylinders	78
2.12	Mean bed porosity under the absence of confinement as a function of the aspect ratio of packings consisting of: A, ellipsoids, aspherical ellipses and lenses; B, spherocylinders; C, cylinders (empty marks), hollow cylinders, frustums and cones; and D, tetrahedra (empty marks), cubes (solid marks) and superellipsoids (star)	86
3.1	Effects of material (A), filling method (B) and diameter ratio (C) on the porosity of a packed bed of spheres.	111
3.2	Experimental results of the porosity of steel (a) and polyamide (b) spheres varying filling method and diameter ratio.	112
3.3	Correlation between the material and the diameter ratio on the porosity of a packed bed of spheres using machine filling.	114
4.1	Schematic drawing of experimental setup for pressure drop measurements.	127
4.2	Experimental results of the mean bed porosity $\bar{\varepsilon}$ plotted against the tube-to-particle diameter ratio λ	129
4.3	Modified Hausner ratio H_{mod} plotted against tube-to-particle diameter ratio λ	129
4.4	Mean bed porosity $\bar{\varepsilon}$ as function of tube-to-particle diameter ratio λ for elongated cylinders with an aspect ratio $a_1 \leq 1$	130
4.5	Mean bed porosity $\bar{\varepsilon}$ as function of tube-to-particle diameter ratio λ for flat cylinders with an aspect ratio $a_1 \geq 1$	130
4.6	Mean bed porosity $\bar{\varepsilon}$ as function of tube-to-particle diameter ratio λ for all polyamide cylinders.	131
4.7	Parity plot of the derived wall effect correlation (4.11) together with (4.12) for cylinders of varying aspect ratios, materials and filling method. The respective parameters are displayed in Table 4.4.	131
4.8	Mean bed porosity $\bar{\varepsilon}$ as function of tube-to-particle diameter ratio λ for hollow cylinders.	133
4.9	Visualization of the hollow cylinder interpenetration.	133
4.10	Mean bed porosity $\bar{\varepsilon}$ decreases with increasing filling time τ (inverse filling rate) until reaching a constant value ε_{SPD}	135
4.11	Maximal porosity deviation $\Delta\bar{\varepsilon}_f/\bar{\varepsilon}_{\text{SPD}}$ obtained from filling time τ (inverse filling rate) variation for packings of cylinders and spheres of different aspect ratio and material.	135
4.12	Dependence of λ on mean bed porosity for spheres packed in various container geometries.	136
4.13	Dependence of λ on mean bed porosity $\bar{\varepsilon}$ of cylinders packed into various container geometries.	137
4.14	Relation of relative pressure drop and filling time τ	138
4.15	Friction factor f' obtained from packings of various tube-to-particle diameter ratios λ when varying Reynolds Re_p	140
5.1	Experimental data for radial profiles taken from literature.	154
5.2	Comparison of literature data for $4 \leq \lambda \leq 4.25$ and literature correlations plotted for $\lambda = 4.25$	155

5.3	Review of experimental results for the mean bed porosity $\bar{\epsilon}$ when varying tube-to-particle diameter λ for mono-sized, smooth, dense packed spheres	156
5.4	Exemplarily depiction of image analysis procedure using FIJI (ImageJ) for detecting circles and their respective centres and diameters comprising (a) the cropped CT-scan, (b) the find-edges-tool, (c) the binarization, and (d) the Hough Circle Transform Plug-In.	158
5.5	Reconstructed 3d packed beds of $\lambda = 3.0, 4.0, 6.25, 6.0, 7.0, 8.0$ and 9.0 based on the determined sphere center positions. The third scan with $\lambda = 6.25$ was the only scan with a packing of 4 mm spheres thus having a different scaling.	161
5.6	Plot of sphere center positions for (a) $\lambda = 3.0$, (b) $\lambda = 4.0$, (c) $\lambda = 6.0$	162
5.7	Axially- and azimuthally-averaged local porosity distribution in radial direction for $\lambda = 3.0$ to 9.0	163
5.8	Comparison of experimental data with literature correlations and Eq. (5.6b) plotted for $\lambda = 8.0$	164
5.9	Radially averaged porosity distribution in axial direction for $\lambda = 3.0$ to 9.0 and the regular close packed equivalent.	166
5.10	Obtained and extrapolated porosity error between apparent and bulk porosity as a function of tube height-to-particle diameter ratio κ	168
5.11	Comparison of radial porosity plots obtained by experiment, DigiDEM TM and Blender TM for $\lambda = 3.0, 4.0, 7.0$ and 8.0	169
5.12	Obtained curve family of radial porosity profiles for a large number of numerically generated packed beds using DigiDEM TM for packed bed sizes between $\lambda = 1.1$ and 6.0	170
5.13	Local bed porosity at the tube's center of numerical data for $\lambda = 1.1$ to 6.0 , compared to experimental data, literature data and typical correlations for radial porosity profiles.	171
5.14	Local porosity and position of extrema of the radial porosity distribution for $\lambda = 1.1$ to 9.0	172
5.15	Visualization of prediction approach of porosity profiles for packings having tube-to-particle diameter ratios < 6	173
5.16	Mean bed porosity for $\lambda = 1.1$ to 6.0 of numerical data, compared to experimental and theoretical data points and known correlations.	174
5.17	Average particle contact number and the standard deviation of its distribution for sphere packings of $\lambda = 1.1$ to 9.0	176
6.1	General simulation procedure.	194
6.2	Shape details of sphere with circumferential duct.	195
6.3	Selection of packed tubes with shapes of dimension (a, β, R)	196
6.4	Comparison of different mesh resolutions of shape $(0.5, 30, 0.5)$	197
6.5	Friction factors f' obtained for a large range of Reynolds numbers Re_p and various turbulence models for the reference packing of spheres.	198
6.6	Residence time distribution curves obtained at various heights along the packed bed.	198
6.7	Distributions of local porosity $\epsilon(x)$ and normalized axial velocity component $u_z(x)/u_0$ as obtained by the post-processing procedure displayed for a packing of the $(0.5, 30, 0.5)$ Yo-Yo shape as (a) axial distribution with $x = z$, (b) radial distribution with $x = r$, and (c) spherical distribution with $x = R$	199

6.8	Comparison of radial and spherical porosity distributions of selected shape families based on reference shape (1.0,30,0.5) and compared with a reference sphere packing.	200
6.9	Contour plot of geometric characteristics: (a,b) average bed porosity $\bar{\varepsilon}$, (c,d) normalized standard deviation $s(\varepsilon)/\bar{\varepsilon}$, and (e,f) geometric surface area a_{geo} , for the rounding radius (left) and the duct deepness (right) against duct width, respectively.	202
6.10	Schematic drawing of relevant velocity components of the flow vector $ u_{\text{mag}} $ with an angle α to the flow direction of superficial velocity u_0 and packing velocity $u_z = u_0/\bar{\varepsilon}$	204
6.11	Comparison of radial and spherical distributions of the axial velocity component u_z of selected shape families based on reference shape (1.0,30,0.5) and compared with a reference sphere packing.	205
6.12	Comparison of flow vector angle α , local porosity $\varepsilon(r)$ and normalized axial $u_z(r)$ and radial $u_r(r)$ velocity component in radial packing direction, exemplarily shown for reference shape (1.0,30,0.5) with solid and reference sphere with empty symbols.	206
6.13	Variation of normalized flow velocity $u_z(r)$ with the packing Reynolds number Re_p , exemplarily shown for shape (0,20,0.5).	207
6.14	Comparison of friction factors f' for all investigated shape variations and the reference sphere packing.	207
6.15	Comparison of friction factors f' for eight selected shapes with constant rounding radius $R = 0.5$ mm but varying superficial velocity.	208
6.16	Residence time distributions obtained with a superficial velocity $u_0 = 1.132 \text{ ms}^{-1}$	209
6.S1	Contour plot of (a,b) volume equivalent diameter d_v and (c,d) Sauter diameter d_p for the rounding radius and the duct deepness against duct width, respectively.	214
6.S2	Comparison of radial and spherical distributions of the radial velocity component u_r of selected shape families.	215
6.S3	Comparison of radial and spherical distributions of the flow vector angle component α of selected shape families.	216
6.S4	Contour plot of flow field characteristics: (a,b) normalized axial velocity $u_z(r)/u_0$, (c,d) normalized standard deviation of axial velocity $s(u_z(r))/u_z(r)$, and (e,f) normalized radial velocity $u_r(r)/u_0$, for the rounding radius (left) and the duct deepness (right) against duct width, respectively.	217
6.S5	Contour plot of geometric characteristics: (a,b) normalized standard deviation of radial velocity $s(u_r(r))/u_r(r)$, (c,d) flow vector angle α , and (e,f) normalized standard deviation of flow vector angle $s(\alpha)/\alpha$ for the rounding radius (left) and the duct deepness (right) against duct width, respectively.	218
7.1	General simulation procedure.	226
7.2	Comparison of the radial porosity distribution $\varepsilon(r)$ for a selection of shapes. In each figure, two parameters selected from the tube-to-particle diameter ratio λ , the cut shape, the duct deepness a and duct width β were varied and two kept constant. For comparison, the respective data for packings of spheres is added.	230
7.3	Effects of parameter variations including duct width β , duct deepness a , cut shape and tube-to-particle diameter ratio λ (from right to left), on the degree of achievement ϕ	231

7.4	Absolute values of the degree of achievement ϕ for all parameter combinations tested in this DoE, which the reference sphere marking the horizontal line at $\phi = 0$	232
7.5	One of presumably a range of possible shapes capable to fulfill the requirements in regard to geometric surface area and pressure drop.	232
8.1	General simulation procedure.	241
8.2	Selection of packed tubes with shapes incorporated in this study.	242
8.3	Comparison of the radial porosity distribution $\varepsilon(r)$ obtained from the investigated packings as a function of the dimensionless distance from the tube wall in particle diameters $z_r = \frac{D/2-r}{d_v}$	244
8.4	Relative deviation of average porosity $\bar{\varepsilon}$ in regard to the reference sphere packing $\bar{\varepsilon}_{\text{ref}}$	246
8.5	Relative deviation of geometric surface area a_{geo} in regard to the reference packing of spheres $a_{\text{geo,ref}}$	247
8.6	Parity plot of the standard deviation of normalized average flow $\frac{s(u_z/u_0)}{u_z/u_0}$ and porosity $s(\bar{\varepsilon})/\bar{\varepsilon}$	248
8.7	Relative deviation of average radial velocity u_r in regard to the reference sphere packing $u_{r,\text{ref}}$	249
8.8	Obtained friction factors f' for all shapes at constant fluid properties as a function of the Reynolds number Re_p	249
8.9	Relative deviation of bed effectivity η_{eff} in regard to the reference sphere packing $\eta_{\text{eff,ref}}$	252
8.10	Relative deviation of bed effectivity η_{flow} in regard to the reference sphere packing $\eta_{\text{flow,ref}}$	253
9.A1	Comparison of spherical porosity distribution $\varepsilon(R)$ of the investigated packings made of particles with certain features as a function of the dimensionless distance from the particle centers in particle diameters $z_R = \frac{2 \cdot R}{d_v}$	257
9.A2	Relative deviation of sauter diameter d_p in regard to a reference sphere $d_{p,\text{ref}}$	258
9.A3	Comparison of the radial distribution of the axial velocity component u_z/u_0 of the investigated packings made of particles with certain features as a function of the dimensionless distance from the tube wall in particle diameters z_r	258
9.A4	Comparison of the spherical distribution of the normalized axial velocity component $u_z(R)/u_0$ of the investigated packings made of particles with certain features as a function of the dimensionless distance from the particle centers in particle diameters z_R	259
9.A5	Relative deviation of average radial velocity u_r in regard to a reference sphere $u_{r,\text{ref}}$	259
9.A6	Comparison of the radial distribution of the normalized radial velocity component $u_r(r)/u_0$ of the investigated packings made of particles with certain features as a function of the dimensionless distance from the particle centers in particle diameters z_r	260
9.A7	Relative deviation of flow vector angle α in regard to a reference sphere α_{ref}	260
9.A8	Comparison of radial distribution of flow vector angle $\alpha(r)$ of the investigated packings made of particles with certain features as a function of the dimensionless distance from the particle centers in particle diameters z_r	261
9.A9	Relative deviation of standard deviation of flow vector angle $s(\alpha)$ in regard to a reference sphere $s(\alpha_{\text{ref}})$	261

List of Tables

1.1	Compositions of a selection of binder sols investigated.	25
1.2	Size distribution characteristics of investigated powders.	26
1.3	Flowability, microstructure and bed density of investigated powders.	27
1.4	Overview of final part analysis.	32
1.5	Visualization of side crush test results.	32
1.A1	Overview of characterization techniques concerning powder and powder bed.	39
1.A2	Overview of characterization techniques concerning binding agents.	40
1.A3	Characterization techniques regarding powder binder interplay.	41
1.A4	Overview of post-processing and final part analysis.	42
2.1	Characteristics of regular sphere packings.	56
2.2	Overview of known correlations relating the mean contact number \bar{N}_c to the packing porosity $\bar{\epsilon}$ of smooth mono-sized sphere packings	61
2.3	Selection of known wall effect correlations for the radial void distribution $\epsilon(r)$ of spherical packed-beds in cylindrical confinements	65
2.4	Overview of known wall effect correlations	71
2.5	Overview of shape-porosity correlations based on the sphericity	75
2.6	Overview of experimental studies relating to the structural analysis of packed-beds of non-spherical particles	79
2.7	Literature review on numerical packing generation studies sorted by shape	85
3.1	Results of fitting data to the correlation of Benyahia and O'Neill for different filling methods.	113
3.2	Properties and results of fitting data to the correlation of Benyahia and O'Neill for different materials.	114
4.1	Shape, material, characteristic diameter $d_p = 6 \cdot v_p/a_p$, cylinder aspect ratio $a_1 = d/h$, hole aspect ratio $a_2 = d_i/d$ and true sphericity $\Psi_W = d_p/d_v$ for all particles used in this study. . .	126
4.2	Shape and dimensions of tubes with hydraulic diameter $D_h = 25$ mm.	127
4.3	Mean modified Hausner ratios for $\lambda > 4$ and their respective standard errors (SE) for packings of smooth steel and rough polyamide spheres.	130
4.4	Correlation parameter overview for Eq. (4.11).	132
4.5	Shape and fitting parameter overview of rough polyamide hollow cylinders packed using the pouring and densification methods.	134
4.6	Parameter overview of filling time (inverse filling rate) relation and error propagation evaluation for packings of in the $D = 25$ mm tube.	139

5.1 Review of reported extrema locations. 156

5.2 Sum of Standard Error (SSE) of selected literature correlations and the correlation of Eq. (5.6a) in regard to the experimental data, and the SSE of the selected literature correlations fitted to the data of $\lambda = 9$ 165

6.1 Overview of designed shapes incorporated in this study. 195

6.2 Overview of flow field parameters of selected shapes and the reference sphere packing. . 206

6.3 Overview of residence time distribution characteristics for selected investigated shapes. . 209

7.1 Overview of designed shapes and their parameter selections incorporated in this study. . 228

8.1 Overview of designed shapes incorporated in this study. 242